UNIVERSIDAD DE SANTIAGO DE COMPOSTELA
Facultad de Física
Departamento de la Materia Condensada
Grupo de Física No Lineal

Effects of Turbulent Flows and Superdiffusion on Reaction-Diffusion Systems

Efecto de Flujos Turbulentos y Superdifusivos sobre un Sistema de Reacción-Difusión
Efecto de Fluxos Turbulentos e Superdifusivos sobre nun Sistema de Reacción-Difusión

Memoria presentada por **Alexandra von Kameke** para optar al grado de Doctor en Ciencias Físicas

PhD Thesis
This work was carried out
by **Alexandra von Kameke**

in the Group of Non-Linear Physics
at the Faculty of Physics
of the University of Santiago de Compostela

Santiago de Compostela, October 2012

Überall ist Wunderland.
Überall ist Leben.
Bei meiner Tante im Strumpfenband
Wie irgendwo daneben.

Überall ist Dunkelheit.
Kinder werden Väter
Fünf Minuten später
Stirbt sich was für einige Zeit.
Überall ist Ewigkeit.

Wenn du einen Schneck behauchst,
Schrumpft er ins Gehäuse.
Wenn du ihn in Kognak tauchst,
Sieht er weiße Mäuse.

Joachim Ringelnatz

Dr. Alberto Pérez-Muñuzuri, **Dr. Vicente Pérez-Muñuzuri** y **Dr. Vicente Pérez Villar**, profesores de la Universidad de Santiago de Compostela

CERTIFICAN

que la presente memoria, titulada *Effects of Turbulent Flows and Superdiffusion on Reaction-Diffusion Systems*, fue realizada por **Alexandra von Kameke** bajo su dirección y que concluye la tesis que presenta para optar al grado de Doctor en Ciencias Físicas.

Santiago de Compostela, October 2012

Alberto Pérez Muñuzuri **Vicente Pérez Muñuzuri**

Vicente Pérez Villar

Contents

Resume

Context of the Study

It is a well established but nonetheless fascinating fact that pattern formation develops from basic rules and principles and does not need a *brain* or decision unit (centralism) that decides which fraction (particle, molecule, plant, animal, etc.) of a compound has to go where in order to produce a macroscopic structure or pattern. The term macroscopic is used here in the sense, that the typical size or wavelength of the resulting structure is orders of magnitudes bigger than any single member of the compound. Pattern formation is all around us and we have gotten so used to it that in our every day lives we hardly ever ask ourselves how these patterns come about or what principles form their basis. Oftentimes, physical forces of very different type determine these principles and lead to similar overall patterns in very different systems as for example the ripples on the sand that appear at low tide and the stripes of the coat of a cat. Patterns help us to orientate in this world. They make us recognize and distinguish objects and living organisms.

Everywhere in nature these self-organized structures and patterns come across our way, in mammalian coats, in molusc shells, in cloud formation, in fish swarms and in chemical reactions, just to name a few [1–3]. The omnipresence of this self-organization, independent from the detailed mechanisms leading to it, suggests that a basic general formulation of the driving forces can be found for all the observed examples. Indeed, even though the physical, chemical and biological rules and principles underlying each of the above mentioned pattern formation processes are very different, similar mathematical formalisms can be used for its description. In this work we will refer to this self-organizing materia as active media, regardless of the details of the observed system.

Mathematical models have become the most important tool in understanding self-organization phenomena. Ilya Prigogine, who received the Nobel prize in 1977 for this work, termed these ubiquitous patterns *dissipative structures* and developed a theory for the non-equilibrium thermodynamics that lead to their formation [4]. His mathematical approach for the description of these non-equilibrium phenomena is based on statistical considerations. In the continuum limit, where single members of the system are not resolved but rather a compound concentration is monitored, non-linear equations can be used for the mathematical description of these systems. This continuum approach involves non-linear partial differential equations that describe the development of a scalar or vector field. Often these equations are derived by considerations of empirical laws stating that the fluxes (heat flow, particle flux, etc...) show a linear dependence on the generalized forces that drive them (temperature gradient, concentration gradient, etc...). Some widely known examples of non-linear partial differential equations are for instance the Navier-Stokes equation, describing the evolution of the velocity field in a fluid, or the reaction-diffusion equations, describing the evolution of concentrations of the constituents of biological or chemical systems. Examples of those non-linear equations will be discussed in the course of this work.

Nowadays, many basic principles of pattern formation and dissipative structures are well understood theoretically and in some cases also demonstrated experimentally. Nevertheless, it is still a great challenge to understand these patterns when the coupling between the different active constituents is only slightly more complicated than a simple reaction-diffusion Ansatz [5–7]. Especially some problems of immediate impact on nature and mankind, such as the velocity of a spreading disease [8], the spread of a bush-fire [9], or the creation of large oceanic plankton blooms [10], have directed attention to the role of the turbulent and chaotic transport of active media. For instance, in order to tackle the problem of disease spread, air-transportation networks [11] and dollar bill dispersal [12] have been analysed and found to be scale-free. Sloppily speaking, scale-free means that active media, here the disease causing agent, can propagate very fast along the scale free transportation paths. The details of this propagation will of course not only depend on the transport process alone, but rather on the interaction of the transport and the reaction taking place while the active media is being transported. It is thus very important to define the typical timescales on which the processes of interest occur, as we will see throughout this work.

Aim of the Study

The basic question underlying the work presented in this thesis concerns the self-organization and pattern formation in inanimate but active media when a fluid flow is present. This thesis studies the active and passive transport in turbulent and chaotic fluid flows. Thereby, the focus is mainly of experimental nature. Special interest is placed on the experimental observation and description of new patterns that emerge, when active media is subjected to a turbulent fluid flow. In particular, the effect of intense mixing as can be achieved by highly chaotic or turbulent fluid flows is to be uncovered. The first goal is to characterize and explain the phenomenon of a global reactive wave observed by Fernández García et al. in 2008 in a similar experimental realization as used in this study. The first step towards this goal is the measurement of the velocity fields caused by the Faraday experiment which is implemented here to induce mixing. This experiment consists in the vertical forcing of a container filled with liquid. Once the velocity fields are characterized, we aim for the definition of suitable analysis methods in order to study the transport of active media on different time and length-scales. To our knowledge, no previous experimental studies of an excitable chemical reaction exist where the Damköhler number is of order unity, i.e. where the timescale of the fluid flow and timescales of the reaction are similar. The analysis tools applied to our experimental model system might also partly be valid for the characterization of other reaction-diffusion-advection processes as found in many natural and men-made systems, such as plankton blooms in the ocean, chemicals in the atmosphere or bioreactors. The understanding of the role of the interplay of the typical timescales of the reaction and advection processes are to be discovered.

Summary of Results

For the generation of a turbulent fluid flow we use the Faraday experiment, which was first described by Michael Faraday in 1831. He found that a vertical vibration of a fluid-fluid interface, here water and air, would cause interfacial surface waves with a typical wavelength λ_F, known today as Faraday waves. We discovered that this experiment, besides inducing the Faraday waves, also causes a turbulent quasi two-dimensional fluid flow, whenever the liquid layer is shallow. Here we name this fluid flow Faraday flow. The velocity fields of the Faraday flow are derived from experimental particle image velocimetry (PIV) measurements. In particular, we observe a double cascade similar to the one for perfect two-dimensional systems as described by Kraichnan in 1967. A clear bend, where the slope changes abruptly can be seen in the energy spectra E_k in the wavenumber space, close to the wavenumber of the Faraday waves k_F. For strong forcings, the scaling below the wavenumber of the bend is close to the Kolmogorov scaling of $E_k \propto k^{-5/3}$, as theoretically predicted for an inverse energy cascade in two-dimensional turbulence. For lower forcings, the scaling is noticeably less steep. This dependency might be due to a decrease in the rate at which energy becomes transported from lower to higher scales. For wavenumbers higher than the wavenumber of the bend, the energy per wavenumber falls off more rapidly for all forcings with a scaling close to the one of a direct enstrophy cascade in two-dimensional turbulence, $E_k \propto k^{-3}$.

Transport in this Faraday fluid flow is analysed via the calculation of the relative and absolute dispersion as well as the Finite-Size-Lyapunov-Exponents (FSLE). Both two-particle measures, i.e., the FSLE and the relative dispersion, show scaling exponents corresponding to Richardson dispersion which is expected in the range of scales of the inverse cascade according to dimensional arguments [13]. These scaling exponents do not change noticeably with the strength of the acceleration of the Faraday experiment. Results are obtained for experimentally tracked particles and also for particles that are numerically advected in the PIV-velocity fields. Since the scaling relation of the inverse energy cascade $E_k \propto k^{-5/3}$ is identical for the direct downwards three-dimensional energy cascade, we also determined the energy- and enstrophy fluxes and their signatures. The findings again agree with the Kraichnan picture of an inverse energy transfer upscale and a direct enstrophy cascade downscale. However, no well defined inertial ranges, where the fluxes remain constant over a wide range of scales, are obtained. This deviation might be most probably due to the presence of bottom friction. The second and third order structure functions calculated for all different forcings show the same behaviour, while the signature of the third order structure function indicates an inverse direction of the energy flux, scaling ranges with a constant slope cannot be distinguished. Nevertheless, extended self-similarity as defined by Benzi et al. in 1993 [14] can be observed for the ratio of the second and the third order structure function, indicating that the structure of the velocity field is self-similar as expected for a turbulent fluid flow. The probability distribution of longitudinal velocity differences at different scales suggests intermittency in the direct enstrophy cascade for spatial scales smaller than the typical Faraday wavelength λ_F.

We find that new patterns arise, when active media, here in form of an excitable CHD-based Belousov-Zhabotinsky chemical reaction, is subjected to the turbulent fluid flow generated by the Faraday experiment. We observe large, boosted spiral and target patterns which are caused by the competition of the chemical reaction and a turbulent diffusion provoked by the turbulent fluid flow. The large scale patterns have typical wavelengths of more than $5\,\mathrm{cm}$ and show an overall similarity to their molecular diffusion driven counterparts. Especially interesting is the observation that the mean velocity of the wavefronts can be predicted by the well-known Fisher-Kolmogorov-Petrovski-Piskunov (FKPP) equation and scales thus as $v_f \propto \sqrt{D_*}$. This is an important result as it supports the validity of the usage of an effective turbulent diffusion coefficient D_*. The effective diffusion coefficient is a fundamental concept, as it allows one to parametrize the overall spatio-temporal dynamics of a fluid flow using only one single constant instead of having to take into account all the details of the velocity field. Nevertheless, besides the overall similarity, also some striking differences to the molecularly driven spiral and target waves are observed for the boosted patterns which are most likely due to the various timescales important during the activation of the excitable chemical reaction. More precisely, the local picture of the leading wavefront is highly filamentary, causing the local front velocities to vary dramatically which suggests that the rapid forward reaction of the chemical activation wave experiences a transport which cannot yet be described by effective diffusion on these timescales. A characterization of the front profiles reveals, that contrarily to what would be expected for perfect diffusive wavefronts, the width of the rising edge of the wavefront does not scale with $\sqrt{D_*}$ but stays rather constant within the error of the measurement.

The local effects of the turbulent transport of the wavefront are studied in detail, because the absolute and relative dispersion appear anomalous on certain time and length scales. We present a novel analysis technique for the local expansion of the boosted wavefront, which we call masking algorithm, and find evidence that the expansion is scale-free on considerable length scales. In agreement with these findings the variance $\sigma^2(t) \propto t^\gamma$ of the reactive wave grows supralinear in time with an exponent $\gamma > 2$ for short times which indicates that the leading wavefront experiences superdiffusive transport. The statistics of single, floating micro particles subjected to the flow are studied. The analysis of the particle trajectories allows us to derive flight time and jump length distributions and find evidence that micro-particles undergo complex trajectories related to Lévy statistics.

In order to better understand the effect that a locally scale-free transport can have when combined with excitable dynamics, we formulate a highly simplified network based model. The scale-free transport is modelled using a geographically scale-free network where each node has connections drawn from a power-law with a finite cut-off value: $p(r) \propto r^{-\mu}$ for $r < r_c$. The excitable dynamics are simulated by a cellular automata. The results from the geographically scale-free network are compared to the results obtained from a network with connections drawn from a Gaussian distribution. The distribution functions of the deviations of the wavefront from a mean wavefront profile, derived from an average over many wavefronts at different timesteps, are calculated for the dynamics of both networks. We find that deviations are much larger and much more frequent in the case of the geographically scale-free network. The distribution of the deviations from the mean of the experimental wavefront are comparable to those observed in the geographically scale-free network. The masking algorithm, also used for the characterisation of the expansion of the experimental wavefront, recovers the scaling exponent introduced when the network is constructed. This hints at the ability of the masking algorithm to detect the underlying locally scale-free dynamics of the excitation process caused by the scale-free transport.

Finally, in the last part of this thesis we focus on the non-trivial dependence of the asymptotic effective relative diffusion in a chaotic flow which mimicks the Gulf Jet Stream on noise. The noise can also be understood here as some kind of parametrized small scale turbulence. Three different diffusion regimes are observed depending on the noise intensity. For intermediate noise levels the asymptotic diffusion decreases with noise intensity at a rate which is linearly dependent on the meandering amplitude of the jet-flow. For an increasing noise level the fluid transport passes through a superdiffusive regime and finally becomes diffusive again at large noise intensities. This results are in contrast to what was stated in literature [15, 16]. The presence of inner circulation regimes in the flow is found to be determinant to explain the observed behaviour. The understanding of the effect of the noise level on chaotic flows is important for oceanographic problems where small scale motion is sometimes parametrized as noise. We show that the exact value of this parametrisation may have crucial effects on the dynamical regime of transport in jet-like fluid flows.

Layout of the Thesis

In this thesis, we will focus on the interaction of reaction and transport processes. In particular, we will mostly be concerned with transport caused by a fluid flow. Large parts of this thesis reports purely experimental work, leaving the numerical and analytical examination of the results as a to-do for the future. An important and surprising result of our studies was the discovery of the Faraday flow, which turned out to be a promising realization of quasi-two dimensional turbulence, as will be seen in Chap. 3. The experimental characterization and description of the Faraday flow forms thus the basis of the subsequent work that deals with the interaction of turbulence and active media, which in this study is represented by a chemical reaction, known as Belousov-Zhabotinsky reaction.

The study of pattern formation in active media in fluid flows involves both, the determination of the properties of velocity fields and the description and analysis of the novel patterns that arise. We will see, that the novel patterns that arise due to this interaction show at the same time both, surprising similarities to their molecular-diffusion-induced counterparts and striking differences.

The work is organized as follows. The first chapter gives a short introduction to the field of study and concentrates thereby on the physical and mathematical fundaments of the different processes involved. In particular, the general mechanisms of reaction-diffusion systems and fluid flows are explained. The fluid flow in our experimental study is created by the Faraday experiment which consists in the vertical vibration of the fluid. This vibration excites surface waves and bulk fluxes [17–19]. Some of the underlying theory of their creation is also treated in this chapter. In chapter 2 the experimental setup and details of the data analysis are explained. Chapter 3 studies the velocity field created by the Faraday experiment and its statistical characteristics. When active media is subjected to this fluid flow, which we termed Faraday flow, interesting patterns can be observed. The global phenomenon of these patterns and its local dynamics are studied in chapter 4 and chapter 5, respectively. Chapter 6 deals with the construction of a simple numerical model that manages to reproduce some of the experimentally observed characteristics. The concepts of enhanced transport and superdiffusion accompanying our results throughout this study are applied to a numerically produced jet-like fluid flow in chapter 7. Finally, in chapter 8 the results of the different parts of this thesis are summarized and evaluated concerning its overall scientific context. Some ideas for further studies and improvements are also discussed.

Several chapters of this theses coincide in large parts with scientific articles published previously in peer-reviewed journals.

- Chapter 3 corresponds in large parts to the published article [20].
- Chapter 5 corresponds in large parts to the published article [21].
- Chapter 7 corresponds in large parts to the published article [15].

Resumen

Contexto del Estudio

Si bien es un hecho establecido que la formación de patrones se desarrolla a partir de normas y principios básicos, no deja de ser fascinante que ésta no necesite de una unidad de decisión o *cerebro* (centralismo) la cual decida qué fracción (partícula, planta, animal, etc) del compuesto, en su sentido más amplio, ha de moverse hacia donde para producir una estructura o patrón macroscópico. El término macroscópico se utiliza aquí en el sentido de que el tamaño típico, por ejemplo, la longitud de onda de la estructura resultante, es ciertos órdenes de magnitud más grande que un solo miembro del conjunto. La formación de patrones está siempre a nuestro alrededor y estamos tan acostumbrados a ella que en nuestro día a día, casi nunca nos preguntamos cómo aparecen estos patrones o qué principios forman su base. A pesar de que las fuerzas físicas que determinan estos principios tienen orígenes diferentes, a menudo conducen a patrones similares globales en sistemas tan diferentes como, por ejemplo, las ondas en la arena que aparecen durante la marea baja o las rayas del pelaje de un gato. Los patrones nos ayudan a orientarnos en este mundo, así como también, a reconocer y distinguir los objetos y los organismos vivos.

Estas estructuras auto-organizadas y los patrones asociados, están presentes en todo momento en la naturaleza, véanse por ejemplo, la formación de extremidades en mamíferos o las conchas en los moluscos, o también, la formación de nubes, las estructuras que aparecen en la piel de muchos peces tropicales, y como no, los patrones de concentración observados en muchos sistemas químicos, así como un largo etcétera [1–3]. La omnipresencia de esta auto-organización, independiente de los mecanismos concretos que conducen a ella, sugiere que se puede encontrar una formulación general básica de los motores de la formación para todos los ejemplos observados. En efecto, a pesar de que las reglas físicas, químicas y biológicas y los principios que subyacen a cada uno de los mencionados procesos de formación de patrones son muy diferentes, se pueden utilizar formalismos matemáticos similares para su descripción. En este trabajo nos referiremos a esta materia de auto-organización con la expresión medio activo, independientemente de los detalles del sistema observado.

Los modelos matemáticos se han convertido en la herramienta más importante para la comprensión de los fenómenos de auto-organización. Ilya Prigogine, quien recibió el premio Nobel en 1977 por este trabajo, denominó estos patrones universales *estructuras disipativas* y desarrolló la teoría de la termodinámica fuera equilibrio que conducen a su formación [4]. Su enfoque matemático para la descripción de estos fenómenos fuera de equilibrio se basa en consideraciones estadísticas. En el límite continuo, donde los miembros individuales del sistema no se resuelven, sino más bien se supervisa una concentración del compuesto, se puede utilizar ecuaciones no lineales para la descripción matemática de dichos sistemas. Este enfoque continuo implica ecuaciones no lineales en derivadas parciales que describen el desarrollo de un escalar o un campo vectorial. A menudo, estas ecuaciones se derivan de considerar leyes empíricas que indican que los flujos (por ejemplo un flujo de calor, flujo de partículas, etc ..) muestran una dependencia lineal con las fuerzas generalizadas que los impulsan (por ejemplo el gradiente de temperatura, gradiente de concentración, etc ..). Algunos ejemplos bien conocidos de ecuaciones no lineales en derivadas parciales son, por ejemplo, la ecuación de Navier-Stokes, que describe la evolución del campo de velocidad en un fluido, o las ecuaciones de reacción-difusión, que se utilizan para describir la evolución de las concentraciones de los constituyentes de los sistemas biológicos o químicos. Ejemplos de esas ecuaciones no lineales se discutirán a lo largo de este trabajo.

Hoy en día muchos principios básicos de formación de patrones y estructuras disipativas son bien comprendidos teóricamente y, en algunos casos, también se han demostrado experimentalmente. Sin embargo, sigue siendo un gran desafío el hecho de entender la formación de estos patrones en presencia de acoplamientos complejos entre los componentes activos diferentes, más allá de un simple Anstaz de reacción-diffusión [5–7]. Es decir, cuando otro tipo de tranporte además de la difusión está presente. Especialmente, en algunos problemas de gran impacto para la naturaleza y la humanidad, como por ejemplo la velocidad de propagación de una enfermedad [8], la propagación de un fuego [9], o la creación de grandes cantidades de plancton oceánico [10], han dirigido la atención del mundo cientifico sobre el papel que juega el transporte turbulento y caótico en la formación de patrones en los medios activos. Por ejemplo, con el fin de abordar el problema de la propagación de una enfermedad, se han analizado las redes de transporte aereo [11] y la dispersión de los billetes de dólar [12] y se ha encontrado que son procesos que carecen de una escala típica. Estos procesos se llaman procesos libres de escala o invariantes de escala. Básicamente, el término libre de escala significa que los medios de comunicación activos, por ejemplo en el caso de un agente que causa una enfermedad, pueden propagarse muy rápidamente a lo largo de estas trayectorias de transporte. Los detalles de esta propagación no dependen, por supuesto, únicamente del proceso de transporte, sino mas bien de la interacción del transporte con las reacciónes que tienen lugar mientras que dichos medios activos están siendo transportados. Por lo tanto, es muy importante definir las escalas de tiempo típicas de estos procesos de interés como veremos a lo largo de este trabajo.

Objetivo del Estudio

La pregunta básica que sustenta el trabajo presentado en esta tesis se refiere a la auto-organización y la formación de patrones en medios inanimados pero activos cuando un flujo de fluido está presente. Esta tesis estudia el transporte activo y pasivo de los flujos de fluidos turbulentos y caóticos. Por ello, la atención se centra principalmente en la exploración de dicho problema de forma experimental. Especial interés se deposita en la observación experimental y la descripción de nuevos patrones emergentes cuando se someten los medios activos a un flujo de fluido turbulento. En particular, el efecto de mezclado intenso como se puede lograr por los flujos de fluido altamente caóticos o turbulentos está por ser descubierto. El primer objetivo es caracterizar y explicar el fenómeno de una onda de elevada concentración global en un medio excitable observada por primera vez por Fernández García et al. en 2008 en una realización experimental similar a la nuestra. El primer paso hacia este objetivo es la detallada medición de la mezcla y del campo de velocidad causado por el experimento de Faraday. Este experimento consiste en la vibración vertical de un recipiente lleno de líquido. Una vez que el campo de velocidad, y de paso la mezcla, se ha caracterizado tratamos de conseguir una definición de unos métodos de análisis adecuados con el fin de estudiar el transporte de medios activos en diferentes tiempos y a las escalas de longitud relevantes para la mezcla. Especialmente nos centramos en el rango intermedio del numero de Damköhler, es decir, cuando las escalas de tiempo del flujo de fluido y de la reacción son similares. Esto, a nuestro conocimiento, no se ha estudiado anteriormente en un sistema experimental con una reacción quimica excitable. Las herramientas de análisis aplicadas a este sistema se pueden entender como modelo experimental, también podrían ser parcialmente válidos para la caracterización de otros procesos de advección-reacción-difusión. Estos se encuentran en muchos sistemas naturales y artificiales, tales como las floraciones de plancton en el océano, los productos químicos en la atmósfera o los biorreactores. La comprensión del papel de la interacción de las escalas de tiempo típicas de la reacción y los procesos de advección están por descubrirse.

Resumen de los Resultados

Para la generación de un flujo de fluido turbulento, se utiliza en este trabajo el experimento de Faraday, el cual fue descrito por primera vez por Michael Faraday en 1831. Se encontró que una modulación vertical de una interfaz líquido-líquido, aquí el agua y el aire, puede causar ondas interfaciales de superficie con una longitud de onda λ_F típica, conocida hoy en día como ondas de Faraday. En esta tesis hemos descubierto que este experimento, además de inducir las ondas de Faraday, también causa un flujo de fluido turbulento cuasi bidimensional, para una capa de líquido superficial. El flujo de fluido se deriva de las mediciones de la velocimetría de imagen experimental de partículas (particle image velocimetry, PIV). En particular, se observa una doble cascada de energia similar a la de sistemas perfectos bidimensionales como fué descrito por Kraichnan en 1967. En el espectro de energía en el espacio de número de onda E_k, se puede ver una curvatura bien discernible, donde la pendiente cambia abruptamente. Para forzamientos fuertes, para el escalado a continuación del número de onda donde se distingue la curvatura, se encuentra una pediente cerca de la de Kolmogorov, con $E_k \propto k^{-5/3}$. Esto se corresponde a lo predicho teóricamente por Kraichnan para una cascada de energía inversa de turbulencia en dos dimensiones. Mientras, para menores forzamientos, la pendiente es notablemente menos empinada, lo que podría ser debido a una disminución en la velocidad a la que la energía se convierte en estructuras de menor a mayor escala. Para números de onda más altos que el número de onda de la curvatura extrema, la energía por número de onda cae más rápidamente para todos los forzamientos con una escala cercana a la de una cascada enstrophy directa en turbulencia bidimensional $E_k \propto k^{-3}$.

El transporte en este flujo de fluido de Faraday es analizado a través del cálculo de la dispersión relativa y absoluta, así como los exponentes de Lyapunov de tamaño finito (FSLE). Ambas medidas de la dispersion de dos partículas, es decir, el FSLE y la dispersión relativa, muestran exponentes de escala correspondientes a la dispersión de Richardson, la cual se espera en el rango de las escalas de la cascada inversa. Estos exponentes del transporte no cambian notablemente con la fuerza de la aceleración del experimento de Faraday. Los resultados se obtienen para las partículas experimentalmente perseguidos y aquellos numéricamente advectados en los campos de velocidad obtenidos mediante PIV. Además, también los flujos de energía y enstrofia se calcularon y sus signos también están de acuerdo con el concepto formulado por Kraichnan que se corresponde a la transferencia de energía hacia escalas espaciales grandes, y la transferencia de la enstrofia hacia escalas pequeñas. Sin embargo, y en contraposición a lo que predice la teoría de Kraichnan, no se obtienen rangos bien definidos inerciales donde los flujos de energia y de enstrofia se mantengan constantes en un amplio rango de numeros de onda. Las funciones de estructura de segundo y tercer orden calculadas para todos los forzamientos diferentes, muestran el mismo comportamiento, mientras que el signo de la función de estructura de tercer orden indica una dirección inversa del flujo de energia, no se pueden distinguir rangos de escala con una pendiente constante. No obstante, se puede observar la auto-similitud extendida según la definición de Benzi et al. en 1993 [14] basado en la relación de la función de la estructura de segundo y tercer orden. Esto indica que la estructura del campo de velocidad es auto-similar, según lo esperado para un flujo de fluido turbulento donde la intermitencia es minima. La distribución de probabilidad de las diferencias de velocidad longitudinal a diferentes escalas sugiere que podria existir una intermitencia en la cascada enstrofia directa para escalas espaciales más pequeñas que la longitud de onda típica de Faraday λ_F.

Encontramos que cuando un medio activo, aquí en forma de una reacción química excitable basado en Belousov-Zhabotinsky con CHD se somete, a un flujo de fluido turbulento alcanzado por el experimento de Faraday, surgen nuevos patrones. Observamos enormes ondas espirales y ondas de tipo target, que son causadas por la competencia de la reacción química y una difusión turbulenta causada por el flujo de fluido turbulento. Los patrones de gran escala que observamos tienen longitudes de onda típicas de más de $5\,$cm y muestran una similitud con sus homólogos impulsados por la difusión molecular. Es especialmente interesante el hecho de que la velocidad media de los frentes de onda de dichos patrones enormes puede ser predicha por la ecuación bien conocida de Fisher-Kolmogorov-Petrovski-Piskunov (FKPP) $v_f \propto \sqrt{D_*}$. Este es un resultado importante ya que apoya la validez del uso de un coeficiente de difusión eficaz turbulento D_*. Este coeficiente de difusión efectivo es un concepto fundamental, ya que permite parametrizar, y por tanto generalizar, la dinámica espacio-temporal del transporte activo y pasivo con un solo valor en lugar de tener que tomar en cuenta todos los detalles del campo de velocidad. Sin embargo, también se observan algunas diferencias notables para los patrones enormes con respecto a las ondas impulsadas molecularmente, muy probablemente debido a las diversas escalas de tiempos relevantes durante la activación de la reacción química excitable. Más en concreto, la forma local del frente de onda de excitacíon es altamente filamentosa en el caso de las ondas enormes. Esto también puede provocar que las velocidades de la frente de onda puedan variar dramáticamente lo que sugiere que la rápida reacción hacia adelante de la onda de activación química experimenta un transporte que aún no se puede describir por difusión sobre estas escalas de tiempo. Una caracterización de los perfiles frontales revela, que, contrariamente a lo que se espera para unas frentes de ondas perfectamente difusivas, el flanco de subida del frente de onda enorme no se escala con $\sqrt{D_*}$ pero se mantiene casi constante dentro del error de la medición .

Los efectos locales del transporte turbulento del frente de onda se estudian en detalle y encontramos que la dispersión absoluta y relativa se comportan de forma anómala para ciertos tiempos y escalas. Se presenta una técnica novedosa para el análisis de la expansión local del frente de onda enorme excitable, lo que llamamos algoritmo de enmascarado, y se encuentran pruebas de que la expansión de dicho frente es libre de escala a escalas de longitud considerables para el sistema. De acuerdo con estos resultados la varianza $\sigma^2(t) \propto t^\gamma$ de la onda enorme crece supralinealmente en el tiempo con un exponente $\gamma > 2$ para tiempos cortos e indica que el frente de onda principal experimenta un transporte superdifusivo. Las estadísticas de micro-partículas flotantes individuales, sometidas al flujo son estudiadas y el análisis de las trayectorias de las partículas nos permite derivar distribuciones del tiempo de vuelo y de la longitud del salto y encontrar pruebas de que las micro-partículas experimentan trayectorias complejas relacionadas con estadísticas de Lévy.

Con el fin de comprender más profundamente el efecto que puede tener un transporte localmente libre de escala cuando se combina con la dinámica excitable, formulamos un modelo basico muy simplificado basado en redes. El transporte libre de escala se modela utilizando una red libre de escala geográfica en la que cada nodo tiene conexiones derivadas de una distribución de potencias con un valor de corte finito que limita el salto mas grande possible: $p(r) \propto r^{-\mu}$ para $r < r_c$. La dinámica excitable de cada nodo esta simulado por un autómata celular. Los resultados de la red geográficamente libre de escala se comparan con los resultados de una red con conexiones extraídas de una distribución Gaussiana. Se calculan para la dinámica de ambas redes las funciones de distribución de las desviaciones del frente de onda de un perfil frontal medio, derivada de un promedio sobre muchos frentes a pasos temporales diferentes. Se encuentra que las desviaciones son mucho más grandes y mucho más frecuentes en el caso de la red geográficamente libre de escala. La distribución de las desviaciones de la media del frente de onda experimental es comparable a la que se observa en la red geográficamente libre de escala. El algoritmo de enmascarado, que también se ha utilizado para la caracterización de la expansión del frente experimental, recupera el exponente de escala introducido cuando la red se construyó. Esto apunta a que el algoritmo de enmascaramiento tiene la capacidad de detectar la dinámica del proceso subyacente de excitación que por la definición es localmente libre de escala.

Finalmente, la última parte de esta tesis se centra en la dependencia no trivial de la difusión asintótica en un flujo caótico cuando un cierto ruido está presente. Este sistema imita la corriente del Golfo (jet del Golfo). La intensidad del ruido se puede entender como una especie de difusión a escalas pequeñas. Se observan tres regímenes de difusión diferentes dependiendo de la intensidad del ruido. Para niveles de ruido intermedianos la difusión asintótica disminuye con la intensidad de ruido a una velocidad que es linealmente dependiente de la amplitud del flujo serpenteante del jet. Aumentando el nivel de ruido el transporte en el flujo pasa por un régimen superdifusivo y finalmente se vuelve difuso de nuevo a intensidades de ruido de gran tamaño. Estos resultados contrastan con lo que se afirma en la literatura [16]. Se encuentra que la presencia de regímenes de circulación internos en el flujo son determinantes para explicar el comportamiento observado. La comprensión del efecto del nivel de ruido en los flujos caóticos es importante para los problemas oceanográficos, donde muchas veces la difusión a pequeña escala esta parametrizada como un ruido. Se demuestra que el valor exacto de esta parametrización puede tener efectos importantes sobre el régimen dinámico de transporte en flujos de fluidos tipo jet, como el de la corriente del Golfo.

Estructura de la Tesis

Esta tesis se centra en la interacción de una reacción con procesos de transporte. En particular, en su mayoría se refiere al transporte causado por el flujo de fluido. Gran parte de esta tesis, se trata de trabajo puramente experimental, dejando el examen analítico y numérico de los resultados como una tarea pendiente para el futuro. Un resultado importante y sorprendente de nuestros estudios fue el descubrimiento del flujo de Faraday, que resultó ser una prometedora realización de un experimento modelo de turbulencia cuasi bidimensional, ver Cap. 3. La caracterización experimental y la descripción del flujo de Faraday forman así la base del trabajo posterior que se ocupa de las interaccióness de la turbulencia y de los medios activos, que en este estudio se representan en una reacción química conocida como Belousov-Zhabotinsky.

El estudio de la formación de patrones en medios activos sometidos a un flujo de fluido implica tanto la determinación de las propiedades de los campos de velocidad como también la descripción y análisis de los patrones novedosos que pueden surgir. Veremos durante los próximos capítulos que surgen nuevos patrones debido a esta espectacular interacción. Observamos que existen al mismo tiempo tanto similitudes sorprendentes como tambén diferencias notables a los patrones homólogos inducidos por la difusión molecular .

El trabajo está organizado de la manera siguiente: En el primer capítulo se ofrece una muy breve introducción al campo de estudio y luego pasa a concentrarse en los fundamentos físicos y matemáticos de los diferentes procesos involucrados. En particular, los mecanismos generales de los sistemas de reacción-difusión y las corrientes de fluido se explican. El flujo de fluido en nuestro estudio experimental se crea por el experimento de Faraday, que consiste en la vibración vertical del fluido. Esta vibración estimula las ondas superficiales y flujos en el interior del fluido [17–19]. Parte de la teoría fundamental de su creación también se tratará en este capítulo. En el capítulo 2 la configuración experimental y los detalles del análisis de datos se explicarán. Capítulo 3 estudia el campo de velocidades creado por el experimento de Faraday y sus características estadísticas como por ejemplo las cascadas de energía y enstrofia. Cuando se somete un medio activo a este flujo de fluido, que denominamos flujo de Faraday, se puede observar patrones interesantes. El fenómeno global de estos patrones y sus dinámicas locales se estudian en el capítulo 4 y el capítulo 5, respectivamente. El capítulo 6 se dedica a la construcción de un modelo numérico simple que logra reproducir algunas de las características observadas en los patrones experimentalmente. Los conceptos de transporte incrementado y de la superdifusión que acompañan a nuestros resultados a lo largo de esta tesis se aplican a un modelo numerico de un flujo de fluido en el capítulo 7.

Por último, en el capítulo 8 se presentan los resultados de las diferentes partes de esta tesis y se evalúa su relación con el contexto científico general. Ademas se proponen algunas ideas para nuevos estudios y mejoras de lo estudiado.

Algunos capítulos de esta tesis coinciden en partes con articulos previamente publicados en distintas revistas científicas:

- Capitulo 3 se corresponde en grandes partes al artículo publicado [20].
- Capitulo 5 se corresponde en grandes partes al artículo publicado [21].
- Capitulo 7 se corresponde en grandes partes al artículo publicado [15].

1

Theoretical Fundaments

The propagation and pattern formation of passive and active media in chaotic flows is a field of study of enormous interest for a variety of different disciplines reaching from biology over chemistry and physics as far as financial mathematics and social studies [12, 22–24]. Especially the influence of advection on the spatiotemporal development of active media is of relevance for many natural systems, such as plankton species in the ocean (see Fig. 1.1), atmospheric chemistry, or convection in the earth mantle [3]. For these reaction-diffusion-advection systems it is of crucial interest to define typical dynamics as pattern formation or the speed of propagation and expansion of the active media.

1.1 Reaction-Diffusion-Advection Systems

Recently, reaction-diffusion-advection systems have received increasing attention in different research areas as they provide the possibility to study many of the above described phenomena. Mathematically, reaction-diffusion-advection systems can be written as partial differential equations

$$\frac{\partial \mathbf{c}}{\partial t} = \mathbf{f}(\mathbf{c}) + \nabla \cdot (D \nabla \mathbf{c}) + (\mathbf{v} \cdot \nabla)\mathbf{c}, \tag{1.1}$$

where $\mathbf{c}$ is the vector of the concentrations of the reactants and $\mathbf{f}(\mathbf{c})$ is the vector of the reaction functions. The second term on the right hand side denotes the diffusion term and the last stands for the advection with $\mathbf{v} = \mathbf{v}(\mathbf{x}, t)$ being the velocity field. The different parts of this equation, the reaction, the diffusion and the advection will be discussed in detail in the course of this chapter. To integrate this equation numerically one needs to evolve the Eulerian velocity field in time. For turbulent flows this can be a rather complex task due to the strong time dependence of the velocity field. If the fluid flow is two-dmensional

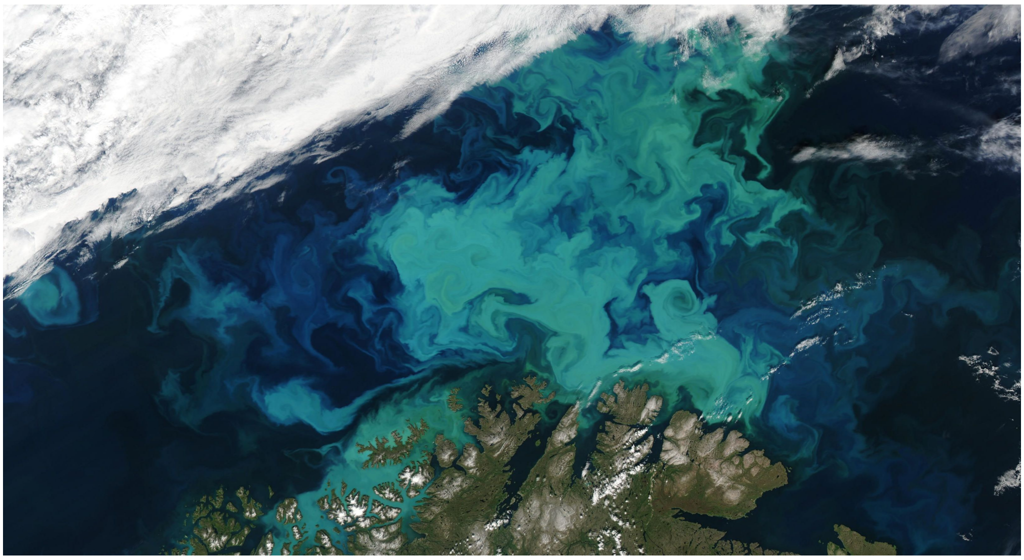

Fig. 1.1: A natural reaction-diffusion-advection phenomenon. Satellite image of a phytoplankton bloom in the Norwegian Sea from the 2003-07-19. Provided by the Visible Earth Project, NASA/Goddard Space Flight Center, $http : //visibleearth.nasa.gov/view\_detail.php?id = 5611$. It is important to raise the question to what extend all three dynamics, reaction, diffusion and advection produce, form and propagate the bloom.

and irrotational a stream function can be formulated that satisfies:

$$\mathbf{v}(\mathbf{x}) = \begin{pmatrix} \frac{\partial \Psi}{\partial y} \\ \\ -\frac{\partial \Psi}{\partial x} \end{pmatrix} \tag{1.2}$$

For stationary flows, where $d\Psi/dt = 0$, the stream function is the equivalent to the Hamiltonian of a point mass and thus the trajectories of the particles are fully known. Lines of constant Ψ are called streamlines.

1.1.1 Reaction-Diffusion Systems

Reaction-diffusion models are used to describe a wide range of pattern formation processes occurring in nature. Especially in biology, physiology and chemistry they have been used with great sucess [2]. Reaction-diffusion systems can be written as partial differential equations:

$$\frac{\partial \mathbf{c}}{\partial t} = \mathbf{f}(\mathbf{c}) + \nabla \cdot (D \nabla \mathbf{c}), \tag{1.3}$$

where $\mathbf{c}$ is again the vector of the concentrations of the reactants and $\mathbf{f}(\mathbf{c})$ is the vector of the reaction functions, and the last term on right hand side denotes the diffusion term. The reaction function $\mathbf{f}$ can be nonlinear which is the case for the autocatalytic Belousov-Zhabotinsky reaction that we study in this thesis (introduced below). An autocatalytic reaction means that at least one of the products of the reaction is also a reactant and is therefore auto-generating itself. If the diffusion coefficient D is independent of the spatial variables the diffusion term can be simplified to $D\Delta\mathbf{c}$.

In this study the reaction term $\mathbf{f}(\mathbf{c})$ represents a chemical reaction. Nevertheless, we want to point out that similar reaction terms can also be formulated for biological processes, population dynamics and even diseases cycles. Thus the results of this study concerning the chemical Belousov-Zhabotinsky reaction might be generalised to other reaction-diffusion-advection problems.

1.1.2 Belousov-Zhabotinsky Reaction

The chemical Belousov-Zhabotinsky reaction (BZ) [25] is an experimentally and theoretically well studied active system, producing spatiotemporal patterns and reaction fronts. The detailed reaction dynamics of the BZ reaction are very complex and a large variety of different chemical intermediate states are formed during the reaction process [26]. The overall process consists in the oxidative bromination of an organic substrate by acidic bromate which is catalyzed by an oxidation-reduction metal ion pair as for instance Cerium Ce^{3+}/Ce^{4+} or Ferroin $Fe^{2+}(phen)_3/Fe^{3+}(phen)_3$. Ferroin has the advantage over Cerium that it can be well observed in the visible range and thus it was used in this study. The originally employed organic malonic acid used as an organic substrate was replaced by $1,4$-cyclohexanedione (CHD) in this study [27].

A variety of different mathematical models exist that describe this reaction. In order to create manageable models many details of intermediate reactions taking place are not accounted for. According to the *slaving principle*, that states that it is possible to disregard those variables that relax very fast to the stationary state, the number of variables in the models can be reduced [28].

Three variable Oregonator

One of the widely accepted and oftentimes employed models that is able to qualitatively reproduce the basic regimes of the BZ reaction is the Oregonator model of three variables. It is named after the University of Oregon, where Field and Noyes first developed this model [29]. The basic scheme of the reaction dynamics considered is shown in Tab. 1.1

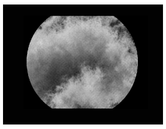

Reaction	Velocity of Reaction
$A + Y \to X + P$	$r = k_3 AY$
$X + Y \to 2P$	$r = k_2 XY$
$A + X \to 2X + 2Z$	$r = k_5 AX$
$2X \to A + P$	$r = k_4 X^2$
$B + Z \to 1/2fY$	$r = k_c BZ$

Table 1.1: Scheme of intermediate reactions of the BZ reaction that are considered for the three variable Oregonator model [29]. $A = [HBrO_3^-]$, B is the concentration of the organic compound malonic acid (or CHD), $P = [HOBr]$, $X = [HBrO_2]$, $Y = [Br^-]$, and Z is the concentration of the catalyst, for instance $[Ce^{3+}]$. The right column shows the velocities of the reactions and k_i are the reaction constants.

As detailed in [29] this leads to the model equations:

$$\begin{aligned} \frac{dX}{dt} &= k_3 AY - k_2 XY + k_5 AX + k_4 X^2 \\ \frac{dY}{dt} &= -k_3 AY - k_2 XY + 1/2 f k_c BZ \\ \frac{dZ}{dt} &= 2k_5 AX - k_c BZ \end{aligned} \tag{1.4}$$

Transforming to dimensionless variables

$$x = \frac{2k_4 X}{k_5 A},\ y = \frac{k_2 Y}{k_5 A},\ z = \frac{k_c k_4 BZ}{(k_5 A)^2},\ \tau = k_c Bt \tag{1.5}$$

leads us to the dimensionless form of the three variable Oregonator model:

$$\begin{aligned} \frac{dx}{d\tau} &= \epsilon(x - x^2 - xy + qy) \\ \frac{dy}{d\tau} &= \acute{\epsilon}(-qy - xy + fz) \\ \frac{dz}{d\tau} &= x - z, \end{aligned} \tag{1.6}$$

where ϵ, $\acute{\epsilon}$ and q are dimensionless parameters:

$$\epsilon = \frac{k_c B}{k_5 A},\ \acute{\epsilon} = \frac{2k_c k_4 Y}{k_5 k_2 A},\ q = \frac{2k_3 k_4}{k_5 k_2} \tag{1.7}$$

Two variable Oregonator. A further reduction to a two variable model was achieved by Tyson [30, 31]. The two variables can be identified with $[HBrO_2]$ (c_1, fast variable) and the oxidation-reduction metal ion pair used (c_2, slow variable). The basic assumption for the derivation of the model is that $\acute{\epsilon} \ll 1$ and $\acute{\epsilon} \ll \epsilon$, so that $\dot{y} \equiv 0$ and therefore $y = f_z/(q+x)$. Then, the two dimensional Oregonator in dimensionless form reads:

$$\frac{dc_1}{dt} = \underbrace{\epsilon(c_1 - c_1^2 - f\ c_2\ \frac{c_1 - q}{c_1 + q})}_{f(c1,c2)} \tag{1.8}$$

$$\frac{dc_2}{dt} = \underbrace{c_1 - c_2}_{g(c1,c2)} \tag{1.9}$$

This two variable model belongs to the class of the activator-inhibitor systems, where the activator c_1 is the autocatalyst that triggers its own production and the c_2 is the inhibitor that suppresses the production of the activator if its concentration becomes too high [28]. Inserting this expression into the reaction-diffusion-advection equation, Eq. 1.1 yields a complete model system able to represent the dynamics. However, it is to note that no direct comparison of the modelled and the real concentrations of reactants can be made because there are too many unknowns and approximations assumed, involving the details of the chemical reaction, when deriving the model. Nevertheless, the model albeit with extensions has proved able to reproduce qualitatively many of the experimentally observed characteristics and patterns, see for instance [32] and references therein.

In this thesis we will not actually model the Belousov-Zhabotinsky reaction and thus will not employ the Oregonator model but its introduction helps us to visualize and explain the complex dynamics of activator-inhibitor systems. If we want to analyse the stable states of the activator-inhibitor system we have to set the rates of change of the concentrations to zero, $dc_1/dt \equiv 0$ and $dc_2/dt \equiv 0$. Now we can draw the stable concentration profiles of one of the chemicals as a function of the concentration of the other. The obtained curves are called *nullclines* [2]. If we plot these two curves in the same diagram we obtain the fixed-points of the reaction dynamics at the intersection points of both curves. By applying linear stability analysis we can test for the stability of these fixed-points. In dependence of the number of stable and unstable fixed-points there are three different dynamical regimes called the *bistable* state, the *excitable* state and the *oscillatory* state. Figure 1.2 shows the nullclines for the different states and explains the dynamical situation of each.

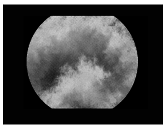

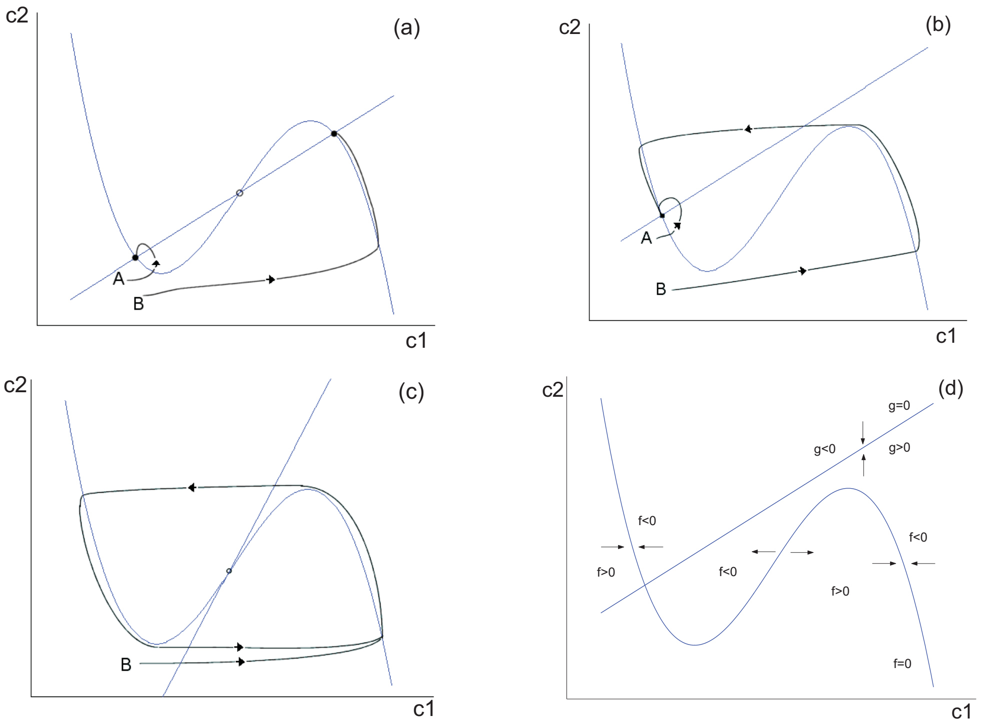

Fig. 1.2: The different stability situations for the oregonator model, bistable, excitable and oscillatory which are derived by drawing the nullclines and applying stability analysis. At the intersections of the nullclines are the fixed-points which can be stable or unstable. In this graphic a stable fixed-point is marked with a filled circle and an unstable one with an open circle. (a) The nullclines of the system intersect in three points but only two of these points are stable. When we perturb the stable state in point A the system will either return to the stable state A or go to the second stable state B, depending on the amplitude of the perturbation. This state is called the bistable state. (b) There is only one fixed-point which is stable but disturbances that are larger than a system-depending threshold can lead to large excursions in phase space (here concentration space) before the steady state is reached again. This state is called excitable. (c) This state is oscillatory and has one unstable fixed-point. The concentrations of c_1 and c_2 change according to a limit cycle solution. (d) This schema of the nullclines shows the stable and unstable branches of the nullclines by indication of the direction of dynamics (arrows). $f = f(c_1, c_2)$ and $g = g(c_1, c_2)$ denote the reaction terms in Eq. 1.8 and 1.9.(Graphic kindly provided by Dr. Alberto Pérez-Muñuzuri, Non-linear Physics Group, Santiago de Compostela)

Propagating Waves and Spatial Patterns. Reaction-diffusion systems can generate a wide variety of different patterns. For an activator-inhibitor system such as the BZ reaction under certain initial conditions, this patterns can be either static dissipative patterns, known as Turing patterns [33], or travelling pulses of different shape, known as autowaves. Precisely, when the diffusion coefficient D_{c2} of the inhibitor is much smaller than the diffusion coefficient D_{c1} of the activator and the inhibitor rate of change is much slower than the activator rate (specified by parameter ϵ), then travelling waves and propagating patterns arise (see right panel of Fig. 1.3). On the other hand, when the inhibitor is fast and the diffusion constant of the inhibitor is larger than the diffusion coefficient of the activator, Turing patterns are formed (see left panel of Fig. 1.3). In this study we are only concerned with the travelling pulses in two dimensions.

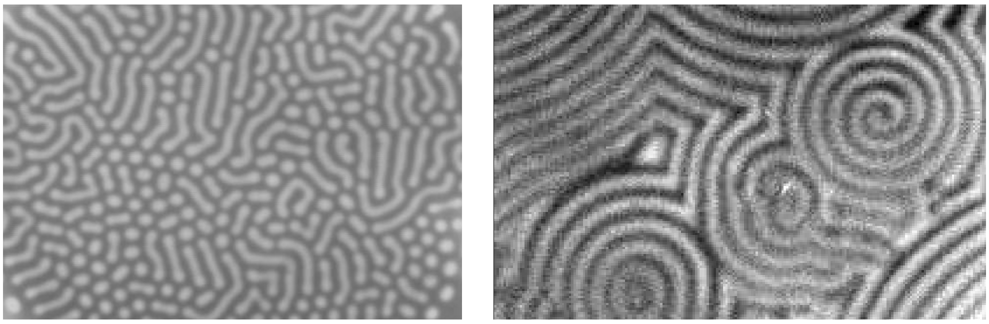

Fig. 1.3: The picture on the left shows an experimentally observed Turing pattern (Courtesy of Daniel Cuiñas Vázquez, Non-linear Physics Group, Santiago de Compostela). The picture on the right shows autowaves in the BZ reaction obtained in the experiments conducted during this study. The front of these autowaves travel slowly through the recipient until they annihilate with another autowave.

Two dimensional autowaves can have many different shapes, as straight lines, spirals and targets (see right panel of Fig. 1.3). These patterns arise experimentally due to impurities or dust and can also be triggered for instance via a small silver wire dipped into the media. The front velocities of these two dimensional waves depend on the curvature of the waves and for slightly curved fronts they obey the *eikonal* equation, see [34] and references therein:

$$v_n = v_0 - D_{c1}K \tag{1.10}$$

Where v_n is the velocity in perpendicular direction to the front, v_0 is the velocity of a plane wave and K is the curvature of the front at the point where the velocity is calculated ($K = 1/R$, where R is the radius of a circle fitted to the front in that point). K is defined to be positive when the centre of the curvature lies behind the propagating front. For a more general overview of the various different possible regimes see [35, 36].

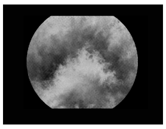

1.2 Fluid Flows and Transport

Defining the transport properties in fluid flows is of maximal practical interest for a variety of different applications. Transport is important on macro-scales regarding contaminants or nutrient spread in the ocean or in the atmosphere [3], and on micro-scales concerning for instance the exchange of ions and enzymes in between cells [37] or the transport in nanotubes [38]. In order to describe the development of a fluid flow mathematically different formalisms can be used. In principle one could intend to derive a microscopic description of the processes in the fluid. This would imply to follow every single particle on its trajectory through space. In practice an impossible thing to do. We are therefore interested in defining the fluid as a continuous medium where the development of state variables (as the velocity field) in space and time is governed by partial differential equations. This implies, that there exist fluid parcels which are small enough to be considered infinitesimal but large enough for the particles in it to be in a local equilibrium.

There are two viewpoints for the description of the fluid dynamics. Either, one can think of *sitting* on the fluid parcel, which is called the *Lagrangian* view, or one can imagine to sit on a grid held into the fluid flow, called the *Eulerian* view. These different perspectives can lead to fundamentally different conclusions. Both descriptions are linked via the material derivative:

$$\frac{d}{dt}\mathbf{F} = \frac{\partial}{\partial t}\mathbf{F} + \mathbf{v} \cdot \nabla \mathbf{F}. \tag{1.11}$$

The term on the left side is the total rate of change of the Eulerian vector- (or scalar-) field in the Lagrangian frame.

From the conservation of momentum and further the consideration that the fluid is incompressible we obtain the famous Navier-Stokes equation for incompressible fluids:

$$\rho(\frac{\partial}{\partial t} + \mathbf{v} \cdot \nabla)\mathbf{v} = -\nabla p + \mu \Delta \mathbf{v} + \mathbf{f} \tag{1.12}$$

where p is the pressure, ρ is the density, μ is the dynamical viscosity [39–41] and $\mathbf{f}$ is an arbitrary force term. The viscous term, second on the r.h.s., represents a Newtonian fluid where the shear stress is proportional to the strain rate. Together with the continuity equation $\nabla \mathbf{v}(\mathbf{x}) = 0$, stemming from the mass conservation for incompressible fluids, the Navier-Stokes equation governs the motion of the fluid.

1.2.1 Chaos and Turbulence in Fluid Flows

Turbulence and chaos are two expressions widely used in the context of advection processes and are often associated with each other and sometimes even used synonymously. Here we want to introduce the basic concepts behind these two expressions and point out some of the differences between both terms. When talking about chaos and turbulence it is of special importance to differentiate between the Lagrangian and the Eulerian frame of reference. Chaos in one frame of reference does not necessarily imply chaos in the other and nowadays the relation between both definitions of chaos is a field of active study [42]. In this thesis we use the term turbulence mainly when we refer to Eulerian velocity fields and the term chaos mainly when we refer to the Lagrangian chaos of particle trajectories.

Eulerian Chaos and Turbulence. Turbulence has an important impact on our everyday lives as most of the flows we encounter in practical applications or nature are turbulent, e.g., the air-flow in the boundary layer on an aircraft wing or the flow in parts of the atmosphere or in oceanic currents. In fact, even though most people can intuitively say if a flow is turbulent or not, there does not exist a simple, precise definition for it. Kundu states in his book *Fluid Mechanics* [43] five characteristics of turbulent flows:

1. Randomness
2. Nonlinearity
3. Diffusivity
4. Vorticity and energy cascade
5. Dissipation

Maybe the most important and widely accepted definition of a turbulent flow results from point 4: Richardson [44] was the first to develop the idea that turbulence implies the transfer of energy from large scales to ever smaller scales until the energy is dissipated due to viscous effects. We will get back to this point when we introduce the statistical measures of turbulence in Subsec. 1.2.2. In practice turbulence is often measured by an estimation of the Reynolds number, Re, which reads:

$$Re = \frac{Ul}{\nu} \tag{1.13}$$

Where U represents a typical velocity of the flow and l is a typical length scale, ν is the kinematic viscosity which is the ratio of μ/ρ as introduced

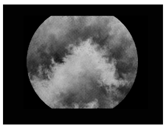

above. The Reynolds number is thus a ratio of the large scale forces driving the movement and the low scale viscosity trying to maintain the local order of different fluid parcels. With respect to the Navier-Stokes equation the Reynolds number can be seen as an approximation of the ratio of the non-linear term (second on the l.h.s. of Eq. 1.12) to the viscous term (second on the r.h.s of Eq. 1.12). This becomes especially clear when reformulating the Navier-Stokes equations as mean flow or Reynolds equations due to the appearance of the Reynolds-stresses [41]. *High* Reynolds numbers are usually identified with turbulence and *low* Reynolds numbers with laminar flow. When increasing the Reynolds number Re the fluid flow experiences a transition from a laminar regime to a turbulent regime (see Fig. 1.4). This transition can be of different kind depending highly on the details of the fluid flow and its boundaries under consideration. During this transition small disturbances in the flow become amplified and the flow goes through a complex sequence of changes that finally end up in a chaotic state (in the Eulerian sense) that is called turbulence when it is high dimensional (an infinite number of modes contribute to the rapidly changing velocity field) [42]. Thus, instead of one critical value Re_c, where the transition happens, there exists a transition region between two Reynolds numbers for which the turbulence is not yet fully developed (Re_{c1}, Re_{c2}) [43]. Thus, by solely estimating the Reynolds number of a flow where we have no other variable measuring the degree of turbulence little is won.

Lagrangian Chaos. Lagrangian chaos in fluid flows seems to be closely related to the transition from laminar to turbulent fluid flow but to date there exists no exact relationship between Eulerian and Lagrangian chaos. Lagrangian chaos can be found in laminar three dimensional flows or in laminar two dimensional time dependent or time-periodic flows and thus, in flows that are not always determined to be chaotic in the Eulerian sense. Also, a fluid flow that is chaotic in the Eulerian sense does not necessarily has to be chaotic in the Lagrangian sense, as is the case for the Lorentz model [42]. Lagrangian chaos is most often defined via the Lyapunov exponent λ_L. This exponent estimates the rate at which the distance $d(d_0, t)$ between two particles, initially close at distance d_0, increases with time.

$$\lambda_L = \lim_{t \to \infty,\, d \to d_0} \frac{1}{t} \ln \frac{|d(d_0, t)|}{|d_0|} \tag{1.14}$$

It is positive for chaotic dynamics. For non-chaotic, periodic or quasi-periodic systems, this Lyapunov exponent will be zero because the distance of the particles does not grow exponentially. For motion towards an attractor this value will become negative as $d(t) \to 0$ for large t. Also the Lyapunov exponent

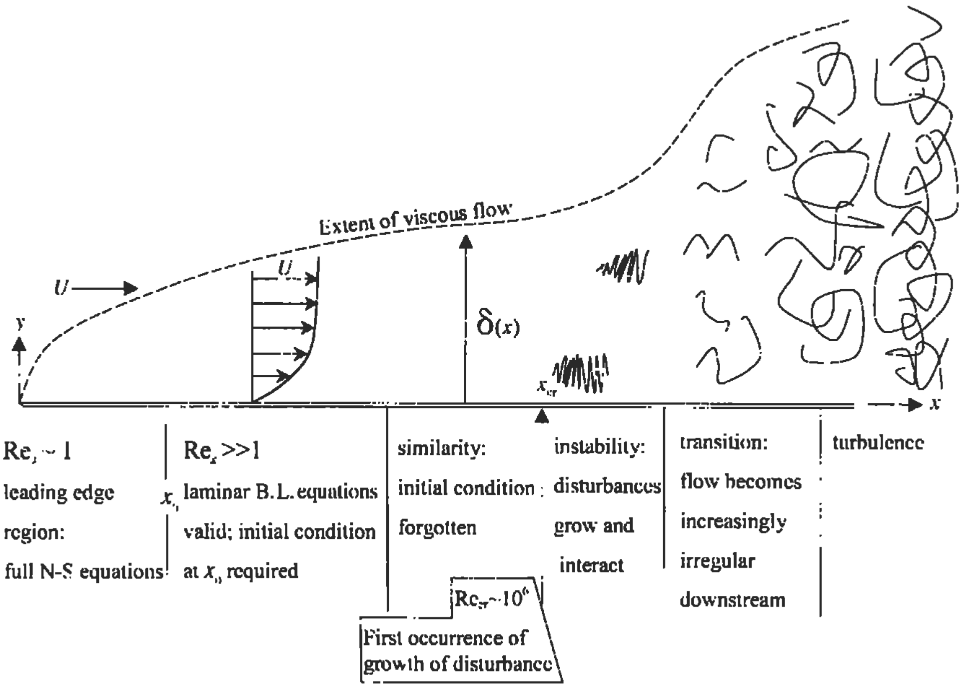

Fig. 1.4: Schematic descritption of a flow on a semi-infinite plate. The transition from a laminar flow to turbulence is depicted. Re is the Reynolds number defined in Equ. 1.13. Graphic taken from [43]

tells us something about the efficiency of mixing. The inverse of the exponent $\tau_{mix} = 1/\lambda_L$ determines the characteristic mixing time [36, 42, 45, 46].

Besides the Lyapunov exponents there are other important quantities that can be observed in the Lagrangian frame, as the absolute and the relative dispersion which will be introduced below.

1.2.2 Statistical Measures of Turbulence in Fluid Flows

Turbulent flows are best described by statistical expressions, as the ensemble-mean or the ensemble-variance of the variable of interest which usually is the velocity field but can also be a passive or active tracer or a temperature field. The ensemble is usually measured as a time average, repeatedly under the same experimental conditions or as a space average, measured at different locations of a velocity field. For well developed turbulence both measures are assumed to produce the same ensemble-means which has been shown to be a good approximation in many turbulent flows [47]. Usual measures for the characterization of turbulence besides the ensemble mean and its standard deviation are

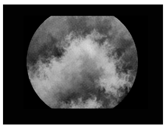

the various correlation and autocorrelation functions of the variables of interest (i.e., usually the velocity) and their corresponding Fourier spectra [47]. In the following we shortly introduce various useful measures and concepts used in this study.

Energy and Enstrophy Spectra. Maybe the most important measures in turbulence research are the energy and the enstrophy spectra of a fluid flow. For simplicity here we consider incompressible, isotropic and homogeneous turbulence, an assumption which often is not fulfilled at large scales but can be relaxed for many of the derived relationships [47]. In a truly turbulent flow energy is transferred from one spatial scale to the other causing a beautiful, self-similar energy cascade termed *inertial*. The word inertial implies that energy in this regime is passed from one spatial scale to the other without losses. The idea is that, in three dimensions, energy introduced for instance by large scale stirring at scale L is passed with a constant rate to ever smaller scales, until it is dissipated by molecular viscous forces at very small scales l. This process is depicted in Fig. 1.5. The picture of a turbulent cascade was first formulated by Richardson in the 1920s and put into quantitative mathematical description by Kolmogorov and others, see [48] and references therein.

When we refer to energy here we really refer to the mean kinetic energy of the discrete velocity field per unit mass of fluid volume, that is:

$$E_{kin} = 1/2 \left\langle \mathbf{v}(\mathbf{x})^2 \right\rangle \tag{1.15}$$

where $\mathbf{v}(\mathbf{x})$ is a two- or three-dimensional velocity field $\mathbf{v} = (v_x, v_y, v_z)$ and the brackets $\langle\rangle$ denote the average over the whole domain. If we choose a discrete spectral representation of the velocity fields

$$\widehat{\mathbf{v}}(\mathbf{k}) = \frac{1}{\sqrt{MNJ}} \sum_{\mathbf{x}} \mathbf{v}(\mathbf{x}) e^{i\mathbf{k}\mathbf{x}} \tag{1.16}$$

[41, 49], where M, N and J are the total number of grid points along the three spatial dimensions, we can write the kinetic energy using the Parseval theorem as [13]:

$$E_{kin} = \sum_{\mathbf{k}} \frac{1}{2} (\|\widehat{v_x}(\mathbf{k})\|^2 + \|\widehat{v_y}(\mathbf{k})\|^2 + \|\widehat{v_z}(\mathbf{k})\|^2) = \sum_{\mathbf{k}} E_{\mathbf{k}}(\mathbf{k}), \tag{1.17}$$

such that $E_{\mathbf{k}}(\mathbf{k}) = \frac{1}{2}(\|\widehat{v_x}(\mathbf{k})\|^2 + \|\widehat{v_y}(\mathbf{k})\|^2 + \|\widehat{v_z}(\mathbf{k})\|^2)$. For an isotropic field we can strip off the directional information of $E_{\mathbf{k}}(\mathbf{k})$ without loss of generality by integrating it over all wavenumbers $\mathbf{k}$ that lie on the surface of a shell S_k, where $k = |\mathbf{k}|$. The shell S_k with its centre in the origin denotes a sphere in

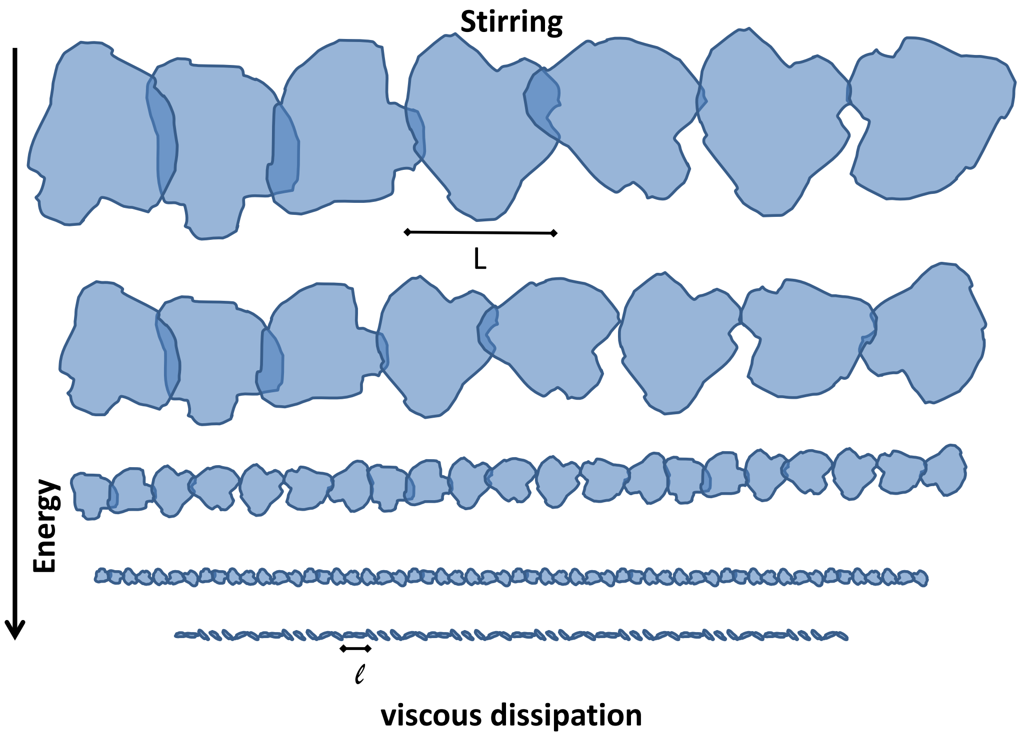

Fig. 1.5: The typical picture of a turbulent energy cascade in three dimensions. Some stirring or forcing on large scales produces structures of scale L. These structures cause the formation of ever smaller structures whereby energy is passed downwards at a constant rate. Finally at very small scales of size l energy is dissipated by viscosity.

three dimensions and a circular shell in two dimensions [41]. In mathematical terms this integration reads:

$$E(k) = \oint_{k=|\mathbf{k}|} E_{\mathbf{k}}(\mathbf{k}) dS_k. \tag{1.18}$$

As an implementation of this integration we use two slightly different approaches detailed in [50] and [49]. We shortly review both algorithms here for the two-dimensional case because the terminology of different references is quite misleading. The spectra obtained from both are very similar and do not affect the results obtained in this study. For the calculation of the spectra caution is also necessary when implementing the discrete Fourier representation of the velocity fields, since neither in literature nor in the standard toolboxes normalization is standardised.

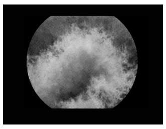

The algorithm used by Singh et al. [49, 51] derives the share of each wavenumber k by summing over $E_{\mathbf{k}}(\mathbf{k})$ that lie in a shell of thickness $2\Delta k$ around k:

$$E(k) = \sum_{k-\Delta k \leq k \leq k+\Delta k} E_{\mathbf{k}}(k_x, k_y). \tag{1.19}$$

There are N_k shells which limits the number of data points experimentally achievable in function of the shell thickness. Note that in two dimensions this procedure implies a multiplication of $E_{\mathbf{k}}(k_x, k_y)$ with k since the area of the shells grows as $A = 2\pi\, k/\Delta k$ and is thus proportional to k.

Fisher et al. [50] (see also [52]) suggest a different algorithm which has the advantage of not having to choose a certain Δk which can alter the slopes slightly. Further, for the datasets treated here the resulting curves are somewhat smoother than the ones calculated with Singhs method. The basic idea is to calculate the cumulative energy spectra $\Xi(k) = \sum_{|\mathbf{k}|\leq k} E_{\mathbf{k}}(k_x, k_y)$ and compute its derivative to yield the energy spectra $E(k)$:

$$E(k) = \frac{d\Xi(k)}{dk}. \tag{1.20}$$

The only disadvantage that we encounter in our calculations using this definition lies in the fact that for very small k the cumulative energy spectra is derived from very little data and thus the derivative gives poor results.

The enstrophy spectra can be derived similarly to the energy spectra. The enstrophy is defined as the square of the vorticity $\Omega = (\nabla \times \mathbf{v})$, while the vorticity can be understood as a measure for the local spin or swirl of a fluid parcel [13, 48]:

$$Z = 1/2 \left\langle \boldsymbol{\Omega}(\mathbf{x})^2 \right\rangle. \tag{1.21}$$

The full spectral expression for the enstrophy reads:

$$Z_{\mathbf{k}}(\mathbf{k}) = \frac{1}{2} \|\widehat{\boldsymbol{\Omega}}(\mathbf{k})\|^2 \tag{1.22}$$

where

$$\widehat{\boldsymbol{\Omega}}(\mathbf{k}) = \frac{1}{\sqrt{MNJ}} \sum_{\mathbf{x}} \boldsymbol{\Omega}(\mathbf{x}) e^{i\mathbf{k}\mathbf{x}}. \tag{1.23}$$

Finally the enstrophy spectra $Z(k)$ for a discrete measured velocity field can be obtained following the above described algorithms for the derivation of $E(k)$. The energy and the enstrophy spectra are related by $Z(k) = k^2 E(k)$ [52].

Enstrophy and Energy Cascades in two-dimensional Turbulence. In a strictly two-dimensional flow the vorticity reads $\boldsymbol{\Omega} = (0, 0, \Omega = \partial v_y/\partial x -$

$\partial v_x/\partial y)$ and has thus only one component in z-direction out of the plane of the flow. When forcing and dissipation terms are absent it can be shown that vorticity along the trajectory of a fluid parcel must be conserved [13]. The conservation of vorticity in two-dimensional turbulence leads to a variety of consequences and restrictions that are detailed in references [13, 53]. One particular important consequence is the conservation of enstrophy $dZ(t)/dt = 0$ in two-dimensions when viscosity is zero and forcing is absent. It can further be shown that the twin conservation of energy and vorticity leads to the contradiction that energy cannot be dissipated at small scales contrary to what happens in three-dimensions [13, 54]. It follows that energy is trapped at large scales and can only be dissipated by large scale friction [52]. If now some forcing occurs at scale k_f, then on average energy has to be conveyed to large scales while enstrophy goes to small scales [54]. If the forcing is confined to k_f and sufficiently well separated from the frictious and dissipative ranges at both ends of the spectra, inertial ranges can form with constant energy and enstrophy fluxes and specific scaling exponents. These relations are pictured in Fig. 1.6.

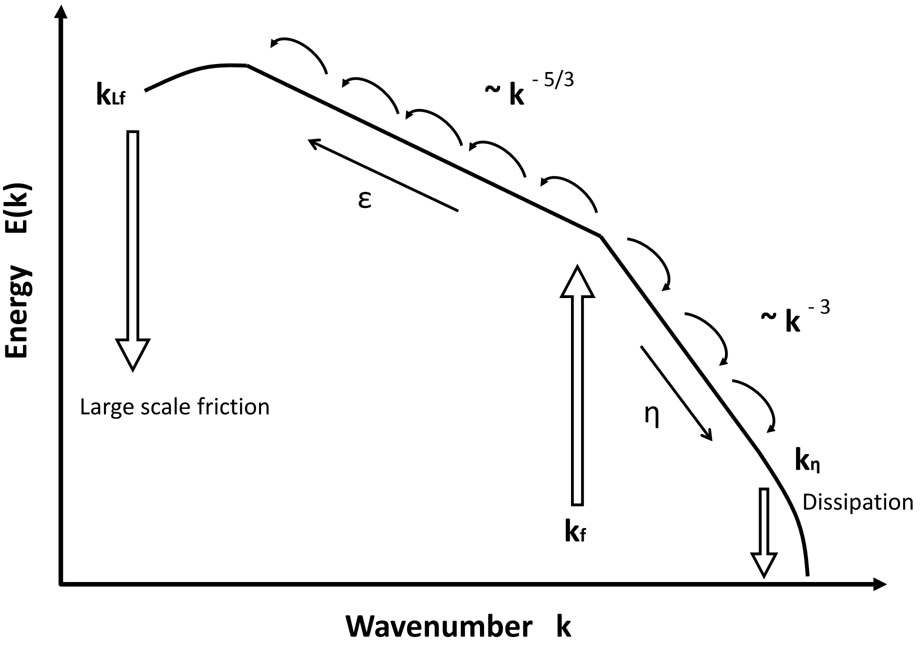

Fig. 1.6: A double energy cascade develops in two-dimensional turbulence when the flow is forced at scale k_f. The upward cascade is called the inverse energy cascade and the downward cascade is called the direct enstrophy cascade. In real flows energy dissipates at both ends of the spectra, due to large scale friction at scale k_{Lf} or viscous dissipation at scale k_η.

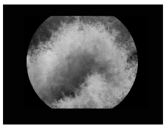

The scaling exponents for both inertial ranges can be determined by dimensional arguments. These scaling relations were first derived by Kraichnan [55] based on the work done by Kolmogorov and others on three-dimensional turbulence [47]. The inertial ranges are defined by constant energy and enstrophy fluxes. If we assume further that energy only goes upscale and enstrophy only goes downscale, the energy and the enstrophy in this ranges can thus only depend on the scale k and the rates of energy and enstrophy transfer, ϵ and η respectively. Since $E(k)$ has the dimensions $[E(k)] = L^3T^{-2}$ and $[\epsilon] = L^2T^{-3}$, $[\eta] = T^{-3}$ and $[k] = L^{-1}$, it follows that [54–56]:

$$\begin{aligned} E(k) &= C_K \epsilon^{2/3} k^{-5/3}, \quad \text{for } k_{Lf} \ll k \ll k_f \\ E(k) &= C'_K \eta^{2/3} k^{-3}, \quad \text{for } k_f \ll k \ll k_\eta. \end{aligned} \tag{1.24}$$

Here C_K and C'_K are constants. C_K is called the Kraichnan-Kolmogorov constant which according to this picture should take the same values for any highly turbulent flow [53]. It was found to be $C_K \approx 7$ for two-dimensional turbulence [56]. The inertial ranges with these energy cascade scalings are called the inverse energy cascade and the direct enstrophy cascade, respectively, due to the directions of the energy and enstrophy fluxes Π_E and Π_Z for which we will formulate a mathematical description below.

In experimental and numerical quasi two-dimensional fluid flows both energy cascades have been observed, for an overview see [53, 57]. The dual cascade has been observed more rarely, in quasi two-dimensional turbulence [58–60] and very recently also in thick fluid layers [61]. Of course though, the overall picture is more complex in the experimental reality than in the Kraichnan theory and scaling exponents are found to vary from the above predictions due to various reasons. In particular, the scaling of the enstrophy cascade has been found to be more complex due to intermittency and non-locality of the cascading process [62]. Further, oftentimes frictious forces cannot be neglected on all scales [63] and finally, in experimental realizations of two-dimensional flow also three-dimensional effects might bias the results. To conclude, it can be stated that the details of the turbulent cascades are still a very active field of study with ongoing high impact discoveries such as the existence of an inverse cascade in an isotropic three-dimensional flow [64].

Energy and Enstrophy Fluxes. The energy and enstrophy fluxes through a certain length scale can be formulated in the wavenumber space or in real space. In this work we use the real space representation since it provides additional spatial information on the sinks and sources of energy and enstrophy on each scale. Using the Reynolds decomposition of the velocity field $\mathbf{v} = \langle \mathbf{v} \rangle + \mathbf{v}'$, where $\mathbf{v}$ is the mean flow and $\mathbf{v}'$ is a fluctuation from the mean, the Navier-Stokes equations can be re-written in a *statistical* sense. After some mathematical manipulations one can obtain a spectral expression for the energy conservation of isotropic turbulence, also called the spectral form of the Kármán-Howarth equation [47, 65]:

$$\frac{\partial E(k,t)}{\partial t} = T(k,t) - 2\nu k^2 E(k,t) + F(k,t). \tag{1.25}$$

This equation describes the redistribution of energy among the different wavenumbers k. The second term on the r.h.s. denotes the energy loss due to viscous dissipation and is due to the viscous term in the Navier-Stokes equations. The third term on the r.h.s. stands for the effect of the forcing driving the turbulence. When integrated over the whole wavenumber range both terms change the total energy content of the fluid flow. The last remaining term $T(k)$ is called the transfer function and arises from the nonlinear term in $\mathbf{v}$ of the Navier-Stokes equations. It can be shown, that, when integrated over the whole wavenumber space this term disappears [51, 65]. Nevertheless this term is of great importance for the cascades introduced above as it causes the energy to redistribute among the different scales. The spectral flux of energy through wavenumber k is defined as:

$$\Pi_E(k) = -\int_0^k T(k')dk'. \tag{1.26}$$

From discrete velocity data the energy flux in real space, $\Pi_E(\mathbf{x},t)$, can be calculated as [66, 67]:

$$\Pi_E(l) = -\sum_{ij} \frac{\partial v(\mathbf{x},t)_i^{(l)}}{\partial x_j}[(v(\mathbf{x},t)_i v(\mathbf{x},t)_j)^{(l)} - v(\mathbf{x},t)_i^{(l)} v(\mathbf{x},t)_j^{(l)}]. \tag{1.27}$$

The superscript (l) denotes a filter at spatial scale l such that the information contained in $v(\mathbf{x},t)_i^{(l)}$ are those of $v(\mathbf{x},t)_i$ at lengthscales larger than l. The filtered fields $v(\mathbf{x},t)_i^{(l)}$ are obtained applying a low-pass filter. In the Fourier-space this filter reads $\widehat{G}(k)_l = exp(k^2 l^2/24)$ [66]. Similarly, the enstrophy flux can be calculated as:

$$\Pi_Z(l) = -\sum_{i} \frac{\partial \Omega(\mathbf{x},t)^{(l)}}{\partial x_i}[(\Omega(\mathbf{x},t) v(\mathbf{x},t)_i)^{(l)} - v(\mathbf{x},t)_i^{(l)} \Omega(\mathbf{x},t)^{(l)}]. \tag{1.28}$$

Often the spectral fluxes are normalized to the mean energy and enstrophy dissipation rates which for homogeneous flows can be written as [53, 65]

$$\begin{aligned} \epsilon &= \nu \sum_{i,j} \left\langle \left(\frac{\partial u_i}{\partial x_j} \right)^2 \right\rangle \\ \eta &= \nu \sum_{i} \left\langle \left(\frac{\partial \Omega}{\partial x_i} \right)^2 \right\rangle . \end{aligned} \tag{1.29}$$

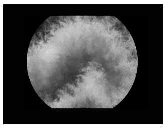

Structure Functions. In order to measure the fine structure of the velocity fields, it is useful to define the structure functions of order n for statistically stationary flows:

$$S_n(\mathbf{r}) = \langle \delta\mathbf{v}(\mathbf{r})^n \rangle \tag{1.30}$$

(which are tensors, $S_{i,j} = \langle \delta v_i(r_j)^n \rangle$) where $\delta\mathbf{v}(\mathbf{r}) = \mathbf{v}(\mathbf{x}+\mathbf{r}) - \mathbf{v}(\mathbf{x})$. The structure functions measure the moments of velocity differences in dependence on spatial direction and scale $|\mathbf{r}|$. Since turbulence is thought of to be self-similar, we expect this differences to show the same scaling across a wide range of lengthscales $|\mathbf{r}|$. Kolmogorov even predicted the scaling relations $S_n(\mathbf{r}) \propto r^{\zeta_n}$ with $\zeta_n = n/3$ for all n. For low-order moments this seems to hold true while for higher order moments deviations from this scaling can be seen as a measure of intermittency [68]. The third order structure function is further closely related to the direction of the energy flux via the transfer function $T(k) = \frac{1}{2}\pi k i \mathbf{k} \left\langle \widehat{S_3(\mathbf{r})} \right\rangle$ and for an inverse energy cascade it must thus be positive [69].

1.2.3 Transport in Turbulent Flows.

Particle trajectories in turbulent velocity fields can be seen as random walks with certain probability distribution functions for the jump length, flight time and waiting time. For some turbulent fluid flows, this distributions have rapidly decreasing tails. In this case the probability density function $P(\mathbf{r}, t)$ to find a particle at time t at the point $\mathbf{r}$ can be derived [70] and taking the continuum limit of the master equation leads to the standard diffusion equation [71]. Thus the turbulent fluid flow enters into the flow equations in the same manner as the molecular diffusion, with the term $D^*\Delta\mathbf{c}$, replacing only the molecular diffusion constant D with the enhanced diffusion constant D^*. In many cases, especially when the turbulence is not fully developed and there are coherent structures, the continuum limit of the master equation does not lead to a simple expression. This can lead to superdiffusion. To experimentally derive the transport characteristics of a turbulent flow, one can either determine these random walk statistics of many particle trajectories, finding the underlying statistic distributions governing the particle movement, or one can study the Eulerian velocity fields that can be measured in the laboratory by particle image velocimetry (PIV) [72, 73].

Absolute and Relative Dispersion. In oceanic and atmospheric physics two prevalently used measures are the absolute and the relative dispersion of tracers exposed to the flow of interest, i.e., balloons in the atmosphere or drifters in the ocean. These tracers are thereby thought of in an idealized way to follow the flow as if they were another fluid parcel and are thus called *passive* tracers. The relative dispersion is defined as the mean separation of two initially close tracers in time:

$$\langle \Delta R^2(t) \rangle = \langle |\mathbf{x}_i(t) - \mathbf{x}_j(t)|^2 \rangle \tag{1.31}$$

The absolute dispersion is defined as the mean separation of a tracer from its initial position.

$$\langle A_i^2(t) \rangle = \langle |\mathbf{x}_i(t) - \mathbf{x}_i(t=0)|^2 \rangle \tag{1.32}$$

They are formally connected via the relation

$$\langle \Delta R^2(t) \rangle = \langle A_i^2(t) \rangle + \langle A_j^2(t) \rangle + \langle |\mathbf{x}_i(t)\mathbf{x}_j(t)| \rangle. \tag{1.33}$$

Both measures of dispersion grasp thereby different qualities of the fluid flow. The absolute dispersion $A_i^2(t)$ is largely affected by the large structures present in the fluid flow depending on the details of the fluid flow in question, i.e., the geometry and the type of turbulent forcing. The relative dispersion on the contrary, depends on the actual distance of the tracers and thus on the velocity gradients at that scale. If for instance a pair of tracers is released close to each other in a large eddy, the eddy will swift them both in the same direction and thus does not add to the pair-separation of the particles [13].

For small times one expects that the Lagrangian velocities of single tracers $\mathbf{v}(\mathbf{X}, t)$, where $\mathbf{X} = \mathbf{X}(\mathbf{x}, t)$ denotes the Lagrangian trajectory, are still correlated and the absolute dispersion shows a scaling proportional to t^2. For long times on the other hand, it can often be assumed that the velocities decorrelate and the scaling will resemble that of molecular diffusion, $\propto t^1$. In the intermediate range in between these two limits the detailed behaviour of the absolute dispersion depends highly on the fluid flow considered, i.e., if there are coherent structures the velocities might eventually decorrelate very slowly. In these cases superdiffusion can occur (see below). For a detailed review on different model flows addressing this issue see [74].

Within the inverse energy cascade with $E(k) \propto k^{-5/3}$ the relative dispersion is expected to scale with time t as $\langle \Delta R^2(t) \rangle \propto t^3$ as can be shown by dimensional arguments [13]. These t^3 scaling was observed experimentally by Richardson prior to the formulation of the Kolmogorov theory [44] and is thus called Richardson dispersion. For tracer pair separations larger than the largest structures of the flow the movements of the two tracers are completely uncorrelated and the rate of separation will be twice the single tracer absolute diffusion, that is, it will scale linear with time ($\propto t^1$) as well.

The Finite Size Lyapunov Exponent (FSLE). The drawback of the relative dispersion measure is the fact that it is an average over tracer separations at

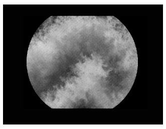

fixed times even though the rate of separation does not depend on time but on the separation itself. This causes regimes of unexpected scalings due to *mixed* averages, i.e., tracer pairs that have already separated more than the size of the largest structures and those who have not are averaged. Instead of using the average over separations at fixed times it is thus often more favourable to use an averaging over the time it takes to reach a certain separation scale. A very useful measure in this regard is the Finite-Size-Lyapunov-Exponent (FSLE) [75]. It is defined as:

$$\lambda(\delta) = ln(r)\frac{1}{\tau(\delta)}. \tag{1.34}$$

Here $\tau(\delta)$ is the average *doubling* time $\tau(\delta) = \langle T(\delta)\rangle = 1/N \sum_i T_i(\delta)$. The doubling time $T_i(\delta)$ is the time it takes for the separation of the tracers to grow from a separation δ^i to a separation δ^{i+1} with the series of separations defined as $\delta^n = r^n \delta^0$ [75]. For a value of $r \gtrsim 1$ the FSLE does not depend on r.

For a turbulent two-dimensional fluid flow the following scaling ranges are expected [13, 75]:

$$\begin{array}{lll} \lambda(\delta) = \lambda, & \text{for } \delta \ll l_f, & \textit{chaotic} \\ \lambda(\delta) \propto \delta^{-2/3}, & \text{for } l_f \ll \delta \ll L_{Lf}, & \textit{Richardson} \\ \lambda(\delta) \propto \delta^{-2}, & \text{for } \delta \gg L_{Lf}, & \textit{diffusive}. \end{array} \tag{1.35}$$

Here L_{Lf} is the lengthscale where large scale friction sets in and l_f is the scale of the forcing, see also k_{Lf} and k_f Fig. 1.6.

Superdiffusion. Superdiffusion is defined as the supralinear growth of the variance $\sigma^2(t)$ of the probability density function (PDF) $P(\mathbf{r}, t)$

$$\sigma^2(t) \propto t^\gamma, \text{ with } \gamma > 1. \tag{1.36}$$

The PDF gives the probability to find a particle at position $\mathbf{r}$ at time t. In one dimension the variance $\sigma^2(t)$ can be written as

$$\sigma^2(t) = \int_{-\infty}^{\infty} (x - \langle x\rangle)^2 P(x,t)dx, \tag{1.37}$$

where $\langle x\rangle$ is the expectation value of the PDF. Of course, for stationary turbulence the variance is just the absolute dispersion $\sigma^2(t) = A_i^2(t)$.

Superdiffusive behaviour of tracers can arise due to a variety of different processes. In real flows, superdiffusion is an effect created by the imperfection of the turbulence, i.e., the existence of coherent structures in the velocity field [42, 76]. The microscopic theory underlying this general random walk is called Continuous Time Random Walk (CTRW) and was formulated by Montroll and

Weiss [77] and extended to the Multistage Random Walk theory (MSRW) by Shlesinger and Klafter [70]. Superdiffusion can also be defined for the relative dispersion as will be done in Chap. 7. Richardson dispersion with $\langle \Delta R^2(t) \rangle \propto t^3$ is thus a special case of superdiffusive relative dispersion.

Random Walks. The chaotic dynamics of a particle in a fluid flow is an intermediate case in between completely random (nonintegrable) and completely regular (integrable) kinetics. Random Walk theory, and especially the Continuous Time Random Walk Theory (CTRW), is an important model for the description of this chaotic dynamics and can be applied to experimental measurements of particle trajectories (for a discussion of different models see [78]). CTRW is explained in detail and applied to our experimental data in Chap. 5. Figure 1.7 shows two examples of random walks, a Gaussian walk and a Lévy walk.

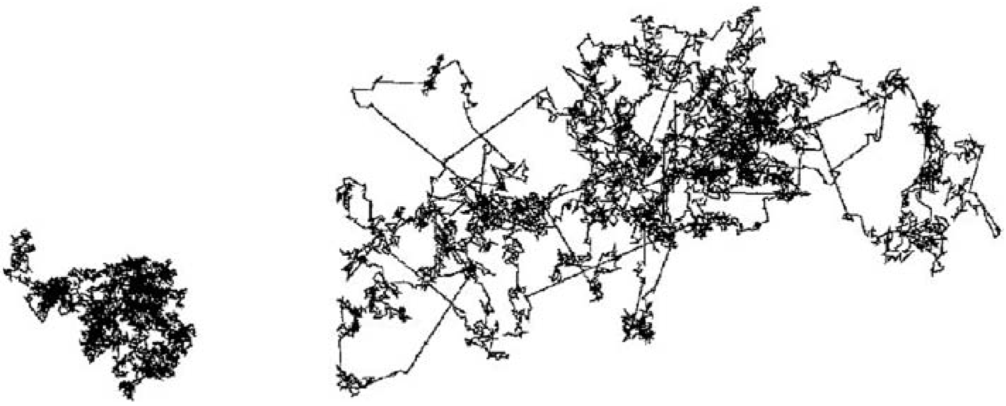

Fig. 1.7: On the left: A Gaussian random walk with 7000 steps. This random walks have a probability density function with finite variance and thus the possibility of making a very long jump is basically zero. On the right: A levy random walk with equal number of steps. The possibility of making a very large step is not zero and the variance of the probability density function grows supralinear. Graphic taken from [24].

1.3 The Faraday Experiment

In 1831, the British scientist Michael Faraday was the first to notice that spatial wave-patterns form on the surface in between two immiscible fluids, when those are subjected to an oscillating vertical forcing [18]. But it was not until 1954, that Benjamin and Ursell published an adequate theoretical description

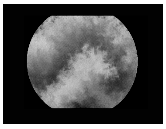

of this surface excitation [79]. Ever since these *Faraday waves* and the detailed mechanisms of their onset, transitions and spatial structures has attracted many researchers and a vast amount of literature on this subject can be found (for a revision see [19, 80, 81]). Faraday waves arise when the two fluids are subjected to a modulated vertical forcing of the form:

$$g(t) = g_0 + a\cos(2\pi f t) \tag{1.38}$$

Where g_0 is the gravitational acceleration, a is the amplitude of the acceleration and f is the frequency of the forcing. The generated waves can show a wide variety of different patterns in dependence on amplitude a, frequency f, system size L and liquid height h, such as stripes, circles, rectangles, pentagons, octagons and even quasi-crystals. Normally, these waves are subharmonic and thus oscillate at half the excitation frequency even though also harmonic solutions are possible but less probable [81, 82].

It is known that Faraday patterns exhibit well defined order-disorder transition for increasing forcing frequency and amplitude, leading from standing waves to a disordered state where the translational correlation length drops dramatically and the orientational correlations of the patterns also decreases [83](see Fig. 1.8). This disorder in the patterns is sometimes referred to as spatiotemporal chaos [84]. Thus, the higher the forcing strength and frequency the more rapid are the fluctuations of the observed patterns. Additionally to the surface pattern, in a thin fluid layer like in our experiment, horizontal convective fluxes are induced that may enhance the long range displacement of particles in the flow [85].

Fluid flows induced by this wave patterns are termed spatiotemporally chaotic, and form an intermediate case between low-dimensional chaotic systems and fully developed turbulence [86, 87]. In principle, for the case where the denser fluid is an aqueous solution and the less dense fluid is air, the system can be described completely by a set of differential (partly non-linear) equations [82]. Due to the complexity of this set of equations it is an intriguing task to solve it numerically. In this study we are not concerned with the detailed modelling of the Faraday waves, but rather we are interested in the fluid flow produced by the Faraday experiment and the transport therein. Further we are also concerned with the question how the fluid flow and the transport change when the parameters of the Faraday forcing are varied. As was shown by different groups, particles on the surface of the induced flows can undergo very complex trajectories and the properties of the transport can be described by statistical means [86, 88, 89]. Even superdiffusive transport was already observed in this type of flows [86].

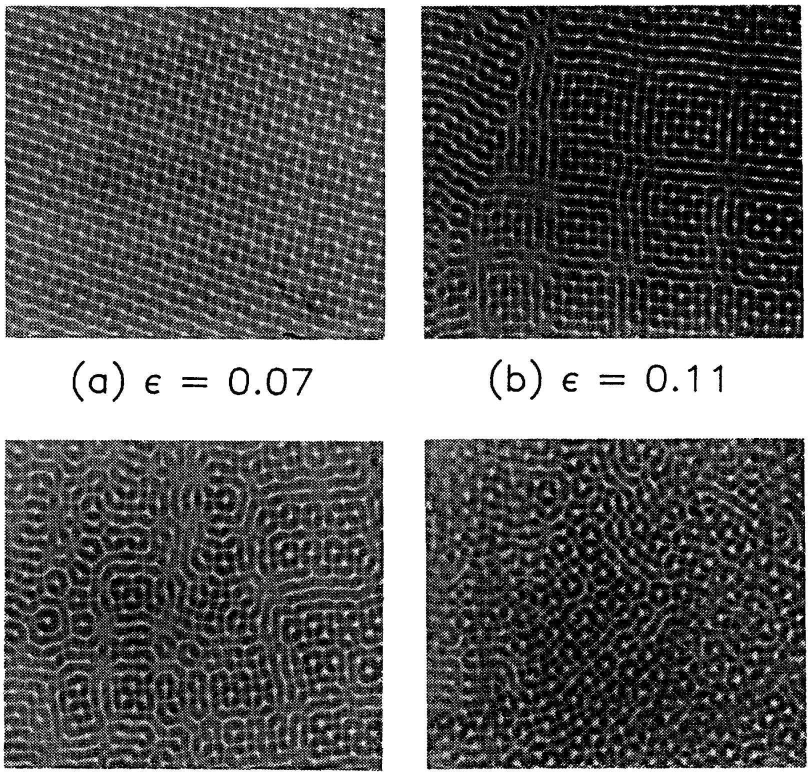

(a) $\epsilon = 0.07$ (b) $\epsilon = 0.11$

(c) $\epsilon = 0.14$ (d) $\epsilon = 0.35$

Fig. 1.8: Faraday waves at different forcing amplitudes but constant forcing frequency recorded by Tufillaro et al. [83]. Here ϵ is the forcing amplitude normalized to the amplitude of the first onset of surface waves. For an increasing forcing amplitude the Faraday waves become more and more disordered.

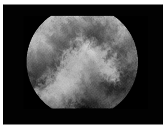

2

Experimental Set-up and Data Analysis

Here we specify in detail the chemical reaction that we used throughout the experiments. We will also provide a short overview over the experimental set up and its various modifications. Various analysis methods will be briefly explained, in particular the concepts of particle image velocimetry and the calibration procedure for obtaining the ferroin concentration in the Belousov-Zhabotinsky reaction.

2.1 The Chemical Belousov-Zhabotinsky Reaction

The complete reaction kinetics involved in the $1,4$-cyclohexanedione (CHD) based Belousov-Zhabotinsky reaction (BZ) used in this study are quite complex. A detailed recent study about the various intermediate reactions taking place in the CHD-BZ reaction by Szalai et al. [90] proposes 19 reaction equations and equally many reaction constants to keep track of all the different intermediate reactions. It is known that the BZ reaction can show different oscillatory and excitable behaviours, even aperiodic oscillations have been observed in a continuously fed stirred tank reactor [91]. If one uses ferroin as a catalyst the dynamics of the CHD-BZ chemical reaction can be well observed in the visible range due to the oxidation of the reddish catalyst ferroin $[Fe(phen)_3^{2+}]$ to the blue ferriin $[Fe(phen)_3^{3+}]$ [27].

In this study we are interested in the identification of the activator state of the chemical reaction which is indicated by the colour change due to the catalyst ferroin. We use the CHD-BZ reaction, from now on referred to simply as the BZ reaction, here as a model-system having the notion in mind that there are various other complex systems that can show similar complex excitation dynamics. Basically, instead of studying the full complex dynamics of the BZ reaction we direct our attention to two transitions: From red to blue (activation) and from blue to red (inhibition).

In our experiments the state of the BZ reaction was determined to be excitable, since when continuously stirred in batch, the chemical liquid showed only one oscillation from blue to red after varying times longer than one hour. This state could only be destabilized by stopping the stirring or inducing some other inhomogeneity like slowing the stirring considerably down. When the BZ reaction is poured into the chemical reactor made out of plexiglass to a height of 2 mm and left to rest for some time, neat target waves appear. These target waves are gradually replaced by the higher frequency spiral waves until the whole reactor with a diameter of 30 cm is completely covered by spiral patterns. The typical wavelength of these patterns, determined by measuring the width of the visible blue waves, was around 1 mm for all experiments. Most likely these patterns arise due to nucleation at tiny disturbances and irregularities in the liquid like dust particles.

2.1.1 Preparation, Procedure and Recipee

The following final concentrations of reactants were used for the excitable BZ reaction: Cyclohexanedione 0.2 M, sulfuric acid 0.6 M, sodium bromate 0.2 M and ferroin 2.8×10^{-4} M. The CHD-solution was freshly prepared for each experiment while the sulfuric acid, the sodium bromate and the ferroin were taken from previously prepared stock solutions. The reactants were mixed in strictly the same order for each experiment, namely the fresh CHD solution was mixed with sulfuric acid while stirred in batch. After ≈ 2 min the sodium bromate solution was added and finally, after another ≈ 2 min, the Ferroin solution was applied. The whole mixture is then stirred for 50 min (60 min, in dependance of the experiment, see the experimental details of each chapter) before being poured into the container described below. The room temperature was held constant during the whole procedure and the experiment at $(23{\pm}1)\,^{\circ}$ C. At this temperature the approximate density of the solution was measured to be $\rho = 1060$ kg/m^3 using a portable densimeter (DMA 35, Anton Paar). The kinematic viscosity of the solution was approximated from measurements on a very similar chemical recipee to be $\nu = 1.4 \pm 0.1\,10^{-6}$ m$^2/s$ [17]. For each experiment slightly more volume than necessary to fill the plexiglass container to a height of 2 mm was prepared so that two probes of liquid volume could be taken out for experimental control. One probe of 3 ml was filled into a tiny plastic cube and inserted into a spectrometer for surveillance of the variations in ferroin concentration, which has a maximum absorption around $500\,\mathrm{nm}$ [92]. The other probe was poured into a small petri-dish for visual surveillance of the regularity of the well known spiral and target autowaves arising from the competition of molecular diffusion and reaction kinetics. In this way we tried to separate those influences of the preparation of the chemicals from those of the experimental set-up when problems or irregularities were detected in the experiments.

2.2 Experimental Set-up and Procedure

In order to induce the Faraday waves we use two versions of the same set-up in this study. The basic difference in between the two set-ups is the placement of the camera and the type of the camera. Experiments presented in Chap. 3 and Chap. 4 use the first version of the experimental set-up (Fig. 2.1) which has the advantage that the surface reflections of the light due to the inclined surfaces of the Faraday waves are absent. However, also in the first set-up the Faraday waves can be distinguished in the recorded images due to differences in the thickness of the liquid. These images are later used to detect the locations of the nodes and antinodes of the Faraday wave pattern. Experiments presented in Chap. 5 use the second version of the experimental set-up (Fig. 2.2). In the two different versions of the set-up we further used two different plexiglass containers. Both containers are conceptually identical with the only difference that they come from different manufacturers and that the container of the experimental set-up No.1 has $4\,\mathrm{mm}$ thick bottom and top plates while for the container of the experimental set-up No.2 they are only $2\,\mathrm{mm}$ thick. The thicker container proved more convenient as it is more robust and thus resonances with the excitation frequencies were less likely. This was especially important for forcings of high amplitude and high frequency where it was noted that the bottom plate started to vibrate stronger in the middle of the container leading to an inhomogeneous distribution of the Faraday wave pattern, i.e. higher Faraday waves in the middle of the container. Both set-ups were monitored regularly during experimental campaigns with a water-level in order to ensure an exact horizontal alignment of the container. Every now and then the alignment was further checked using a laser light reflecting at the cover of the container when this was vibrated. A mere straight line indicated that the system was well aligned while a circle or curve indicated the need of adjustment. Nevertheless, an aligned and everywhere equally thick fluid layer is of course an idealization as production procedures of plexiglass containers always have a limited accuracy.

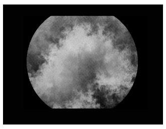

Experimental Set-up No.1. A circular container (or reactor) made of plexiglass is filled with liquid (BZ or water) up to a height of $2\,\mathrm{mm}$. The reactor is fixed on top of an electromagnetic shaker and vertical vibrations produced by the shaker induce Faraday waves and bulk fluxes in the liquid. To minimize the influence of capillary effects on the creation of Faraday waves the reactor is constructed with an inner border that closes up with the liquid surface [93]. Figure 2.1 shows a schematic of the set-up where the letters denote the following parts:

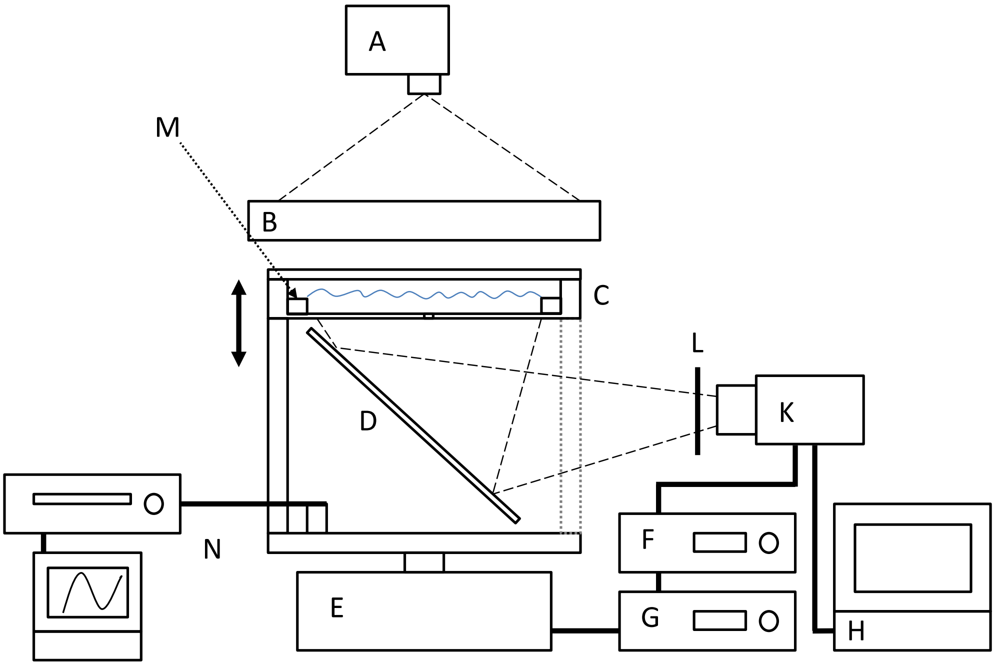

Fig. 2.1: Experimental Set-up No. 1.

- **A** Beamer or backlight, white light.
- **B** Diffuser.
- **C** Cylindric container with closed cover and fluid (aqueous BZ reaction) of depth $2\,\mathrm{mm}$. Inert argon atmosphere to avoid oxygen inhibition of the reaction dynamics [94].
- **D** $45\,^\circ$ mirror.
- **E** Electromagnetic shaker TIRAvib S511, TIRA GmbH, that vertically vibrates the container. The acceleration of the reactor is modulated as

$A(t) = a \cos \omega t$, $\omega = 2\pi f$. The shaker supplies a 75 N rated peak force, a maximum acceleration of $50\, g_0$, where g_0 is the gravitational acceleration, a maximum rated travel of 10 mm and a clean frequency range of 2 Hz to 7000 Hz, as specified by the manufacturer.

- **F** Function generator HP 33120A which triggers the camera (**K**) and the power amplifier (**G**) of the electromagnetic shaker (**E**).
- **G** Power amplifier TIRAvib BAA 120 of the electromagnetic shaker (**E**).
- **H** PC for data acquisition and analysis.
- **K** Images were recorded with a Pike F-032-B AVT camera at $12.5{-}200$ fps and (480×640) pixel^2 resolution.
- **L** Contrast enhancing green filter foil with maximal transmission around wavelength $\lambda \approx 500$ nm and a maximal absorption around $\lambda \approx 625$ nm.
- **M** Inner border that closes up with the liquid surface to minimize influence of capillary effects.
- **N** Piezoelectric accelerometer PCB Piezotronics 353B18 measures the amplitude of the acceleration of the container. It is connected to a signal amplifier 480C02 from the same manufacturer. The signal is read out using a HP 54645A oscilloscope.

In order to ensure that the camera looks perpendicular onto the container we used a second mirror placed on top of the plexiglass container. The position of the camera was then adjusted to see itself in the middle of the field of view.

Experimental Set-up No. 2. Experimental Set-up No. 2 is illuminated with a backlight instead of a beamer, which is placed below the container while the camera (Guppy, AVT) records from above. Note that the camera is different from the one introduced above and could not be triggered externally. As a consequence in these measurements it was nearly impossible to tune the recording of the camera to the flat fluid surface every nth image at equal phase of the surface waves. Therefore, after recording of the full image stack, each pixel intensity time series was smoothed using a Gaussian filter in time. Care was taken that this filter only removes the rapid intensity changes in time due to the Faraday waves without filtering out spatial edges due to the chemical excitation wave which are the signal that we want to analyse. An example of the filtering procedure for one pixel can be found in Fig. 5.5 in Sec. 5.

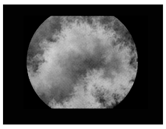

As stated above the container used in this set-up is slightly different from the former one. Note that in this experiments we did not use a contrast enhancing green filter foil and the experiments carried out with this set-up (Chap. 5) can thus not be calibrated to obtain the approximate ferroin concentration as described below. Rather in this experiments we look at intensities of counts per frame per pixel and define the activator state and the inhibitor state by applying a carefully chosen intensity threshold.

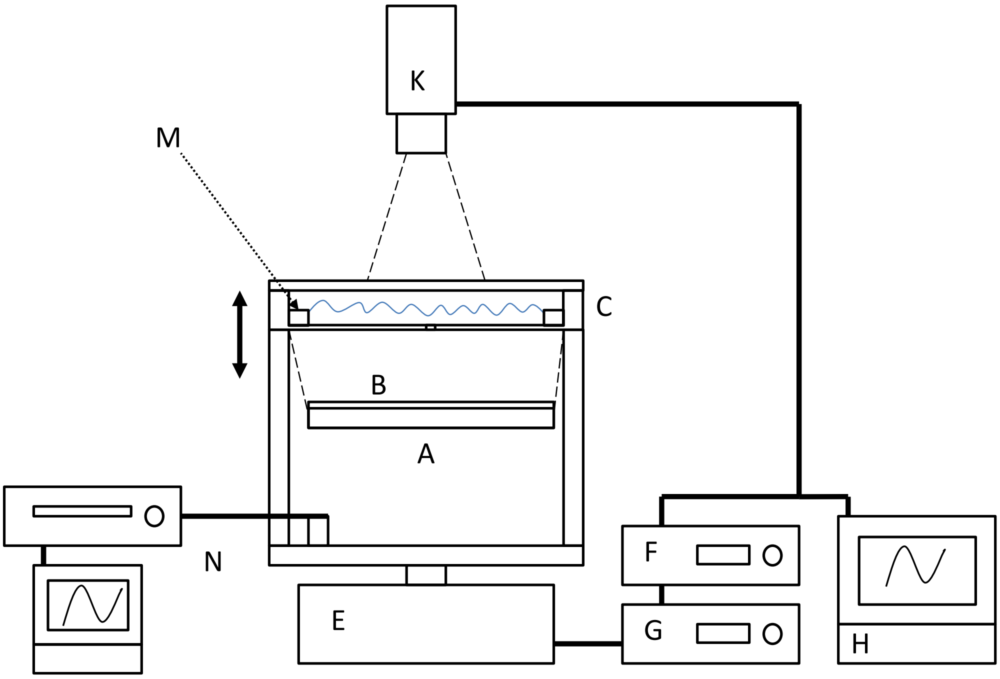

Fig. 2.2: Experimental Set-up No. 2.

The following parts of the set-up shown in Fig. 2.2 can be identified:

- **A** Backlight (laptop monitor, CCFL (cold cathode fluorescent light) bulb).
- **B** Diffuser (diffuser sheets from monitor).
- **C** Cylindric container with closed cover and fluid (aqueous BZ reaction) of depth $2\,\mathrm{mm}$. Inert argon atmosphere to avoid oxygen inhibition of the reaction dynamics [94].
- **E** Electromagnetic shaker TIRAvib S511, TIRA GmbH, that vertically vibrates the container. The acceleration of the reactor is modulated as

$A(t) = a\cos\omega t$, $\omega = 2\pi f$. The shaker supplies a $75\,$N rated peak force, a maximum acceleration of $50\,g_0$, where g_0 is the gravitational acceleration, a maximum rated travel of $10\,$mm and a clean frequency range of $2\,$Hz to $7000\,$Hz, as specified by the manufacturer.

- **F** Function generator HP 33120A which triggers the power amplifier (**G**) of the electromagnetic shaker (**E**).
- **G** Power amplifier TIRAvib BAA 120 of the electromagnetic shaker (**E**).
- **H** PC for data acquisition and analysis.
- **K** Images were recorded with a monochrome firewire camera (Guppy, AVT) at a frame rate of 60 Hz and a resolution of (480×640) pixel^2.
- **M** Inner border that closes up with the liquid surface to minimize influence of capillary effects.
- **N** Piezoelectric accelerometer PCB Piezotronics 353B18 measures the amplitude of the acceleration of the container. It is connected to a signal amplifier 480C02 from the same manufacturer. The signal is read out using a HP 54645A oscilloscope.

Experimental Procedure with Chemical Reaction. After pouring the chemical solution into the container, inert argon gas inflow is provided for $10\,$min to prevent that oxygen interferes in the chemical reaction. Even though some tests without the inert atmosphere did not show any changes in the results obtained in this study. Instead, light conditions did seem to have a slight influence on the dynamics of the chemical reaction and they were thus carefully checked to be identical for all experiments within one experimental campaign. When the inflow of argon is stopped the light source is switched on and the zoom levels of interest are adjusted. The liquid is left to rest until target and spiral patterns appear. Then the forcing is slowly switched on and set to the desired frequency f and amplitude a and recording is started when the Faraday waves show a homogeneous distribution over the whole container.

Experimental Procedure with Passive Particles. Floating passive particles were applied to the fluid flow for two distinct reasons:

- For particle image velocimetry (Chap. 3) which yields an estimate of the horizontal velocity field induced by the Faraday waves. For details of the particles used see Sec. 3.2.

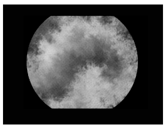

- For particle tracking (Chap. 3 and Chap. 5) which yields an estimate of the horizontal dispersion and the characteristics of the random walks of the particles. For details of the particles used in the respective experiments see Sec. 3.2 and Sec. 5.2.3.

Then the forcing is slowly switched on and set to the desired frequency f and amplitude a and recording is started when the Faraday waves show a homogeneous distribution over the whole container. When doing the particle image velocimetry experiments the camera (experimental Set-up No.1) was triggered externally and recorded such, that spurious particle movements from the Faraday waves were nearly eliminated. This was achieved by choosing only images for the further analysis that were recorded at equal phase of the Faraday waves when the fluid shows an almost flat surface, see schematic in Fig. 2.3.

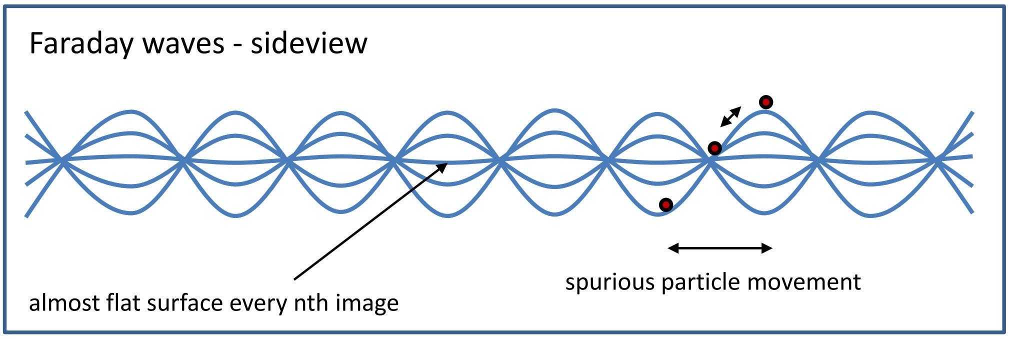

Fig. 2.3: With the camera used in experimental set-up No.1 the recording can be triggered to coincide with an almost flat surface. In this way we avoid to record the spurious movements of the particles during one oscillation which does not affect its overall dispersion.

2.3 Image Analysis Methods

Two image analysis methods were used to study the horizontal transport produced by the Faraday experiment, namely particle image velocimetry and particle tracking. Further, for the analysis of the chemical wave fronts in Chap. 4 we calibrated the set-up for the measurement of the ferroin concentration.

2.3.1 Particle Image Velocimetry (PIV)

Particle image velocimetry, in short PIV, is the an optical method to derive velocity fields from tiny particles dispersed in a fluid flow [72]. The velocity fields are thereby constructed from the finite position difference of the particles between two images at subsequent times. The tracers are chosen such that they follow the fluid motion as exactly as possible. Ideally, the particles themselves should not interfere with the fluid flow and follow it passively just as if they were fluid parcels. For this end the particles have to be small and, for three dimensional PIV, should have a very similar density as the liquid they are dispersed in. In practice, perfectly following particles are of course difficult to find and, since one needs comparative measurements, the perfect tracking is also hard to prove. Nevertheless, progress has been made and it was shown that particles of different sizes imply sometimes varying quality of fluid parcel tracking [95]. It is further important to find the right particle density since very dense suspensions will obviously change the fluid flow due to particle-particle interactions, while very sparse suspensions will be difficult to analyse with the PIV algorithm, since it depends on correlations of different image-windows as we will see below.

The usual PIV experiments often use a laser sheet for illumination of a 3D flow while a camera looks perpendicular onto the laser sheet to record the particle motion. Here we use a fairly different approach since our experimental system is quasi two-dimensional. We use a technique called *shadowing* which basically consists in the backlight illumination of the fluid suspension of floating particles. Particles are recorded by a camera opposed to the backlight (see Fig. 2.1) and thus the *shadows* of the particles fall onto the camera sensor. In our studies we chose the particle density as sparse as possible to diminish the effects of particle-particle interactions and influences on the surface tension which would also imply small changes in the evolution of the Faraday waves [93].

The PIV analysis consists in the derivation of a velocity vector at position (X_k, Y_l) of the image: a small square window of width $2d+1$ is taken from image I_t and compared with windows of the same size in the subsequent image in time I_{t+1} that are shifted by a displacement $(\Delta x, \Delta y)$. The cost function

$$C_{kl}(\Delta x, \Delta y) = \sum_{i=-d}^{d} \sum_{j=-d}^{d} \left| I_t(X_{k+i}, Y_{l+j}) - I_{t+1}(X_{k+i} + \Delta x, Y_{l+j} + \Delta y) \right| \tag{2.1}$$

measures the difference in grayscale values between the two shifted windows. The algorithm searches for the window for which this cost function is minimal. The shift $(\Delta x_{min}, \Delta y_{min})$ of the window determined in such a way is taken as an estimation for the displacement of the fluid parcel defined by this window.

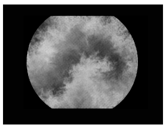

The velocity is thus estimated as

$$\mathbf{v}(X_k, Y_l) = \frac{1}{\Delta t} \left(\Delta x_{min}, \Delta y_{min} \right). \tag{2.2}$$

The windows are chosen in an overlapping fashion as such that the typical minimal fluid parcel is somewhat smaller than the window size, i.e., the grid point resolution is higher than the ratio of the image size and the window size. Whenever the cost function C_{kl} does not have a clear minimum, which preferably happens in regions of large velocity gradients, velocities from the neighbouring grid points are interpolated. For the numerical realization of the PIV analysis as described above we use an open source Matlab toolbox developed by Nobuhito Mori and Kuang-An Chang from the Kyoto University [96]. We use a recursive windows option provided by the toolbox (called super-resolution PIV) which starts off with a large window size and iteratively makes the windows smaller until the desired window size is reached. This technique provides a higher accuracy as the single window technique as was checked with various trials. For most of the velocity fields considered in this work we started with a window size of (32×32) pixel^2 and then went down to a desired resolution of (4×4) pixel^2. In combination with a window-overlap of 40% and in dependence of the zoom level adjusted with the objective and the camera position, this settings defined the final resolution. An example image pair of particles can be seen in Fig. 2.4.

To test the validity of our particle image velocimetry we advected ideal virtual tracers in the velocity fields derived from the PIV and compared their statistics to dispersion experiments done with larger tracking particles (in very sparse suspension, single tracked) as detailed in Chap. 3. Even though the scaling exponents of the statistics were about the same for both measurements the velocity of separation was somewhat higher for the larger tracking particles. This could be due to two different reasons: First, the larger particles are likely to have more inertia which can lead to higher velocities as shown by [95]. Second, the suspension of the particles could have some effect on the surface tension and thus the Faraday waves were slightly modified as such that the fluid flow was statistically similar but slightly slower. However, with our set-up we were unable to prove or discard either one of the possible causes. Another rather very qualitative test, suggested by Cardoso et al. [97], compares the stream lines from the vorticity fields to the streamlines obtained by averaging over several images in time. An overlay of both in our study showed good qualitative agreement. Finally, it is to note that for high forcing amplitudes the PIV quality decreases for two reasons, blurring of the particles due to their fast motion and difficulties of the PIV algorithm due to large displacements in between the two images. Here, in contrast to other experiments the large displacements can not be encountered with higher recording frame-rates since

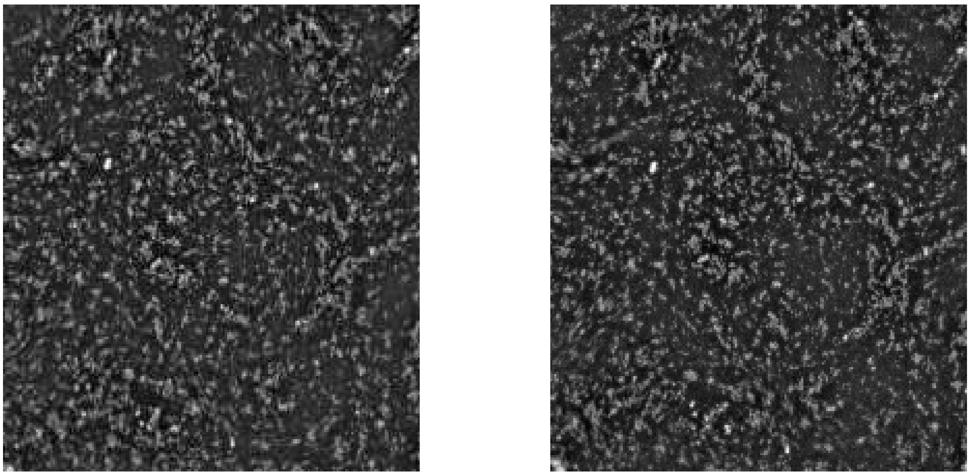

Fig. 2.4: Two consecutive images of the PIV-particles used in this study. For a better visualization here the negative image is shown (the particles really appear in black on white ground). The resolution is approximately 0.14 mm/pixel. An image region of (200×200) pixel^2 is shown. PIV particles are floating hollow glass spheres with a density of $0.2\,\mathrm{g/cm^3}$ and a diameter of $(46 \pm 30)\,\mu\mathrm{m}$ (Q-Cel 5020FPS, Potters Europe).

these are restricted by the triggering to the *almost flat* surface. The motion blur could be reduced by using a flashing light source, like a pulsed laser or LED, with high intensity and less exposure time.

2.3.2 Particle Tracking

The routine for the particle tracking is based on a minimal distance approach. When a particle has been detected in image I_t the algorithm looks for the closest detected particle in image I_{t+1} and associates its positions. The successive positions are stored into a vector and one obtains thus the trajectory of the particle. The algorithm is very reliable for sparsely loaded flows, since it discards a particle when it comes too close to any other particle. Here this value was set to a few pixel (3-4). Particle detection is achieved by simply calculating the second derivative of the images and thresholding the result appropriately. An example of identified particles is shown in Fig. 2.5. The routine was custom made and written in Matlab.

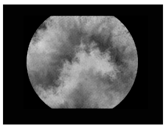

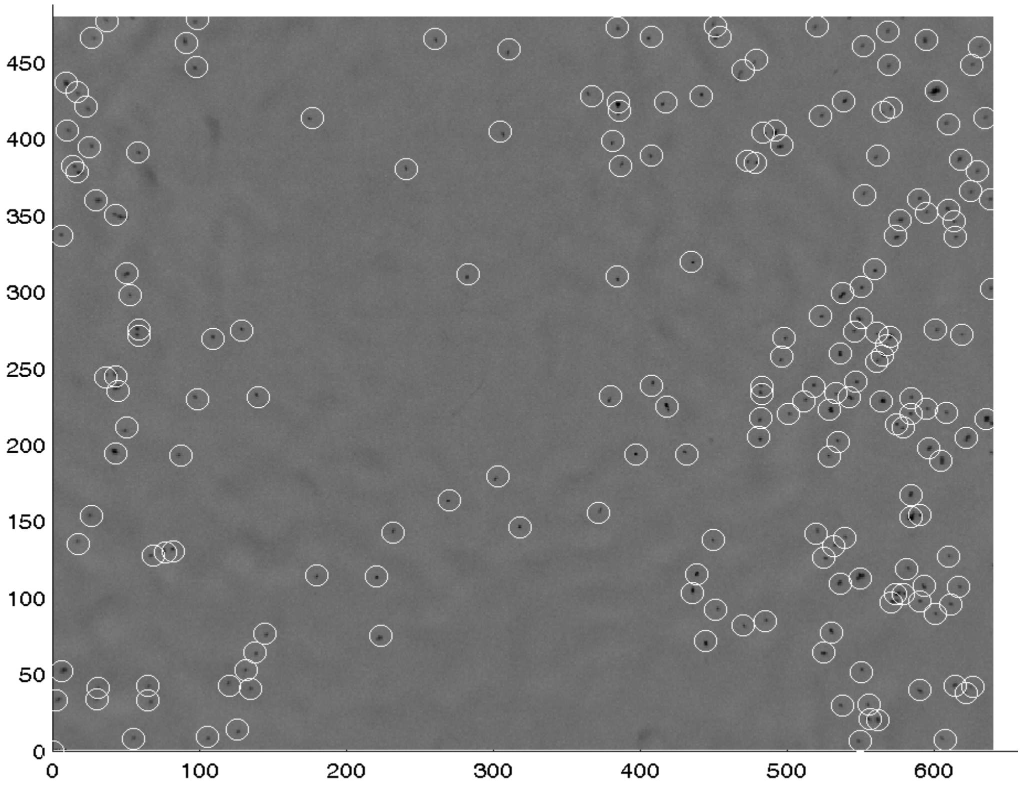

Fig. 2.5: For particle tracking experiments we used bigger particles to be able to faithfully track every single one of it ($300\,\mu$m diameter, Black CromoSpheres, Brookhaven Instruments). The tracking algorithm was based on a minimal distance approach.

2.3.3 Calibration of the Ferroin Concentration

In order to be able to identify the intensity changes, provoked by the excitation of the chemical reaction, with approximate values of the ferriin concentration (here the indicator for the activation) we calibrated set-up No.1 (Fig. 2.1). The basic idea of our calibration lies in the fact that, in the visible wavelength, the main part of the intensity changes can be attributed to changes in ferroin $[Fe(phen)_3^{2+}]$ and ferriin $[Fe(phen)_3^{3+}]$ concentrations which appear as red and blue coloured liquids. Both concentrations are linked via the formula:

$$[Fe(phen)_3^{3+}] = [Fe(phen)_3^{2+}]_0 - [Fe(phen)_3^{2+}], \tag{2.3}$$

where $[Fe(phen)_3^{2+}]_0$ is the initial concentration of the freshly prepared solution before any reactions occur. It is known from preparation.

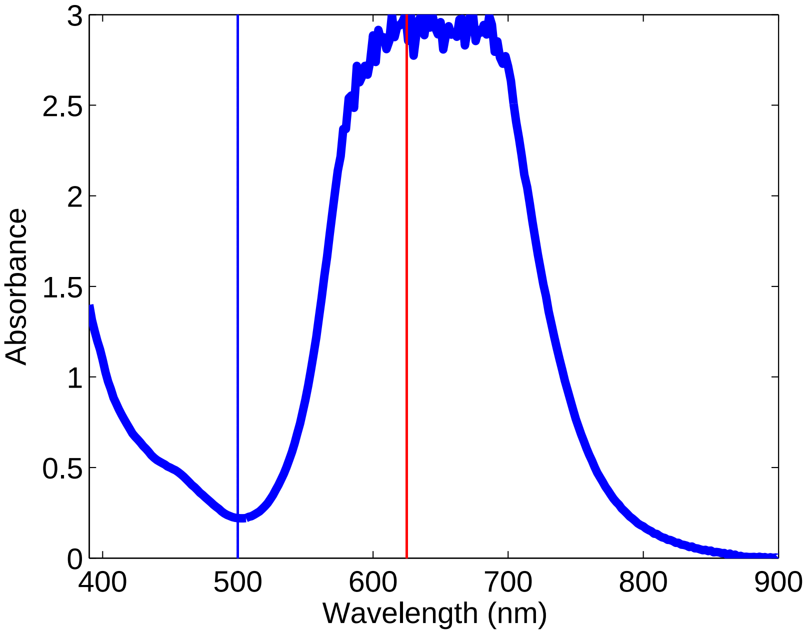

Fig. 2.6: The contrast enhancing filter that we use has its maximum transmission around the wavelength where ferroin has its maximal absorption. Thus, at this wavelength (≈ 500 nm, see blue line) we see the maximal changes when ferroin goes to its oxidized state ferriin. On the other hand, the changes of the ferriin concentration which has maximal absorption in the red (≈ 625 nm, see red line) are filtered out. The absorbance measures the logarithmic ratio of the light falling onto the filter I_0 and the light transmitted through the filter I. Since the logarithm is to base 10, the value 3 signifies that I_0 is thousand times larger than I.

To maximize the intensity change when the chemical reaction is excited we install a contrast enhancing green filter foil with maximal transmission around wavelength $\lambda \approx 500$ nm and a maximal absorption around $\lambda \approx 625$ nm. The maximal absorption of ferroin occurs around 500 nm while the maximal absorption of ferriin around 625 nm and thus, with this filter, absorption spectra of both constituents can be separated. The absorption spectra of the filter can be seen in Fig. 2.6 (compare with Fig. 2.8 showing the absorption spectra for ferroin and ferriin).

For the calibration we prepare a stock solution of ferroin of 0.025 Mol and add it in steps of $162.5\,\mu$l to the container filled up to a height of $d = 2$ mm with purified water. This procedure is repeated until we reach the maximal concentration of ferroin possible in the chemical reaction experiments, which equals the initial experimental concentration. For each step an image sequence

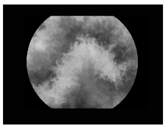

is recorded for offline analysis, while all the other settings, such as light and temperature remain constant.

Further, we checked that the zero-intensity levels of water and of the chemical reaction in the light blue state (maximal ferriin concentration) can be considered equal within the magnitude of the noise level for each pixel. We can thus assume that approximately every change in the intensity of each pixel above its noise level was caused solely by changes in the ferroin concentration while changes in the ferriin concentration were invisible to our camera due to the contrast enhancing filter. Figure 2.7 shows the resulting curve from the above described calibration procedure. The curve was derived from an average over all pixels in 100 frames with equal conditions. Beforehand each pixel was normalized to its maximum value. The standard deviation of all pixels for each value of ferroin concentration is plotted as an error. A repetition of the experiment on another day yielded the same results.

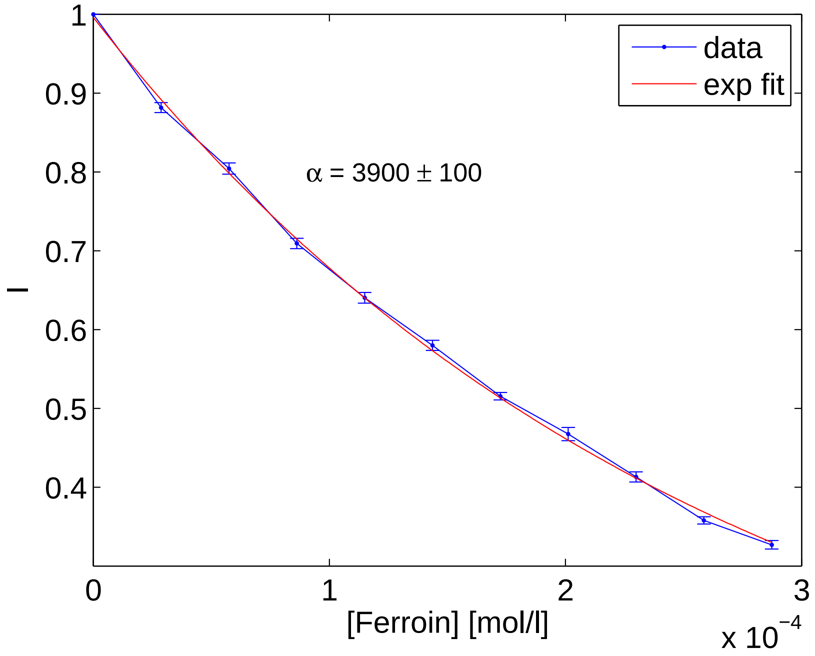

Fig. 2.7: The calibration procedure described in the text leads to an exponential relationship of the measured intensity and the ferroin concentration. The measurements were repeated twice and yielded a very similar exponent of $\alpha \approx 3900 \pm 100$.

We are now able to relate each intensity level measured by our set-up to a ferroin concentration if we assume that no other chemical apart from ferroin adds to the absorption at the monitored wavelengths around $\lambda \approx 500\,\mathrm{nm}$. The relationship of intensity and concentration can be fitted as an exponential function, see also the fit in Fig. 2.7:

$$I/I_0 = \exp(-\alpha[Fe(phen)_3^{2+}]). \tag{2.4}$$

Here, I_0 is the maximal intensity we see when $[Fe(phen)_3^{2+}] = 0$, and α is a fit parameter.

For our chemical reaction the assumption that no other chemical adds to the absorption is quite justified because in the visible range there is only one more chemical which could interfere crucially, namely B_r^- but its concentration does only increase slowly during the whole experiment. To account for this change in B_r^- during the experiment we always normalize the maximum I_0 of the curve shown above to the maximum intensity measured at every pixel when the last activation wave passed through the reactor (see Chap. 4 for an example of an activation wave).

In order to determine the ferriin concentration one has to simply solve Eq. 2.4 for $[Fe(phen)_3^{2+}]$ and insert it into Eq. 2.3 to get:

$$[Fe(phen)_3^{3+}] = [Fe(phen)_3^{2+}]_0 - \left(\frac{1}{\alpha}\ln(I_0/I)\right) \tag{2.5}$$

This is value has of course errors due to the various approximations assumed in the calibration process as the independence of the absorption spectra of $[Fe(phen)_3^{3+}]$ and $[Fe(phen)_3^{2+}]$ and the negligence of any other possible derivates of the reaction in the absorption spectra. Nevertheless, these errors are within the noise of intensity for each pixel. Further, the relative changes obtained by this calibration for the ferriin and ferroin concentrations agree well with the ones stated in the literature [32].

Note: The above exponential rule Eq. 2.4 can also be seen as an approximate version of the Lambert-Beer law, which strictly is only valid for monochrome light [98]. Here, since on the wavelengths of recording, that is were the contrast enhancing filter has its minimum in absorbance, the absorption spectra of ferroin changes rather little, see Fig. 2.8, curve (a). It it thus justified to use the Lambert-Beer law with a mean absorbtivity $\Gamma = \langle\gamma_\lambda\rangle$ such that the above exponent alpha can be identified as the product of Γ and d, the thickness of the layer. However, we want to stress that our calibration does not rely on the validity of the Lambert-Beer law in this context but on the measurement of intensity values for each pixel in dependence on the ferroin concentration as explained above.

Note: The absolute quantum efficiency spectra of the camera (F-032-B, AVT) as provided by the manufacturer is shown in Fig. 2.9. It shows that

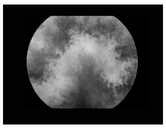

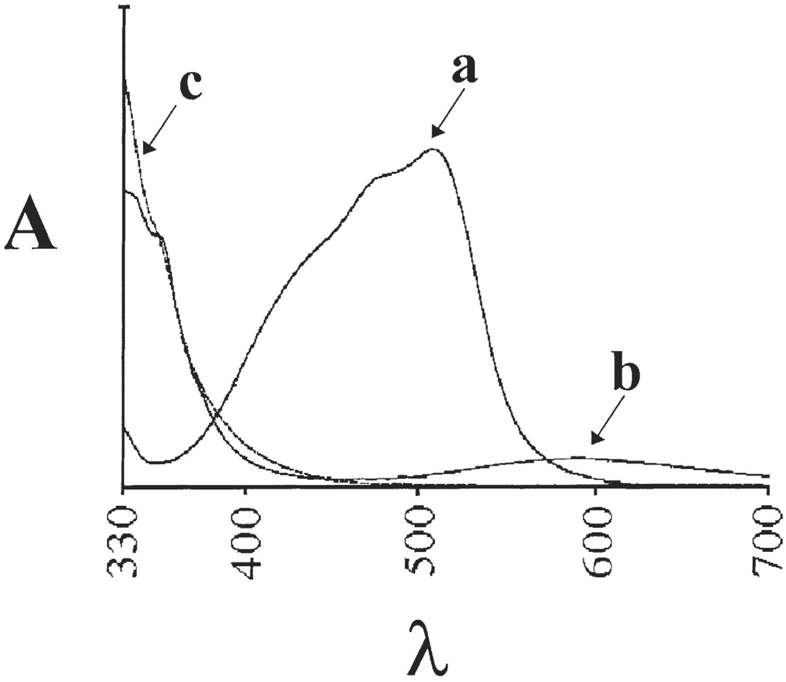

Fig. 2.8: The absorption spectra (absorbance A vs. wavelength λ) of ferroin (a), ferriin (b) and the phenantroline complex (c). It is obvious that the absorption spectra of ferroin and ferriin are well separated by our contrast enhancing filter. Graphic was taken from [99].

the camera is maximally sensitive at the wavelength of measurement around $\lambda \approx 500\,\mathrm{nm}$.

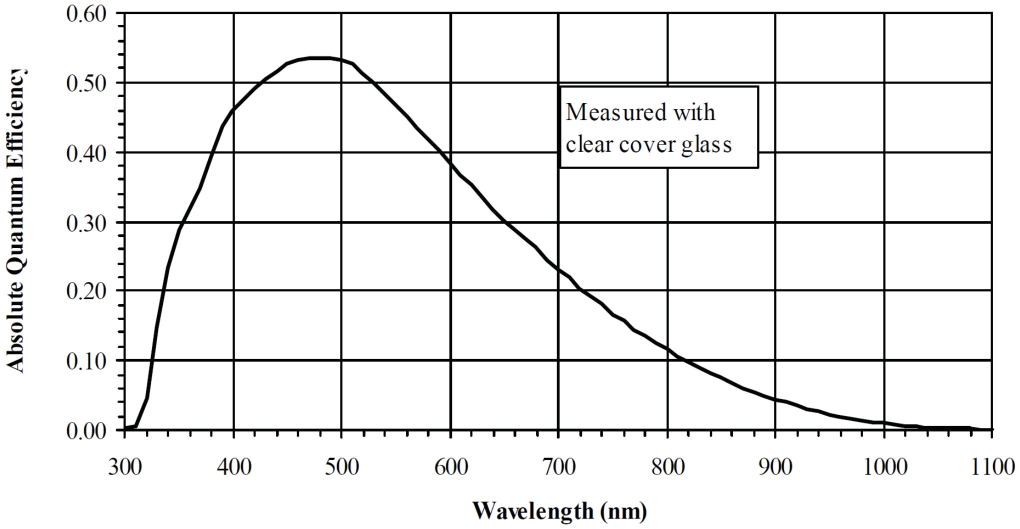

Fig. 2.9: The quantum efficiency of the camera as specified by the manufacturer (F-032-B, AVT). We see that the maximum efficiency of the camera coincides with the wavelength of our measurements (≈ 500 nm).

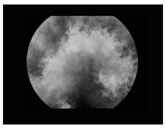

3

The Faraday Flow and Turbulence

This chapter deals with the experimental observation of Richardson dispersion and a double energy cascade in a thin horizontal fluid flow induced by Faraday waves. The energy spectra and the mean spectral energy flux as well as the longitudinal structure functions obtained from Particle Image Velocimetry (PIV) data suggest an inverse energy cascade with Kolmogorov type scaling $E(k) \propto k^{\gamma}, \gamma \approx -5/3$ and an $E(k) \propto k^{\gamma}, \gamma \approx -3$ enstrophy cascade. Particle transport is studied analyzing absolute and relative dispersion as well as the Finite Size Lyapunov Exponent (FSLE) via the direct tracking of real particles and numerical advection of virtual particles. For the relative dispersion measure Richardson dispersion with $\langle R^2(t) \rangle \propto t^3$ is observed and is also reflected in the slopes of the FSLE ($\Lambda \propto \Delta R^{-2/3}$) for virtual and real particles. The measurements are repeated for different vertical forcing accelerations of the Faraday experiment and we find that the turbulence is enhanced for increased forcing.

The contents of this chapter correspond in large parts to the published article [20]

3.1 The Discovery of the Faraday Flow

Faraday waves are a thoroughly studied phenomenon displaying a rich variety of curious wave patterns on the fluid surface as a function of the driving acceleration and frequency [18, 93]. Faraday waves are an important phenomenon in different types of physical systems, ranging from material sciences and biomedical application to Bose-Einstein condensation [100, 101]. They even serve as a visual analogon of the wave-particle dualism [102]. The ripples excited on the surface are known to undergo order-disorder transitions as the forcing is altered, leading from standing waves to a disordered state where the translational correlation length drops dramatically and the orientational correlation of the patterns also decreases [83]. This disorder in the patterns is sometimes referred to as spatiotemporal chaos [84]. The transition is eventually explained phenomenologically by transverse amplitude modulational instability, see [84] and references therein. Generally, for low viscosities, the higher the forcing strength and the frequency the more rapid are the fluctuations of the observed patterns.

Fluid flows induced by this wave patterns are termed spatiotemporally chaotic, an intermediate case between low-dimensional chaotic systems and fully developed turbulence [86]. This spatio-temporal disorder in the wave pattern causes particles floating on the surface of the fluid to undergo complex random walks in the horizontal plane [21, 86, 89]. Experiments by Mesquita et al. [103] indicate further that the horizontal transport of particles in this type of flows is caused by fluctuations in the Stokes drift that arise due to nonlinear effects causing traveling waves and imperfections in the Faraday pattern [86, 100]. Especially in a thin fluid layer like in our experiment presented here (liquid height $= 2$ mm), convective fluxes are induced that may enhance the long range displacement of particles in the flow [100]. To date, most of the studies about the Faraday experiment focus on the evolution and transitions of the surface waves and only a few consider the horizontal transport of particles floating on the fluid surface (Sec. 1.3). In consideration of the abundance of numerical, experimental and theoretical studies about the Faraday waves it is surprising that no direct observation of the evoked horizontal velocity field has been performed so far. Here, motivated by our previous studies of active media applied to this fluid flow [21, 104], we perform an experimental study of the horizontal Faraday velocity field via Particle Image Velocimetry (PIV), see Sec. 2.3.1 and [72]. Our results indicate that transport on the surface of the fluid flow is turbulent. In the following, we will call the flow induced by the Faraday experiment simply the Faraday flow.

Turbulent flows are characterized by their full energy spectrum which is derived from the Fourier transform $\widehat{(\cdot)}$ of their velocity components $\mathbf{v} = (v_x, v_x, v_x)$ (see Eq. 1.17 in Sec. 1.2.2):

$$E_{\mathbf{k}}(\mathbf{k}) = \frac{1}{2}(\|\widehat{v_x}(\mathbf{k})\|^2 + \|\widehat{v_y}(\mathbf{k})\|^2 + \|\widehat{v_z}(\mathbf{k})\|^2), \tag{3.1}$$

where $\mathbf{k}$ is the wave vector. When a turbulent flow can be approximated as two-dimensional another characteristic quantity is the full enstrophy spectrum (Sec. 1.2.2):

$$Z_{\mathbf{k}}(\mathbf{k}) = \frac{1}{2}\|\widehat{\Omega}(\mathbf{k})\|^2), \tag{3.2}$$

Ω being the vorticity [53, 105]. Assuming isotropy, the energy and enstrophy spectra $E(k)$ and $Z(k)$ are then calculated as stated in Sec. 1.2.2. Kraichnans theory of forced two dimensional turbulence predicts the development of a double energy cascade [13, 55]. When the flow is forced at the wavelength λ_f the energy is passed on to larger wavelengths generating an inverse energy cascade with the same scaling as in three dimensional turbulence ($E(k) \propto k^{-5/3}$ for $k < k_f$). In contrast, enstrophy is passed to smaller wavelengths and in this range energy scales as $E(k) \propto k^{-3}$ for $k > k_f$ ($Z(k) \propto k^{-1}$), see also Sec. 1.2.2. Kraichnans theory is strongly supported by recent numerical [60, 106] and experimental results [53, 58, 59, 63], but has not been doubtlessly verified up to now [60, 63].

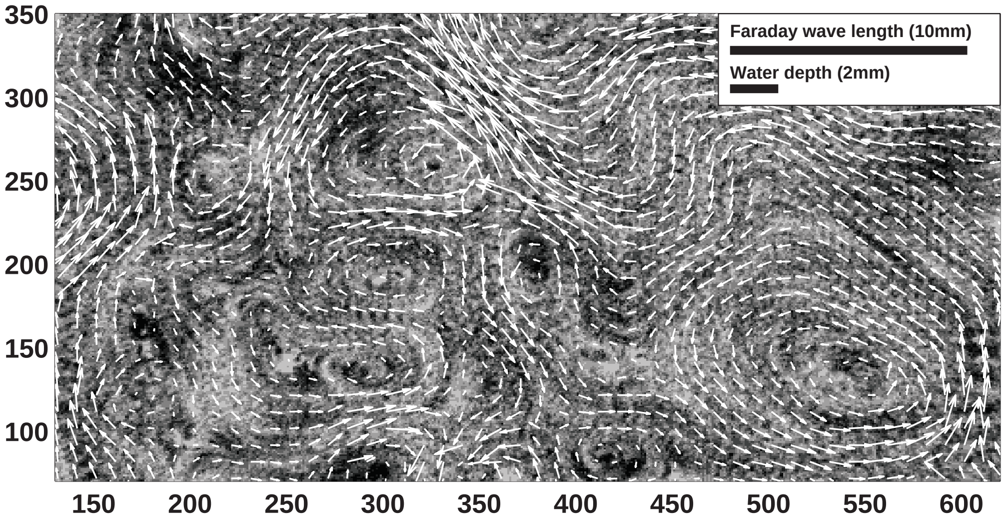

Fig. 3.1: The horizontal surface fluid flow induced by the Faraday waves at a forcing frequency of $f = 50$ Hz and acceleration $a = 1.5\,g_0$. Every second velocity arrow is shown. RMS velocity is $v_{rms} \approx 1.15$ cm/s. Reynolds number based on the Faraday wavelength and v_{rms} is $Re \approx 100$.

We find that the horizontal Faraday flow exhibits interesting characteristics of two dimensional turbulence. Fig. 3.1 shows a mean image of six successive experimental frames of the PIV particles, overlaid with a velocity field obtained via PIV analysis. Several length scales can be identified ranging from vortices

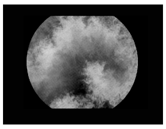

considerably smaller ($\approx 2\,$mm) than the typical Faraday wavelength ($\approx 10\,$mm) to jets spanning almost over the whole field of view. The indicated fluid depth of $2\,$mm illustrates the high aspect ratio of horizontal to vertical scales. Using the 2-D PIV velocity fields we obtain energy and enstrophy spectra as well as their spectral fluxes. Both show dual cascades similar to those predicted by Kraichnan [55]. Analysis of the horizontal transport supports the existence of a Kolmogorov type scaling range: Tracers on the fluid surface undergo Richardson relative dispersion. The overall agreement of simulated and real tracers reinforces the accuracy of the PIV measurements.

3.2 Experimental Details

For our experiments we use the setup described in Sec. 2.2, Fig. 2.1. The circular plexiglass container of $30\,$cm inner diameter is mounted on top of the electromagnetic shaker (TIRAvib S511, TIRA GmbH) which vertically vibrates with an acceleration modulated as $g(t) = g_0 + a\cos(2\pi f t)$, g_0 being the gravitational acceleration. Forcing frequency and amplitude are fixed to $f = 50$ Hz and $a = 1.5\,g_0$ if not explicitly mentioned otherwise. Faraday waves obtained have a rectangular shape and their dominant frequency is half the forcing frequency f (subharmonic response, see Sec. 1.3) [18, 83, 86]. The fluid layer, distilled water, was chosen as shallow as feasible with a depth of $2\,$mm. The maximal Faraday wave amplitude was estimated to be $A_{max} \approx 0.5\,$mm. For the forcing applied the observed wave pattern is time-dependent with travelling pattern defects. Images are recorded with the monochrome firewire camera (Pike, AVT) at a resolution of 480 x $640\,$pixel^2 for three different zoom levels. The camera looks through the bottom plate of the container via a 45° mirror. A white backlight or video-projector light source is placed above the fluid container. Image recording is triggered with $200\,$Hz ($4 \times f$). For the real particle tracking experiments we use $300\,\mu$m diameter sized, black particles (Black CromoSpheres, Brookhaven Instruments). Some hundreds of particles are added to the liquid's surface and trajectories are extracted by a minimal distance based tracking algorithm see Sec. 2.3.2. For PIV measurements (Sec. 2.3.1) floating hollow glass spheres with a density of $0.2\,\mathrm{g/cm^3}$ and a diameter of $(46 \pm 30)\,\mu\mathrm{m}$ (Q-Cel 5020FPS, Potters Europe) are added to the fluid and stay homogeneously distributed throughout the experiment, i.e., particles do not gather at nodes or antinodes as reported elsewhere [107, 108]. Every eighth image is chosen to enter the PIV analysis matching zero phase of the Faraday waves (approximately flat water surface). This minimizes the recording of spurious periodic particle movements and only the horizontal Stokes drift remains. The resulting PIV interframe time of $0.04\,$s is more than ten times smaller than the Eulerian integral timescale $T_E \approx 0.5\,$s of the flow. Velocity fields are obtained using a minimum quadratic difference based open source Matlab algorithm (mpiv) [96], see Sec. 2.3.1. Resolution of the velocity field is $1/5$ of the image resolution (95 x 127 velocity grid-points). The isotropy of the resulting velocity fields was checked for by determining the distributions of the mean velocities $\langle v_x \rangle$ and $\langle v_y \rangle$ in x and y direction respectively, see Fig. 3.2. From these velocity fields we integrate the paths of thousands of virtual tracers using a 4th order Runge-Kutta integration scheme and a x-y-t cubic spline interpolation.

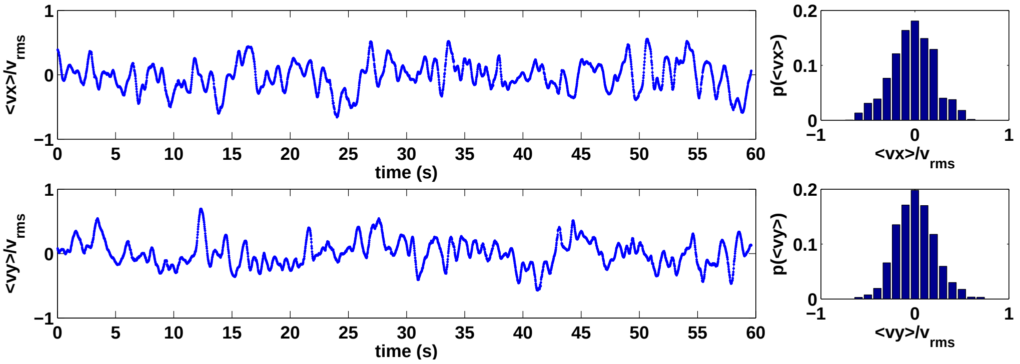

Fig. 3.2: The fluctuations of the mean velocities $\langle v_x \rangle$ and $\langle v_y \rangle$ in x and y direction, normalized to the root mean square velocity, are shown on the left. On the right the normalized distributions of $\langle v_x \rangle$ and $\langle v_y \rangle$ show that the fluctuations have a zero mean and are similar in both directions. It is thus tolerable to approximate the velocities as isotropic. We will get back to the detail of the assumption of isotropy when considering the energy spectra in Fig. 3.10.

3.3 Results

In this section, we define the term Faraday flow and determine its characteristics by considering a fixed forcing strength as described in the experimental details Sec. 3.2. We then start to vary the forcing strength by changing the acceleration amplitude a in order to observe alterations in the turbulent flow. Finally, we estimate the scaling of the third and second order structure function. The results are compared to theory and other quasi two-dimensional flows.

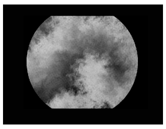

3.3.1 The Faraday Flow

Turbulent Energy and Enstrophy Spectra

Figure 3.3 shows the radially averaged energy (a) and enstrophy spectra (b) of the velocity fields for three zoom levels. In all spectra a bend wavenumber k_b can clearly be distinguished where the slope of the spectra changes (see arrows). We argue that $k_b \approx 0.12\,mm^{-1}$ is the approximate value of the forcing wavenumber where energy is introduced into the flow as the spatial Faraday wavelength lies in the same range $\lambda_F = (10 \pm 2)$ mm equivalent to $k_F = 1/\lambda_F = (0.10 \pm 0.02)\,mm^{-1}$, see Fig. 3.4.

At wavenumbers $k < k_b$ a dependence $E(k) \propto k^{\gamma}, \gamma = -5/3$ fits the data well (Kolmogorov scaling, Sec. 1.2.2). For $k > k_b$ the slope is much steeper, $\gamma \approx -3$. Also the slope of the enstrophy spectra changes at k_b but it is steeper than $\beta = -1, Z(k) \propto k^{\beta}$ as predicted by Kraichnan theory for $k > k_b$ (Sec. 1.2.2). Only for the closest zoom-level the slope approaches $\beta = -1$ for high wavenumbers. In order to determine the directions of the observed cascades, in Fig. 3.3c we calculate the mean spectral energy and enstrophy fluxes, Π_E and Π_Z, as in [109, 110] (for details see Sec. 1.2.2). A negative spectral flux means that energy (or enstrophy) is transported upscale to larger wavelengths. A positive spectral flux means that energy (or enstrophy) is transported downscale to smaller wavelengths. The spectral fluxes we obtain agree with the Kraichnan-theory insofar as the forcing in a narrow wavenumber range around $\approx k_b$ (Fig. 3.4) causes a dual cascade: an inverse energy cascade upscale from k_b (negative mean spectral energy flux) and a direct enstrophy cascade downscale from k_b (positive mean spectral enstrophy flux). However, the spectral fluxes do not show a clear inertial range with constant flux (similar to experiments reported by Chen et al. [110]). This could be due to the spectral proximity of forcing and dissipation ranges. Other experimental observations of dual cascades also observed exponents for the enstrophy cascade $\gamma = -(3+\mu)$, $\mu \geq 0$ [58, 59, 63]. Boffetta et al. [63] showed that μ can be understood as a correction of the Kraichnan scaling due to bottom friction. Deviations from Kraichnan scaling in our experiment may additionally be caused by 3-D effects, i.e., out of plane flow and thus divergence of the velocity field $\nabla \cdot \mathbf{v} \neq 0$ [67]. The root-mean-square divergence of the velocity fields was found to be 3 to 10 times lower than the value of the root-mean-square vorticity in dependence of the forcing strength. For higher forcing amplitudes the divergence becomes more important and at spatio-temporally localized spots this ratio can be inverted, see Fig. 3.5.

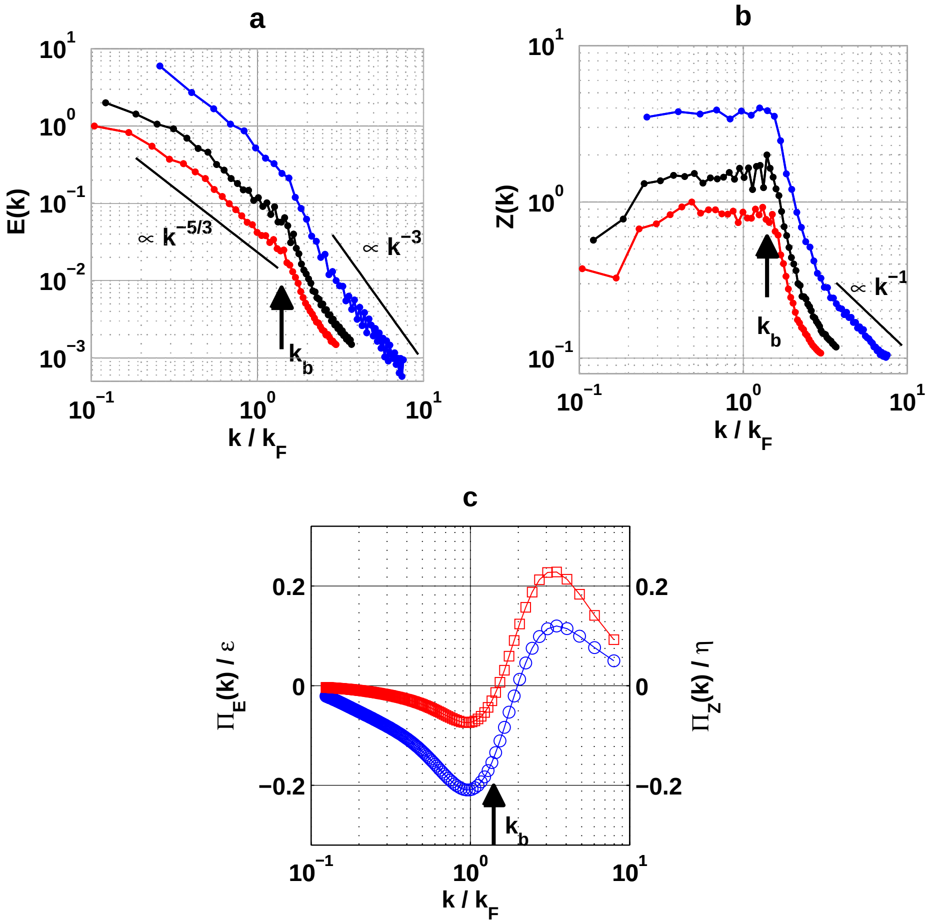

Fig. 3.3: The energy (a) and the enstrophy spectra (b) for three different zoom-levels ($134 \times 100\,\mathrm{mm}^2$, red, lowest; $108 \times 81\,\mathrm{mm}^2$, black, middle; $52 \times 33\,\mathrm{mm}^2$, blue, upper) reveal a double cascade (scaled by Faraday wavenumber $k_F = 0.1\,mm^{-1}$). (c) The mean spectral energy flux Π_E (blue circles) and enstrophy flux Π_Z (red squares) for the closest zoom, normalized with the mean energy and enstrophy dissipation rates $\epsilon = \nu\langle|\nabla \otimes \mathbf{v}|^2\rangle$ and $\eta = \nu\langle|\nabla\Omega|^2\rangle$.

Transport and Diffusion in the Faraday Flow

In order to study the horizontal transport in the Faraday flow and to validate the PIV analysis we analyze the absolute dispersion (Sec. 1.2.3) of the real and the virtual tracers $\langle A^2(t)\rangle = \langle|\mathbf{r}(t) - \mathbf{r}(t_0)|^2\rangle \propto t^{\gamma}$, shown in Fig. 3.6a. The slope of the absolute dispersion of both tracers behaves nearly identical at most scales, which shows that the PIV velocity fields reflect important statistical characteristics of the Faraday flow. Only for the smallest initial separations both measures deviate. This is most likely due to the limited resolution of the PIV

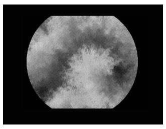

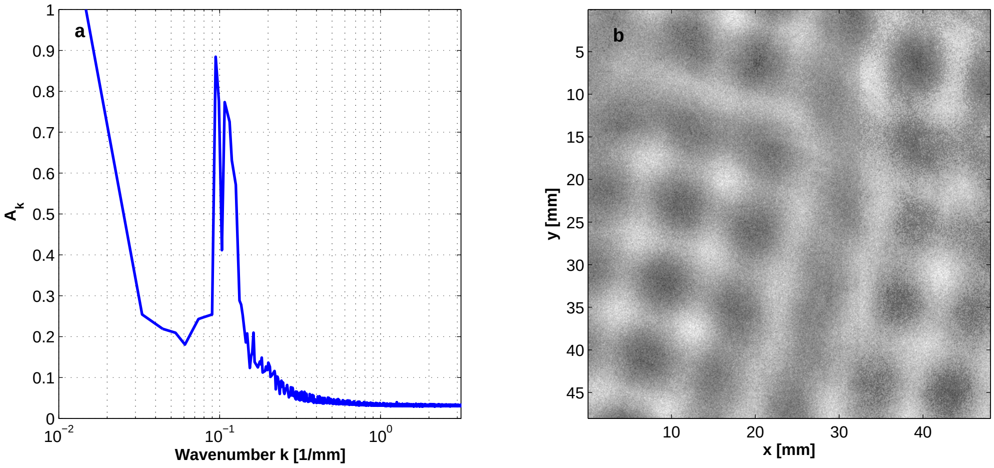

Fig. 3.4: Spectrum Faraday wavelength. A typical wavelength $\lambda_F = (10 \pm 2)$ mm equivalent to $k_F = 1/\lambda_F = (0.10 \pm 0.02)\, mm^{-1}$ can be easily distinguished in the spectrum (a) computed by a Fourier transform of the images taken at non-flat surface in an experiment without particles (b). In this experiment a dye and different diffuser settings are used to enhance the contrast of nodes and antinodes .

measurements as we will discuss later on. For short times the absolute dispersion of both tracers inclines steeply with a slope of $\gamma \geq 2$ before it gradually declines, revealing an important transient region with a slope $1 < \gamma < 2$ [21], see also Sec. 1.2.3 and Chap. 5. We will see in Sec. 3.3.2 that the size of this transient region depends on the acceleration of the vertical forcing.

While the absolute dispersion depends sensitively on the large scale motion of the turbulent flow, the relative dispersion depends on the structures (vortices or eddies) of the size of the actual particle separation (Sec. 1.2.3) [53, 74, 111]. The relative dispersion of two particles is proportional to the dispersion of a particle cloud, but it does not give insights about the shape of the particle cloud which can be very complex and even fractal [45, 112]. The implications of this fact will be discussed in more detail in Chap. 6. Kolmogorov scaling, as observed in the energy spectra, should be reflected in the relative dispersion and in the FSLE spectra. This relationship is a direct consequence of the Kolmogorov scaling of the second order structure function which we calculate below, see [57, 75, 113] and Sec. 1.2.3.

Figure 3.6b shows the relative dispersion for virtual and real tracers. The relative dispersion is a notoriously difficult measure as it depends sensitively on the initial distance of the tracked particles and thus on the definition of an initial time t_0 even for highly turbulent flows [113–116]. The basic problem with

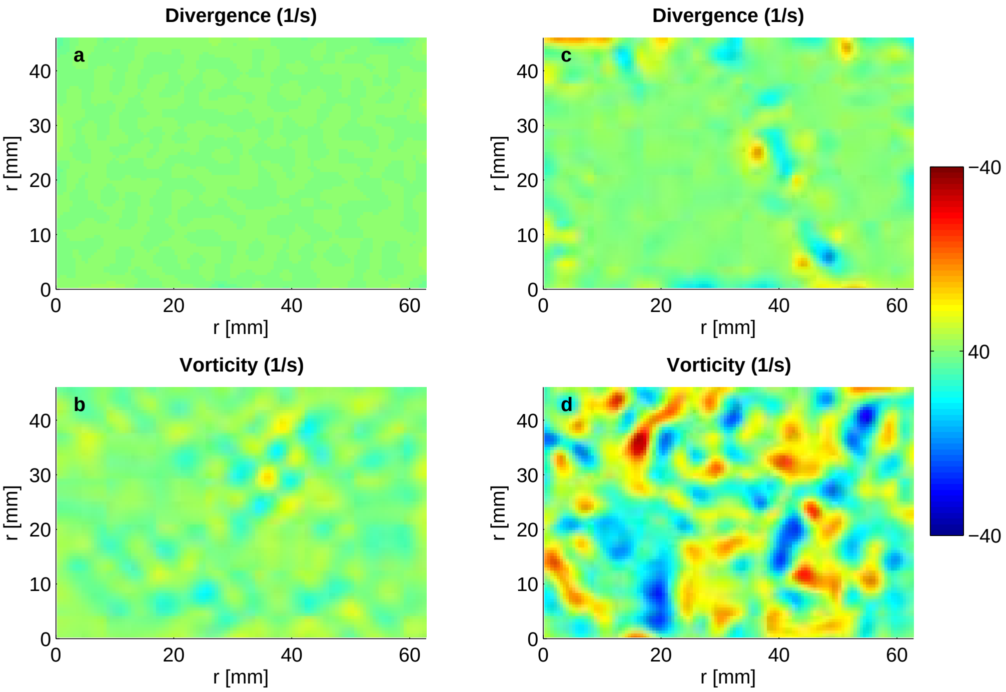

Fig. 3.5: The divergence and the vorticity for a very low forcing of $a = 1.25\, g_0$, (a) and (b), are small compared to the ones of large forcing of $a = 2.18\, g_0$ (c) and (d). The divergence is a much smaller than the vorticity in most areas. Only in spatiotemporal discrete points the divergence becomes important.

this measure is that the average over different particle-pairs is taken over time and not over their actual separation. Thus one mixes up separation information from different scales and biases the curve that would result if all particles were released at the very same point of the flow and at the very same time. This is, at least experimentally, deemed impossible. This dependency on the initial distance of the particles is also observed in our experiments. Smallest experimentally feasible initial distance of the real tracers was found to be in between 3 and 4 pixels ($0.63 - 0.84\,$mm for the farthest zoom-level). We determine $t_0 = -0.22\,$s for the real particles using the method of Ott and Mann [114]. This is the estimated mean time for two infinitesimal close particles to reach the initial experimental separation. For the virtual tracers the initial distance can be chosen arbitrarily small (here $0.5\,$pixel) and $t_0 \approx 0$ [115]. The slopes of both measurements show Richardson scaling $\langle \Delta R^2(t) \rangle \propto (t - t_0)^3$ for nearly one decade. It is difficult to ascertain if the subsequent flattening of the slope is real or if it is solely due to the fact that quickly separating particles leave

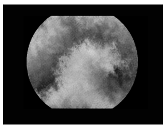

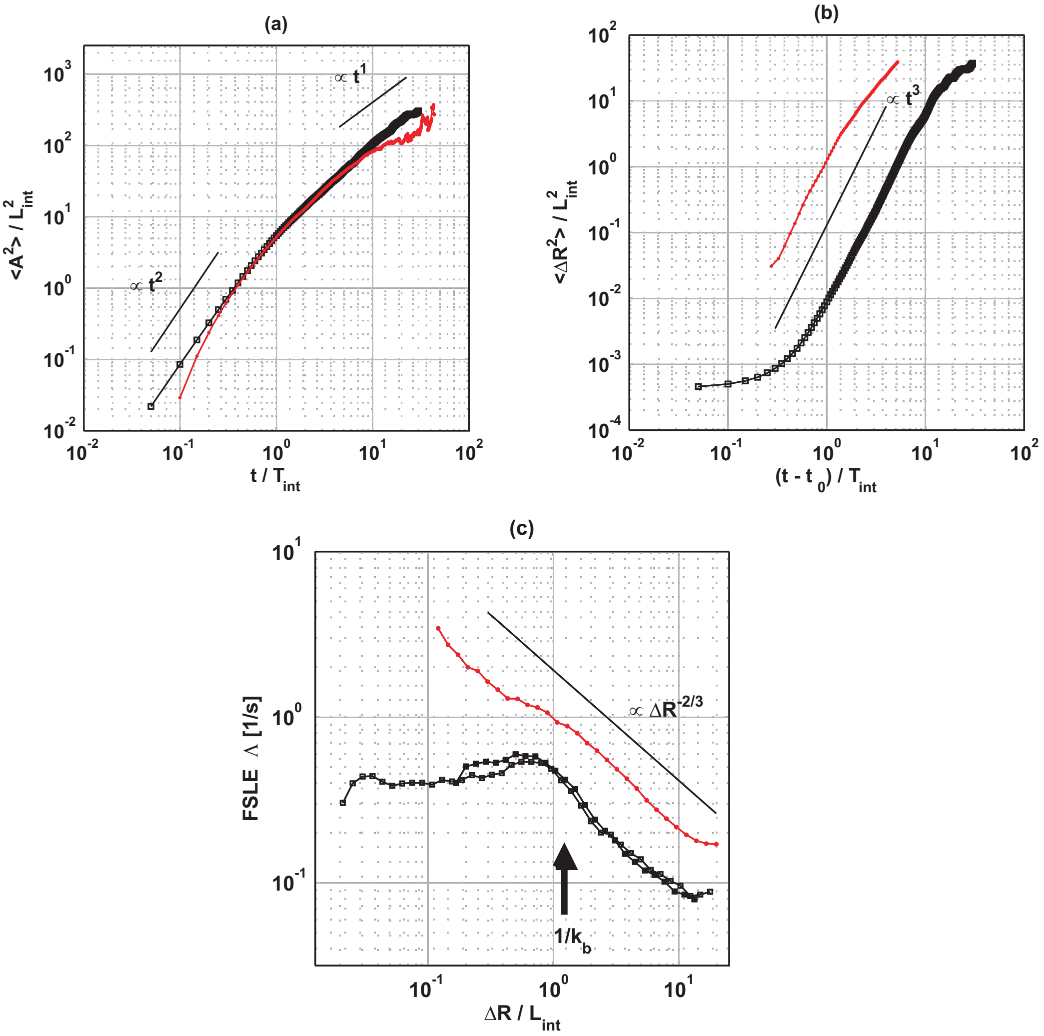

Fig. 3.6: Absolute dispersion (a), relative dispersion plotted against $(t - t_0)$ (b) and FSLE (c) of real (red dots) and virtual (black squares) tracers (zoom level: $134 \times 100\,\mathrm{mm}^2$) normalized by the Lagrangian integral time $T_{int} \approx 0.8$s and Eulerian integral length scale $L_{int} \approx 5\,$mm. The FSLE spectra of the artificial tracers is calculated for two different initial separations: 0.5 pixel (open squares) and 5 pixel (solid squares).

the field of view more rapidly. Definitely, one expects that $\langle \Delta R^2(t) \rangle$ saturates (slope zero) when it approaches system size as side walls restrict further separation. It is to mention that the absolute values of the relative dispersion are higher for the real tracers. This is partly due to the bigger initial distance of the real tracer as was checked launching the artificial tracers with an initial distance of $3-4$ pixels. However, while the relative dispersion of virtual tracers grows exponentially for small times, for real tracers it does not.

Since the relative dispersion is a delicate measure [116] we additionally compute the more robust Finite-Size-Lyapunov-Exponent (FSLE) $\Lambda(\Delta R)$ [111] for real and virtual tracers in Fig. 3.6c (Sec. 1.2.3). In contrast to relative dispersion, the averaging is performed over particle pairs that reached the same separation, and thus, the FSLE avoids the problems of intermingling different scales. Moreover it gives detailed clarity about the range of scales on which the Richardson scaling occurs. Real and virtual FSLE measurements reveal a Richardson scaling $\Lambda(\Delta R) \propto \Delta R^{-2/3}$ for $\Delta R/L_{int} > 1$ as expected for Kolmogorov scaling of the energy spectrum. Again the FSLE values of the real tracers are somewhat higher than that of the virtual ones. Also the FSLE values of the virtual tracers show a clear plateau which corresponds to exponential (chaotic) particle separation for small ΔR. Such a chaotic regime is theoretically expected for the enstrophy cascade (Sec. 1.2.2). In contrast, the FSLE values of the real tracers only insinuate this plateau. Rather for $\Delta R/L_{int} < 1$ the FSLE values of the real tracers again follow the Richardson scaling and thus disagree with the virtual ones and with the existence of an enstrophy cascade. This discrepancies could be owed to different effects: First, it is likely that the real tracer particles have more inertia than the PIV particles. We find that inertia has a stronger effect on relative statistics than on absolute statistics (cp. Fig. 3.6a with Fig. 3.6b,c) which also agrees with actual findings [95]. Second, the PIV algorithm might miss some of the small scale dynamics leading to less dispersion of the virtual tracers in that ranges. Third, it is possible that the small PIV particles change the characteristics of the fluid surface slightly which could change the dynamics of the Faraday waves and result in a somewhat less turbulent flow [117]. Further, it must be noted that for the real tracers chance pairs were measured. Here, particles are termed chance pairs when they come closer than 4 pixels to any other particle at some time during their sojourn in the field of view. Possible bias due to chance pairs has been reported [118].

3.3.2 Variation of the Forcing Strength and Reynolds Numbers

Finally, more questions about the Faraday flow remain to be answered concerning its variation with forcing frequency, amplitude or liquid height. Here, we vary the forcing amplitude by varying the acceleration a and observe how the turbulence and its transport characteristics change. Figure. 3.7 clearly shows an increase of the root-mean-square velocity v_{rms} with increased acceleration a. Interestingly, for the range observed the increase in a has a slight influence

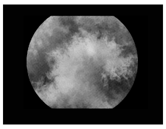

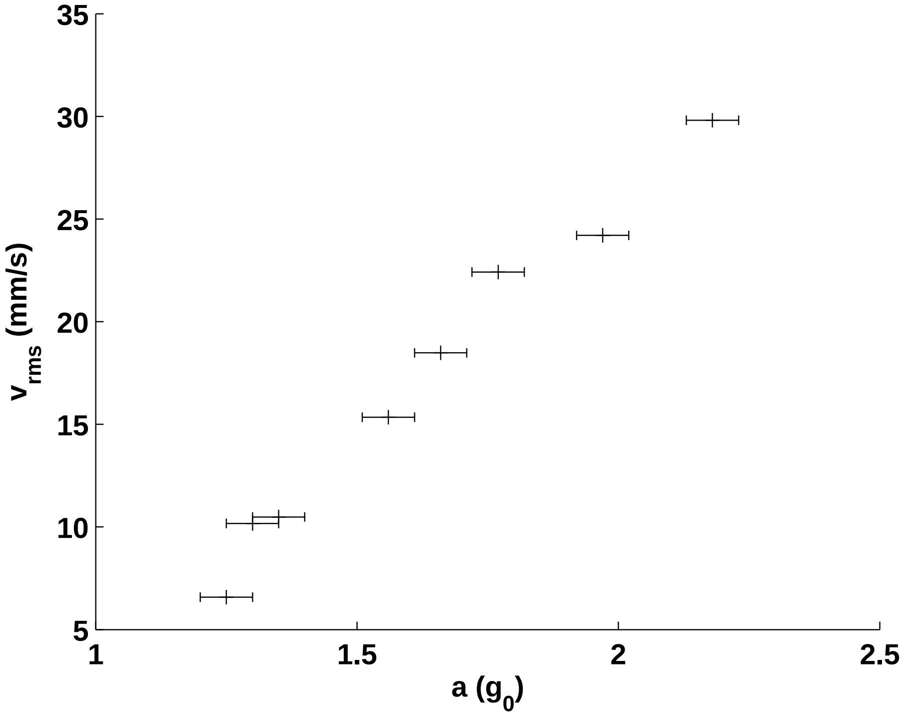

Fig. 3.7: By varying the amplitude of the vertical acceleration of the forcing a we increment the root-mean-square velocity v_{rms} of the measured velocity fields.

on the energy spectra $E(k)$ as can be seen in Fig. 3.8. The absolute energy of the system augments which indicates that the increased vertical energy insertion is at least partly translated to a stronger horizontal movement. Further, the slope of the inverse energy cascade regime becomes steeper with increasing amplitude a, being more shallow than the $k^{-5/3}$ prediction for low forcings. The enstrophy cascade seems to experience little changes for higher values of a and is similar to the theoretical k^{-3} dependence from Kraichnan theory. The $E(k)$ curves for strong forcing values seem to come closest to the Kraichnan prediction of a dual cascade.

We can further try to approximate the Kraichnan-Kolmogorov constant C_K for two-dimensional turbulence from our measurements of the energy spectra. In principle, we simply have to compensate the spectra E_k with $\epsilon^{-2/3}k^{5/3}$, where ϵ is the mean energy dissipation rate and read out the corresponding value on the y axis [56]. Since we do not have perfect inertial ranges, i.e., no constant energy flux Π_E (Fig. 3.14), we use instead of ϵ rather the mean value of the measured energy flux over the whole wavenumber range, similar to Paret et al. [119]. We obtain approximately $\langle \Pi_E \rangle \approx 0.17\epsilon$. With this value for the

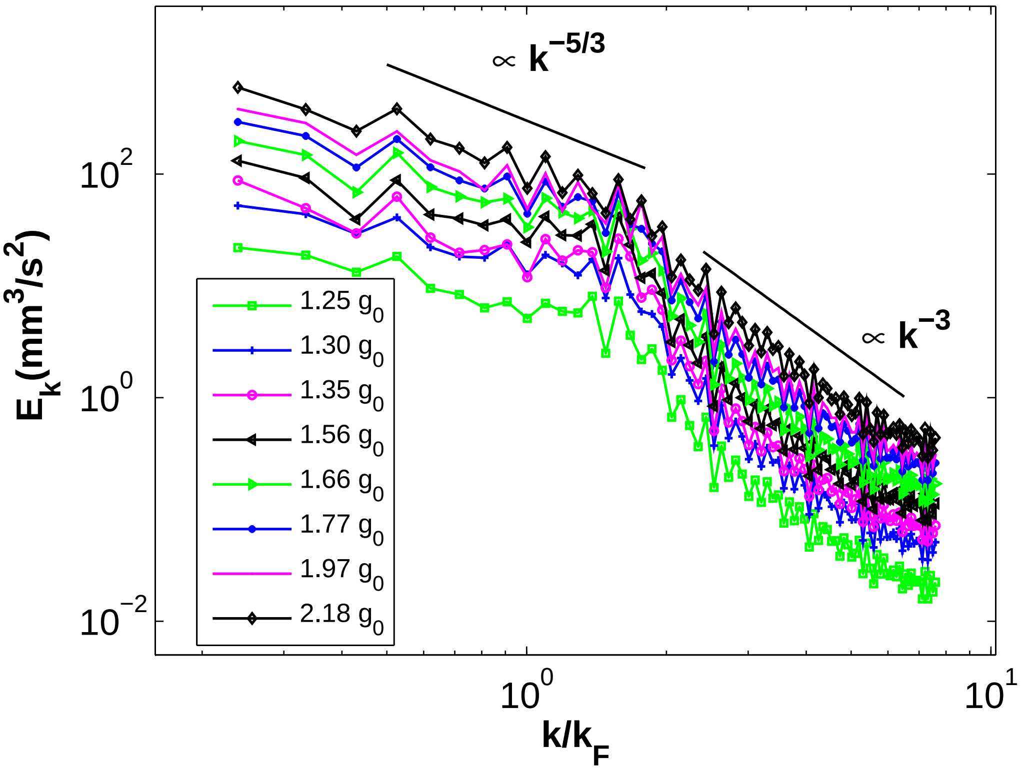

Fig. 3.8: The energy spectra for increasing forcing amplitude a contain more enrgy which indicates that the additional energy input is at least partly translated into a horizontal movement. The black lines indicate the theoretical Kraichnan predictions for a double cascade. Seemingly, the slopes suit best for strong forcing accelerations. For low forcings and small k the slope is more shallow than predicted by Kraichnan theory.

mean energy flux on all scales our compensated spectra lies in the range of the numerically accredited value of the two-dimensional Kolmogorov constant, $C_K \approx 7$ as can be seen in Fig. 3.9.

In a strict sense the energy spectra $E(k)$ does only represents the full spectrum $E_{\mathbf{k}}(\mathbf{k})$ if this is fully isotropic. Figure 3.10 shows the full spectra for the highest and the lowest forcing respectively. The spectra are averages over 1500 different images corresponding to $60\,\mathrm{s}$ of recording. The temporally averaged spectrum $E_{\mathbf{k}}(\mathbf{k})$, Fig. 3.10a, of the highest forcing is almost fully isotropic and only for very low wave numbers a cross-like structure can be identified. In the case of lowest forcing this cross-like structure becomes more pronounced and clear peaks located around the wave number k_f can be distinguished. This

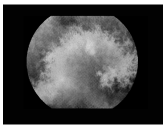

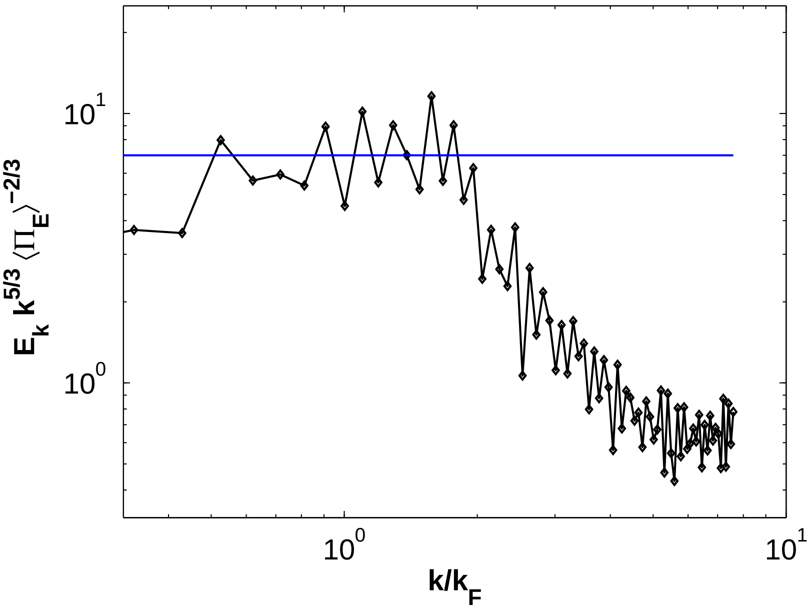

Fig. 3.9: When we compensate the energy spectra E_k for the highest forcing of $a = 2.18\,g_0$ with $\langle \Pi_E \rangle^{-2/3} k^{5/3}$, we approximately obtain the Kraichnan-Kolmogorov constant of $C_K \approx 7$ as found from numerical simulations [56]. The blue line indicates the value 7.

cross tells us that there are two preferred directions in the velocity fields and that energy is located around the typical Faraday wave number k_f.

The existence of a preferred direction in the full energy spectra can be explained by looking at the distribution of vorticity in the velocity field, which seems to be closely correlated to the underlying Faraday pattern. Figure 3.11a shows the nodes and antinodes of the Faraday pattern, where the difference in intensity is computed between two subsequent images at maximal wave amplitude with a phase shift of π. In Fig. 3.11b, the same nodes and antinodes are indicated as black contour lines, while the colour indicates now the strength of the vorticity. It is clearly seen, that the vorticity lies on a grid with a similar wavelength as the Faraday waves which is slightly shifted. High vorticity values are preferably located on the nodes of the Faraday waves. This dominant vorticity pattern thus suggests that the flow is forced by a grid of vortices arranged according to the Faraday wave pattern. For short times, this grid maintains its orientation which is then reflected in the two-dimensional energy spectra.

We argue that the turbulence is still isotropic for long times because the orientation of the Faraday waves changes slowly with time smoothing out the directional dependencies. For higher forcings, the spectrum from the same

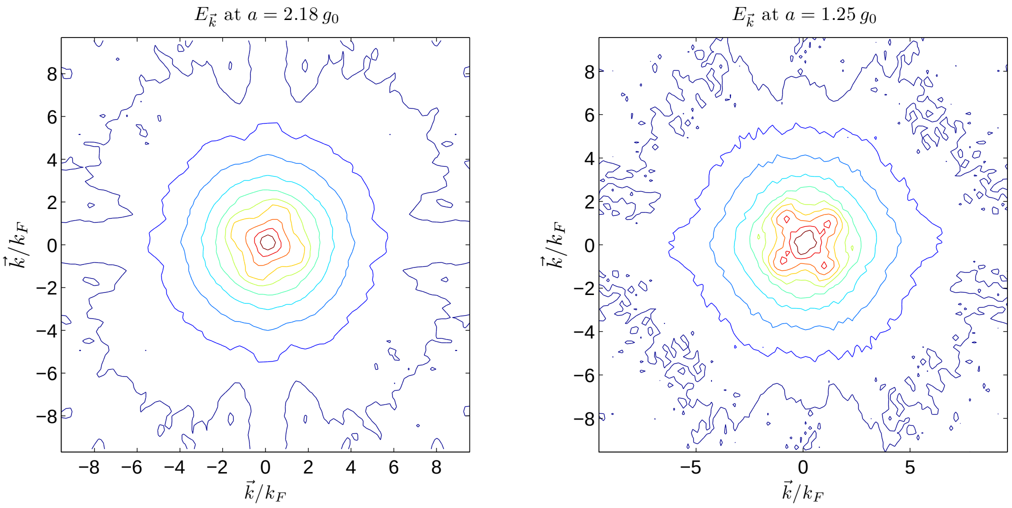

Fig. 3.10: The full energy spectra $E_{\mathbf{k}}(\mathbf{k})$ for highest (left) and lowest (right) forcing acceleration amplitude a give us some insight into the structure of the velocity field. The yellow and red cross-like structures in the middle of the spectra indicate that there are two preferred directions in the velocity fields. These peaks can be identified with the structure imposed by the Faraday waves which change their orientation in time only slowly and are located around the Faraday wavelength k_F.

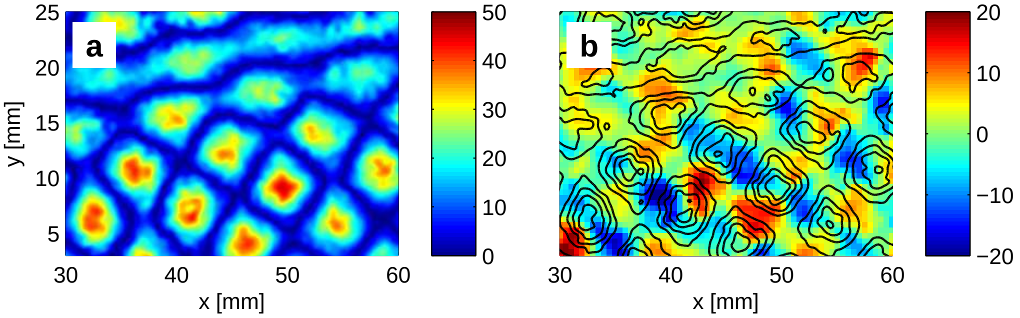

Fig. 3.11: (a) The nodes and antinodes of the Faraday waves can be distinguished via their different intensity level due to the different fluid thickness. The fluid thickness is constant at the nodes and changes at the antinodes. (b) The vorticity of the fluid flow is distributed on a similar grid as the Faraday waves where the highest absolute vorticity values preferably occur on the nodes.

timespan seems much more isotropic because the orientation of the Faraday wave field changes much quicker and its general appearance is much more turbulent [83] (see also Sec. 1.3). Figure 3.12 shows the temporal fluctuations in the Faraday wave pattern. The nodes and antinodes of the Faraday pattern

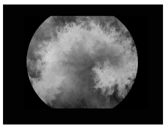

can be seen in the left panel. A space-time plot in the right panel immediately reveals the differences in the typical timescales of both patterns at different forcing intensities.

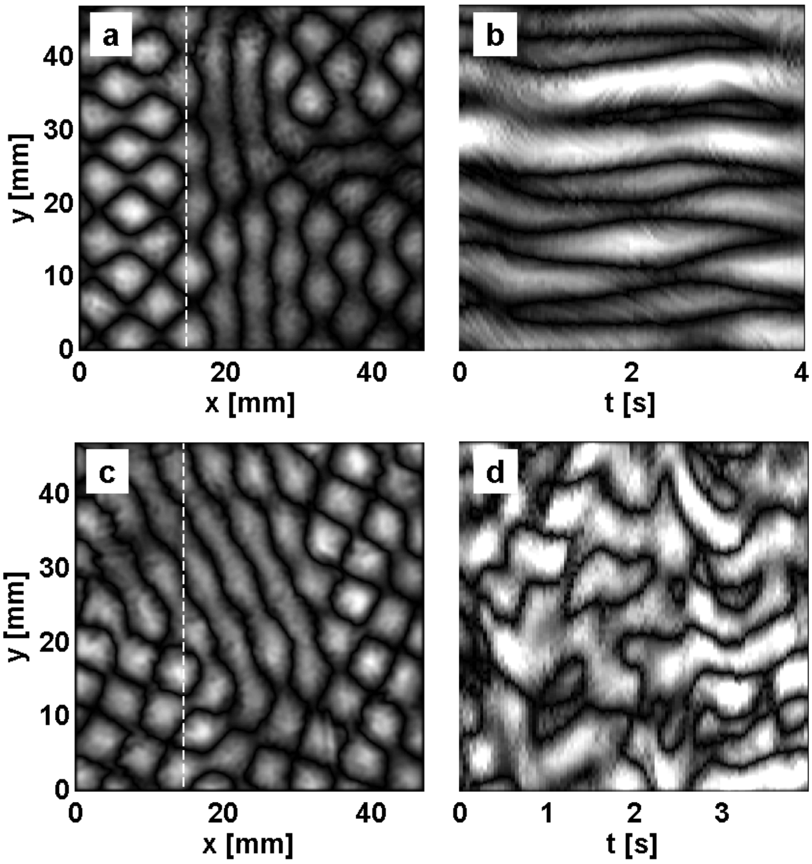

Fig. 3.12: Nodes and antinodes of the Faraday waves. The instantaneous patterns (not the wave heights) for low forcing amplitudes $a \approx 1.35\, g_0$ (a) and high forcing amplitudes $a \approx 2.18\, g_0$ (c), both at $f = 50$,Hz, are similar. However, the timescales of persistence and reordering of the patterns are very different: A space-time plot of the evolution of the pattern at fixed x, indicated as a white striped line, shows much longer correlated structures for the low forcing (b) than for the strong one (d).

Similarly to the Faraday patterns also the vorticity patterns, shown in Fig. 3.13, reveal temporal fluctuations. Differences in the typical lifetimes of the vorticity patterns at different forcing intensities are also observed. To our knowledge there are no experimental studies about the dependency of the type of turbulence arising on the correlation times of the driving forces and its impact remains to be studied.

The anisotropy in the energy spectrum for the low forcing falls off fast towards higher wave numbers and the outer cross-like structures in Fig. 3.10 are owed to cut-off artefacts of the windowing procedure during the fast Fourier transformation. Similar peaks as the ones we see for the low forcing, due to the geometry of the forcing, were also found in electromagnetically driven flows in shallow electrolytic solutions, see [53, 120]. Even though the magnets which cause the forcing in these experiments do not change their position slowly in time, in contrast to the Faraday waves which cause the Faraday flow, the authors of these studies also claim their spectra to be sufficiently isotropic.

The normalized energy and enstrophy fluxes, Π_E/ϵ and Π_Z/ϵ also increase for stronger forcing, seen in Fig. 3.14. For all forcing strengths the energy flux is negative or zero over the whole range of scales possibly observable with our resolution. This is valid even for those wavelengths where a pronounced positive enstrophy flux can be observed. We believe that this behaviour depends on the quality and resolution of the PIV on small scales since for the closest zoom used in this study (Fig. 3.3c, $a = 1.5\,g_0$, zoom $\approx 0.08\,\mathrm{mm/pixel}$) the positive energy flux can be observed.

Further, we find that the peak of the maximal negative energy flux shifts towards higher wavelengths (lower wavenumber) for stronger forcings (Fig. 3.14). This can be interpreted as an increase in the typical large-scale dissipation scale l_{Lf}. Dimensional arguments explain this shift since l_{Lf} depends only on the large scale energy dissipation rate α_{Lf} and the rate at which energy is transferred to large scales ϵ: $l_{Lf} = (\epsilon/\alpha_{Lf})^{1/2}$. Thus, the two possible methods to increase l_{Lf} and broaden the inertial scaling range are either to diminish the friction at large scales or to increment ϵ, the energy that is transferred to large scales [60]. Here, we do the latter, since we enhance the forcing at intermediate lengthscales by augmenting the acceleration of the container filled with the liquid. This mechanism can also explain the decrease of the slope in the energy cascades for lower forcings as shown in Fig. 3.8. For lower forcings the cascade has a very limited range to develop because the friction lengthscale l_{Lf} is very close to λ_F the lengthscale of the Faraday waves. Energy is thus immediately at its feeding scale removed again by friction causing the slope to become more shallow.

To visualize the details of the spectral energy and enstrophy fluxes Fig. 3.15 depicts the normalized fluxes trough different length-scales r for a forcing acceleration of $a = 1.77\,g_0$ overlaid by the actual velocity field. While strong energy fluxes can be distinguished within the whole domain shown (right), the strong enstrophy fluxes seem to be localized at the vortex-like structures (left). Figure 3.16 shows the temporal evolution of the same structures at a fixed scale of $\approx 5\,\mathrm{mm}$ which is about half the size of the Faraday wavelength, a scale on

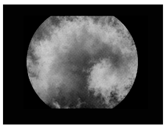

which many vortices develop. Again the evolution of the vortex just on the right of the middle coincides with the highest enstrophy flux values. It seems that enstrophy flux gets transported into the vortex. Another smaller vortex just below the big one vanishes during the image sequence, producing also a reduction in the intensity of the enstrophy fluxes. However, the evolution of the spectral fluxes in time and through different scales are an active field of study and have not been fully understood up to now. Recent findings by Kelley and Ouellette suggest that the regions defined by similar values of spectral fluxes are being transported and confined by Lagrangian structures [67].

The variation of the spectral fluxes in time might also partly be due to temporal changes in the energy and enstrophy content of the velocity field, see Fig. 3.17a and Fig. 3.18a, where we calculate $v_x^2(t)$ and $v_y^2(t)$ and $\Omega(t)^2$ respectively. This fluctuations could be due to variations in energy (enstrophy) input provided in some way by the Faraday waves. Since we can not simultaneously observe the full container but only a limited field of view of a few centimeters the fluctuations could also be caused by energy (enstrophy) entering from the sides. In many numerical studies the temporal fluctuations of the forcing, and thus of the energy and enstrophy input, is assumed to be a Gaussian stochastic forcing and its temporal dependence is considered to be white noise [56]. By calculating the Fourier transform of our signal we find that the energy fluctuations are rather described by a brown or Brownian noise which scales with $I \propto f^{-2}$, where I is the power spectral density of the energy or enstrophy, Fig. 3.17b and Fig. 3.18b.

Also for the different forcings we can calculate the transport statistics. Figure 3.19 shows the absolute and the relative diffusion as well as the FSLE for the different forcing amplitudes. As one would expect, since the fluid flow becomes faster when more energy is introduced into the system, also the transport is enhanced for higher forcing accelerations a. This can be clearly distinguished for all three dispersion measures. Again the scaling of the different measures agree with the existence of a double cascade. Especially the scaling of the relative dispersion shows an accurate increase corresponding to Richardson dispersion, $\langle \Delta R^2 \rangle \propto t^3$. Here no bias of finite initial particle pair separation as mentioned above was encountered because only artificial tracers were used which can be launched arbitrarily close (see above).

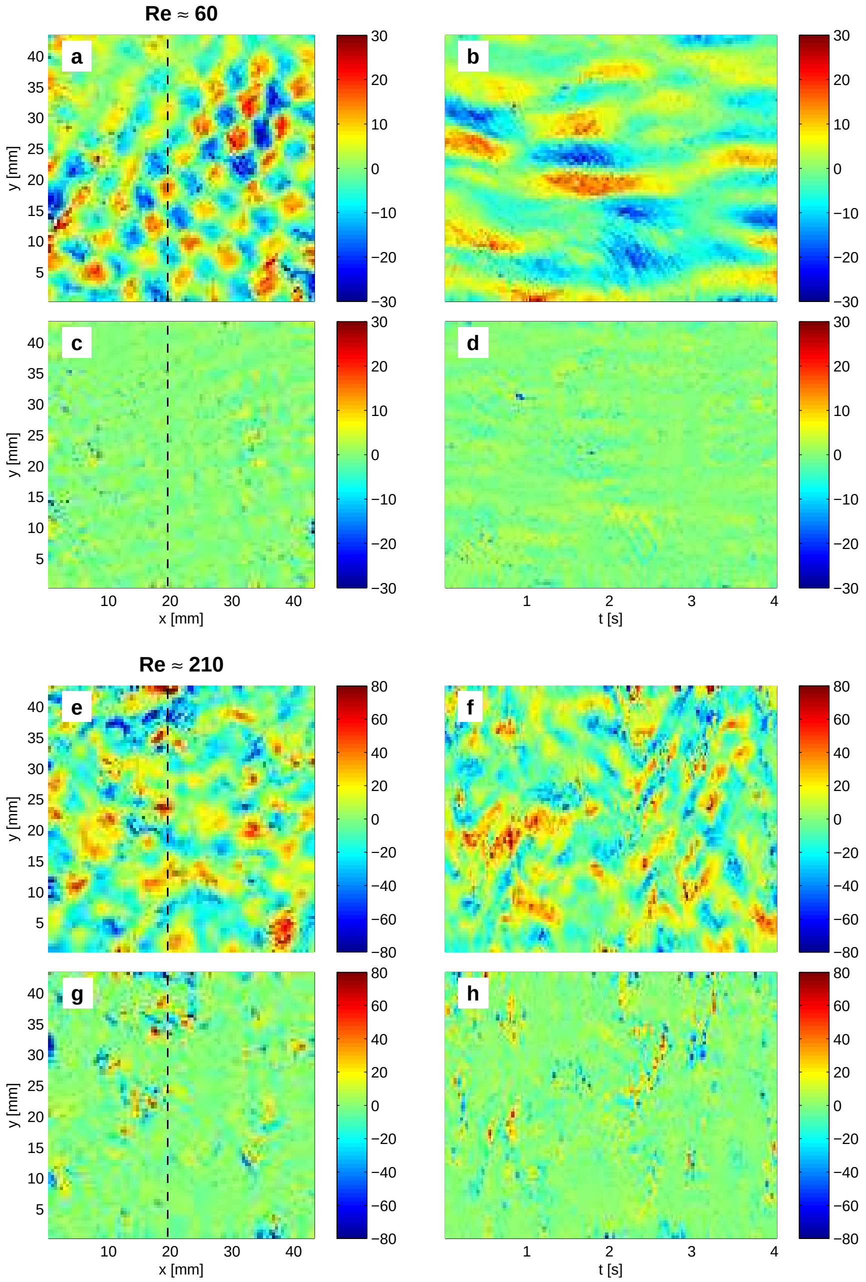

Fig. 3.13: Vorticity patterns for two different forcing accelerations. The instantaneous vorticity patterns for low forcing amplitudes $a \approx 1.35\, g_0$ (a) and high forcing amplitudes $a \approx 2.18\, g_0$ (e), both at $f = 50$,Hz. Similarly to what we observe for the Faraday waves the timescales of persistence and reordering of the patterns are very different: A space-time plot of the evolution of the pattern at fixed x, indicated as a black striped line, shows much longer correlated structures for the vorticity at low forcing (b) than for at strong forcing (f). For comparison also the divergence patterns are plotted for the low forcing (c),(d) and for the high forcing (g),(h)

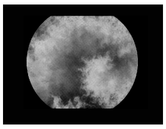

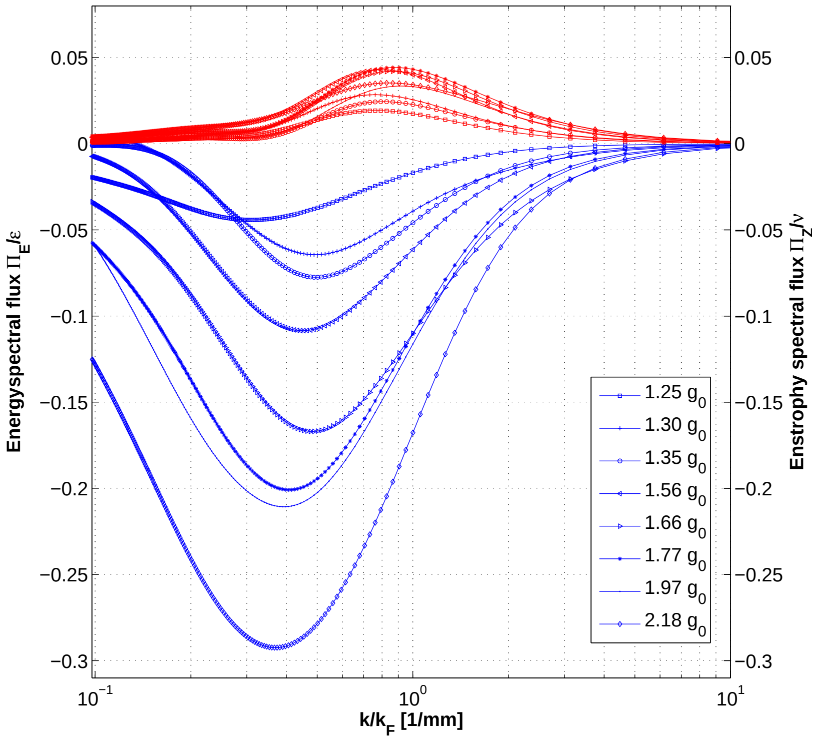

Fig. 3.14: The normalized energy and enstrophy spectral fluxes increase for increasing forcing amplitude a which means that more energy (enstrophy) is transported through the different length scales. Further, a weak displacement of the corresponding enstrophy and energy fluxes to higher wavenumbers (small scales) can be observed. Strangely no positive energy flux at low scales is observed (see text).

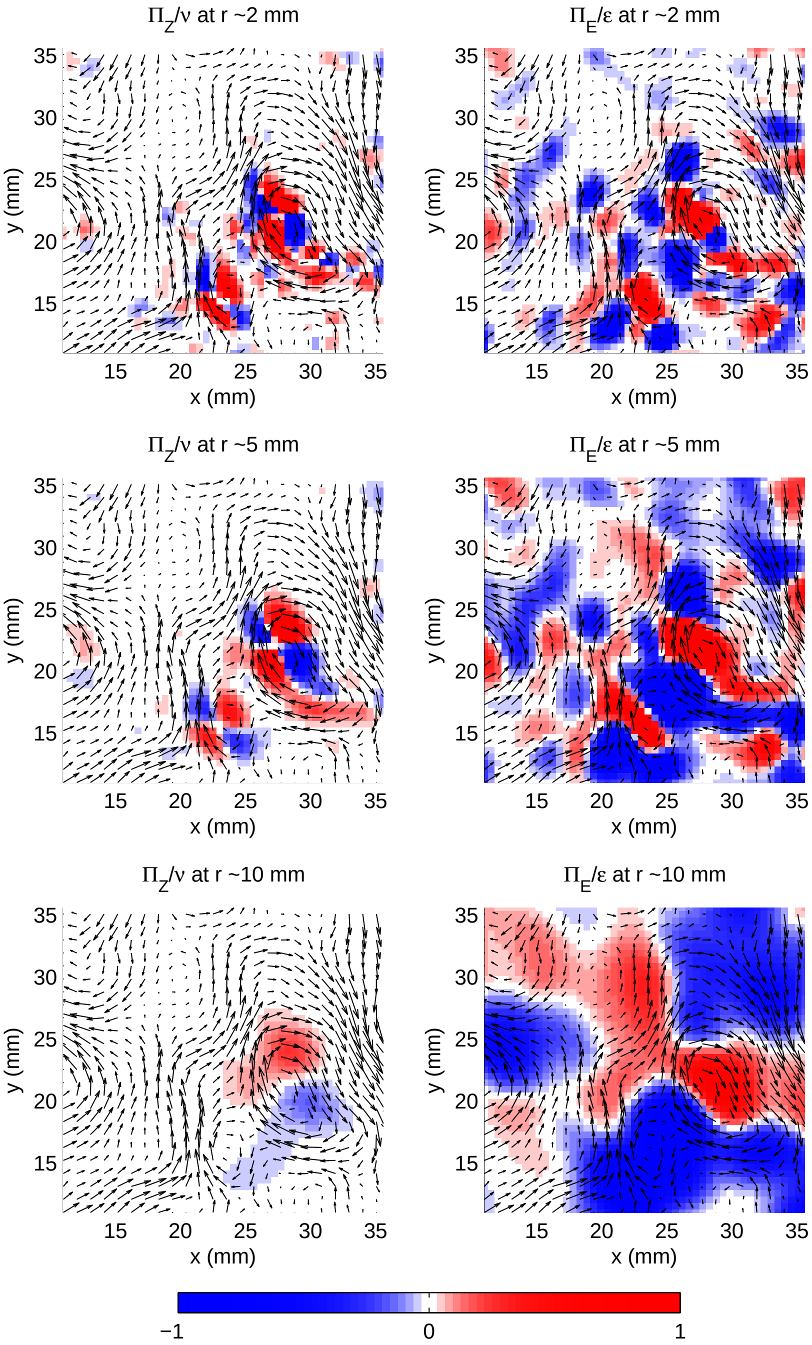

Fig. 3.15: The enstrophy and energy fluxes are calculated locally on three different scales, $r = 2\,\mathrm{mm}$, $r = 5\,\mathrm{mm}$ and $r = 10\,\mathrm{mm}$. While the energy flux seems to be of considerable size on all lengthscales the enstrophy flux vanishes on large scales.

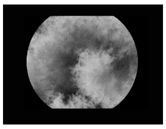

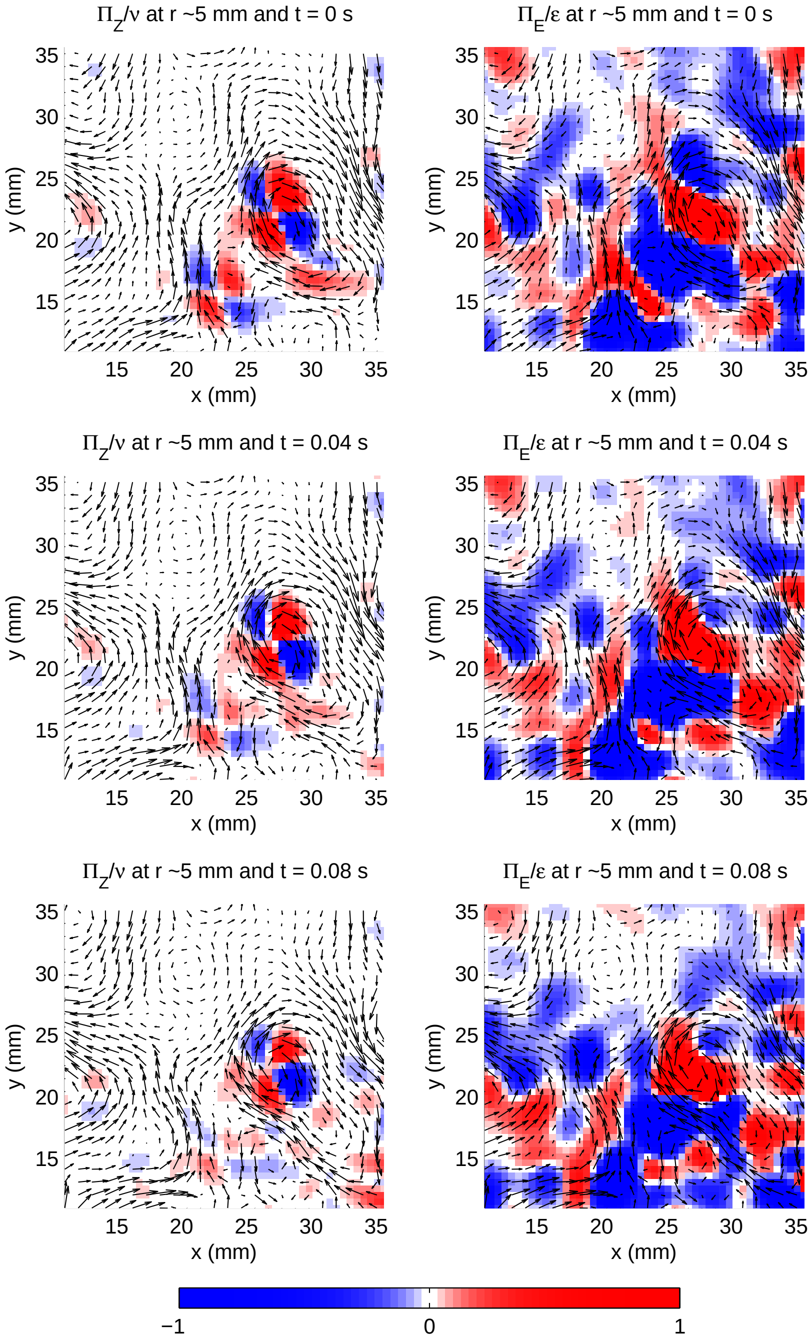

Fig. 3.16: The enstrophy and energy fluxes are calculated locally on scales $r = 5\,\mathrm{mm}$ which corresponds to half the Faraday wavelength λ_F. The fluxes are not constant in time and seem to move through the velocity fields. Entrophy flux seems to be higher at vortex-like structures while energy flux is more equally spread.

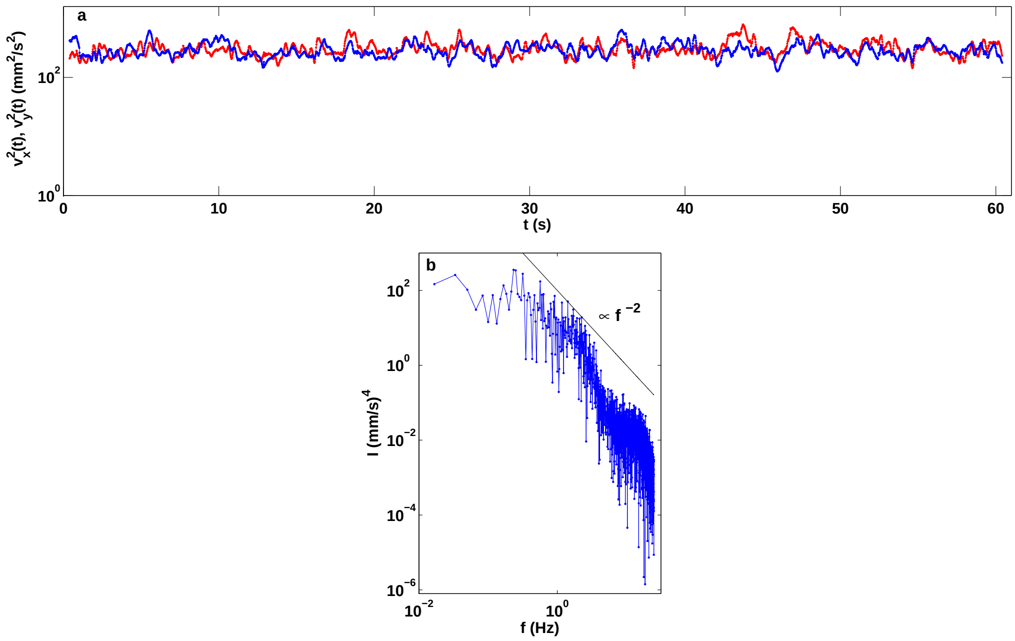

Fig. 3.17: (a) The total mean energy stored in the system $\langle E(t)\rangle = 1/2(\langle v_x(t)^2\rangle + \langle v_y(t)^2\rangle)$ fluctuates around a stable value. (b) We find that the power spectral density I of the Fourier transform $\widehat{\langle \mathbf{v}(\mathbf{t})^2\rangle}$ of the velocities resembles Brownian noise, i.e. $I \propto f^{-2}$.

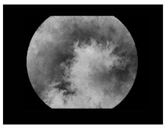

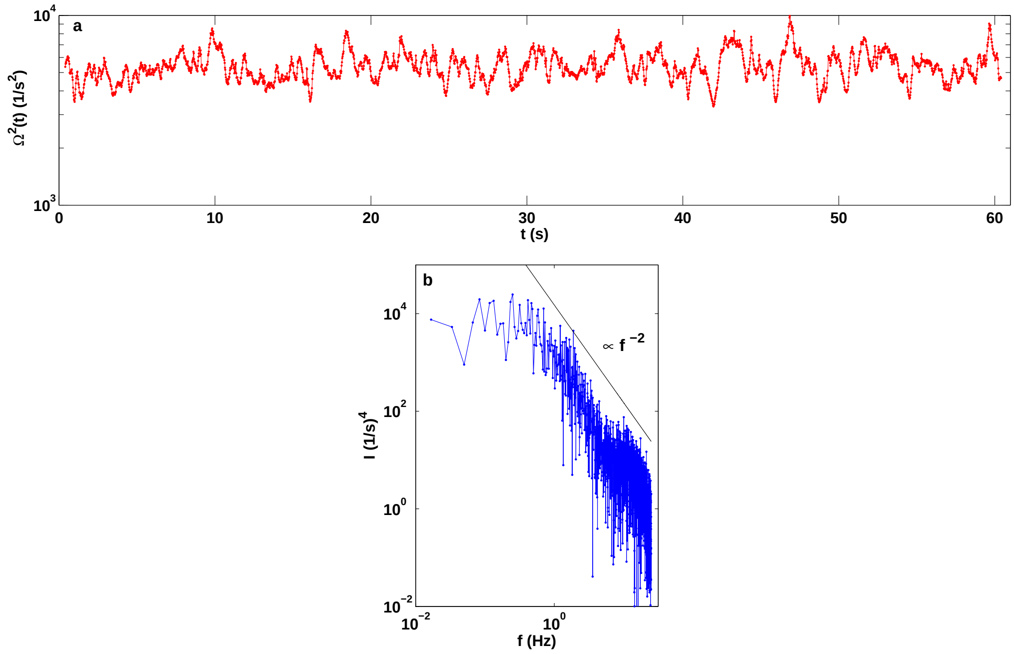

Fig. 3.18: (a) The total mean enstrophy stored in the system $\langle Z\rangle = 1/2\langle\Omega(t)^2\rangle$ fluctuates around a stable value. (b) We find that the power spectral density I of the Fourier transform $\langle\widehat{\Omega(t)^2}\rangle$ of the enstrophy resembles Brownian noise, i.e. $I \propto f^{-2}$. The results are similar to the ones obtained for the energy fluctuations.

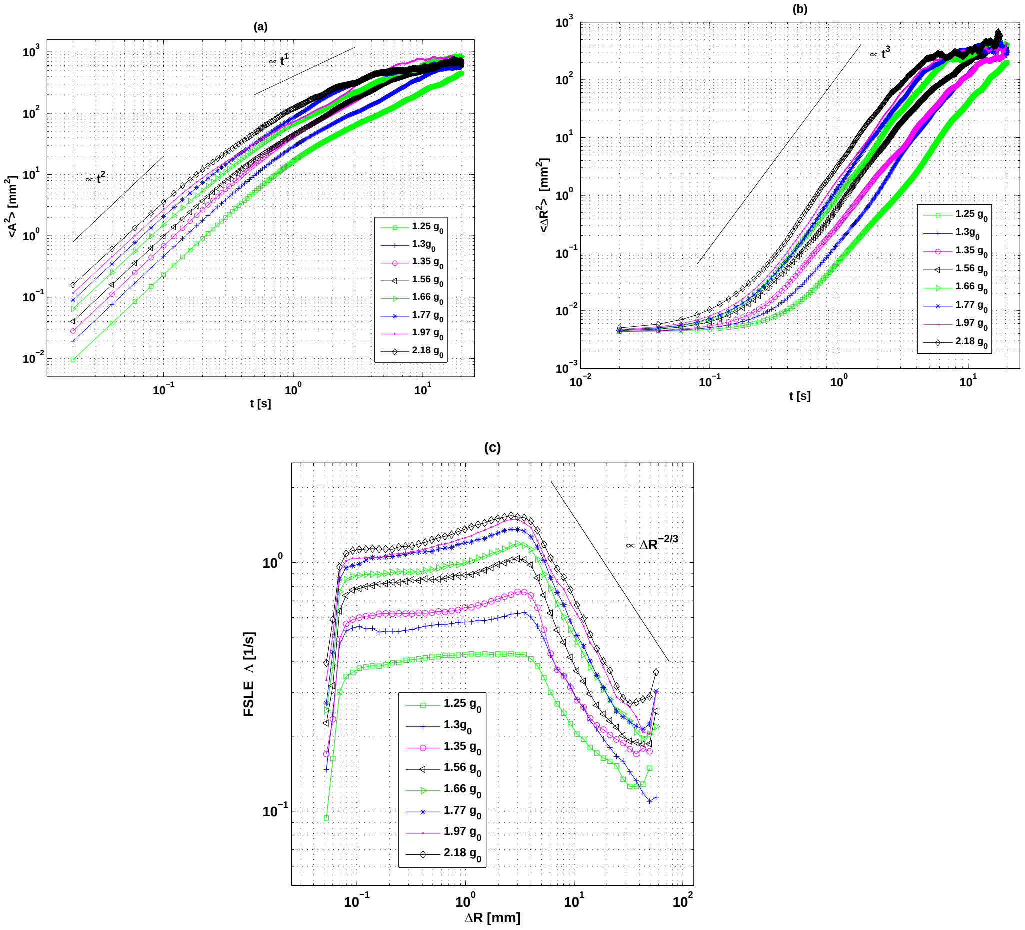

Fig. 3.19: Three different measures of dispersion, absolute (a) and relative dispersion (b) and the finite-size Lyapunov exponent (FSLE) (c) for different aceleration amplitudes a of the forcing. The mixing is enhanced when the forcing amplitude is increased.

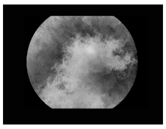

3.3.3 Scaling of the Structure Functions

One of the most important concepts of turbulence research are the n-th order structure functions $S_n(\mathbf{r}) = \langle \delta\mathbf{v}(\mathbf{r})^n \rangle$ (which are tensors) where $\delta\mathbf{v}(\mathbf{r}) = \mathbf{v}(\mathbf{x}+\mathbf{r}) - \mathbf{v}(\mathbf{x})$ as introduced in Sec. 1.2.3, see also references [47, 56, 57, 121]. Additionally, one can calculate the absolute structure functions $G_n(\mathbf{r}) = \langle |\delta\mathbf{v}(\mathbf{r})|^n \rangle$ using the absolute velocity differences $|\delta\mathbf{v}(\mathbf{r})|$. This formulation is also often found in literature but can not be rigorously related to the original one [14, 68, 122] and, most importantly, gives no insight about the direction of the energy cascade. It has been shown, that the scaling behaviour of the structure functions is closely related to the details of the energy spectrum and the direction of energy flux [57, 69]. In particular, for isotropic turbulence, the second order structure function S_2 is directly related to the two-dimensional energy spectrum via:

$$E(k) = \pi k \, \langle \widehat{\mathbf{v}\mathbf{v}'} \rangle \tag{3.3}$$

and

$$\langle \mathbf{v}\mathbf{v}' \rangle = \langle \mathbf{v}\mathbf{v} \rangle - \frac{1}{2} \langle \delta\mathbf{v}(\mathbf{r}) \delta\mathbf{v}'(\mathbf{r}) \rangle \tag{3.4}$$

where $\widehat{\bullet}$ denotes the Fourier transform and $\langle \mathbf{v}\mathbf{v}' \rangle$ is the two point velocity correlation [47] with $\mathbf{v} = \mathbf{v}(\mathbf{x})$ and $\mathbf{v}' = \mathbf{v}(\mathbf{x}+\mathbf{r})$. The sign of the third order structure function S_3 determines the direction of the energy cascade because it relates to the energy flux $\Pi_{E,k}$ in the Fourier space via the energy transfer function T_k in the following way [69] (for a proof see [68]):

$$T_k = \frac{1}{2} \pi k i \mathbf{k} \, \langle \delta\mathbf{v}(\mathbf{r}) \widehat{\delta\mathbf{v}(\mathbf{r})} \delta\mathbf{v}(\mathbf{r}) \rangle \tag{3.5}$$

$$\Pi_{E,k}(k) = - \int_0^k T(q) dq \tag{3.6}$$

where again $\widehat{\bullet}$ again denotes the Fourier transform over the product of all three tensors $\delta\mathbf{v}(\mathbf{r})$.

The scaling relations of the second and third order structure functions can be obtained from manipulations of the Navier-Stokes equation [56, 69]. Considering isotropy of the third and second order structure tensors for the longitudinal structure functions

$$S_n^L = \langle \delta\mathbf{v}(\mathbf{r})^n \rangle \, \frac{\mathbf{r}}{r}, \tag{3.7}$$

which compare only the longitudinal velocity differences along vector $\mathbf{r}$, one finds [56, 69]:

$$S_2^L \propto r^2 \tag{3.8}$$

and

$$S_3^L = \frac{1}{8} \eta r^3 \tag{3.9}$$

for the range of the direct enstrophy cascade and

$$S_2^L = C_2 \epsilon^{2/3} r^{2/3} \tag{3.10}$$

and

$$S_3^L = \frac{3}{2} \epsilon r \tag{3.11}$$

for the inverse cascade range. Here, η and ϵ are the mean enstrophy and energy dissipation rates and C_2 is related to the Kolmogorov constant C [56]. These scalings were observed experimentally and numerically by a variety of groups, see [57] and references therein. In addition to the information about the direction of the cascades and their energy spectra, Eq. 3.11 allows to directly derive the mean energy dissipation rate ϵ.

We calculate the first three moments of the longitudinal velocity differences in the Faraday flow. We find that the expected scaling regions for two dimensional turbulence are at least roughly attained. The velocity differences were calculated not only by a spatiotemporal averaging but also by orientational averaging as follows: In each velocity field a square of centred 4×4 or 10×10 pixel^2 was chosen and longitudinal differences, along the connecting vector $\mathbf{r}$, to all other pixels were calculated. The velocity differences were stored in correspondence to the separation $|\mathbf{r}|$. This procedure was repeated for 3000 velocity fields yielding thus around $6000 - 48000$ values of velocity difference measurements for each separation $|\mathbf{r}|$. Subsequent logarithmic binning in $|\mathbf{r}|$ increases the statistics for each measurement $S_n^L(|\mathbf{r}|)$ even further. First, in order to confirm the direction of the energy flux we exemplarily show the third longitudinal structure function in Fig. 3.20 for the two highest forcing accelerations applied ($a = 1.97\, g_0$ and $a = 2.18\, g_0$). Despite the large number of velocity differences used to calculate the third order structure function, it is very noisy due to cancellation effects from negative and positive values of $\delta \mathbf{v}(\mathbf{r})$. The cancellation effects are related to the small skewness $s = S_3^L/(S_2^L)^{3/2} \approx 0.03$ of the probability distribution function of the velocity differences which was also observed in other studies of two-dimensional turbulence [56]. Therefore, it is hard to detect a thorough scaling region for $S_3^L(|\mathbf{r}|)$ and both theoretically expected curves $S_3^L \propto |\mathbf{r}|^3$ for the direct enstrophy and $S_3^L \propto |\mathbf{r}|$ for the inverse energy cascade can only be insinuated in the noisy data. Nevertheless, the fact that it is positive coincides with the idea of an upscale energy flux as also seen above in the energyfluxes shown Fig. 3.14 and thus confirms the existence of an inverse energy cascade. Further, a kind of bend, similar to the one observed in the energy spectrum, can also be distinguished. It seems that this bend is slightly shifted to larger scales in comparison to the one in the energy spectra. Other groups also report differences in the scaling behaviour of the structure

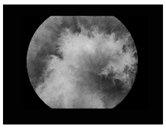

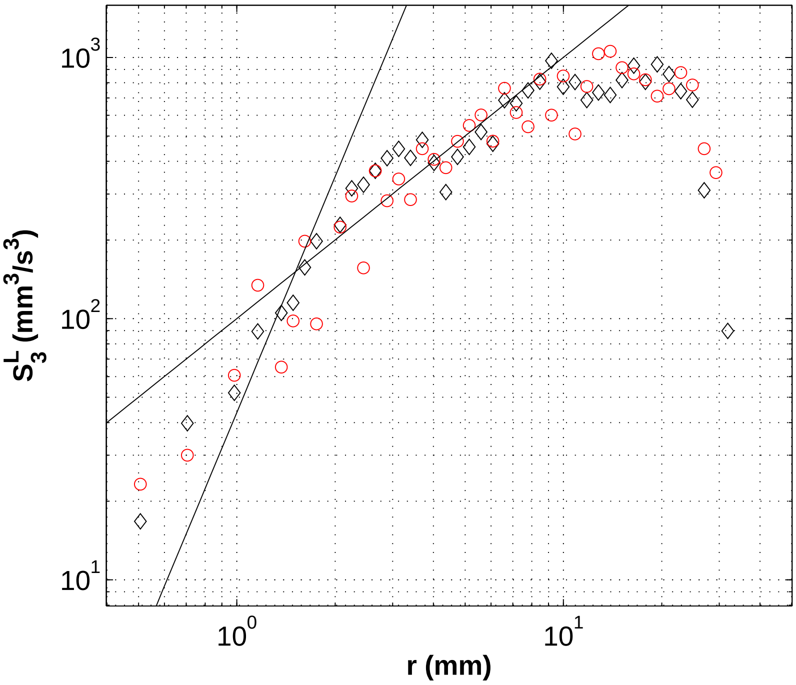

Fig. 3.20: The third order longitudinal structure function $S_3^L(r)$ is shown for the two highest forcing accelerations, $a = 1.97\,g_0$ as red spheres and $a = 2.18\,g_0$ as black diamonds. The curves are noisy and show only short scaling ranges but a linear fit using Eq. 3.11 and the mean energy dissipation rate calculated as $\epsilon = \nu\langle|\nabla \otimes \mathbf{v}|^2\rangle$ fits the data within an order of magnitude. The fact that the curve for S_3^L is positive confirms that there is an inverse cascade and that the flow exhibits two-dimensional characteristics.

functions and the energy spectra and even claim that a cascade might be visible in one and absent in the other [69]. The flattening of the third structure function for large scales is most likely due to poor statistics as the limited field of view allowed only for a largest scale of $|\mathbf{r}| \approx 34\,\mathrm{mm}$. If we nevertheless try to fit a linear curve to the range of S_3^L where the inverse cascade is insinuated, we can use Eq. 3.11 and insert the value of the mean square dissipation calculated as $\epsilon = \nu\langle|\nabla \otimes \mathbf{v}|^2\rangle$. This procedure leads to the upper black line in Fig. 3.20 and thus fits the data quite well. We can further check our data and derive the important constant C_2 which is related to the two-dimensional Kolmogorov constant by $C_2 \approx 2.15 C_K$. We use the fact that the skewness $s = S_3^L/(S_2^L)^{3/2} = 3/2\,1/C_2^{3/2}$ and derive thus $C_2 \approx 15$ which yields $C_K \approx 7$, close to the experimentally and numerically derived values reported by other groups [56, 57].

In order to circumvent the cancellation problems mentioned above many studies use the absolute longitudinal structure functions $G_n^L(\mathbf{r}) = \langle |\delta \mathbf{v}(\mathbf{r})|^n \rangle \ \mathbf{r}\, 1/r$ instead of the S_n^L which, of course, coincide for n being even [57, 122]. For odd n they deviate in the proportionality constant and possibly in sign, but they are expected to obey the same scaling with distance $|\mathbf{r}|$. Figure 3.21 shows the absolute third order longitudinal structure functions for all forcing accelerations compensated by the distance $|\mathbf{r}|$. Since $G_3^L(\mathbf{r})$ is much smoother than S_3^L the inverse energy cascade regime is more obvious. For completenes, we show the

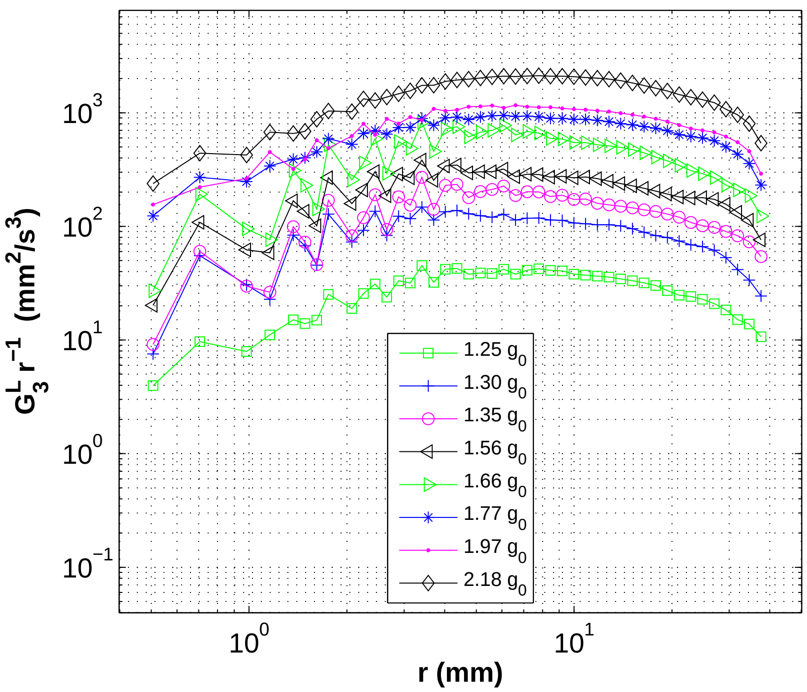

Fig. 3.21: A range of nearly linear scaling can be observed in the compensated absolute third order longitudinal structure functions $G_3^L(\mathbf{r})$ for all forcing accelerations.

second order structure functions for all forcings in Fig. 3.22. Again the two scaling regions theoretically expected $S_2^L \propto |\mathbf{r}|^2$ and $S_2^L \propto |\mathbf{r}|^{2/3}$ can be insinuated.

In order to determine intermittency effects in the data, in Fig. 3.23 we calculate the extended self similarity (ESS) rule introduced by Benzi et al. in 1993 [14] for all forcings. ESS compares the scaling of the nth order longitudinal structure function S_n^L and the absolute third order longitudinal structure function G_3^L. ESS was used in a variety of studies where no cascade region with constant slope could be observed [57, 122–124]. In our study, the collapse of the data for different forcings and its extended self-similar scaling indicates that our flow is self-similar in the sense of Kolmogorov, i.e., if the filtered velocity

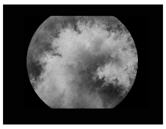

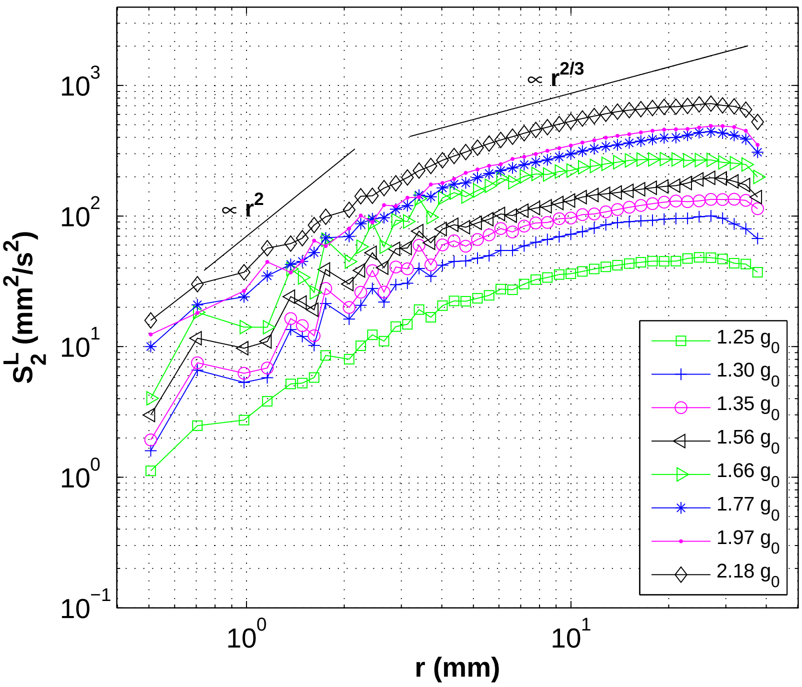

Fig. 3.22: The second order longitudinal structure function shows two scaling regimes which are somewhat less steep than predicted by theory. For lower forcing the bend where the slope changes seems to be more pronounced.

field from a small scale is upscaled, it is on the average indistinguishable from a large scale velocity field. However, there exists another measure for intermittency effects, the probability distribution functions (pdfs) of the longitudinal velocity increments in dependence of $|\mathbf{r}|$. These are shown in Fig. 3.24 and seem to have exponential tails for small separations $|\mathbf{r}|$ (light green lines). The shape of the pdfs also varies with distance $|\mathbf{r}|$ while $|\mathbf{r}|$ is small. This indicates that intermittency cannot be neglected on small scales, in the enstrophy cascade range. Pdfs are shown for scale $|\mathbf{r}|$ varying from 0.5 mm to 28.5 mm in steps of 1 mm. These findings are in disagreement to the scaling behaviour of the velocity difference pdf's in other studies of two-dimensional turbulence, where the curves collapse with a Gaussian shape [53, 60, 123, 124]. We cannot explain this deviation on small scales from the expected behaviour yet. It would be necessary to conduct new experiments at higher spatial resolution to verify the large velocity deviations on small scales. It is possible that measurement errors, like finite divergence affects the tails of the pdfs on small scales. It is interesting to note that the different pdfs do collapse for values of $|\mathbf{r}| > \lambda_F$, where λ_F is the Faraday wavelength and thus, within the inverse cascade, intermittency is

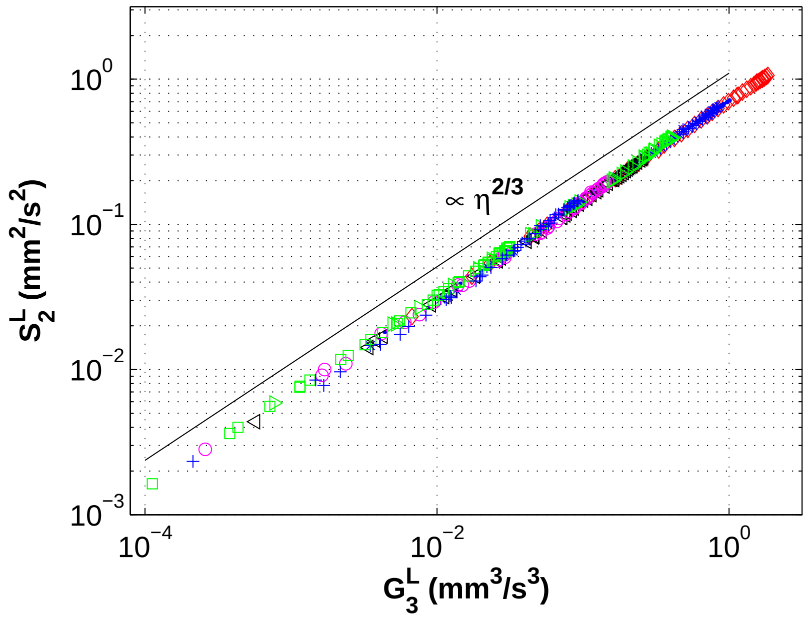

Fig. 3.23: Self similarity is an inherent characteristic of the turbulent cascades. Here we find that the extended self similarity (ESS) applies for the second order longitudinal structure function.

small [60].

3.3.4 Discussion and Comparison to other Studies

The field of two-dimensional turbulence is a very active field of research which is largely motivated by applications to quasi two-dimensional geostrophic flows in the ocean and the atmosphere. Furthermore, two dimensional turbulence is easier to access than three-dimensional turbulence both experimentally and numerically and many concepts can be transferred from one to the other. Recently, also the interaction of three-dimensional and quasi two-dimensional turbulence has attracted attention because of its likely importance for processes like the appearance of atmospheric large scale structures [61, 69]. Here we seem to encounter such a system where a forcing applied in the vertical dimension causes a horizontal two-dimensional flow and an inverse cascade. Maybe it is not completely absurd to conjecture that similar vertical processes of waves or energy exchange on small scales could produce large scale flows in the atmosphere as well. In order to follow this thought using the Faraday experiment, more and better equipped experiments would be necessary. Actually, one needs to measure the three-dimensional velocity field and the Faraday waves at the same

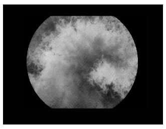

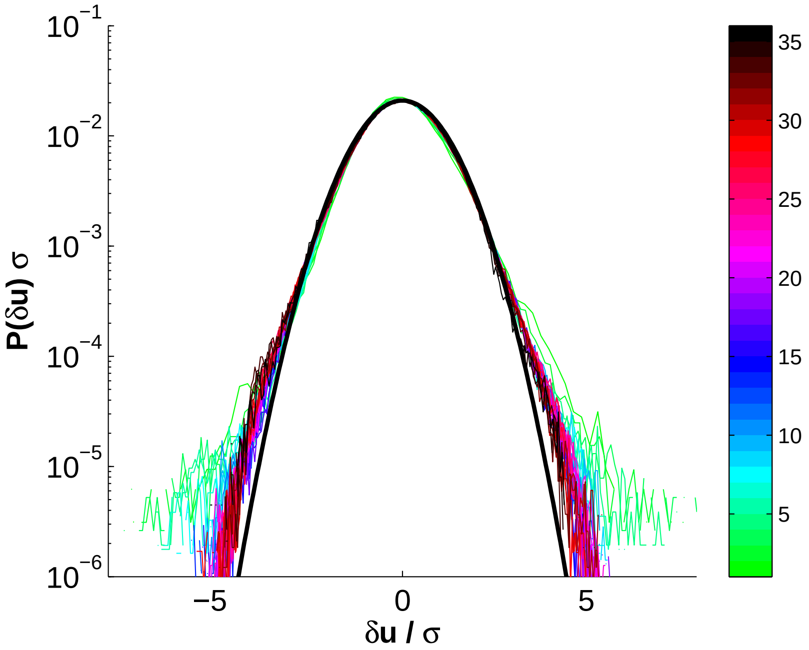

Fig. 3.24: In a perfect self-similar velocity cascade the pdfs of the longitudinal velocity increments $P(\delta\mathbf{v}(\mathbf{r}))$ do not depend on $|\mathbf{r}|$. Here a dependence on $|\mathbf{r}|$ (colour-coded) can be observed for $|\mathbf{r}| < \lambda_F$, where $\lambda_F \approx 10\,\mathrm{mm}$ is the typical Faraday wavelength. Also, it seems that on small scales the pdfs have exponential tails which deviate from a Gaussian distribution drawn for comparison (inner black line). The colourbar indicates the pdfs for $|\mathbf{r}| = 0.5\,\mathrm{mm}$ to $|\mathbf{r}| = 28.5\,\mathrm{mm}$ in steps of $1\,\mathrm{mm}$. The data is normalized with its standard deviation σ. The data shown is from the highest forcing $a \approx 2.18\,g_0$.

time. Preliminary observations indicate that the Faraday waves act similarly to little pumps. To our knowledge no similar study has been conducted so far although the vertical profile of the root-mean-square velocity in the third dimension of the Faraday flow has been measured by Haslam and Ronney [87]. There also exist some theoretical studies relating the evolution of the Faraday waves to the existence to a drift flow [125, 126].

One of the most important difference, of our experiment compared to other ones concerning two-dimensional turbulence is the fact that they use an external forcing that is fixed in space, e.g., fixed magnets in a electromagnetically driven flow [56]. In the Faraday experiment the surface waves are constantly changing direction and location, albeit slowly for low forcing accelerations, causing the velocity field to do the same. In this regard the Faraday flow, at least for strong forcing, might be advantageous and more isotropic. Obviously, velocity measurements are more difficult in the Faraday flow due to the surface waves which also put a serious limit to temporal resolution for high forcing frequencies and acceleration amplitudes: The flow becomes very fast but the recording is limited to 'almost' flat fluid surfaces at each $\Delta t = 1/f$, where f is the frequency of the forcing. Thus, if the forcing becomes too strong the temporal resolution is too poor to apply particle image velocimetry successfully.

3.4 Conclusion

To conclude, we have measured the horizontal surface flow induced by Faraday waves in a thin fluid layer. We call this horizontal velocity field Faraday flow. It reveals interesting two-dimensional characteristics. An inverse energy cascade with negative mean spectral energy flux and a Kolmogorov type scaling range can be identified by analysis of various measures such as the energy spectrum, the scale dependent energy flux and the longitudinal structure functions. Moreover, the data suggest, albeit only for a small range and with a steeper slope than predicted by Kraichnan, the existence of a direct enstrophy cascade with a positive mean spectral enstrophy flux. Tracking of real and virtual particles reveals Richardson scaling in the relative dispersion and in the FSLE spectra. We managed to manipulate the strength of the turbulent flow by variation of the forcing acceleration. The Faraday flow becomes faster (slower) with the increase (decrease) of the forcing acceleration, but the main characteristics concerning the double cascade and the Richardson dispersion remain valid. For slower forcings the inverse cascade becomes more shallow than the Kraichnan scaling of $-5/3$. Altogether, our findings shine a new light on the Faraday waves and allow the reconsideration of this beautiful, low cost experiment for new fields of applications, e.g., the effect of Richardson turbulence on reactive or living tracers. A further intriguing idea for future research on quasi two-dimensional systems has its bases in the scalability of the flow: The higher the forcing frequency of the electromagnetic shaker, the smaller the Faraday waves. This characteristic allows to easily switch the energy injection scale within the very same experiment. The recording of the full three-dimensional velocity field and its interaction with the Faraday waves would aid an interpretation and applicability of the results. Equally, the up-scaling to a bigger container using a more powerful electromagnetic shaker would be of interest to obtain larger cascading regions.

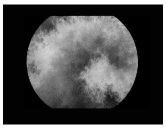

4

Boosted Pattern Formation in Two-dimensional Turbulence

Pattern formation in reaction-diffusion-advection systems is an important process in many natural and man-made systems, e.g., plankton growth in the ocean, dispersion of pollutants in the atmosphere, and optimal mixing in chemical reactors [3]. It is known that excitable reaction-diffusion systems, in absence of advection, are able to organize into spatiotemporal patterns. In particular, target and spiral waves [127] have been observed in various active media, e.g., in chicken retina [128], cardiac tissue [129] or chemical reactions [130]. It is a widely accepted view that whenever the advection can be parameterised in terms of effective or turbulent diffusion D_*, these spatiotemporal patterns should be attainable on much greater, boosted lengthscale [131]. However, so far, experimental evidence of these boosted patterns in turbulent flow was lacking. Here, we report the experimental observation of boosted target and spiral patterns in an excitable chemical reaction in a quasi two-dimensional turbulent flow. The wave patterns observed are ~ 50 times larger than in the case of molecular diffusion only. We vary the turbulent diffusion coefficient D_* of the flow and find that the fundamental Fisher-Kolmogorov-Petrovsky-Piskunov (FKPP) equation $v_f \propto \sqrt{D_*}$ for the asymptotic speed of a reactive wave for molecular diffusion remains valid. However, not all measures of the boosted wave scale with D_* as expected from molecular diffusion, since the wavefront turns out to be very filamentous. Our results can have important implications in all systems where excitable dynamics and turbulent transport coincide.

4.1 Introduction

As a first approximation, many of the current geophysical engineering problems involving turbulent fluid flow, e.g. iron fertilization [132] or cloud seeding [133], can be described using reaction-diffusion-advection (RDA) equations. Despite the importance of pattern formation in RDA systems only very few laboratory experiments on turbulent fluid flow involve reaction kinetics [134]. Considerable numerical and experimental effort has focused on cellular and chaotic flows due to the simpler realization [3, 135, 136]. However, in those flows the derivation of a global diffusion coefficient seems to be more involved than in fully developed turbulence [74], and thus the propagation of reactive waves is likely to depend on the details of the flow [135].

4.2 Experimental Details

In this study, a quasi two-dimensional turbulent flow is created by the Faraday experiment [20], i.e. we vertically vibrate a circular container of 30 cm diameter filled with 2 mm of an excitable cyclohexandione and ferroin based Belousov-Zhabotinsky reaction (BZ) [21] (see also Sec. 1.3 and Fig. 2.1 for a detailed description of the Faraday experiment and the experimental setup). The dynamics of this chemical reaction can be well observed in the visible range due to the oxidation of the reddish catalyst ferroin $[Fe(phen)_3^{2+}]$ to the blue ferriin $[Fe(phen)_3^{3+}]$ (see Sec. 1.1.2) [27]. The details of the chemical recipe are given in Sec. 2.1.1. The reactants are mixed in strictly the same order for each experiment and stirred for 50 min before the reactants are poured into the reactor on top of the shaker. The recipient is then closed with a transparent plexiglass cover and the BZ reaction is left to rest for another 15-30 min until the typical patterns of an BZ reaction, targets and spirals, occur (Fig. 1.3, right panel). The forcing is slowly switched on and some time is given to the system to become resonant before recording is started. During the recording, the strength of the forcing is continuously monitored with an accelerometer. Experiments are performed for a frequency range of 20-150 Hz and accelerations $a = 0.6$–2.5 g_0, g_0 being the gravitational constant. The upper limit of the forcing range is given by the onset of droplet formation on the surface of the liquid and wetting of the cover which makes recording unfeasible.

In order to enhance the contrast of the ferroin-ferriin concentration patterns that arise a green filter was placed in front of the camera with a maximal transmission around $\lambda = 500$ nm (maximum absorption of ferroin). Images were recorded with a Pike F-032-B AVT camera at $12.5-200$ fps and 480×640 pixel^2 resolution. Greyscale values were calibrated to different ferriin $[Fe(phen)_3^{2+}]$

concentrations in aqueous solution. Feriin concentrations were then calculated using the relationship $[Fe(phen)_3^{3+}] = [Fe(phen)_3^{2+}]_0 - [Fe(phen)_3^{2+}]$. The details of the calibration of the ferroin are explained in Sec. 2.3.3.

As we have shown in the preceding section, Chap. 3, the velocity fields and the passive transport in the Faraday flow are turbulent [20, 87]. Here, as in Sec. 3.3.2, the intensity of the turbulence and thus the turbulent diffusion constant [74] D_* was varied by changing the forcing strength, i.e., altering the amplitude a of the acceleration and the frequency f of the vertical forcing. In order to measure the effective absolute diffusion $A(t)$ in the turbulent flow, floating particles were added to the liquid and particle image velocimetry was performed [20] for different forcing amplitudes a. Subsequently, the resulting velocity fields were used for the numerical advection of virtual particles (point-like) which was achieved using a fourth order Runge-Kutta algorithm [137]. From the dispersion of the virtual particles an effective diffusion coefficient was estimated.

4.3 Results

4.3.1 Boosted Patterns

Figure 4.1 shows examples of the boosted patterns in the turbulent flow. The upper panel, 1–3, shows an image sequence of a spontaneous boosted spiral and the lower panel, 1–3, a spontaneous boosted target wave (see App. A: supplementary image sequences, movies M1 and M2). Without any fluid flow the much smaller usual target and spiral patterns can be observed which are shown for comparison on the right (image 4). The boosted patterns are a very robust phenomenon and were found for a large range of forcing parameters, $f =$ 30–140 Hz, $a = 0.6$–$2.5\ g_0$, g_0 being the gravitational constant. The temporal persistence of the target patterns varies from some minutes for high forcing amplitudes a, to up to one hour for lower ones. The probability for a target to form is higher for lower forcing. This is most likely related to more long-lived structures in the fluid flow [138] that favor the occurrence of a perturbation that is persistent and big enough to trigger a new wave [92]. Usually, but not always, target waves are triggered at the border of the container. Spiral waves form spontaneously, most often created by the breakup of target waves due to interactions with the turbulent fluid flow or the boundary, but they can also be created intentionally by an abrupt short interruption of the forcing. Figure 4.1 (upper panel, image 2) shows the trajectory of a spiral tip in time. The temporal persistence of the spiral is limited due to the complex movement of the tip [35] since it eventually hits the border or another pattern, causing

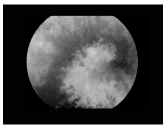

the spiral to vanish (see App. A: supplementary image sequences, movies M1 and M3). Qualitative observations suggest that the displacement of the spiral tip is a superposition of a random movement due to the filamentary structure of the front and a migration along the border of the container [36].

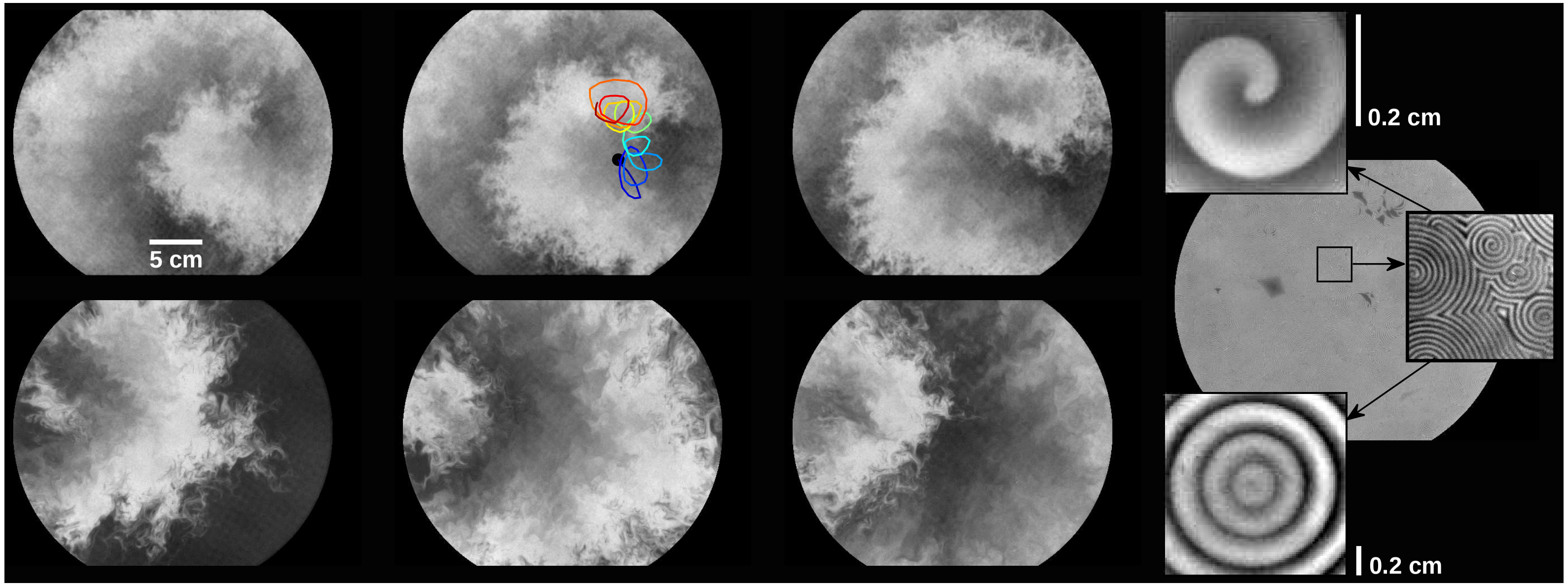

Fig. 4.1: Boosted spiral and target patterns in a turbulent flow. The turbulent flow is induced by the Faraday experiment. The chemical reaction is a cyclohexandione based bubble free Belousov-Zhabotinsky reaction in an excitable state. Greyscale indicates concentration of ferriin, $Fe(phen)_3^{3+}$. Upper panel, 1-3: Image sequence of boosted spiral with $\Delta t \approx 3.6$ s, $f = 70$ Hz, $a_0 \approx 1.8\ g_0$, $[H_2SO_4] = 1.2$ M, period of spiral $T = (13 \pm 1)$ s. 2nd image: Trajectory of spiral tip in time (color code: early position blue, late position red). Lower panel, 1-3: Image sequence of boosted target wave with $\Delta t \approx 12.4$ s, $f = 50$ Hz, $a_0 \approx 1.2\ g_0$, $[H_2SO_4] = 0.6$ M. Both patterns form spontaneously and are persistent phenomena that can last from a few minutes up to one hour. The boosted wavefronts have a highly filamentary structure. For corresponding movies see supplementary material (M1, M2). Right: Three close-ups show molecular-diffusion-induced spiral and target patterns in absence of fluid flow in the same container. Note the large difference in scales between these usual and the boosted patterns.

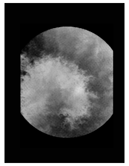

For a quantitative analysis of the periods of the boosted spirals we varied the turbulent diffusion of the Faraday flow as described in Sec. 3.3.2. This was achieved by changing only the forcing amplitude a leaving the forcing frequency, and thus the Faraday wavelength λ_F constant ($f = 50$ Hz, $[H_2SO_4] = 0.6$ M, see App. A: supplementary example image sequence, movie M3). The periods of the boosted spirals at $f = 50$ Hz are in the range $T = 30$–50 s for all forcing amplitudes with a slight tendency towards higher periods for stronger forcings. This might be explained by the augmentation of the width of the boosted autowaves such that the spirals seem to be restricted by their own tail [35]. This self-restriction could also explain why the period of the molecular-diffusion-induced spirals, $T_{mol} = 18$–25 s, was somewhat lower. Further, in order to prevent the spiral to drift, we pinned its tip to a round obstacle of 54 mm diameter, placed in the middle of the container. These pinned spirals last for up to ~ 1 h (see App. A: supplementary data, image sequences, movies M4, M5 and M6).

In addition to the spiral and target patterns we also observe double spirals with two free curling ends (see App. A: supplementary image sequence, movie M7), as well as up to 3 simultaneously existing spirals. All reactive waves have the typical characteristics of autowaves, in particular, they annihilate when they meet. In contrast to the wavefronts caused by molecular diffusion, the wavefronts of the boosted waves have a highly filamentary structure which is more pronounced for lower forcing strengths. This is most likely due to flow structures that are more long-lived with respect to the reaction timescales [139], see also discussion of Fig. 4.8.

4.3.2 Dispersion Characteristics of the Flow

In Fig. 4.2 the measured turbulent diffusion coefficient D_* is plotted as a function of the estimated Reynolds number for different forcing amplitudes. The turbulent diffusion increases approximately linearly with the Reynolds number as expected, and mixing is enhanced. At these Reynolds numbers the flow is turbulent as the energy spectra in Fig. 3.8 (Sec. 3.3.2) reveal a double cascade and a Kolmogorov type scaling ($E_k \propto k^{-5/3}$), [20, 56, 134].

The turbulent diffusion coefficients D_* were derived from measurements of the absolute dispersion $A(t)$ shown in Fig. 4.3. For every acceleration amplitude a the absolute diffusion is calculated from advected virtual particles in at least 3 different recordings of the velocity field. For all amplitudes a the absolute dispersion $A(t)$ (cf. Fig. 3.19 a) shows an initial ballistic growth in time close to $A(t) \propto t^2$ as is expected for short times when the successive movements of the particles are still correlated. For longer times the absolute dispersion approaches a linear growth corresponding to a diffusive regime. The effective

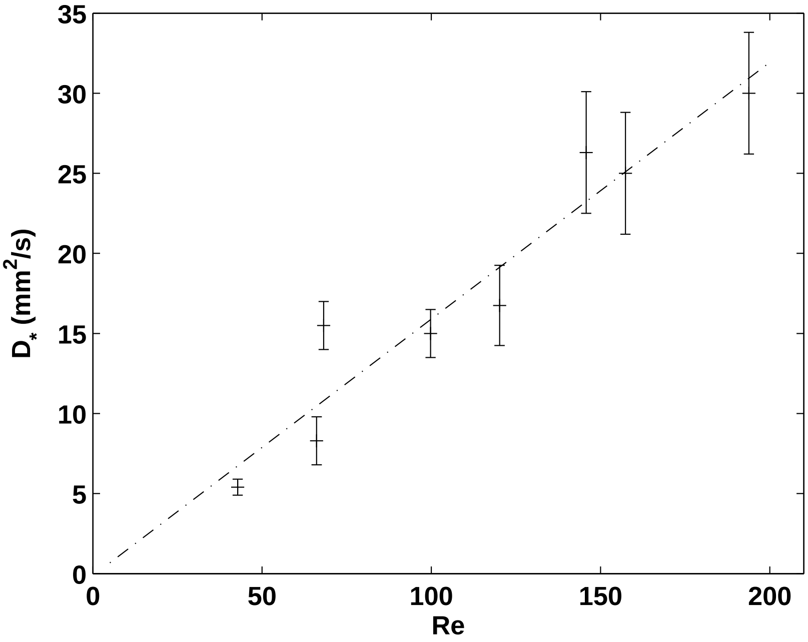

Fig. 4.2: The measured diffusion coefficients are shown as a function of the Reynolds number $Re = v_{rms}\lambda_F/\nu$ indicating the turbulence strength, where ν is the kinematic viscosity of the fluid.

or turbulent diffusion coefficients were estimated by a linear fit to this regime of linear growth, see Figure 4.3. For the more turbulent flows with higher Reynolds numbers, linear growth appears only for a short range of scales as particles start to leave the field of view and statistics become biased. Especially for intermediate values of the forcing an important transient region can be identified, where $A(t) \propto t^\gamma$ with $1 < \gamma < 2$. This phenomenon will be studied in more detail in chapter Chap. 5.

As mentioned in the introduction, in cellular flows one cannot neglect the molecular diffusion when calculating the global diffusion constant [74]. In order to show that in our study the influence of the molecular diffusion D_{mol} on the transport processes is neglectable we calculate the Péclet number $Pe = v_{rms}/(\lambda_f D_{mol})$ of the turbulent velocity field (Fig. 4.4). When the Péclet number of is much greater than unity, $Pe \gg 1$, the influence of the molecular diffusion on the transport is neglectable [74]. In our study this limit is reached for all forcings.

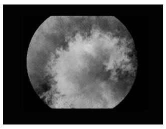

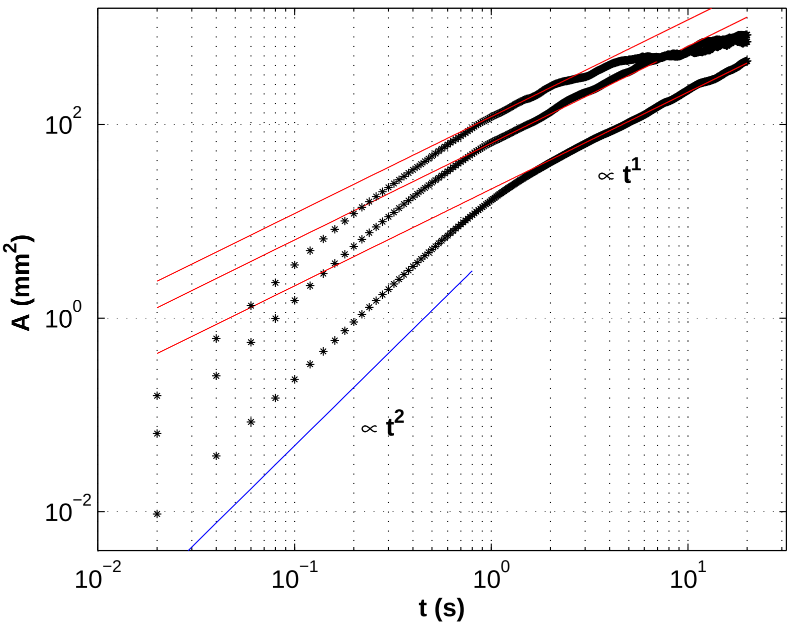

Fig. 4.3: The turbulent diffusion coefficients are estimated by a linear fit to the range of linear growth of the absolute diffusion curve, exemplary for $Re \approx 43$, $Re \approx 120$ and $Re \approx 194$.

4.3.3 Boosted Targets and the FKPP Relation

Figure 4.5 and its inset (i) show that the FKPP relation for the front velocity v_f remains valid for well developed boosted target waves in the quasi two-dimensional turbulent flow, i.e., $v_f = 2\sqrt{D_*/\tau_{reac}}$, τ_{reac} being the reaction timescale [131]. Surprisingly, the boosted data points agree with the prediction derived from the FKPP equation using only measurements from experiments with molecular diffusion: The solid line is the solution of the FKPP relation, where the typical reaction timescale τ_{reac} was estimated from the velocity measurement of the molecular-diffusion-induced target wave to be $\tau_{reac} = (0.8 \pm 0.3)$ s and the molecular diffusion coefficient was estimated from the literature to be $D_{mol} \approx (1.3 - 2.0)\ 10^{-3}\ \mathrm{mm}^2/\mathrm{s}$ [32, 92, 140] (at room-temperature(23 ± 1) °C). The turbulent diffusion coefficient was varied by adjusting again only the amplitude of the forcing while the frequency $f = 50$ Hz was held constant [83, 87]. Theoretically, when the reaction timescale is small in comparison to the timescale of the fluid flow, the front velocity v_f is bounded by the unidirectional root-mean-square velocity of the flow instead of obeying the FKPP relation [141]. In this regard, inset (ii) in Fig. 4.5 shows that in our experiments this limit is only approached for low forcing. We noted that

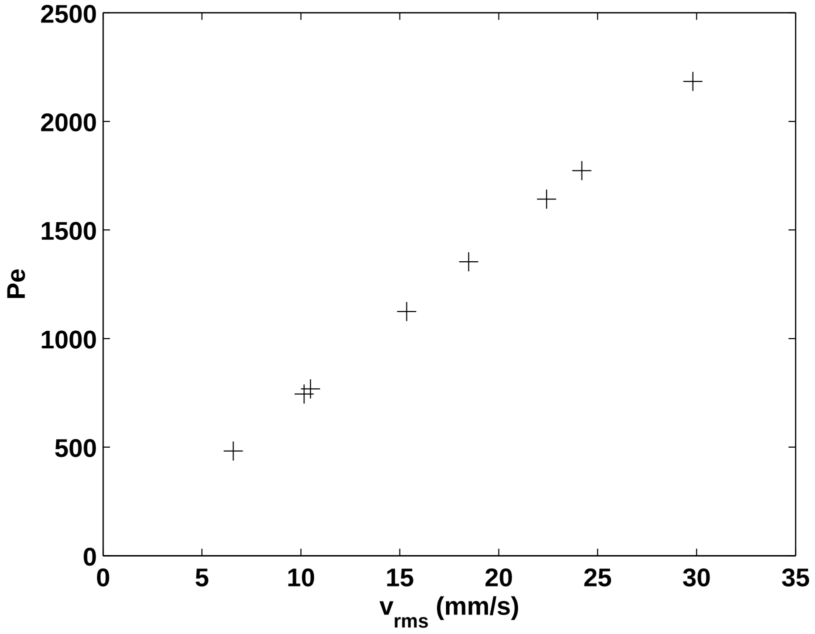

Fig. 4.4: The Péclet number of $Pe \gg 1$ indicates that molecular diffusion is small compared to the mixing provided by the fluid flow.

the variation of the front velocity at constant forcing strength is related to the interval in between successive waves which suggests that they might obey a dispersion relation analogue to usual target waves [142].

The front velocity of each target was measured by averaging over the intensity of an image stripe along the direction of front propagation, Fig. 4.6 a, and the successive determination of the spatial evolution of the minimal first spatial derivative of the signal in time, Fig. 4.6 b, c. The front velocity is then derived by a linear fit to the points extracted, Fig. 4.6 d. The movement seems to be consist of an alternation of acceleration events and events with almost constant velocity. Front velocity measurements were taken as a mean of at least two different realizations of the experiment and more than 15 different target waves. Error bars indicate the standard deviation. The error in between different experiments was within the error of one experiment. We also varied the amplitude of the forcing within one experiment recovering the same dependency.

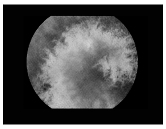

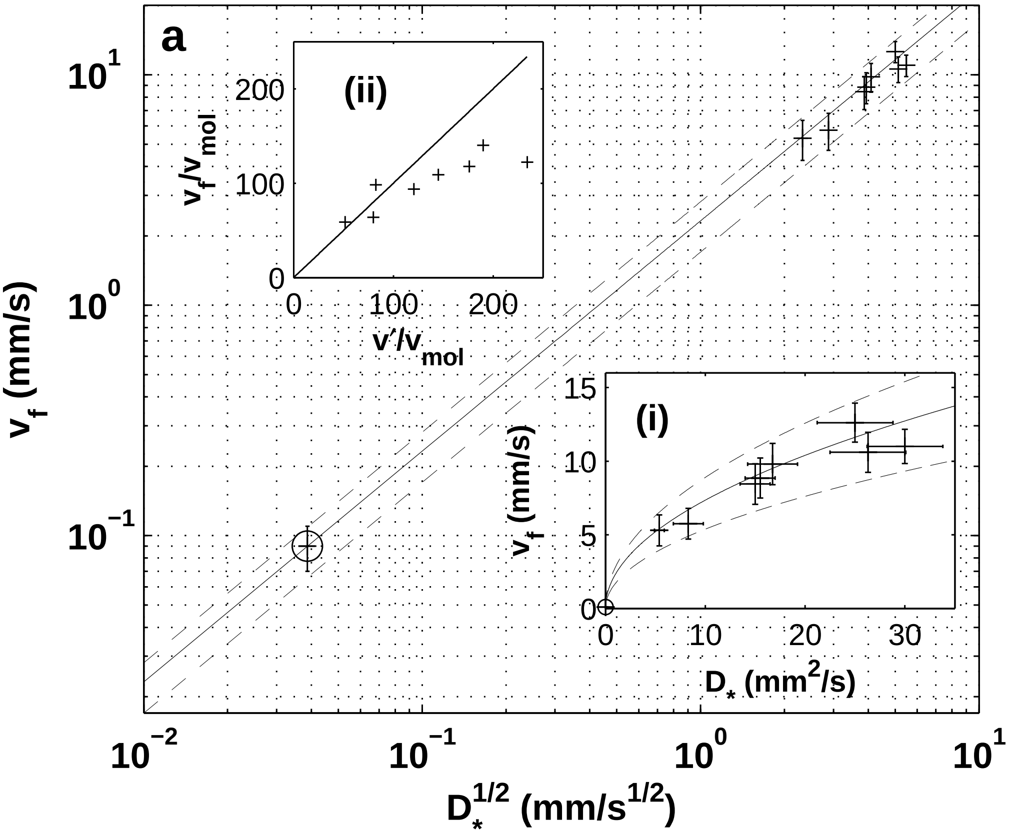

Fig. 4.5: Front velocity of reactive waves in dependence of turbulent diffusion. The velocity of the target wave fronts v_f scales with $\sqrt{D_*}$ and follows the FKPP prediction $v_f = 2\sqrt{D/\tau_{reac}}$ (solid line). The time constant of the reaction $\tau_{reac} = (0.8 \pm 0.3)$ s was derived from the molecular case (circle) but adjusts also well for the turbulent data (crosses). Dashed lines indicate the error bounds estimated from the standard deviation of the velocity measurements from the molecular-diffusion-induced target wave. Inset (i) shows a close up of the turbulent data pairs. (ii) Target front velocity v_f vs. turbulent root-mean-square velocity in one direction $v' = v_{rms}/\sqrt{2}$, both normalized to the front velocity v_{mol} of the molecular-diffusion-induced target wave.

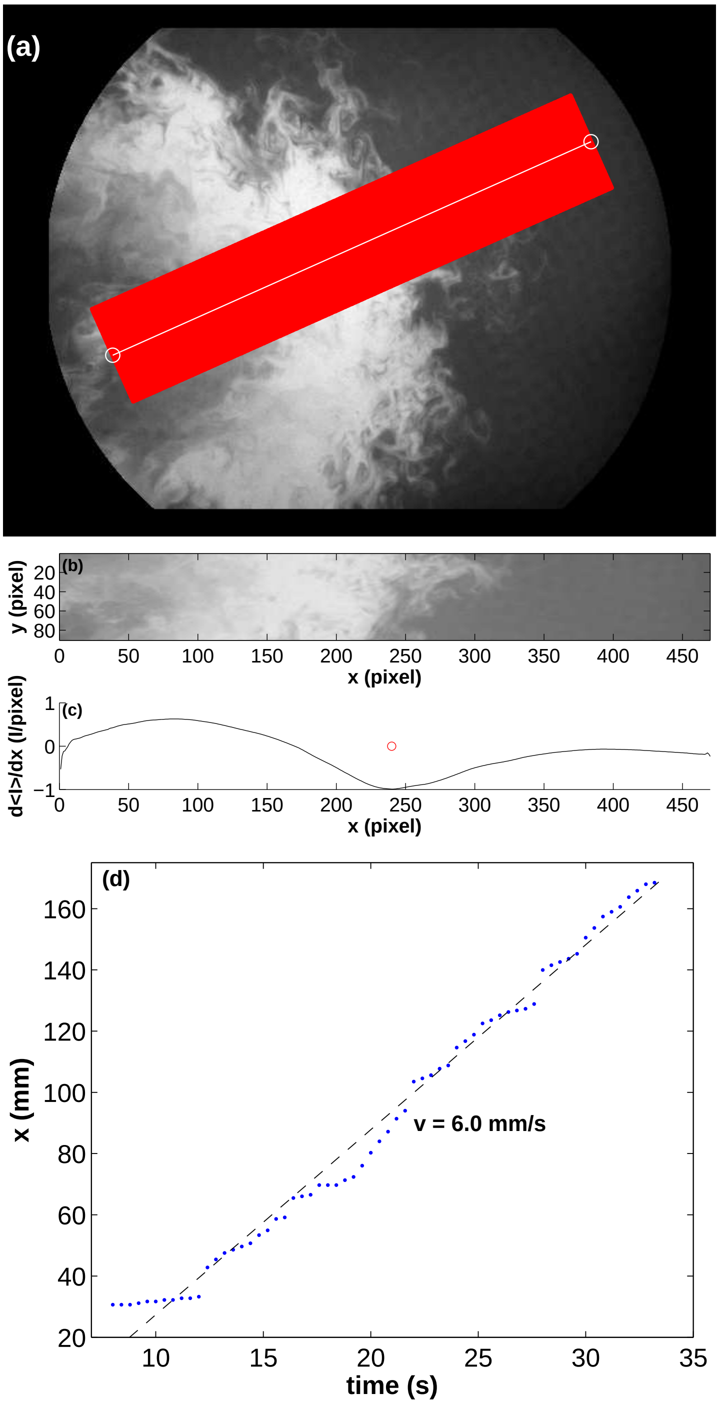

Fig. 4.6: Determination of the front velocity of the targets. A rectangle (a) is laid perpendicular to the front and the intensity is averaged over the short side of the rectangle, the y-axis in (b). The derivative of the average intensity signal in x-direction dI/dx is calculated and the minimum tracked (c). The blue dots show the spatial locations of $min(dI/dx)$ in time. A linear fit allows the derivation of a mean velocity.

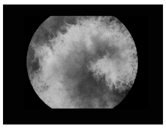

4.3.4 Molecular Patterns vs. Boosted Patterns

Despite the validity of the FKPP prediction for the front speed Fig. 4.8 demonstrates that the boosted target waves do not entirely behave like their molecular diffusion counterparts. An important difference is the complex structure of the reaction front with its highly filamentous appearance which is related to the small scale stretching and folding processes in the turbulent dynamics (Fig. 4.8 a, b and Fig. 4.1) [134, 141, 143] (F.H., in preparation). For smaller turbulent diffusion (see space-time plot Fig. 4.8 a) the filamentary structure increases due to two distinct processes:

First, the increase of the length and persistence of the filaments can be explained by coherent flow structures, i.e., little eddies and jets, that order the flow on timescales longer than the reaction time τ_{reac}. An imprint of the filaments can be seen in the ferriin concentration profiles (Fig. 4.8 c). The peaks of high concentration ahead of the front show the intermittency of the turbulent diffusion process on these spatiotemporal scales. For higher turbulent forcing the fronts are less intermittent (Fig. 4.8 d).

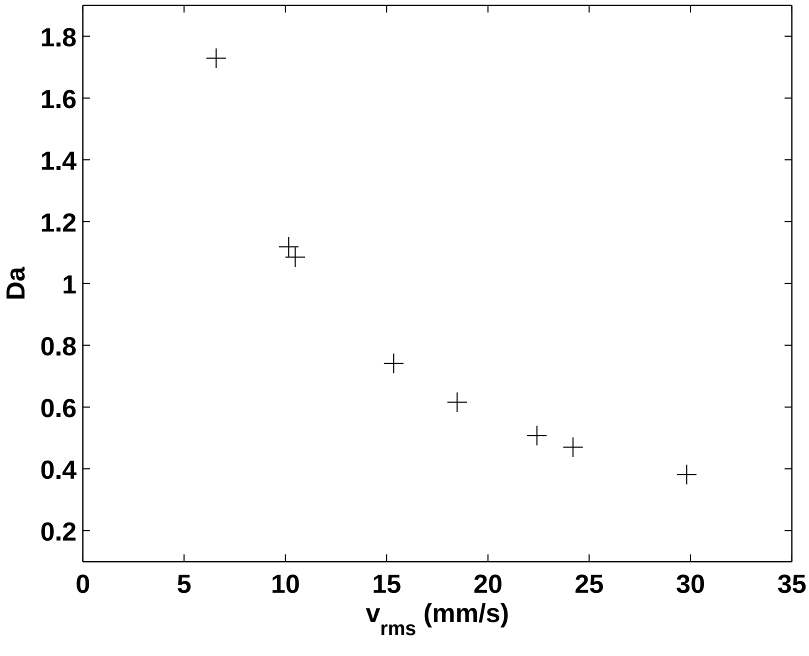

Fig. 4.7: The Damköhler number, $Da = \tau_{flow}/\tau_{reac}$, is the ratio of the typical timescales of the flow and the reaction. A Damköhler numer ≈ 1 indicates that the timescales are similar. Even though this case seems to be of special interest analytical approximations mostly consider the extreme cases of $Da \gg 1$ or $Da \ll 1$.

Second, the sharper and more pronounced appearance of the filaments can be explained by the Damköhler number, $Da = \tau_{flow}/\tau_{reac}$, the ratio of the typical timescales of the flow and the reaction. The flow timescales were estimated to be the ratio of the Faraday wavelength and the root-mean-square flow velocity, $\tau_{flow} = \lambda_f / v_{rms}$. Da varied from $Da \approx 0.4$ for the highest forcing to $Da \approx 1.8$ which is summarized in Fig. 4.7. For small Da, the fluid flow is fast compared to the reaction timescale which causes the front to be smoother in agreement to what we find for strong forcing. For large Da, and thus lower forcing, the front appears sharper and its velocity approaches the root mean square velocity in one direction, $v' = v_{rms}/\sqrt{2}$ [141, 143]. This limit is reached in our experiments for small forcings as is reflected by inset (ii) in Fig. 4.5.

Furthermore, in the space time plots in Fig. 4.8 a, b, it is easy to observe by eye the differences in the target front velocities, the frequencies of spontaneous target formation, and the target widths for the two extreme cases of the measured turbulent diffusion. The space-time plots were derived by averaging over the intensity taken from a stripe of width ~ 26.5 mm perpendicular to the direction of the target propagation for the smallest and the highest turbulent diffusion coefficient measured. In order to quantify the dependence of the width on the turbulent diffusion, Fig. 4.8 g depicts the mean profiles of the boosted target for the two turbulent diffusion coefficients. These measurements were repeated for all turbulent diffusion coefficients (Fig. 4.8 h). We find that while the full width w_2 of the boosted target waves increases according to $w_2 \propto \sqrt{D_*}$, as expected for an ideal reaction-diffusion system [2], the width of the rising edge w_1 does not change within the error of the measurement. A possible explanation for this unexpected behaviour of w_1 is the intermittency of the mixing process: Averaging over many sharply defined filaments could give a similar width for the mean profile as the average over a smoother and broader front. This indicates that for low forcings and on the timescales of the fast forward reaction occurring at the leading edge of the front, mixing might not yet be well defined by a diffusive process. According to this picture, w_2 augments diffusively as the inhibitor reaction at the tail of the front is much slower and sees a well developed diffusive process. Timescales of the forward and the backward reaction can be estimated as the times of rise and fall of the ferriin concentration in Fig. 4.8 e, f.

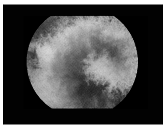

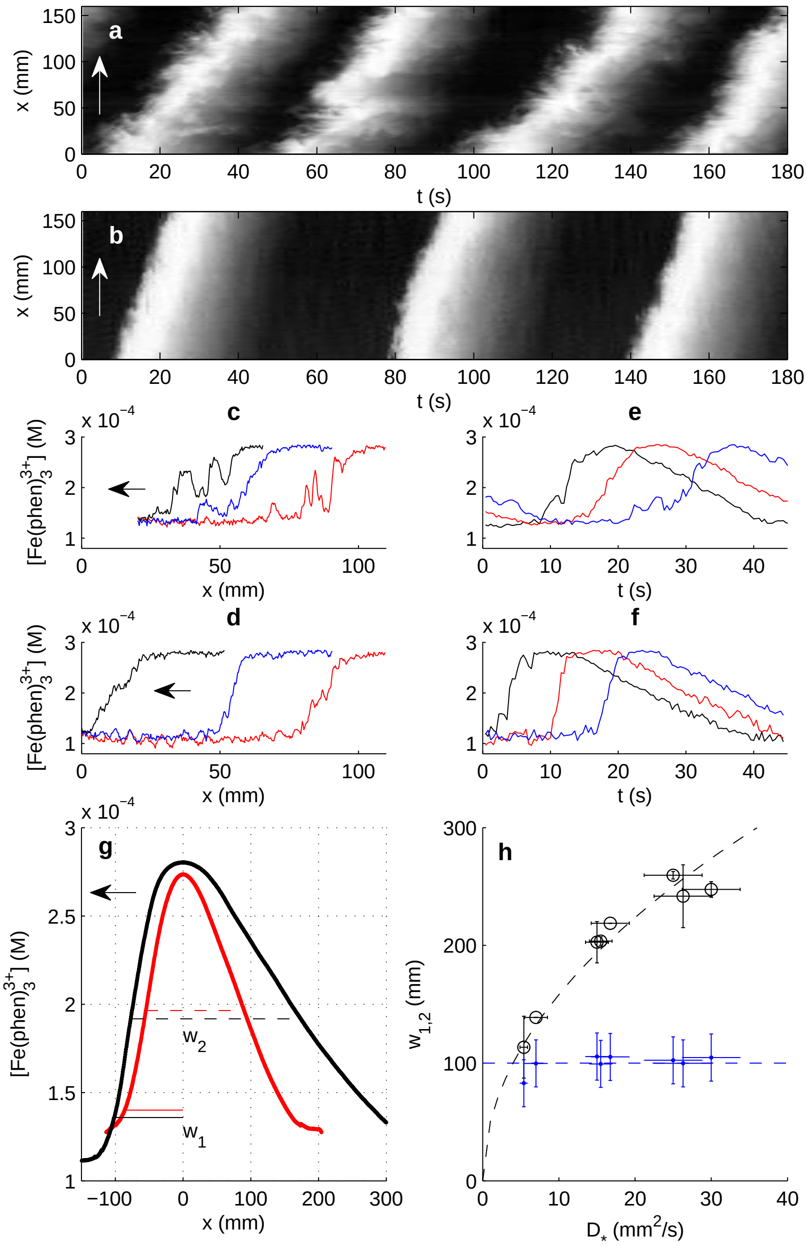

Fig. 4.8: Front characteristics of boosted target waves. (a), (b) Space-time plots of boosted targets for $D_* \approx 5.4\,\mathrm{mm}^2/\mathrm{s}$ ($a \approx 1.3\ g_0$) and $D_* \approx 30.0\ \mathrm{mm}^2/\mathrm{s}$ ($a \approx 2.2\ g_0$). Arrows indicate the direction of front propagation (Supplementary movies M2 and M8). The target waves are narrower, slower and more filamentous for the smaller diffusion coefficient. (c), (d) Ferriin concentration profiles, $[Fe(phen)_3^{3+}]$, along a line at three different instances of time, $\Delta t \approx 6.4$ s, for $D_* \approx 5.4\,\mathrm{mm}^2/\mathrm{s}$ and $D_* \approx 30.0\,\mathrm{mm}^2/\mathrm{s}$ respectively. (e), (f) Ferriin concentrations time series for the same values of D_* at three different points in space ($\Delta x \approx 53$ mm, $\Delta x \approx 80$ mm). (g) The mean profile of the target waves for both diffusion coefficients estimated by averaging over all targets measured. (h) Different widths w_1 and w_2 of the profile in dependence of the diffusion coefficient D_*. The full width w_2 of the target wave grows with $\sqrt{D_*}$ as expected while the width of the rising edge w_1 stays constant.

4.4 Conclusion

In summary, we conclude that complex spatiotemporal patterns, such as target and spiral waves known from reaction-diffusion systems, occur in turbulent fluid flows as was shown experimentally. Measuring turbulent diffusion coefficients and the reaction front velocities at various Reynolds numbers we find that they obey the FKPP relation for reaction-diffusion systems. The overall patterns resemble those of their molecular counterparts, however, an important difference is the filamentary appearance of the front which leads to an unexpected scaling of the front width. We suggest that these phenomena can be understood by the existence or absence of coherent structures in the flow that are known to exist in many turbulent flows. We expect our results to increase the attention on pattern formation in systems where excitable dynamics evolve in turbulent flows, such as plankton growth in the ocean where a ring-like structure, similar to a target, has been reported [144, 145].

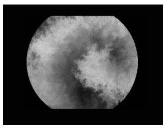

5

Local Expansion of an Excitable Front in Two-dimensional Turbulence

Pattern formation in reaction-diffusion systems is an important self-organizing mechanism in nature. Dynamics of systems with normal diffusion do not always reflect the processes that take place in real systems when diffusion is enhanced by a fluid flow. In such reaction-diffusion-advection systems diffusion might be anomalous for certain time and length scales. We experimentally study the propagation of a boosted autowave occurring in a Belousov-Zhabotinsky (BZ) reaction subjected to the quasi two-dimensional turbulent flow created by the Faraday experiment at medium forcing acceleration $a = 1.5g_0$. At this forcing strength the absolute and relative dispersion appear anomalous on certain time and lengthscales. We present a novel analysis technique for the local expansion of the boosted wavefront and find evidence of its superdiffusivity on considerable lengthscales. In agreement with these findings the variance $\sigma^2(t) \propto t^\gamma$ of the reactive wave grows supralinear in time with an exponent $\gamma > 1$. Instead of deriving the complete velocity field of the Faraday flow as in the previous sections we study here the statistics of single, floating micro particles subjected to the flow. The analysis of the particle trajectories allows us to derive flight time and jump length distributions and find evidence that micro-particles undergo complex trajectories related to Lévy statistics. The propagation of active and passive media in the flow is compared.

The contents of this chapter correspond in large parts to the published article [21]

5.1 Introduction

As was discussed in the previous Chap. 4, the propagation of passive and active tracers in chaotic and turbulent flows is a field of study of enormous interest for a variety of different disciplines reaching from biology over chemistry and physics as far as financial mathematics and social studies [12, 22–24]. Especially the influence of advection on the spatiotemporal development of active media is of relevance for many natural systems such as plankton species in the ocean, atmospheric chemistry or convection in the earth mantle [3]. For these reaction-diffusion-advection systems it is of crucial interest to define typical dynamics as pattern formation or the speed of propagation. An experimentally and theoretically well studied active system, producing spatiotemporal patterns and reaction fronts, is the Belousov-Zhabotinsky reaction (BZ) [127] that we use throughout this study. For the generation of the fluid flow we use again the Faraday experiment which consists in the vertical vibration of the fluid. This vibration excites surface waves and bulk fluxes [18, 19, 104] and we named it Faraday flow (Chap. 3).

Let us recall that reaction fronts of target waves in reaction-diffusion systems travel with a constant velocity v_{front} that is usually obtained from the Fisher-Kolmogorov-Petrovskii-Piskunov (FKPP) prediction,

$$v_{front} = 2\sqrt{D/\tau_{reac}}, \tag{5.1}$$

where D is the molecular diffusion constant and τ_{reac} is the reaction timescale [127, 135, 146]. Reaction-diffusion-advection systems are often described by replacing the molecular diffusion constant D with an effective diffusion constant D^*. However, recent experiments have shown that the FKPP prediction does not hold for the case of enhanced diffusion caused by a fluid flow that induces chaotic mixing [135]. Additionally, normal enhanced diffusion might not be a good approximation for some important time and length scales of a chaotic or turbulent flow. In this case the assumption that the underlying random walk of the reactants can be described by a probability function with a finite second moment (e.g., a Gaussian distribution) does not hold. This raises the question how dynamics change when the system exhibits superdiffusion.

Superdiffusion is defined as the supralinear growth of the variance $\sigma^2(t)$ of the probability density function (PDF) $P(\mathbf{r}, t)$ (Sec. 1.2.3)

$$\sigma^2(t) \propto t^\gamma, \text{ with } \gamma > 1. \tag{5.2}$$

$P(\mathbf{r}, t)$ is the probability to find a particle at a location $\mathbf{r}$ at time t. Numerical studies of two-dimensional and quasi-geostrophic flows have shown, that a considerable transient superdiffusive range can exist with $\gamma = 5/4$ or $\gamma = 5/3$ in dependence of the details of the flow [147–149]. The same was also observed for numerically advected tracers in the western Mediterranean Sea [150]. For drifters, subjected to Faraday induced capillary waves, a similar transient region has also been reported [86, 89]. In our experiments such a transient region is especially well pronounced for intermediate forcing accelerations as a simple compensation of the measured absolute diffusion with t^{γ} of the artificial tracers reveals, see Fig. 5.1. It is thus expected, that the reaction front of the forward BZ-reaction, introduced in the previous Chap. 4 also moves superdiffusively. Nevertheless, in this chapter we will not use the absolute diffusion derived from the artificial tracers advected in the measured velocity fields. Instead we will use direct tracking of real particles as explained in Sec. 5.2.3.

The microscopic theory underlying the general random walk which can lead to superdiffusion is called Continuous Time Random Walk (CTRW) and was formulated by Montroll and Weiss [77] and extended to the Multistage Random Walk theory (MSRW) by Shlesinger and Klafter [151]. This probabilistic point of view is especially useful in systems where the full information about the underlying velocity field and its evolution in time is not known. Passive particles that experience superdiffusive transport for certain time and length scales in chaotic flows have been studied experimentally [86, 88, 89, 152–154] and numerically [155–159] by a variety of different groups. Even though numerical and theoretical studies of reaction-superdiffusion systems exist, they focus (to our knowledge) on one dimensional systems and can be divided into two different classes of which the first deals with bistable reaction processes [160–162] while the second class deals with oscillatory or excitable reaction dynamics [7]. Experimental studies of active media in this context are more scarce [17, 104, 135, 163, 164]. The difficulties of studying active media experimentally with a probabilistic approach arise from the dilemma that the underlying statistics are only valid for point particles in the flow while active media is studied in terms of concentration fields. Expressions for the PDFs (or equally: concentrations $c(\mathbf{r}, t)$) that solve the Master Equations in the Continuum Limit depend strongly on the specific underlying microscopic random walk process [24, 165] and do not have a simple closed formulation. A consequence of this dilemma is the intricacy of finding measureable variables (other than the variance growth of the concentration-field) that can be compared to the existing theory.

Figure 5.2 shows different patterns we have observed in the Belousov-Zhabotinsky reaction when it is advected by the Faraday flow [18, 19]. For a certain forcing range an activator autowave forms that propagates periodically through the entire reactor as described in Chap. 4. However, due to our limited field of view in this study we observe the front details and the local expansion of this wave (Fig. 5.2 (d)-(f)) rather than the whole structure as in

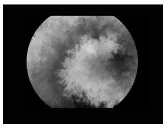

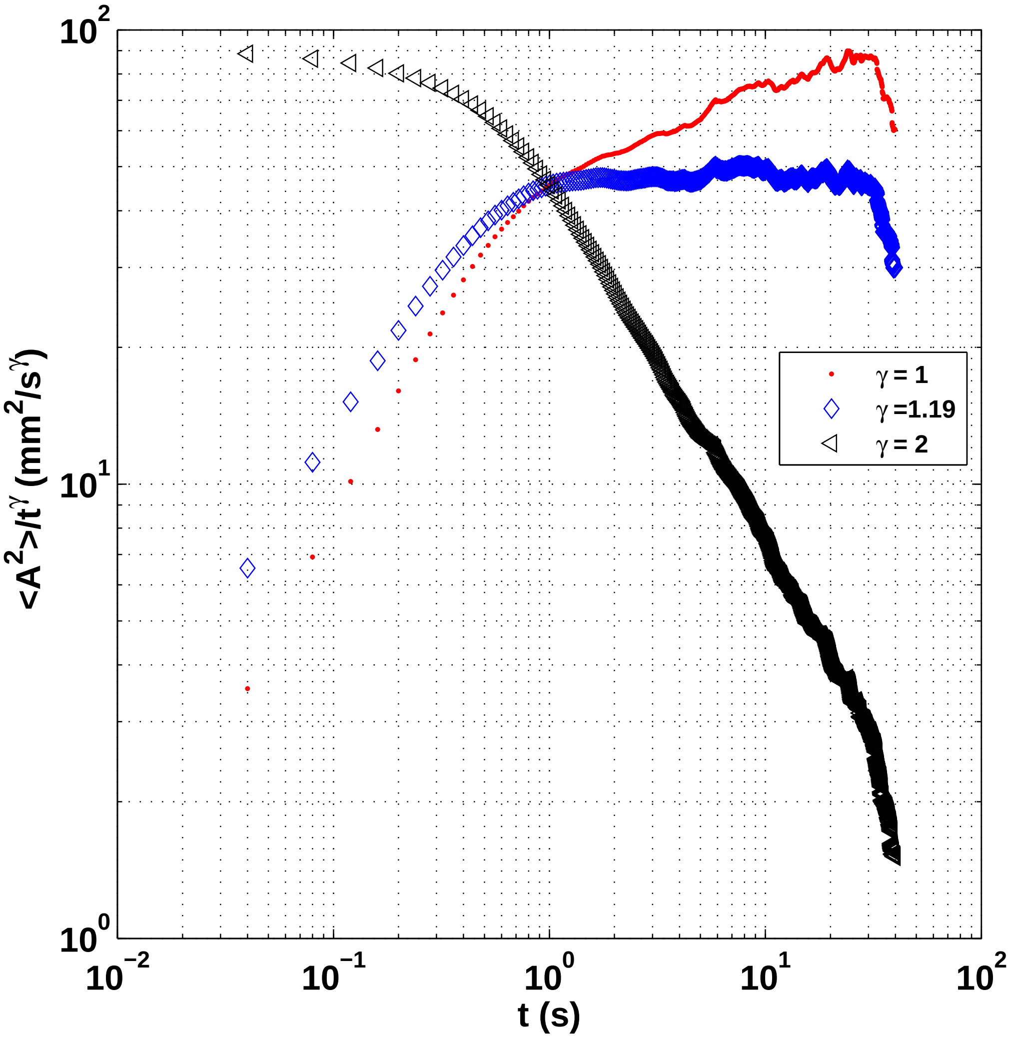

Fig. 5.1: The measured root-mean-square displacement $\langle A^2(t)\rangle$ of the artificial tracers (Sec. 3.3.1) is compensated by t^γ for $\gamma = 1$, $\gamma = 1.19$ and $\gamma = 2$. For small times, when velocities are still correlated the absolute dispersion shows an almost ballistic growth. For very large times, a diffusive behaviour with $\gamma \approx 1$ is expected. At intermediate timescales an anomalous scaling region with $\gamma \approx 1.19$ can be observed. Here exemplarily shown for the acceleration $a = 1.5\,g_0$. Since the forward BZ-reaction, introduced in the previous Chap. 4, Fig. 4.8, occurs on timescales of 3-8 s it is reasonable to expect that the reaction front also moves superdiffusively.

Fig. 4.1. For lower forcings the patterns are filamentous elongated structures which are only locally in phase. Here we propose a novel approach for the analysis of the local propagation of a chemical wave on the timescales where the flow can be considered superdiffusive. Our approach is based on the simple assumption that in a first approximation small volumes of the activator experience random displacements just as particles would. In Section 5.2 a description of the experimental procedure for the measurements with active and passive media in the flow is given. Section 5.3 describes the statistical analysis techniques used and puts special emphasis on the theory of the underlying stochastical processes. In Section 5.4 the results are presented: We show that the flow is superdiffusive on certain time and lengthscales and that particles in the flow experience Lévy walks which results in superdiffusion and an anomalous variance growth $\sigma^2(t) = t^\gamma, \text{ with } \gamma > 1$ for short times. We find that the reactive front on the time and length scales measured here also propagates superdiffusively, i.e., intervals of propagation with constant velocity interchange with intervals of constant acceleration when parts of the front move rapidly forward with jets occurring in the flow. Finally, in Section 5.5 we compare and discuss the results from active and passive media experiments.

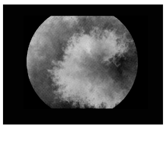

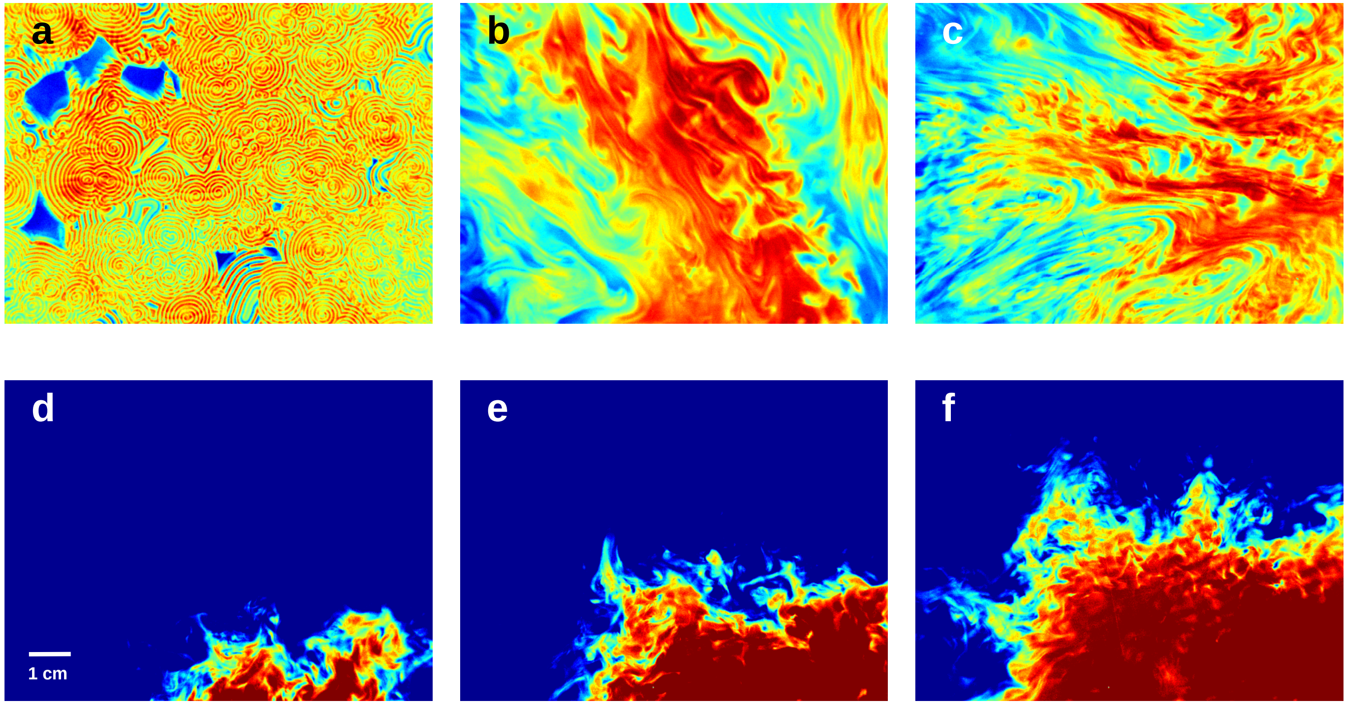

Fig. 5.2: Patterns observed for the BZ reaction subjected to different frequencies and accelerations of vertical vibration (Faraday Experiment). Transitional changes in the patterns are observed and different regions of pattern formation can be distinguished as the forcing increases. (a) Without forcing the typical targets and spirals of the BZ reaction are observed [127]. (b) and (c) For a forcing of $f = 20$ Hz and $f = 30$ Hz ($a = 1g_0$) filamentary patterns develop. (d)-(f) For a forcing of $f = 60$ Hz and $a = 0.5g_0$ a single boosted autowave propagates through the reactor.

5.2 Experimental Procedure

5.2.1 Setup

The experiments are conducted in a circular reactor of 30 cm diameter with an inner border that reduces capillary effects [93] (see Fig. 2.2). This container was slightly different than the one used for the experiments of the study in the previous Chap. 4, since it came from another manufacturer. The container used in this study was lighter but also less solid than the one used in Chap. 4. Therefore, even though the basic observations remain the same, the onset of the Faraday instability is slightly shifted towards lower accelerations and makes a direct comparison of the acceleration values used in the two studies impossible. Images are recorded with a monochrome firewire camera (Guppy, AVT) at a frame rate of 60 Hz and a resolution of 480 x 640 pixel^2. The selected field of view is 8.0×10.7 cm^2, so that 1 pixel ≈ 0.017 cm. For further processing images are stored to a hard disk and analysed off-line as described in Sec. 5.3. The Faraday waves obtained in this experiments have all rectangular or hexagonal shape for the forcing range studied and the fluid layer of 2 mm which is used here. The Faraday wavelength varies from 0.5-1.0 cm in dependence of the frequency and the dominant temporal wave frequency is half the forcing frequency (subharmonic response) [18, 83]. For all forcings applied the wave pattern observed is time-dependent, i.e., for the lower forcings defects in the Faraday wave pattern travel through the reactor and for higher forcings these defects dominate the pattern.

5.2.2 Experiments with Chemical Reaction

The recipe for the aqueous solution of the BZ reaction was chosen in order to obtain a high contrast for recording and is identical to the one used in the study presented in the previous Chap. 4. The details of the chemical recipe are given in Sec. 2.1.1. The reactants are mixed in strictly the same order for each experiment and stirred for 60 min. Then the reactants are poured into the reactor on top of the shaker. The reactor is filled up to a height of 2 mm and inert argon gas is injected for 15 min to avoid oxygen inhibition in the BZ dynamics [94, 166]. The recipient is then closed with a transparent plexiglass cover and the BZ reaction is left to rest for another 15-20 min until the typical patterns of an BZ reaction, targets and spirals, occur (Fig. 5.2 (a)). Afterwards the forcing is slowly switched on and another 15 min are given to the system to become resonant before recording is started. During the recording the strength of the forcing is continuously monitored with an accelerometer. Experiments are performed for a frequency range of 10 Hz - 70 Hz (in steps of 10 Hz) and

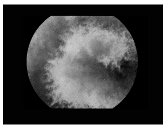

accelerations a of $0.5\,g_0$, $0.75\,g_0$, $1\,g_0$ and $1.5\,g_0$. The upper limit of the forcing range is given, either by the onset of droplet formation on the surface of the liquid and subsequent wetting of the cover making recording unfeasible or, by inhomogeneities in the vibration of the container at high frequencies. The room temperature was kept constant at $23 \pm 1°$C during all experiments.

5.2.3 Experiments with Particles

For the experiments with single particles pure water is chosen as fluid media because it gives a better contrast for image analysis than the BZ solution and has very similar properties concerning density, viscosity and surface tension. The particles (Black CromoSpheres, Brookhaven Instruments) have a mean diameter of $502 \pm 24\,\mu$m with a density of $d \approx 1.06$ g/cm^3 slightly higher than the density of water at room temperature ($23°$C, 1.00 g/cm^3). Despite that higher density particles usually float on the surface of the fluid and only a few particles sink and are thus sorted out from analysis. For the experiment with the particles the same reactor as for the chemical experiments is used, changing only the transparent cover with a nearly identical one that has a hole of the diameter 0.5 cm to facilitate the application of the particles. Particles are applied to the reactor one after the other and the trajectories are recorded until the particles leave the field of view. Experiments are performed for a frequency range of 30 Hz - 60 Hz (in steps of 10 Hz) and an acceleration of $a = 1\,g_0$. In order to ensure that particles follow the fluid motion, the Stokes number S needs to be small, $S \ll 1$ [154]. It can be calculated as $S \approx Ud^2/18\nu L$ where U is a typical velocity of the particles, d is their diameter, ν is the viscosity and L is a typical length scale of the flow. In our experiments the Stokes number S is of the order 10^{-2} so that the particle motion can be considered a reasonable approximation to the fluid motion.

5.3 Analysis

The analysis is split into two parts. The first introduces analysis concepts used for the passive particles in the flow and the second part focuses on the description of the analysis technique applied to the boosted autowave in the BZ reaction. The analysis of the boosted autowave is based on the assumption that some characteristics of the particle motion also represent the movement of finite fluid volumes. This assumption has not been thoroughly tested and more analytical and numerical evaluation is needed in further studies.

5.3.1 Random Walks of the Particles and Continuous Time Random Walk Theory

The chaotic dynamics of a particle in a fluid flow is an intermediate case in between completely random (nonintegrable) and completely regular (integrable) kinetics. Continuous Time Random Walk theory (CTRW) is an important model to describe this chaotic dynamics and can be applied to experimental measurements of particle trajectories (for a discussion of different models see [78]).

Concepts of Continuous Time Random Walk Theory

We want to summarize some of the important concepts of CTRW theory following the arguments presented in the references [70, 71, 151, 165]. In CTRW theory the trajectory of a particle in a fluid flow is described statistically by three elementary functions, the jump length distribution $p(\Delta R)$, the waiting time distribution $\varphi(\Delta t_{wait})$ and the flight time distribution $q(\Delta t_{flight})$. A walker (a particle) is assumed to make a jump of length ΔR and duration Δt_{flight} to a resting point where it rests a time Δt_{wait} until the next jump. From these three distributions the expression for the probability density function $P(\mathbf{r}, t)$ to find a particle at time t at the point $\mathbf{r}$ can be derived [70]. Thus, also the evolution of the variance $\sigma^2(t)$, Eq. 1.37, can be written in terms of these three distributions [78, 167, 168]. In a fully turbulent flow the particle is never at rest and the waiting time can be neglected. Hence, $P(\mathbf{r}, t)$ is calculated using only the jump length and the flight time distribution and, importantly, some assumption about the coupling of the jump length and flight time which introduces the concept of Lévy walks [70, 167, 169]. Lévy walks arise when the jump length and the flight time distribution are coupled such that longer jumps take longer times to complete due to a finite velocity of the particles in real flows. The coupled probability of a jump to last a time Δt_{flight} and overcome thereby a distance ΔR can be written as [70]

$$\Phi(\Delta R, \Delta t_{flight}) = p(\Delta R|\Delta t) q(\Delta t_{flight}) \tag{5.3}$$

or equivalent

$$\Phi(\Delta R, \Delta t_{flight}) = q(\Delta t_{flight}|\Delta R) p(\Delta R), \tag{5.4}$$

where we consider that ΔR is the jump distance $|\mathbf{r}|$ and the process is isotropic. The probabilities in Eq. 5.3 and Eq. 5.4 obey the experimentally useful relationships [70]

$$\sum_{\Delta R} \Phi(\Delta R, \Delta t_{flight}) = q(\Delta t_{flight}) \tag{5.5}$$

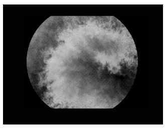

and

$$\sum_{\Delta t} \Phi(\Delta R, \Delta t_{flight}) = p(\Delta R). \tag{5.6}$$

These independent probability distributions on the r.h.s. of Eq. 5.5 and Eq. 5.6 can be measured experimentally by defining the turning points of the trajectory of the random walker. The distance between these turning points is defined as the jump length ΔR and the duration of the jump as the flight time Δt. Superdiffusion ($\sigma^2(t) \propto t^\gamma, \gamma > 1$) occurs when the flight time and the jump length distributions have heavy tails of the form

$$q(\Delta t_{flight}) \propto \Delta t^{-\eta} \tag{5.7}$$

$$p(\Delta R) \propto \Delta R^{-\mu_p}. \tag{5.8}$$

In order to obtain the variance growth from Eqs.(5.7,5.8) two different coupling laws have been studied theoretically by different authors [70, 167, 168, 170]. The first coupling model, for turbulent flows, was suggested by Shlesinger and Klafter [70]

$$q(\Delta t_{flight}|\Delta R) = \delta\left(\Delta t - \frac{|\Delta R|}{|V(\Delta R)|}\right), \tag{5.9}$$

where δ denotes the δ-function and $V(\Delta R)$ is an expression for turbulent velocity. They show that if this coupling is considered for the calculation of $P(\mathbf{r}, t)$ it leads to an exponent γ_{turb} of the variance growth (Eq. (1.37)),

$$\gamma_{turb} = \begin{cases} 3 & \text{if } (\mu_p - 1) \leq \frac{1}{3} \\ 2 + \frac{3}{2}(2 - \mu_p) & \text{if } \frac{1}{3} \leq (\mu_p - 1) \leq \frac{5}{3} \\ 1 & \text{if } (\mu_p - 1) \geq \frac{5}{3} \end{cases} \tag{5.10}$$

The second frequently discussed coupling is of the form

$$q(\Delta t_{flight}|\Delta R) = \delta\left(\Delta t^\nu - \Delta R\right), \tag{5.11}$$

where the temporal and the spatial step are coupled by a δ function. For a given time step, Δt, the points that can be reached with one spatial step lie on a shell around the starting point. The exponent ν which can be calculated from μ_p and η defines the scaling between the time and the spatial steps. This coupling leads to a different expression for the variance growth exponent, here denoted as γ_ν that is more complicated and thus not shown here (for a detailed description see [167, 168]). These two different couplings will be used for an estimation of the variance growth exponent γ from the measurements of exponents μ_p and η. However, it should be kept in mind that the details of the real coupling are not known and it is possible that neither of the two couplings considered here reflects the real coupling.

Definition of Experimental Random Walk Process

The particle position data $\mathbf{r}(t)$ obtained from our experiments has a temporal resolution of 60 Hz and a subpixel spatial resolution. In order to obtain the jump length distribution $p(\Delta R)$ and the flight time distribution $q(\Delta t)$ the turning points of the random walk in radial direction have to be defined. Figure 5.3 shows a random walk derived by this definition.

As the isotropy of the flow is indispensable for this definition, the congruence of the jump distributions in x- and y- direction of the image coordinates has been verified. An arbitrary starting point $\mathbf{r}(t_0)$ from the position data is selected as the first turning point. The point $\mathbf{r}(t_n)$ where the radial distance

$$\Delta R_n = |\mathbf{r}(t_0) - \mathbf{r}(t_n)| \tag{5.12}$$

reaches its first local maximum is set as the next turning point and the new starting point for the algorithm.

We obtain the jump length distributions (5.5) and flight time distributions (5.6) from the random walk and estimate the heavy-tail exponents μ_p and η (5.7, 5.8) by fitting (see Fig. 5.6). The exponents μ_p and η together with a theoretical assumption of the coupling law for Δt and ΔR as introduced in Eqs. (5.9, 5.10) determine the exponent γ of the variance growth. In Section 5.4.1 the variance growth exponents γ_ν and γ_{turb} will be calculated from μ_p and η and compared to the directly measured values of the variance growth.

5.3.2 Analysis of the Wave Front

Figure 5.2 shows the different regimes observed in the BZ patterns in dependence of the forcing acceleration and frequency and the resulting flow. Without forcing, the typical molecular-diffusion-induced target and spiral patterns of the BZ reaction can be seen (Fig. 5.2(a)). Above a critical forcing the patterns observed exhibit important structural changes. For weak forcing (forcing acceleration and forcing frequency low, e.g. $f = 20$ Hz, $a = 0.75\, g_0$), targets and spirals are only slightly stretched (not shown). Then, for a higher forcing filamentary patterns appear (Fig. 5.2 b, c, $f = 20$ Hz, $a = 1\, g_0$). For an even stronger forcing multiple boosted autowaves appear in different parts of the reactor (not shown) and finally, if the forcing is further augmented, a single boosted autowave propagates from one side of the reactor to the other (Fig. 5.2 d-f, $f = 60$ Hz, $a = 0.5\, g_0$). When the forcing is too strong, all patterns disappear and the media becomes totally homogeneous [104] (see Fig. 5.9 for an overview of the parameter range where boosted autowaves were observed). This is remarkable, especially because after switching off the forcing the typical molecular-diffusion-induced spirals and targets reappear again. This

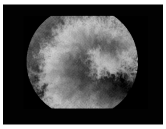

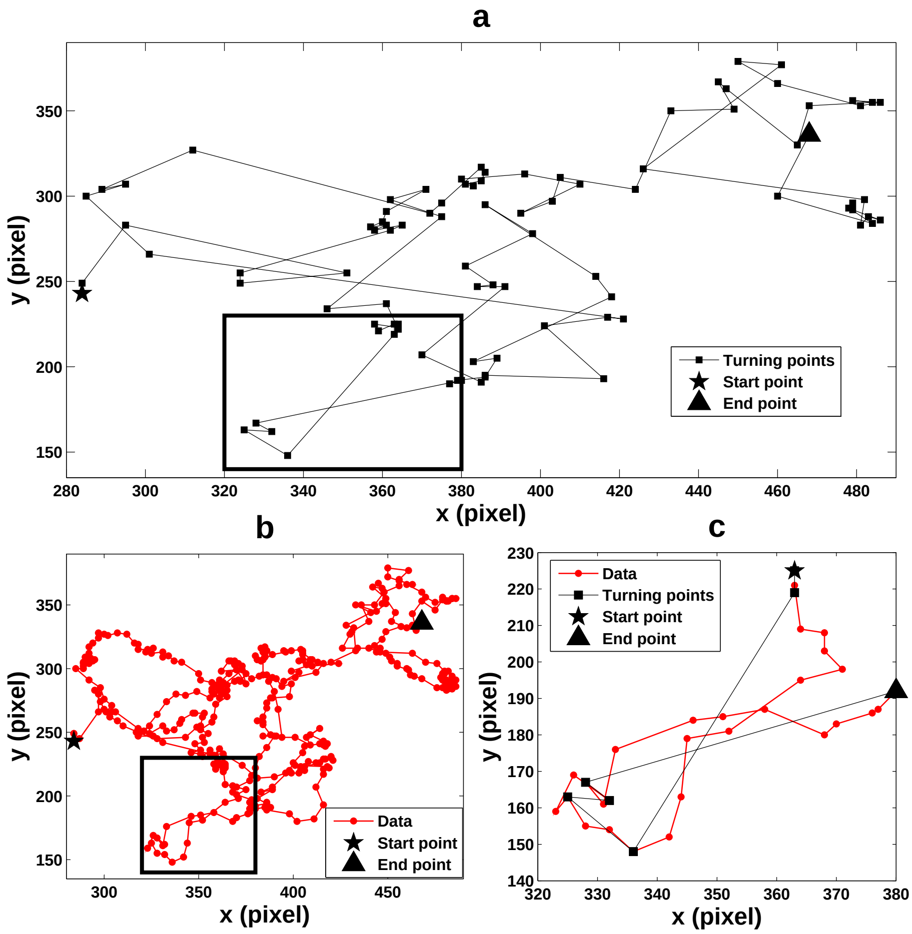

Fig. 5.3: (a) A typical random walk trajectory (forcing: 60 Hz, $a = 1\,g_0$) where the turning points (black squares) are obtained from recorded data points shown in (b). The random walk shows a variety of different scales of the jump length ΔR. The lack of a typical length scale leads to heavy-tailed jump length distributions that cause superdiffusion. (b) The original measured data of the trajectory (red dots). Note the small high frequency oscillations of the particle due to the Faraday waves. This oscillations do not contribute to the overall displacement of the particle. (c) Detail from the highlighted frame in (a) and (b) presented in order to illustrate the definition of the turning points (data: red dots, turning points: black squares). Whenever the distances between the current turning point $\mathbf{r}(t_0)$ and two following data points $\mathbf{r}(t_{n+1})$ and $\mathbf{r}(t_n)$ behaves as $\Delta R_{n+1} < \Delta R_n$ the data point $\mathbf{r}(t_n)$ is chosen as a new turning point and the same procedure is applied to it. In this way successively a set of turning points is obtained. The high oscillations due to the Faraday waves are mostly filtered out by this procedure.

circumstance itself already suggests that the boosted autowave is not a mere effect of enhanced mixing but critically depends on the detailed dynamics of the flow. The absence of any pattern above a critical forcing seems to coincide with droplet formation on the surface of the liquid and thus with an instability of the Faraday waves.

The direct way to characterize the front dynamics of the boosted autowave is the measurement of the variance growth of the activator spot in time. Exemplary measurements of the variance growth have been realized. The variance was calculated from the images as the weighted sum of the squared radii of the area covered by the boosted autowave at time t: $\sigma_r^2(t) = \sum_r r^2 w_r(t)$, where $w_r(t)$ is the number of occurrence of radius r. However, the initiation of a boosted autowave in the middle of the field of view by chance is a rare event as it normally starts at the boundary of the reactor, presumably due to perturbations. Provoked initiation of a boosted autowave within the field of view by introduction of a silver wire [130] proved to be difficult.

We therefore designed an analysis for the front propagation in analogy to the jump length distribution in the particle random walk described above. We define a probability $\lambda(\Delta R, \Delta t)$ to find a volume of high activator concentration after a time Δt at a distance ΔR to a beforehand defined front. This analysis is realized by an algorithm that detects the front line of an boosted autowave in an image I_t and then draws n new equidistant lines (masks) where mask$_n$ is n pixels apart from the front line and $n \in (1, 2, 3, ..., N)$. Once these N masks are created, the intersection of image $I_{t+\Delta t}$ with each mask of the image I_t is calculated. This counts how many pixels at a distance n away from the front have become activated after a time Δt. A schematic of this masking algorithm is depicted in Fig. 5.4.

This procedure is applied on each image pair I_t and $I_{t+\Delta t}$ while the boosted autowave passes through the field of view (around 400-500 images) and the jump distribution $\lambda(\Delta R, \Delta t)$ for jumps ahead of the front is obtained. Fitting a Lévy function [171, 172] to the data allows for the extraction of an exponent μ_r that describes the heavy tail behaviour of the distribution $\lambda(\Delta R, \Delta t) \propto \Delta R^{-\mu_r(\Delta t)}$. For a random walk in one (two) dimension $\mu_r < 3$ (< 4) implies that the walker experiences large displacements that lead to Levy walks and superdiffusion.

The definition of a wavefront involves the determination of a threshold of activator concentration. In order to define the wavefront we implement the following two steps before applying the masking algorithm introduced above: First, we apply a temporal low-pass Gaussian-filter to each data-pixel in time to smooth out shadowing effects from the Faraday waves which have a comparably high temporal frequency. The effect of the filter on the temporal appearance of the signal can be seen in Fig. 5.5. Second, for each pixel we define a threshold

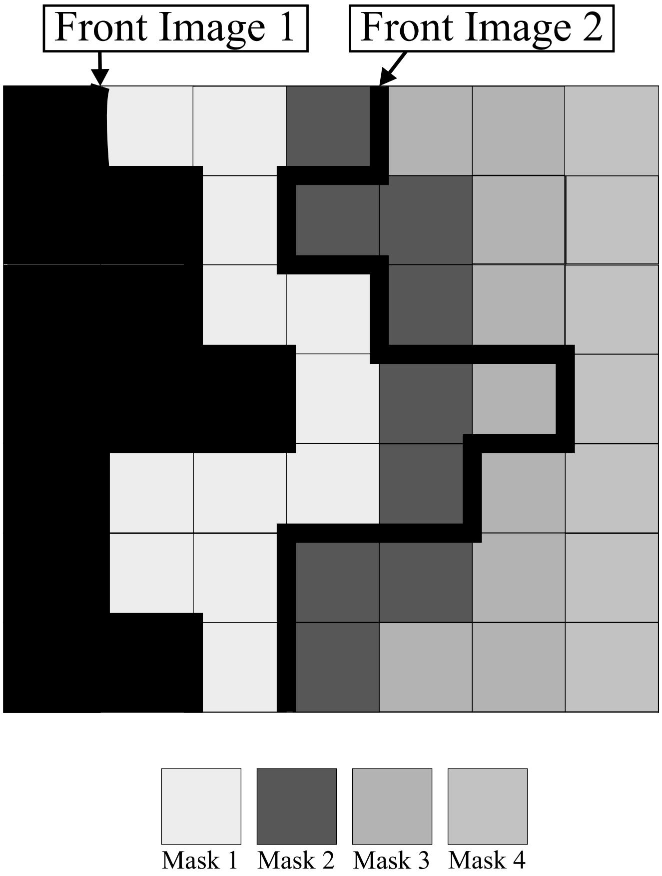

Fig. 5.4: A schematic of the counting algorithm to locally define the spread of the front. Masks at different distances to the front of image $I_{t=1}$ are drawn. After a time Δt (in image $I_{(t+\Delta t)=2}$) the front has advanced. Now for every mask of $I_{t=1}$ we count the pixels that have become filled with active media. From this procedure we can derive a probability distribution $\lambda(\Delta R, \Delta t)$ for activator volumes to jump a distance ΔR perpendicular to the reaction front. An example of such a statistic is shown in Fig. 5.8

based on the mean and standard deviation from the temporal data when no chemical autowave pass through the pixel. Every pixel with a value below this threshold is considered as unexcited while every pixel with a value above this threshold is considered to be excited. It was checked that the value of the threshold had no impact on the overall results presented here as long as a reasonable choice was made for this value.

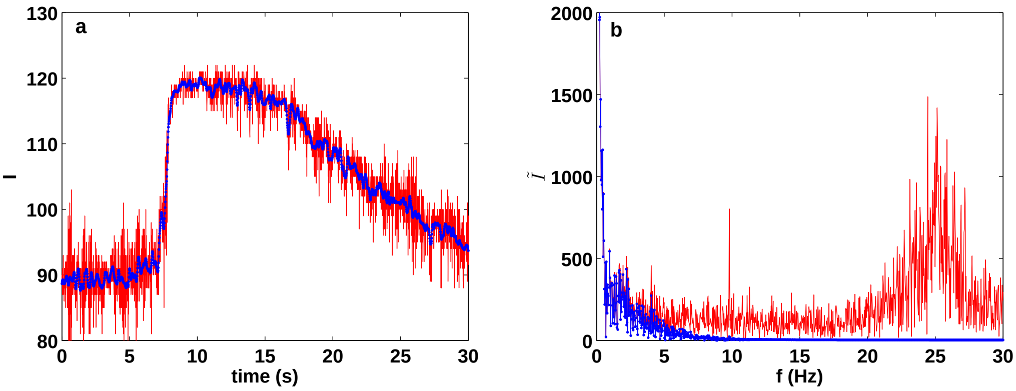

Fig. 5.5: A Gaussian-filter is used to remove the high temporal frequency fluctuations around $25\,$Hz in the intensity signal I caused by the Faraday waves. (a) The original signal is shown in red and the filtered signal in blue. (b) The amplitude spectra $\tilde{I}$ (i.e., the Fourier transform) of the filtered and unfiltered signal using the same colour-code. Subsequently a threshold is derived for each individual pixel using its standard deviation and mean value derived when no active wavefront passes through the image pixel.

5.4 Results

This section is divided in two parts. First, the results for the particle experiments are presented and it is shown that the flow produced by the Faraday experiment for an acceleration $a = 1\,g_0$ is superdiffusive for forcing frequencies $f \geq 40$ Hz, while at 30 Hz the flow is not superdiffusive. In the second part we show that the front of the boosted autowave also propagates superdiffusively and accelerated for short times.

5.4.1 Particles

Figure 5.6 shows the jump length distributions $p(\Delta R)$ obtained for different forcing frequencies (at $a = 1\,g_0$). Jump length exponents μ_p are estimated by power-law fitting to the recorded data. The flight time distribution exponents η are obtained in the very same way from the corresponding distributions. In Table 5.1 the exponents of the jump length and the flight time distributions are summarized. Using CTRW theory the exponents γ_ν and γ_{turb} for the variance

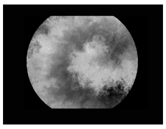

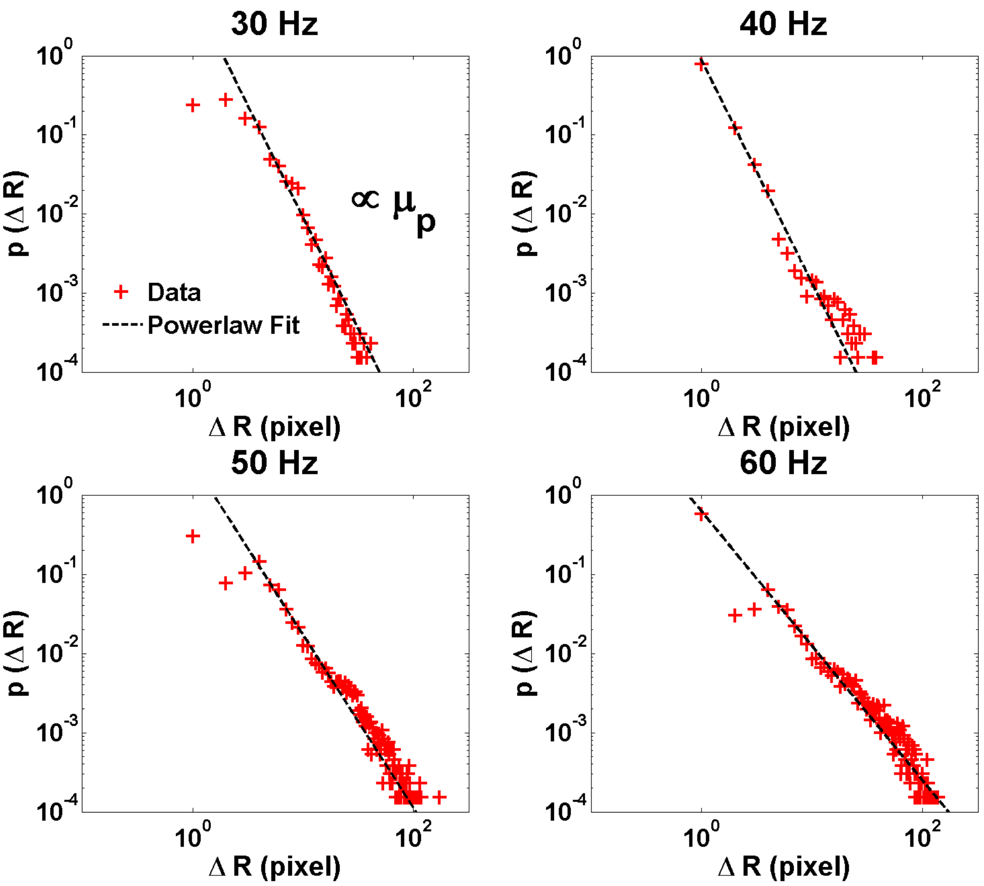

Fig. 5.6: Jump length distributions of the particle experiments $p(\Delta R)$, Eq. 5.8, for the different forcing frequencies derived from the data (log-log scale). The exponents μ_p $(2.8 \pm 0.1,\ 2.6 \pm 0.1,\ 2.2 \pm 0.1,\ 1.7 \pm 0.1)$ are obtained by fitting a power-law (dashed line) to the jump length distributions for the different forcing frequencies (30 Hz, 40 Hz, 50 Hz, 60 Hz, $a = 1\,g_0$).

growth are calculated from μ_p and η as described in Section 5.3.1 and shown in Table 5.1. For the values of the exponents μ_p and ν extracted from these fittings CTRW theory predicts superdiffusion, $\gamma > 1$, except for $\gamma_{turb}(30\ \mathrm{Hz})$. This indicates the lack of a typical scale in the dynamics of the flow, even though there is a largest scale as the experimental setup has finite boundaries.

Figure 5.7 shows the measured variance growth directly obtained from particle trajectories. The experimental variance growth exponents γ_{exp} are extracted by power-law fits to the data. The directly measured variance growth for a forcing of $f = 50$ Hz at $a = 1g_0$ is shown for timescales of considerable importance

		30 Hz	40 Hz	50 Hz	60 Hz
experiment	μ_p	2.8 ± 0.1	2.6 ± 0.1	2.2 ± 0.1	1.7 ± 0.1
	η	1.9 ± 0.2	2.3 ± 0.2	1.9 ± 0.2	1.8 ± 0.2
	γ_{exp}	1.0 ± 0.1	1.3 ± 0.1	1.4 ± 0.1	1.3 ± 0.1
from theory	γ_ν	≈ 1.4	≈ 1.5	≈ 1.7	≈ 2.1
	γ_{turb}	≈ 1	≈ 1.1	≈ 1.7	≈ 2.45

Table 5.1: List of exponents μ_p (jump length distribution) and η (flight time distribution), Eq. 5.7 and Eq. 5.8, for the particle random walks at an acceleration $a = 1\, g_0$. From these values we calculate the theoretically derived variance growth exponents (γ_ν, γ_{turb}) and compare them to the measured ones γ_{exp}. At higher frequencies the theoretical values exceed the measured ones and overestimate the superdiffusivity considerably.

for the dynamics compared to velocity values in the range of some cm/s. The variance is calculated from 200 different experiments. Clearly a transition from a ballistic growth of the variance $\gamma \approx 2$ to a superdiffusive $1 < \gamma_{exp} < 2$ can be observed in the data and is accounted for by two different fitting regimes. The experimentally obtained values of γ_{exp} for the different forcing frequencies are also found in Table 5.1 to facilitate comparison to the derived values γ_ν and γ_{turb}. The inset in Fig. 5.7 shows the Lagrangian velocity autocorrelation function $C = \mathbf{v}_{t_0+t}\mathbf{v}_{\mathbf{t_0}}/(|\mathbf{v}_{t_0+t}|\,|\mathbf{v}_{\mathbf{t_0}}|)$. This function sheds light on the timescales τ_{corr} on which the motion of the particles is still correlated. The ballistic growth of the variance changes to superdiffusive around that correlation time τ_{corr}.

Comparing the different variance growth exponents γ in Table 5.1, we find a transition from normal diffusion to superdiffusion in the flow in between 30 Hz-40 Hz (at $a = 1\, g_0$) for γ_{exp} and γ_{turb}. The values of exponent γ_ν do not show this transition. In contrast to the derived γ_ν and γ_{turb} the directly obtained γ_{exp} does not show a strong increase towards higher values of the forcing frequency. This suggests that the real coupling in between Δt and ΔR in the flow differs from the two theoretical ones and that they overestimate the superdiffusion.

5.4.2 Active Media

The superdiffusion in the flow is also observable in the dynamics of the boosted autowave. Figure 5.8 shows that the jump length distribution of the front $\lambda(\Delta R, \Delta t)$ is well described by a Lévy function while a Gaussian strongly underestimates the probability for long jumps of activator volume. An exponent α is obtained from the Lévy fit [171, 172], where $\mu_r = \alpha + 1$ is the behaviour of the heavy tail of $\lambda(\Delta R, \Delta t)$. An exponent $\mu_r(\Delta t) < 3$ signifies that on local

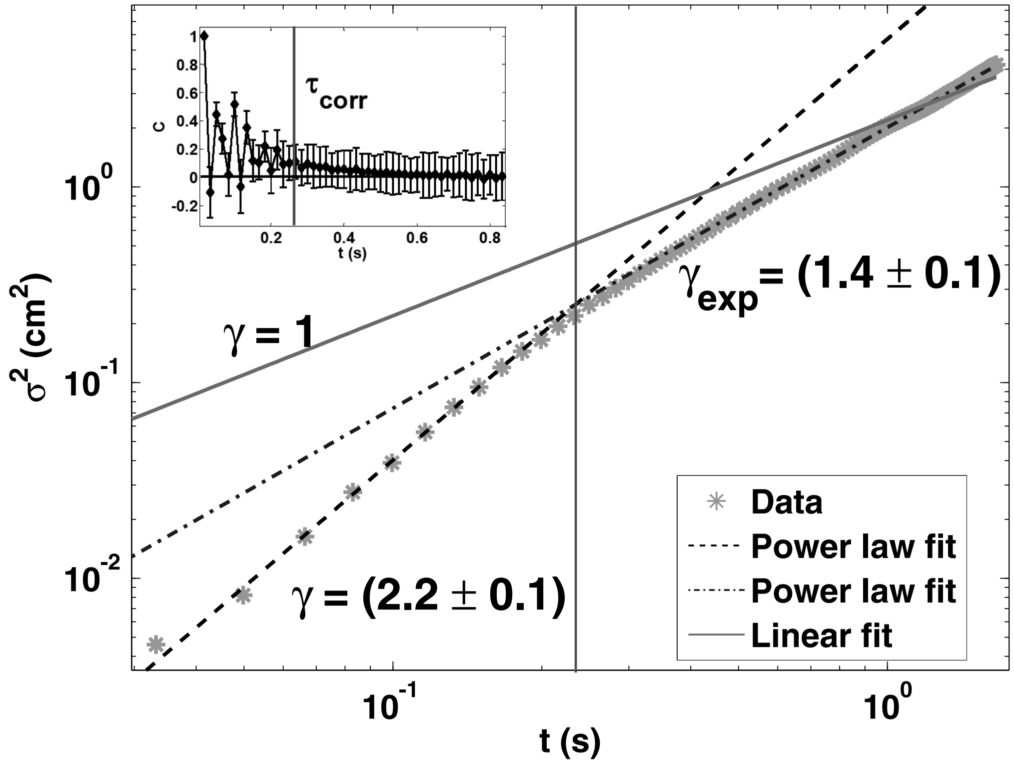

Fig. 5.7: Variance growth of the particle experiments (50 Hz, $a = 1\,g_0$, log-log scale). Two different regimes can be identified: Up to a correlation time τ_{corr} the variance growth is close to ballistic (dashed line) while above that time the variance grows superdiffusively (dash-dotted line) with an exponent $\gamma_{exp} = 1.4 \pm 0.1$. For comparison a power-law with an exponent $\gamma = 1$ as expected for normal diffusion is plotted (continuous line). Inset: The correlation time (vertical bar) can also be estimated from the velocity autocorrelation function.

time and length scales the front propagates superdiffusively and the volumes of high activator concentration exhibit Lévy walks.

Figure 5.9 shows the exponents $\mu_r(\Delta t)$ as a function of the frequency and the amplitude of the forcing for two different Δt ($\Delta t = 1/60$ s and $\Delta t = 2/60$ s). We find that the exponent $\mu_r(\Delta t)$ decreases with increasing forcing, i.e., long jumps get more probable. Also long jumps are slightly more probable for larger times Δt (Fig. 5.9 b). Figure 5.9 also visualizes the limited parameter range for which an boosted autowave exists. The white fields represent forcing parameters where no clear single boosted autowave could be observed.

Figure 5.10 shows the variance growth $\sigma_r^2(t) \propto t_r^\gamma$ of a centred boosted

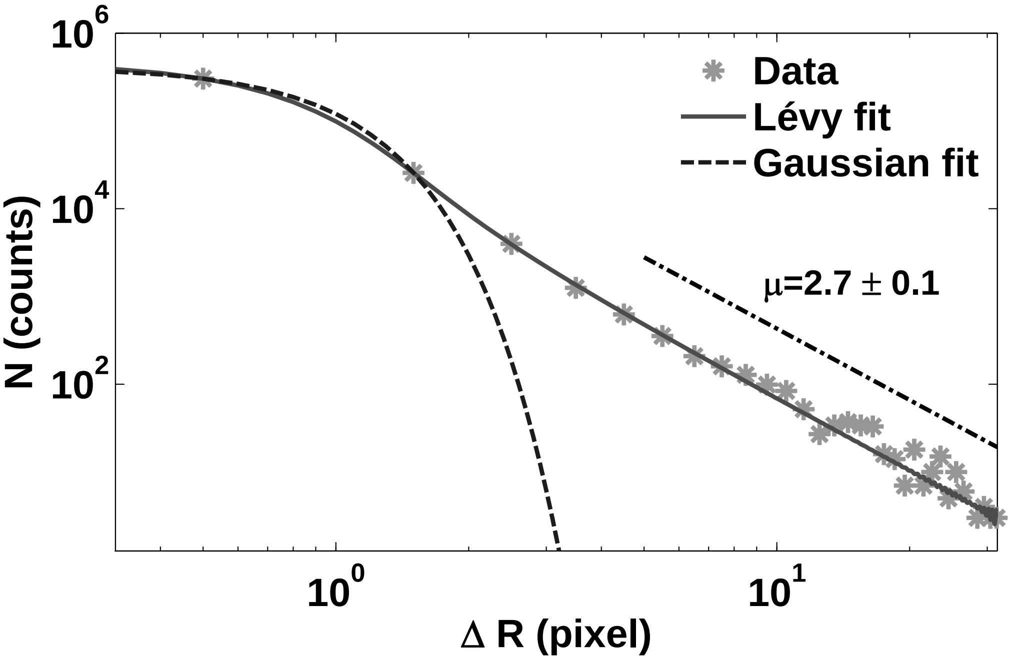

Fig. 5.8: The probability distribution $\lambda(\Delta R, \Delta t)$ for activator volumes to jump a distance ΔR perpendicular to the reaction front is well fitted by a Lévy function (continuous line). A Gaussian distribution (dashed line) underestimates the probability of large displacements. The dash dotted line shows the heavy tail behaviour of the Lévy fit from which the exponent $\mu_r = 2.7 \pm 0.1$ is obtained. An exponent $\mu_r < 3$ expresses that the activator volumes experience Lévy walks which can lead to superdiffusion. Data $(50$ Hz, $a = 1\, g_0$, $\Delta t = 1/60$ s) are shown on log-log scales and obtained from around 550 image pairs using the masking algorithm described in section 5.3.2.

autowave in time. We find that for an experiment with a forcing frequency of $f = 50$ Hz at $a = 1\, g_0$ the variance of the boosted autowave monitored grows with an exponent $\gamma_r = 3.4 \pm 0.2$ and that the mean displacement in radial direction $\langle r(t) \rangle$ grows with $\zeta = 1.7 \pm 0.2$. For other forcing strengths and triggered boosted autowaves, values of γ_r lie in the same range.

We conclude that $\gamma_r > 2$ and $\zeta > 1$ which indicates that the front of the boosted autowave travels in an accelerated way and not with a constant velocity. Qualitative observations suggest that intervals of propagation with a nearly constant velocity interchange with intervals of acceleration when parts of the front move rapidly forward with jets occurring in the flow.

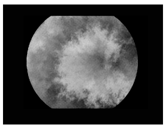

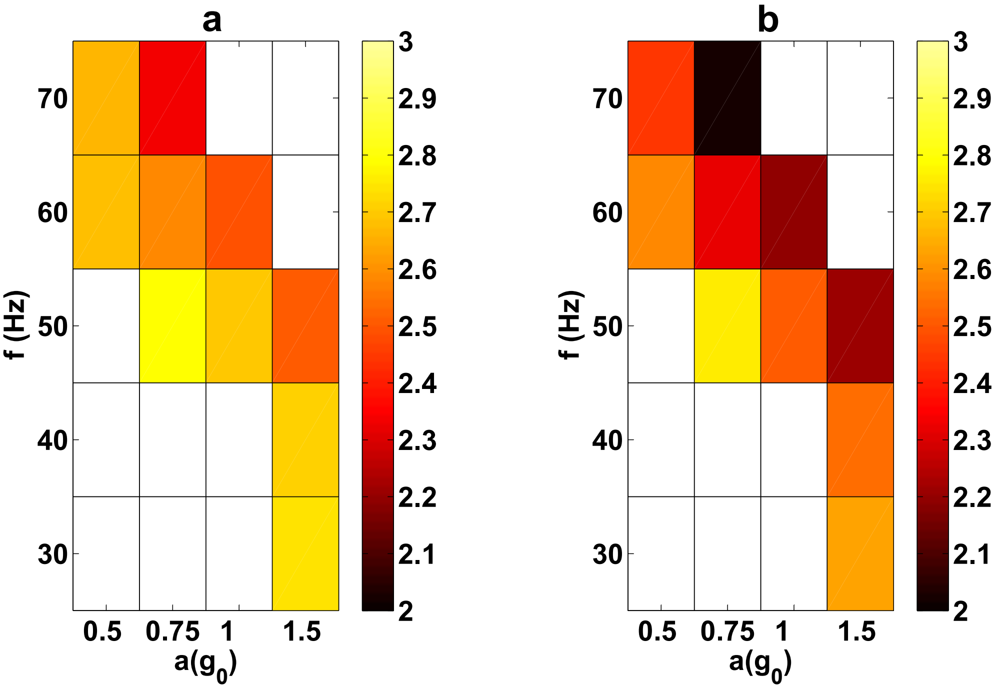

Fig. 5.9: Heavy-tail exponent $\mu_r(\Delta t)$ obtained from jump length distribution of the reaction front. The exponent decreases for higher forcing (in frequency and in amplitude) and longer times (a) $\Delta t = 1/60$ s, (b) $\Delta t = 2/60$ s) which indicates that the probability to make a long jump increases. For all boosted autowaves analysed the exponent is in the range $2 < \mu_r(\Delta t) < 3$ and thus superdiffusive propagation of the front is expected. A single boosted autowave that propagates through the whole reactor can only be observed for a confined range of the forcing parameters (coloured fields).

5.5 Discussion

The quasi 2-dimensional flow produced by the Faraday experiment experiences a transition from normal diffusion to superdiffusion around a forcing frequency of 30-40 Hz $(a = 1g_0)$. This has been shown by analysing the trajectories of micro-particles applied to the flow at different forcing frequencies. Two different analysis techniques were used: application of concepts from CTRW theory and direct measurement of the variance growth.

The BZ reaction subjected to the Faraday experiment exhibits important structural changes in dependency of the forcing parameters. For a limited parameter range a single boosted autowave can be observed that propagates

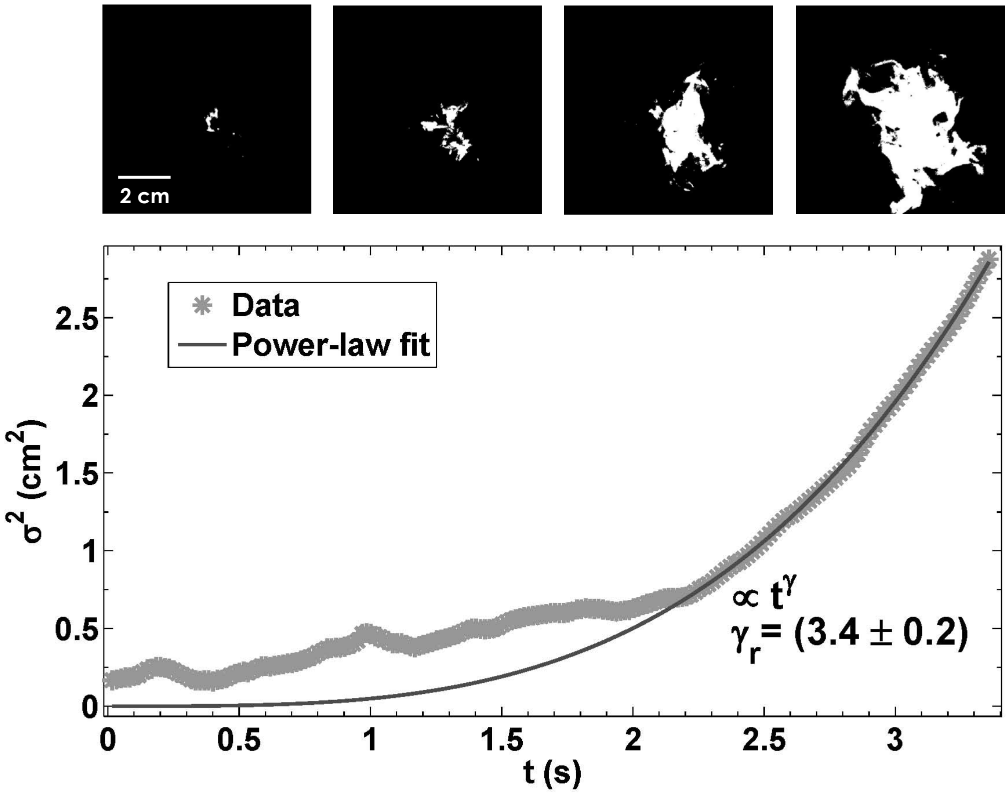

Fig. 5.10: Variance growth of a centred reactive wave (asterisks)(50 Hz, $a = 1\, g_0$). A power-law $\sigma_r^2(t) \propto t^{\gamma_r}$ with $\gamma_r = 3.4 \pm 0.2$ fits the data after a continuous spot has formed (continuous line). This indicates that the front of the boosted autowave propagates in an accelerated way in the superdiffusive flow. Top: Binary image series shows the expansion of the active spot ($\Delta t \approx 0.84$ s in between frames).

from one side of the reactor to the other. The propagation of the wave front is analysed with a masking algorithm that counts the number of excited pixels ahead of the front. Probability distributions for jumps of activator volumes perpendicular to the reaction front are obtained for different forcings. The distributions are well fitted by Lévy functions which allows for the extraction of heavy-tail exponents $\mu_r(\Delta t)$. These exponents are a measure for the probability of long jumps. A value $\mu_r(\Delta t) < 3$ indicates superdiffusion on the considered time scale. The values $\mu_r(\Delta t)$ decrease for higher forcings and longer times Δt which means that long jumps become more probable. Exemplary variance measurements for the boosted autowave show a variance growth in time that is supralinear which signifies that the wave front propagates accelerated and the front velocity increases with time.

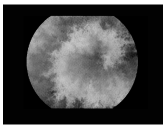

Comparison of the results obtained from particle experiments with the results from the analysis of the boosted autowave indicates that the onset of the superdiffusivity of the flow coincides with the occurrence of an boosted autowave. The transition of the flow from normal diffusion to superdiffusion observed with the particles happens around the same frequency (40 Hz, $a = 1\,g_0$) as the transition in the BZ reaction from filamentary patterns to boosted autowave occurrence. However, a direct quantitative comparison of the analysed variables (as the variances γ_{exp} and γ_r or the jump length distribution exponents μ_p and $\mu_r(\Delta t)$) from the particle experiments and the boosted autowave experiments is awkward for a variety of reasons. First, the microscopic description of a random walk with reaction differs from a description of a passive random walk, because there is an additional reaction probability for the activator. To our knowledge such statistical descriptions of random walks with active media exist only for bistable reactions [160–162, 173, 174] and not for oscillatory or excitable media as we have studied in our experiment. Second, the suggested analysis of the reaction front using the masking algorithm is only valid for short time steps Δt when the overall shape of the front between two images has not changed much. Therefore, the exponents $\mu_r(\Delta t)$ depend on the time step and can only be reliably derived for short times Δt. In spite of this limitation, the masking algorithm can be an option for the description of the dynamics of systems where variance growth measurements are not practicable. Especially the application of the masking algorithm to the reactive waves occurring in bigger reactors or in nature might be worthwhile where it can be unfeasible to capture the whole reactive wave with a sufficient spatial resolution. In particular, when length and time scales of practical importance are small compared to the scales of the entire reactive wave, the propagation of the irregular front can be characterized by the masking algorithm. Possible applications could be waves in geophysical flows like plankton blooms in the ocean [23] or depletion of ozone layer [175], among others.

5.6 Conclusion

In conclusion, we have found that the quasi two-dimensional flow in our reactor is superdiffusive on certain time and length scales for some forcing parameters. In a BZ reaction subjected to this flow a boosted autowave occurs that propagates with accelerated front velocities for short length and timescales. The local propagation of the wavefront can be characterized by an exponent $\mu_r(\Delta t)$ which defines the probability for large jumps of activator volumes perpendicular to the reaction front. In consideration of the results from the last chapter, Chap. 4, we can further conclude that the accelerated growth of the wavefront must be limited, not only by the limits of the container, but also by the preceding autowave. As we have seen various times in our BZ recipe the inhibitor reaction is much slower than the forward reaction and thus it is likely that the backward reaction 'sees' a well developed normal diffusion process. When a new autowave forms, it first expands rapidly on fresh reactants but then it will eventually be stopped by the well mixed decaying tail of the former autowave.

6

A simple Model: Active Media and Superdiffusion on a Network

Motivated by our experimental findings on active and passive media in the turbulent Faraday flow, we present a numeric study consisting in a simple excitable cellular automata on different network geometries. In particular, we choose the edges of the network in function of the separation of the nodes either from a Gaussian random distribution or a power-law random distribution, latter we call a geographically scale-free network. We find that the power-law exponent of the geographically scale-free network, in combination with maximum jump length cut-off value, plays an important role for the characteristics of the excitation wave. We show that front dynamics and pattern formation on the geographically scale-free networks differ from those with finite scale (Gaussian) by using Fourier analysis and the masking analysis technique used on the experimental data in the previous chapter, Chap. 5. We compare the propagation of the modelled reaction front with the dynamics observed in the experimental reaction-diffusion-advection system introduced in the previous chapters and with results from fractional diffusion theory.

6.1 Introduction

Many real world problems, e.g., plankton blooms in the ocean, the spread of epidemics, or combustion in reactors, involve simultaneous transport- and reaction dynamics. Mathematically, these type of systems are frequently described by reaction-diffusion-advection (RDA) equations. Unfortunately, the exact details of the transport process involved are often both, difficult to measure and intricate to model. It is therefore widespread practice to describe the transport as a diffusive process, relying on the hypothesis that the objects of interest experience a mathematically manageable random walk [176].

Turbulent transport in fluid flows often shows spatial intermittency, i.e., after some time t the distribution of particles previously released together at $x_0(t_0)$ is non-homogeneous in space [45]. In real world turbulent transport problems, such as oil spill control or atmospheric contamination, the knowledge about this intermittency can be crucial for live saving steps like environment protection or evacuation plans. The type of clustering in the cloud of particles, or tracers, cannot be detected using typical transport measures such as absolute and relative dispersion. Only with the knowledge of the whole particle probability density function (pdf) at each time step we can predict if the tracer accumulates at certain spots and accounts for the filamentary structures formed by tracers in chaotic and turbulent flows. Diffusion parametrization of such flows using limit theorems can thus never account for many intermittent phenomena observed in real flows. This is also seen from the results obtained in Chap. 4 and Chap. 5 where the filamentary structure of the chemical wavefront cannot be accounted for by mere enhanced turbulent diffusion, but is tightly coupled to the filaments occurring on certain timescales in the flow. In order to statistically represent the filaments, spatially dependent many particle measures, i.e., the relative separation of a particle cloud with regard to its centre or the Finite Size Lyapunov Exponent (FSLE) can be applied [45]. Nevertheless, this measures do not facilitate the parametrization in order to derive a simple expression for the spread of the cloud. Whenever active tracers, like a chemical reaction or biologic matter are involved, the transport on the timescales of the active renewal process is crucial to determine the overall shape and spread of the active media.

Our experimental observations of passive particles in the turbulent Faraday flow as described in [20, 21], Chap. 4 and Chap. 5, give some evidence that the particles subjected to the flow experience jumps that are distributed as power law tails. Thus, transport might be modelled by scale-free transport as was the idea of references [70, 157] (see also Sec. 1.2.3). Here, we adapt the statistical transport viewpoint and try to model the spread of an active tracer subjected to turbulent transport by a scale-free jump probability distribution function. To accomplish this we use a network approach with geographically scale-free connections. We call connections geographically scale-free when the probability of connections of two nodes is described by a power-law depending on their distance r, $p(r) \propto r^{-(\mu)}$, with a finite cut-off b. Even though a network approach to model the complex turbulent transport will never allow a completely realistic study of the filamentary structure of the excitation patterns, it can help to understand the basic ingredients for a locally scale-free propagation of an excitation wave as found in the previous chapter (Chap. 5).

Motivated by our experimentally observed boosted autowaves occurring when an excitable chemical reaction is subjected to a turbulent flow, Chap. 4 and Chap. 5 [20, 21], we develop a simple model with excitable kinetics on this network. We study in detail, if the model is able to reproduce some of the observations obtained from the real experiments. The simplistic cellular automata (CA) model that we employ helps us thus to learn about the underlying principles causing the details of the spread of the reaction front. We will show that the overall spread is limited by the finite cut-off value b, while the local front expansion reflects the scale-free connectivity of the network. The local expansion is thereby derived in the very same fashion as in the previous chapter, Chap. 5. Comparing the results from networks with Gaussian connectivity and those with power-law connectivity, we find that also the complicated spatial structure and the space time-plots of the power-law case resemble more closely the experimental observations.

6.2 Numerical Ansatz - A Cellular Automaton on Different Networks

In order to understand what the basic ingredients for a phenomenon like the experimentally observed boosted autowaves are, we chose to simulate an excitable dynamic system as simple as possible, but with the ability to produce spatio temporal patterns like the molecular spiral and target autowaves: A cellular automata (CA). Our model is a slight modification of the model originally introduced by Markus and Hess [177], especially here we use different network structures. We introduce the rules for our CA considering generic neighbour connections between the cells rather than nearest neighbour ones, because this will give us the freedom to let the system evolve on different network structures, which we will discuss subsequently.

6.2.1 The Cellular Automaton

We use a modified version of an excitable CA model first reported in [177] using a randomized cell discretization to achieve an isotropic wave propagation in all directions. Importantly, the phase space and time are discretized in the CA models.

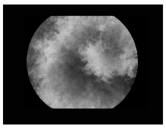

Basic CA Algorithm

The basic CA algorithm as introduced by [177] calculates a status $S(t)$ for every cell and every iteration. This status $S(t)$ can be receptive (1), recovering (2) or excited (3). The time for this model is discretized as such that the transition of a cell from a recovering to an excited state takes 1 timestep while the back-transition has a much slower dynamic and takes more iterations. In the original model there are $n+2$ states (including zero) where the $S(t)=0$ is the receptive state and $S(t)=n+1$ is the excited state. All other states are recovering states. The model has three more parameters, S_{max}, m_0 and p which are introduced below. S_{max} defines a threshold for the state, above which a cell cannot be excited (excitability threshold). This actually defines a limit on the refractory time of the system $t_{ref}=n+1-S_{max}$ rather than $t_{ref}=n+1$ as was stated in the original version [177] (their statement is obviously only true for $S_{max}=0$). Each cell i is connected to N neighbours and in dependence of their neighbour-statuses $S_{j\neq i}(t)$ and their own $S_i(t)$ status the cells state is updated every iteration step according to the following rules:

1. If $(S_i(t) \leq S_{max}$ and $\nu(t) \geq m_0 + p * S_i(t))$, then $S_i(t+1) = n+1$ (the excited state); Here $\nu(t)$ is the number of excited neighbours at time t and m_0 and p are two control parameters, regulating the details of the excitation.

2. Else if $(S_i(t) = 0$ and $\nu < m0 + p * S_i(t))$ then $S_i(t+1) = 0$.

3. Else: $S(t+1) = S_i(t) - 1$.

We want to stress the fact, that in the original model as introduced here, only excited neighbours can cause excitation of a cell. At the same time this also implies a strong restriction on the temporal dynamics of the system: Each cell is only able to excite its neighbours during one iteration step and then it has to go through the whole refractory process before being able to excite again. This behaviour does not reflect the experimental observations which show that excited parts of the fluid are able to excite neighbouring unexcited parts during a considerable timespan and thus we will adapt the dynamics of the CA to fit our needs (see below Sec. 6.2.1). After all cell statuses are updated in the above described manner the result is further smoothed by an averaging procedure. The status of each cell is then finally defined by the average over all the statuses of the neighbours of each cell including the cell itself. When a cell has the status $S_i(t+1) = 0$ or $S_i(t+1) = n+1$ it is excluded from averaging because numerical instabilities can occur [177]. The single cell dynamics resulting from the algorithm are visualized in Fig. 6.1.

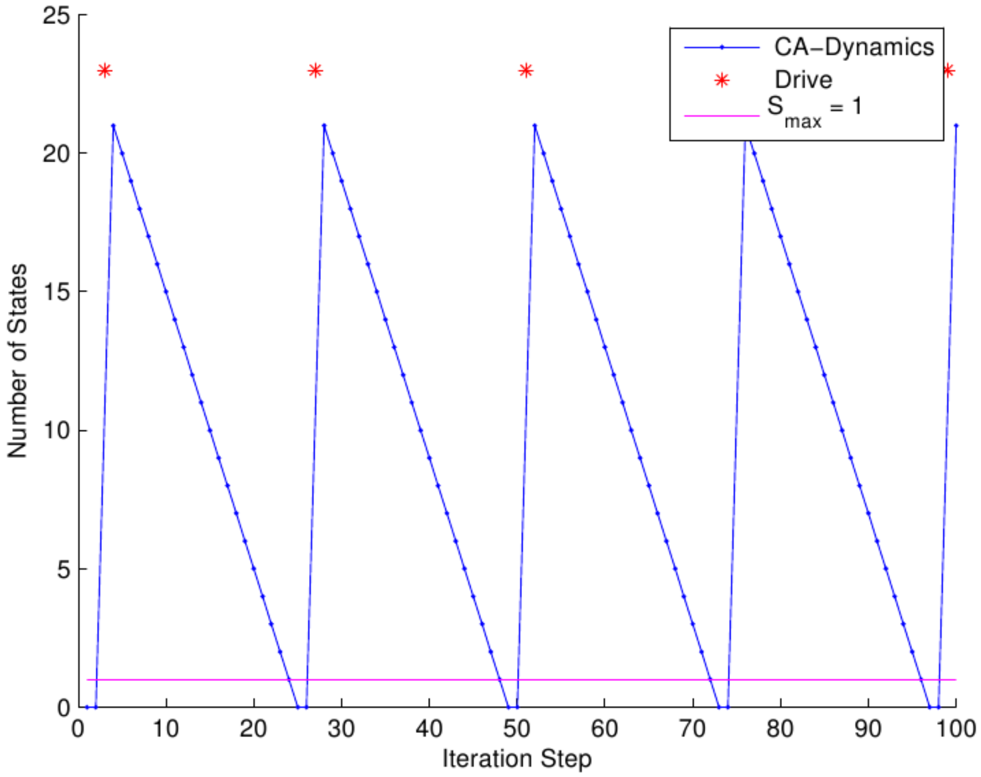

Fig. 6.1: The dynamic of a single cell following the rules explained in the text. The red stars (*) indicate an external drive exciting the cell which can be interpreted as the influence of neighbouring excited cells. The temporal dynamics of the excitation is $\Delta t = 1$ iteration step. The refractory period depends on the total number of states here 22 with $n = 20$, and the value of the excitability threshold, here $S_{max} = 1$.

Changing the Excitation Dynamics of the CA by introducing another Threshold

As we pointed out above, the discretisation of the time and especially the existence of solely one excited state is a crucial limitation for the dynamics we try to reproduce , because it means that neighbouring cells can only be in an excited state at the same time, when they become excited at the very same time step. From our experiments with the Belousov-Zhabotinsky reaction we know that this would not reflect the dynamics we want to study since the fluid parcels remain in an excited state for a finite time which allows for an excitation of nearby unexcited fluid. We therefore modify the CA as introduced by [177] by allowing more than one excited state. We change the algorithm in a way,

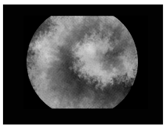

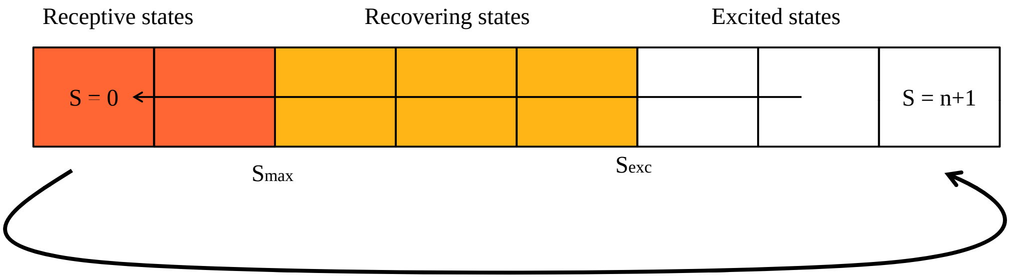

Fig. 6.2: The schema visualizes the modification we added to the Cellular Automata (CA) introduced by [177]. Symmetrical to the excitability threshold S_{max} we added a second threshold S_{exc} above which all states are excited and thus able to excite neighbouring cells. States are still counted down each iteration step $S_i(t+1) = S_i(t) - 1$ and thus the single cell dynamic does still look the same, see Fig. 6.1, even though the network dynamics changes drastically.

that every state $S_i(t+1) \geq S_{exc}$ is an excited state, where $S_{max} < S_{exc} < n+1$ is in between the excitability threshold and the maximal state. The schema of the CA is then as shown in Fig.6.2

Parameters of the CA

In total, the CA we use has five control parameters: The excitation regulating parameters p and m_0, the total number of states $n+2$ (including 0) and the two thresholds regulating the refractory time S_{max} and the time that a cell can excite others S_{exc}. There is also another "hidden" parameter that is the smoothing applied after the states $S_i(t+1)$ have been updated. In the original work by [177] the cell $S_i(t+1)$ is excluded from smoothing if the former state $S_i(t)$ is either 0, 1 or $n+1$. As we amplified the number of excited states introducing the parameter S_{exc} we excluded all states $S_i(t) > S_{exc}$ from the smoothing procedure as well.

6.2.2 The Networks

The CA was run on two different network realizations whose algorithms are discussed in detail below. The differences in the patterns that develop will be discussed in the next section. A short introduction to the nearest neighbour connection network as used in the original model [177] is given for comparison.

Nearest Neighbours with Circular Neighbourhood

Reference [177] uses a randomized two-dimensional grid and a circular neighbourhood to achieve isotropy of the patterns that form. This means that each cell is connected to every other cell that lies within a circular neighbourhood of radius R. Fig.6.3 visualizes this procedure.

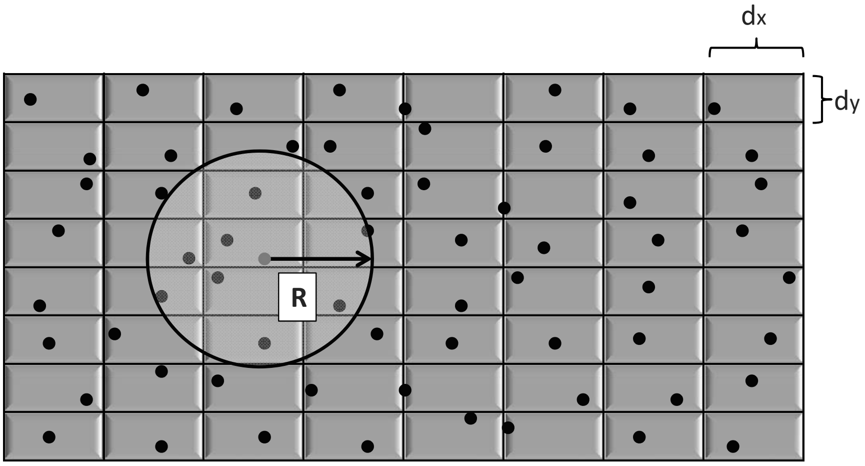

Fig. 6.3: In the original model the cells lie on a randomized grid and are connected to every cell in a circular neighbourhood within a radius R [177]. The lattice constants d_x and d_y were chosen to be $d_x = d_y = 1$ for our study.

We checked for the reproducibility of the spiral and target patterns reported by Markus and Hess [177] and ran the simulations in two dimensions using this network connectivity. If the original initial conditions are chosen, targets and spiral waves are obtained. See Fig. 6.4 for the example of a target wave. The algorithm that we used to produce such a nearest neighbour network connectivity is straightforward and will not be elaborated upon here.

Reconnected Networks

The usual procedure to obtain differently connected networks consists in the reconnection of the circular nearest neighbourhood network. We will not use this procedure in this study, because for the network sizes we work with it would be much too slow. We will use a method taking advantage of the reconnectivity matrix, described below. However, since the approach we choose tries to capture all of the characteristics of a fully reconnected network, we will explain the procedure here shortly. The reconnection algorithm is an adapted version from [178] and is based on the following rules:

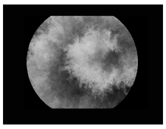

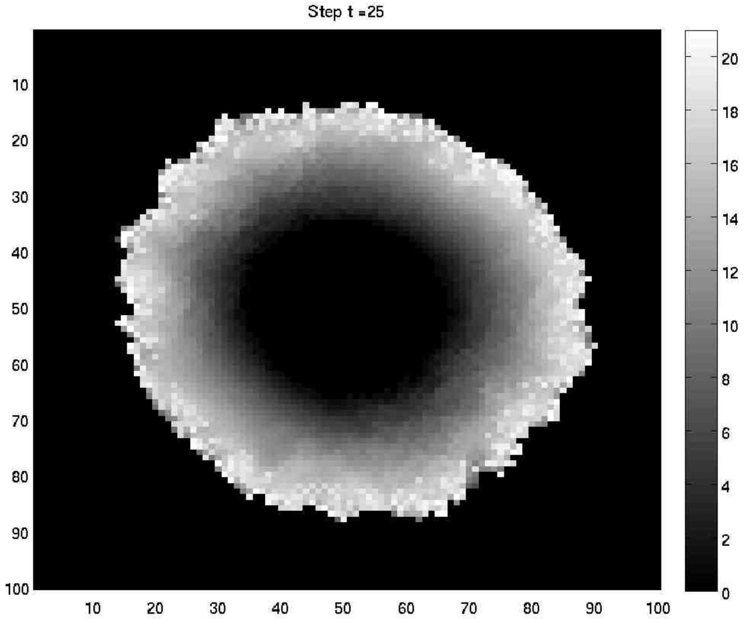

Fig. 6.4: Example of a target that develops from a square initial condition in the centre of the numerical domain as originally reported by [177]. The ripples at the border of the target stem from the random distribution of the cells within the grid as explained in Fig. 6.3. The parameters here were the following: $S_{max} = 0$, $S_{exc} = 16$, $S_{max} = 0$, total number of states 22 (including zero), $m_0 = 1$ and $R = 2$.

1. A arbitrary cell $C_{i,j}$ of the network is picked to be randomly reconnected to another cell of the network. One of its circular neighbourhood connections is then randomly chosen to be removed. This procedure preserves the total number of connections (or edges) within the network,thus rendering it impossible that this number has impact on the results.

2. In the case of the distance dependent connectivity-networks a random number d, representing a distance, is drawn from a specified probability distribution (Gaussian or power-law). From all the cells $C_{k,l}$ in the network which satisfy $|C_{i,j} - C_{k,l}| = d$, $d \neq 0$, one is randomly picked and a new connection (edge) is established. For small-world networks the connectivity does not depend on the distance and thus the procedure is greatly simplified by just randomly picking any cell $C_{k,l}$ from the network for a new connection.

3. The procedures described in 1. and 2. are repeated until q parts of the

former connections $N_{conn} = 2 * N_{edge}$ are rewired. The factor 2 comes from the fact that here the network is bidirectional. This means that every edge is actually a two way street where information (or excitation) can pass in both directions. The value q is called the reconnectivity.

The Adjacency Matrix

The connections in between the different cells in a connected network can be visualized with the adjacency matrix $A = a_{i,j}$ of size $N \times N$, where N is the number of cells. $a_{i,j}$ is one when there is a connection in between node i and node j and zero if there is not. We use the concept of the adjacency matrix here instead of the slow process of reconnecting all edges, yielding $q = 1$, to obtain the desired distribution of connections, i.e. Gaussian or power-law in space. We construct an adjacency matrix where connections are drawn from a probability distribution $p(r)$ depending on the distance r, as such that each point has in principle the same out degree $k_{out} = const$. Since we use open boundary conditions, some out-connections of each cell might be outside the numerical domain and will thus reduce the actual degree of the cell. Due to this open boundary conditions especially cells close to the border of the domain are affected and have an actual out degree $k_{out} \leq const$. In order to handle very large networks the adjacency matrices are numerically treated as lists but for small networks they can be easily visualized, see examples for networks with 30 cells in Fig. 6.5.

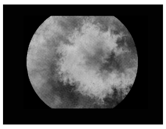

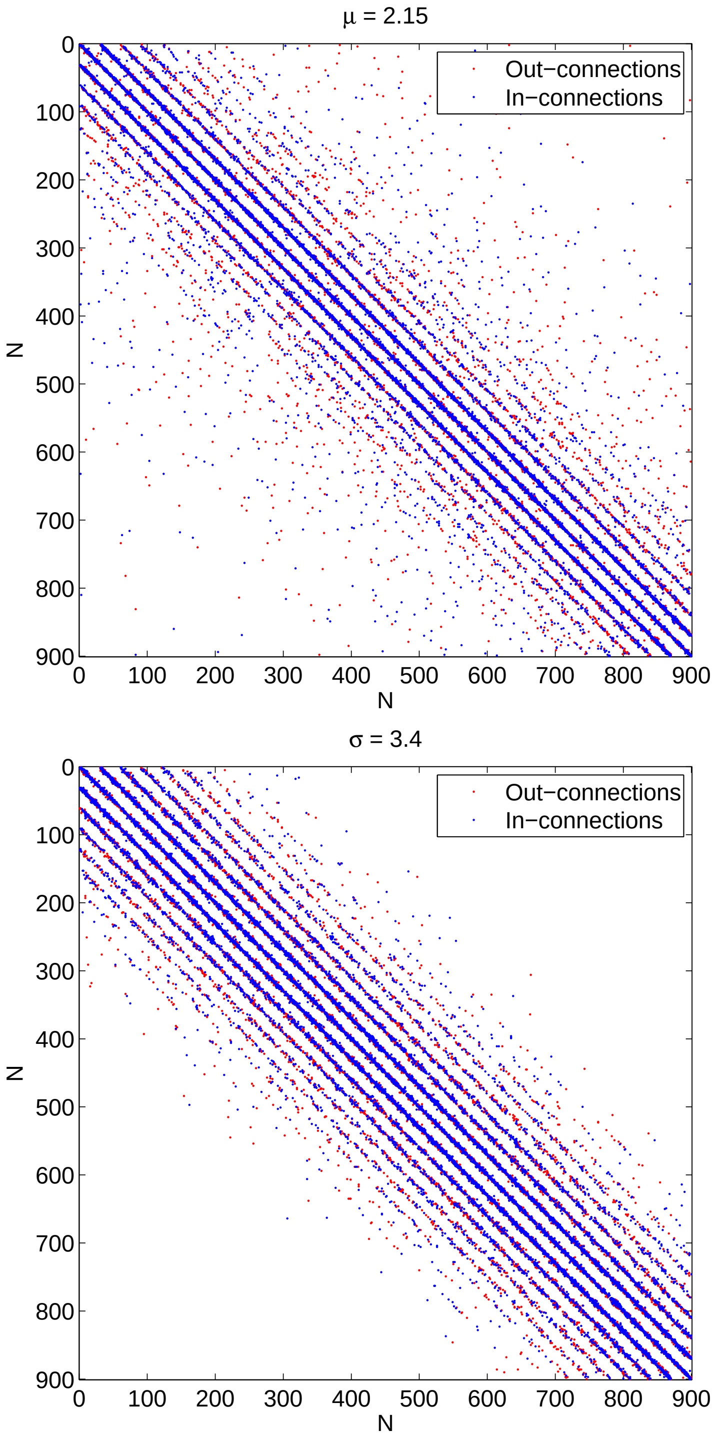

Fig. 6.5: The adjacency matrices for the in- and out-connections of each node are constructed from a power-law (upper panel) and a Gaussian (lower panel) distribution. The parameters were: μ and σ as indicated, $N = 30 \times 30$ and for the power-law cut-off value $b = 100$.

Geographically Scale-Free Network or Power-Law Network

To construct the network with power-law distributed connectivity we use the inverse method [179] in order to draw the random numbers constituting the distances at which to find a neighbour for a new connection. We call this network a geographically scale-free network to distinguish it from the *scale-free* network used in the literature, where the term *scale-free* refers to the degree distribution [180]. In short, we want to obtain a power-law function of distance r for the distribution of neighbours:

$$p(r) \propto r^{-\mu} \tag{6.1}$$

Certainly, this function does not supply us with the random number we need to draw to establish a connection and we need to perform a few more steps. Using the inverse method, we can create a non-uniform random number generator from this function and an arbitrary uniform random number generator [179]. The first step is the calculation of the cumulative distribution function on an interval $[a, b]$:

$$Y = P(r) = \int_a^r Cp(r')dr' = C\frac{1}{-\mu+1}\left(r^{-\mu+1} - a^{-\mu+1}\right). \tag{6.2}$$

where $a \leq r \leq b$ and C is the constant derived from normalizing the power-law probability distribution to unity. We can now calculate the inverse function of $P(r)$ yielding:

$$r = (b^{-\mu+1}Y + a^{-\mu+1}(1-Y))^{1/(-\mu+1)} \tag{6.3}$$

If we now draw Y from a uniform distribution on the interval $[0, 1]$ we find the desired random numbers r having a power-law distribution. In order to generate the uniform random number Y, we used the pseudorandom number generator Mersenne Twister [181, 182]. In summary we then obtain three new parameters in the model, μ, b and a. We will vary only the former two and leave the lower bound $a = 1 = const$. An example of the connections drawn from this procedure can be found in Fig. 6.6.

Gaussian Network

The Gaussian distributed connectivity is achieved by drawing a random number from a Gaussian random number generator which is part of the Mersenne Twister class used here [181, 182]. An example of the connections drawn from this procedure can be found in Fig. 6.7. the resulting Gaussian probability distribution reads:

$$p(r) = \frac{1}{\sigma\sqrt{2\pi}}e^{-(r-\nu)^2/2\sigma^2} \tag{6.4}$$

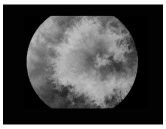

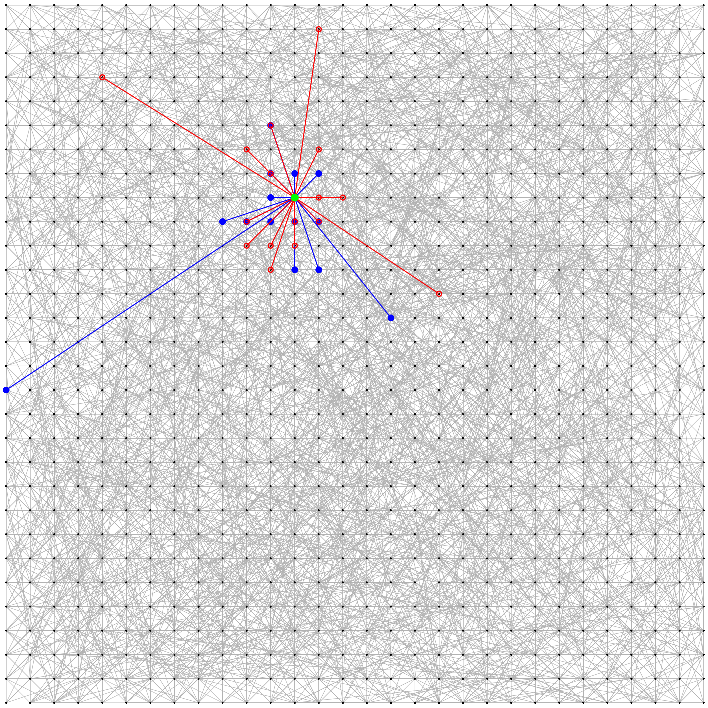

Fig. 6.6: The in- and out- connections from an exemplary cell in a geographically scale-free network (incoming connections in red, outgoing in blue). Note the few very long reaching connections. The connections between all cells are drawn in the back in light grey. For clarity the cells are plotted on top of the grid points and not at the randomized location as explained above in Fig. 6.3. The network shown here consists of 30×30 cells, $\mu = 2.15$, $b = 100$ and the maximal out-degree is $k_{out} = 20$. The resulting in- and out- degree distributions are shown in Fig. 6.9.

The new model parameters when using the Gaussian distribution are thus the standard deviation σ and the distribution mean ν, which we will set to $\nu = 0$ throughout the study.

Compare Networks

One can try to make the power-law network and the Gaussian network comparable in the sense that the typical neighbourhood sizes of a cell roughly coincide. To accomplish this we calculate the mean of the power-law distribution m_p (which is only possible because of the finite cut-off of the distribution due to parameter b, otherwise it would diverge) and use the value $\sigma = 1/2m_p$ as standard deviation of the Gaussian. The resulting distributions are shown in Fig.6.8

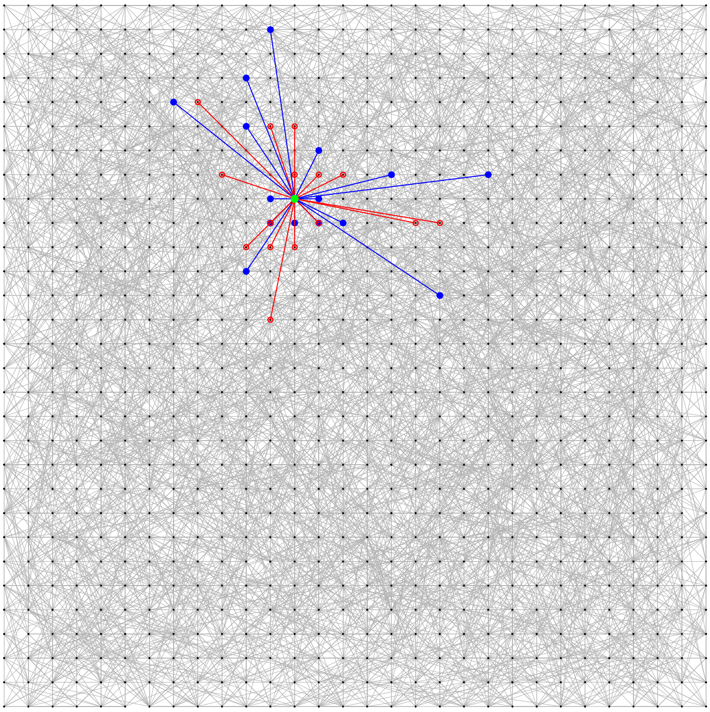

Fig. 6.7: The in- and out- connections from an exemplary cell in a Gaussian network (incoming connections in red, outgoing in blue). The connections between all cells are drawn in the back in light grey. For clarity the cells are plotted on top of the grid points and not at the randomized location as explained above in Fig. 6.3. The network shown here consists of 30×30 cells, $\sigma = 3.4$ and the maximal out-degree is $k_{out} = 20$. The resulting in- and out- degree distributions are shown in Fig. 6.9.

The Degree Distribution

The above procedure for the construction of the connectivity of the network leads to a degree distribution which depends on the parameters of the probability distributions chosen and the size of the network due to the boundary conditions. Figure 6.9 shows two examples of degree distributions for the two different network connectivities used: Connections drawn from a power-law or a Gaussian distribution.

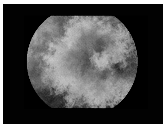

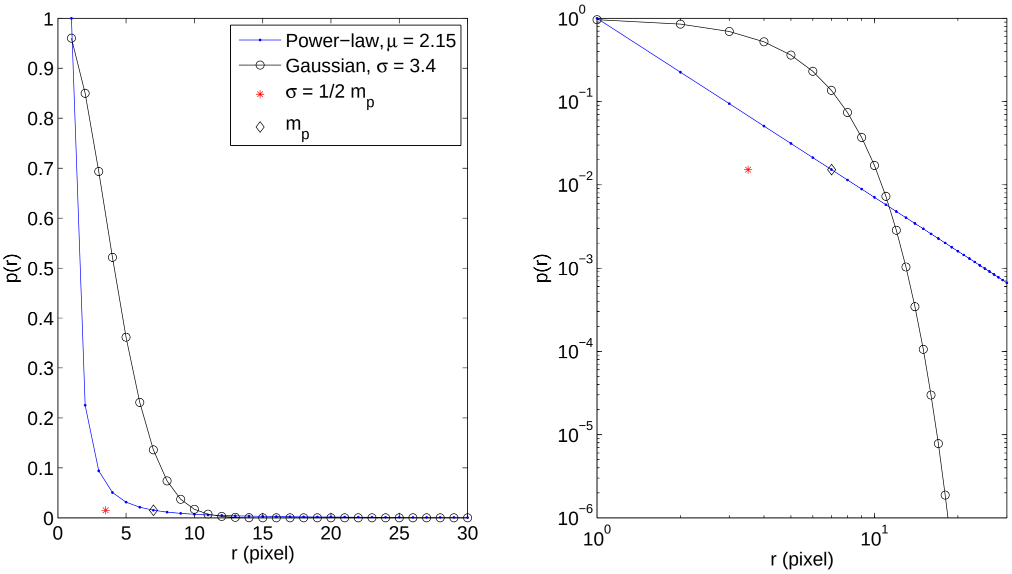

Fig. 6.8: The standard deviation for the Gaussian distribution was set to a value derived by the mean of the power-law distribution with cut-off b in order to yield comparable influence of both network connectivities in terms of neighbourhood size. In the double logarithmic plot on the right side, we can see that the power-law distribution has a tail which makes large displacements much more probable than for the Gaussian.

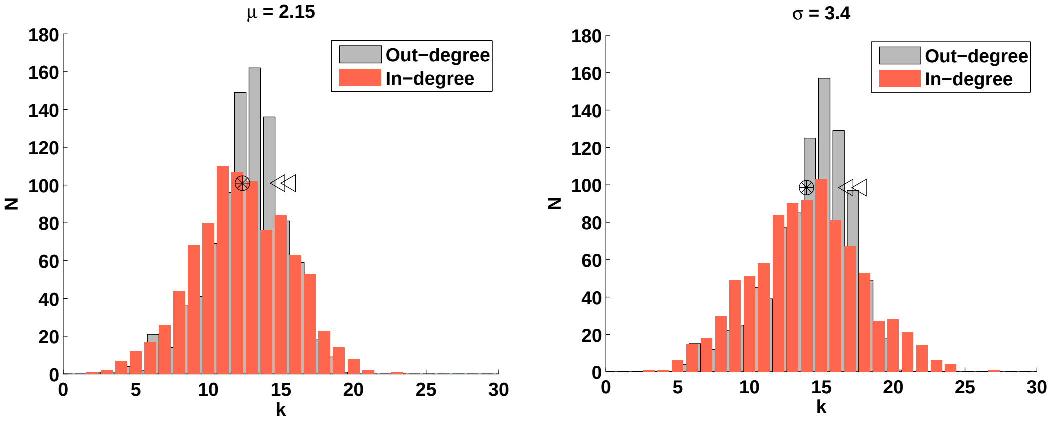

Fig. 6.9: The in- and out-degree distributions of the cells for connections drawn from a power-law (left) and a Gaussian (right) distribution. The mean and the standard deviation of the distributions are indicated by the star-circles and the triangles. The node degree was originally set to $k_{out} = 20$ but due to the boundary effects in a small network of 30×30 most of the cells have fewer connections. The in-degree of a cell was not limited.

6.3 Results

Our simple CA model on a geographically scale-free network can be used to study what happens, when excitable dynamics are combined with scale-free transport. Since there is some experimental evidence that transport in the Faraday flow can be described by scale-free transport in a range of scales we expect that our model will at least partly reflect the observed dynamics of the chemical reaction subjected to the turbulent Faraday flow. We contrast the results from the geographically scale-free network with those from a Gaussian network.

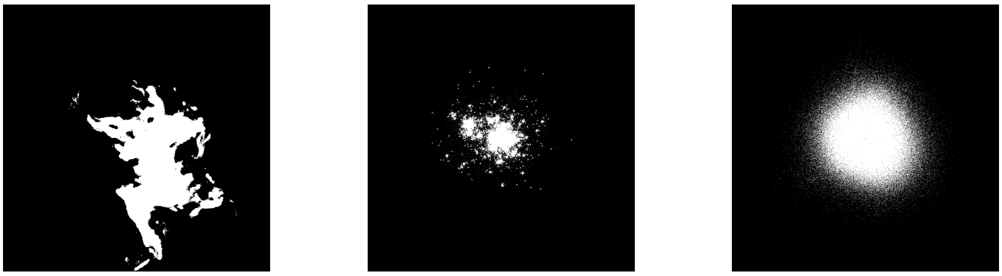

Fig. 6.10: Images of the excitation waves for the experimental system, the power-law network, and the Gaussian network (from left to right).

6.4 Spread of Activation in Gaussian and Power-Law Networks

We introduced networks where the probability of a connection between two cells depends on their distance, namely via a Gaussian or a power-law distribution function. Especially in the case of a power-law distribution we obtain activation patterns which, at a first glance in Fig. 6.10, show some similarity with those observed experimentally in that there are structures of multiple scales. In the simulation on a Gaussian network on the other hand, there are only two typical scales, the scale of a single pixel and the scale of the Gaussian blob. This observation by eye is further confirmed by the amplitude spectra derived from the Fourier transform of the images, see Fig. 6.11. Fourier analysis is a natural tool to differentiate and classify patterns. The Fourier transform of the Gaussian activation pattern resembles a Gaussian while the spectra of the other two patterns rather resemble a power-law function.

The spread of the excitation is fundamentally different in both networks, as is visualized in the image sequences in Fig. 6.12 and Fig. 6.13. Both systems were

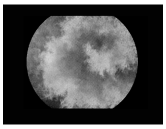

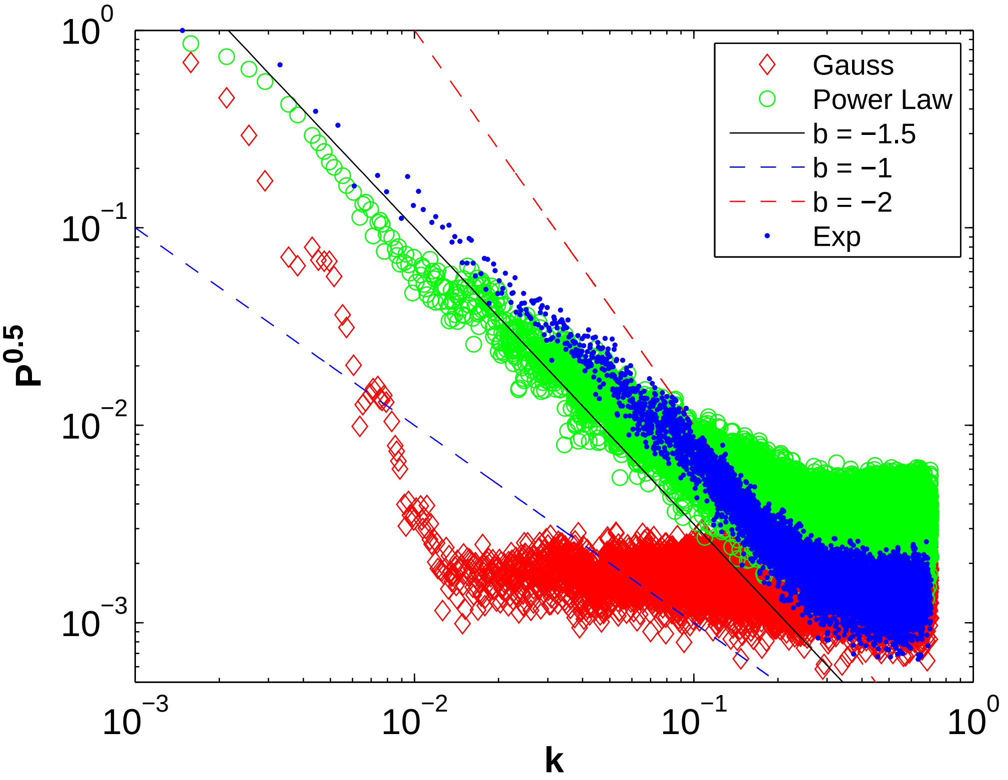

Fig. 6.11: Amplitude spectra of the excitation waves for the experimental system, the power-law network and the Gaussian network.

excitable without failure when only a few cells (here 4) were set to an excited state as a initial condition and both show a propagation of this excitation. In the case of the power-law network, the excitation pattern exhibits clusters and the spread of the excitation is intermittent and enhanced. In the Gaussian network there is no such clustering and the spread of the excitation seems to be more continuous.

In comparison to the experimental observations, it is to note that a simple network model with isotropic time-independent connections can never realistically describe the filamentary structure of active and passive tracers in a turbulent flow at one instance of time. Rather, a network model can intend to model the transport from a statistical point of view, that reflects the particle distribution function resulting from many experiments with passive or active tracers. Its advantage over the reaction-effective diffusion Ansatz are, besides its faster numerical performance, the possibility to chose the local transport process by using different network connectivities. Thus, the network approach is in some sense more flexible and even allows one to consider different transport mechanisms on different scales.

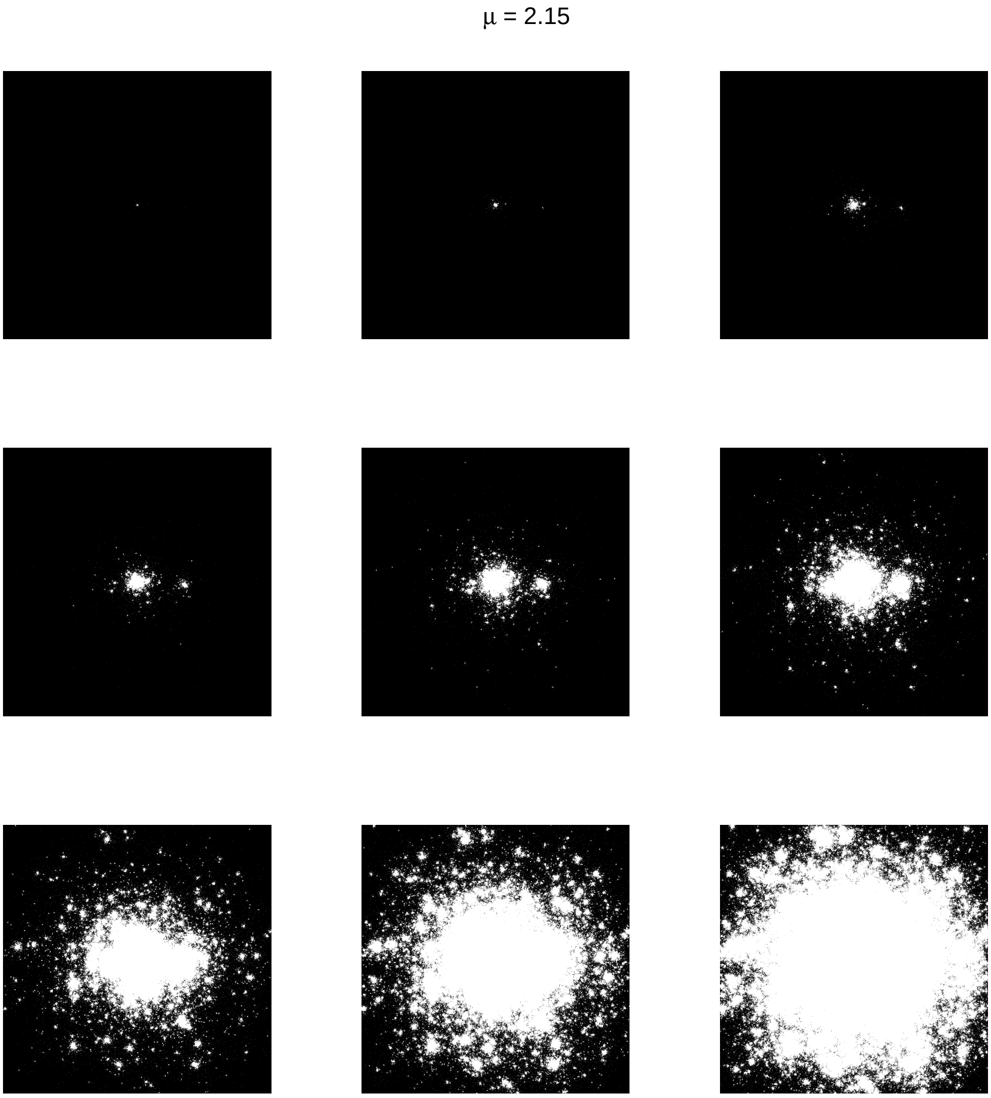

Fig. 6.12: A time sequence of one excitation wave travelling on the power-law network. Parameters: $\langle k \rangle = 20$, $\mu = 2.15$, $b = 500$, $dim = 1000 \times 1000$. Initial condition: 4 excited cells at the centre of the domain. The images are recorded at each $\Delta t = 1$ iteration step.

The most intuitive way of analysing the front propagation is the determination of the front velocity. The space-time diagrams for the front propagation on the Gaussian network and the power-law network in dependence on σ, the power-law exponent μ (with constant cut-off value b) and b (with constant μ)

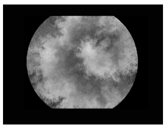

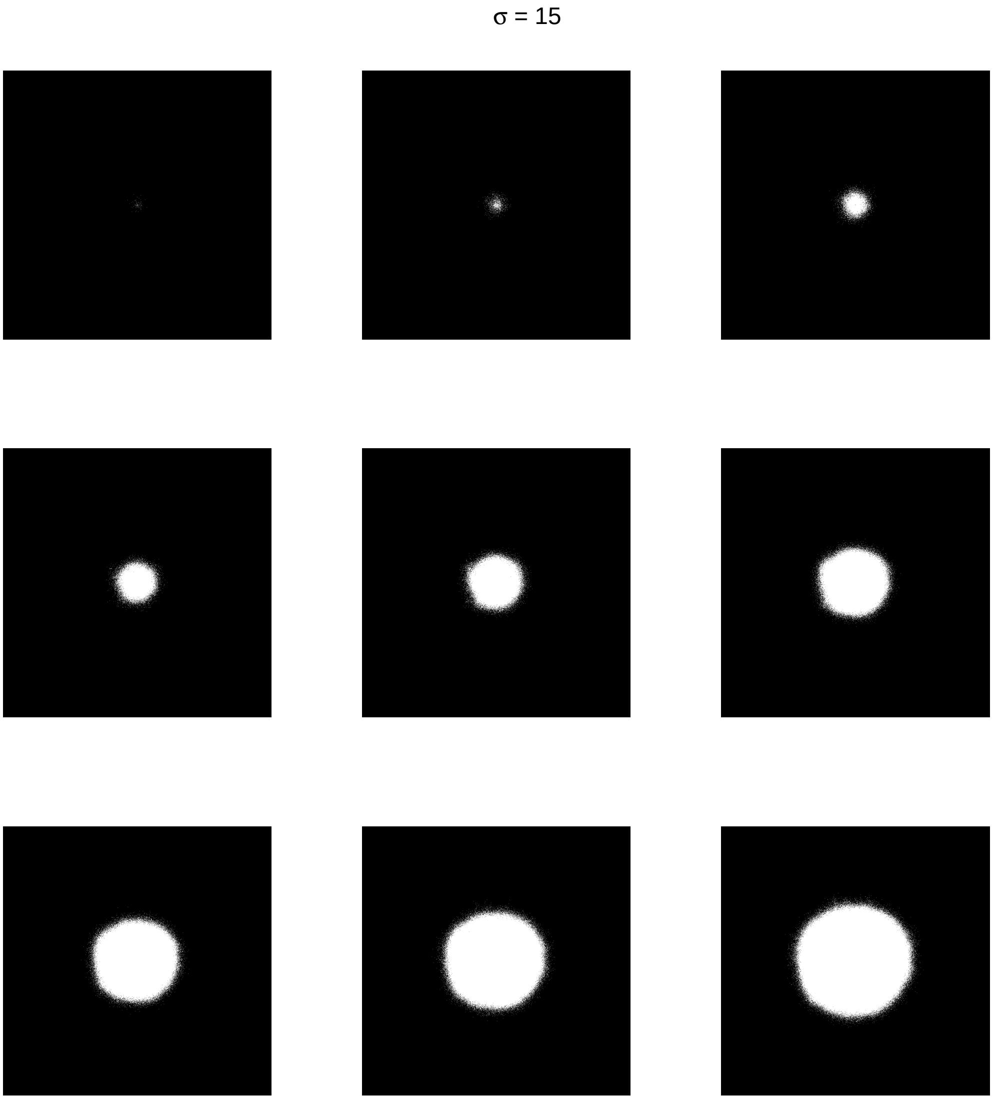

Fig. 6.13: A time sequence of one excitation wave travelling on the Gaussian network. Parameters: $\langle k \rangle = 20$, $\sigma = 15$, $dim = 1000 \times 1000$. Initial condition: 4 excited cells at the centre of the domain.The images are recorded at each $\Delta t = 1$ iteration step.

are shown in Fig. 6.15, Fig. 6.16 and Fig. 6.14 respectively. The mean velocities of the fronts are indicated as green lines. We find that the excitation wave front travels faster in the Gaussian network for larger σ. This is of course a trivial result and can be understood within the picture of reaction-diffusion systems as a mere increase in the diffusion constant. In the power-law connected network we see that the excitation wave front travels faster for lower values of μ which is expected due to the more pronounced tails of the distribution function for these values (Fig. 6.16). Further also a higher cut off length b, which causes the increase in the longest existing connections r_c, has a similar effect on the overall velocity of the front, see Fig. 6.14.

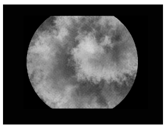

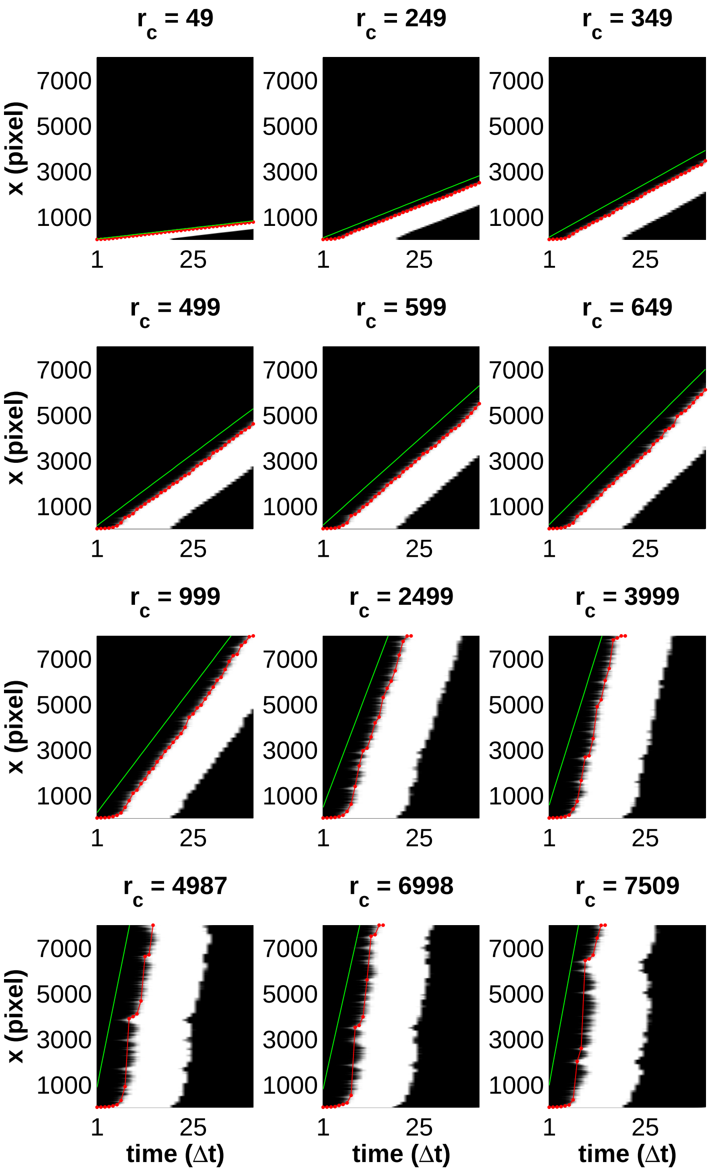

Fig. 6.14: Space time plot for the power-law network along the x-direction. The domain size (y,x) is 200×8000 pixel. The initial condition is a line of excited pixels of width $w = 1$ pixel along the y-direction so that the excitation spreads along the x-direction. An increase in the cut-off length b causes an increase in r_c, the maximal length of a connection occurring in the network. The power-law exponent was fixed to $\mu = 2.15$. The occurrence of *jumps* in the front increases with increasing r_c and thus the definition of a mean velocity becomes more intriguing. The *jumps* are indicated by the red dots while the mean velocity is indicated in green. The red dots were determined by using a threshold of $T = 0.8 \times \langle P \rangle_{max}$ the maximal excitation averaged along the y-direction (and thus $< P >_{max} = 200$). The results do not change qualitatively when threshold T is varied. The mean velocity was simply defined by the timesteps it takes until the red dots reach the end of the computational domain in x-direction.

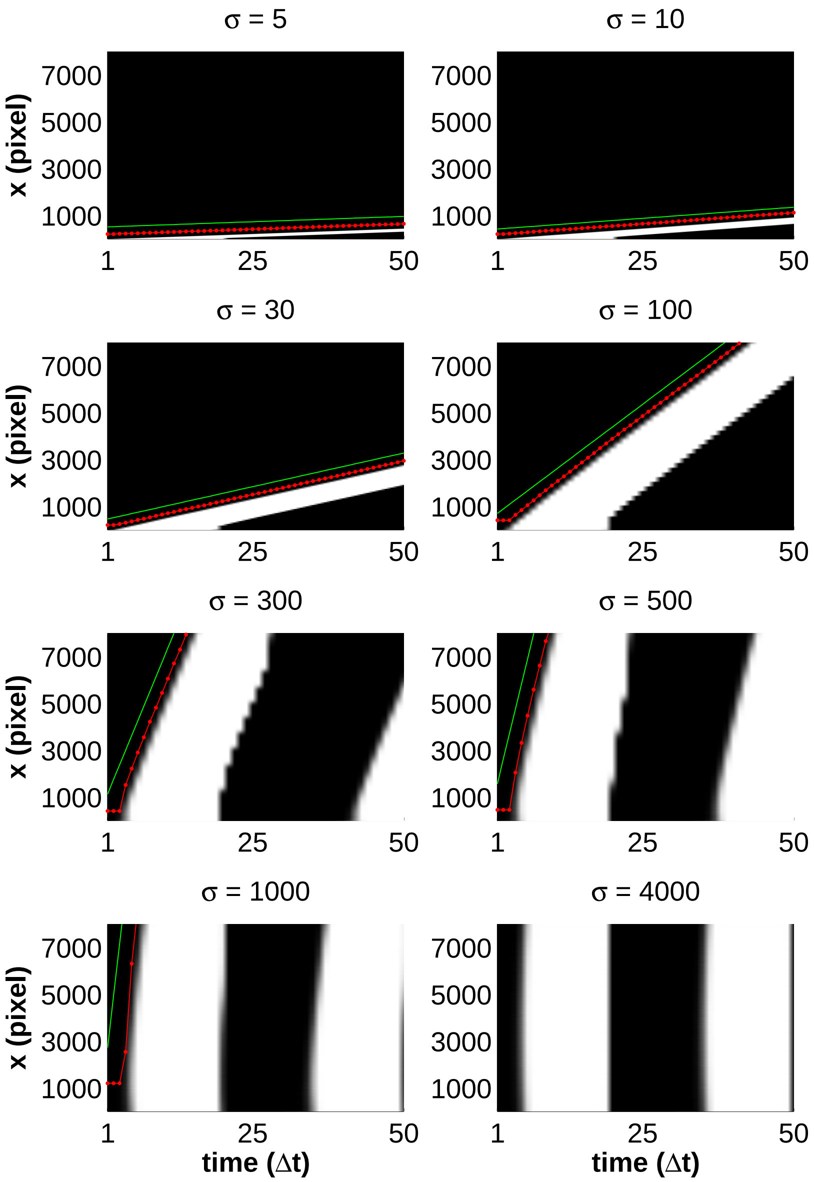

Fig. 6.15: Space time plot for the Gaussian network along the x-direction. The domain size (y,x) is 200×8000 pixel. The initial condition is a line of excited pixels of width 1 pixel along the y-direction so that the excitation spreads along the x-direction. In the Gaussian network there are no *jumps* but the propagation velocity of the excitation waves increases with increasing σ. The succession of the excitation front is indicated by the red dots while the mean velocity is indicated in green. The red dots were determined by using a threshold of $T = 0.8 \times \langle P\rangle_{max}$ the maximal excitation averaged along the y-direction (and thus $< P >_{max} = 200$). The results do not change qualitatively when threshold T is varied. The mean velocity was simply defined by the timesteps it takes until the red dots reach the end of the computational domain in x-direction.

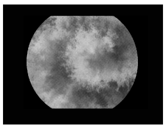

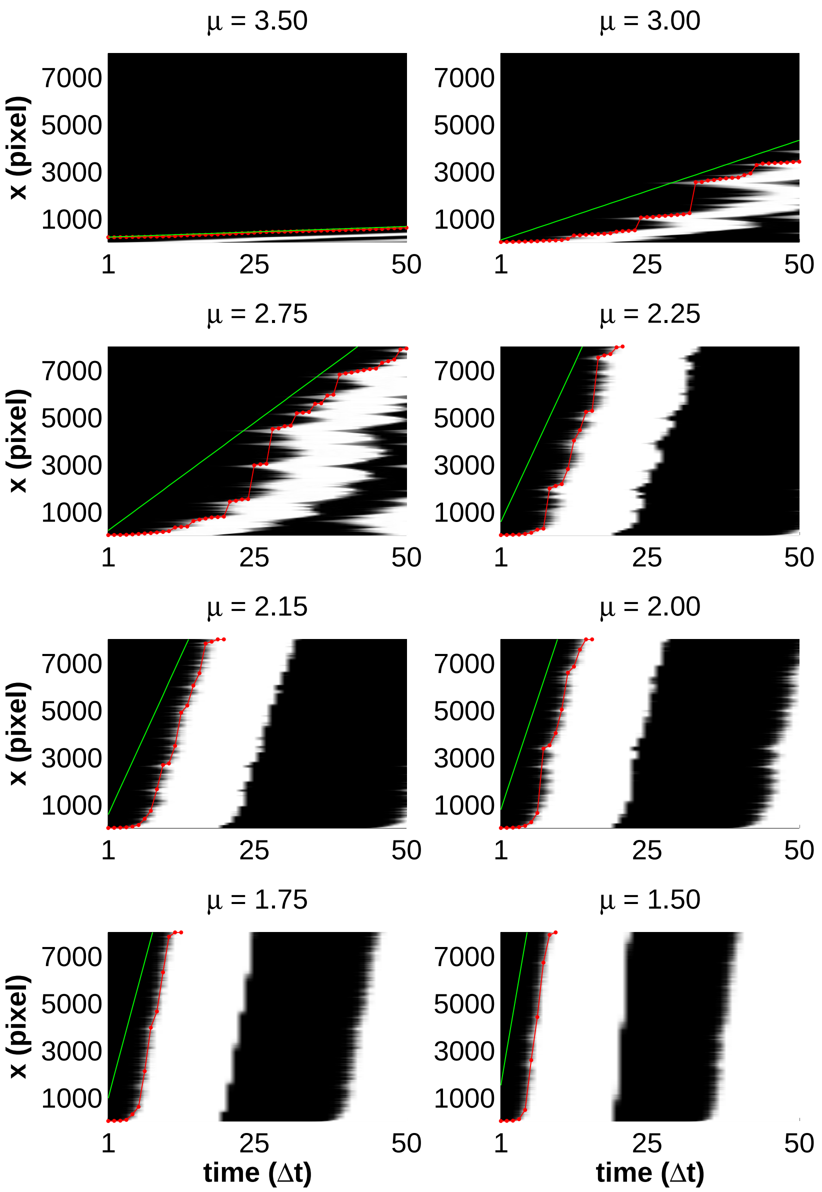

Fig. 6.16: Space time plot for the power-law network along the x-direction. The domain size (y,x) is 200×8000 pixel. The initial condition is a line of excited pixels of width 1 pixel along the y-direction so that the excitation spreads along the x-direction. Here we vary the exponent μ which causes an increase in the front velocity and the occurrence of jumps. For values of $\mu > 2.5$ the front is not well defined as the systems turns auto-sustainable, i.e., there are back connections in the network that facilitate an excitation of an area only recently excited. The cut-off value was fixed to $b = 3999$ pixel. The occurrence of *jumps* in the front increases with increasing μ. The *jumps* are indicated by the red dots while the mean velocity is indicated in green. The red dots were determined by using a threshold of $T = 0.8 \times \langle P \rangle_{max}$ the maximal excitation averaged along the y-direction (and thus $\langle P \rangle_{max} = 200$). The results do not change qualitatively when threshold T is varied. The mean velocity was simply defined by the timesteps it takes until the red dots reach the end of the computational domain in x-direction.

The velocities of the wave fronts in dependence of σ, μ and b are summarized in Fig. 6.17, Fig. 6.18 and Fig. 6.19

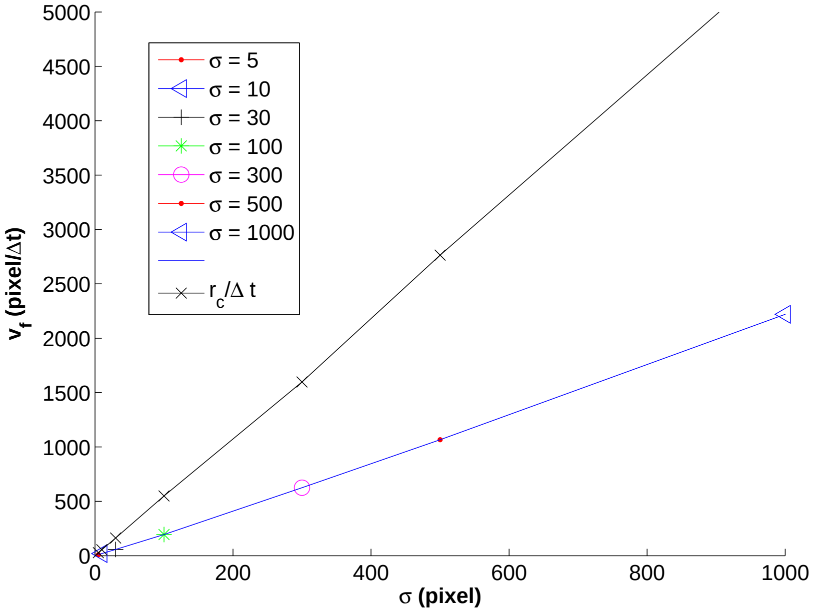

Fig. 6.17: The front velocity of the excitation wave in the Gaussian network depends on the standard deviation σ of the Gaussian distribution used to generate the network. This is a trivial result as a larger σ simply means that longer connections occur more often. Interestingly though, the mean velocity of the front is lower than the limit velocity $v_c = r_c/\Delta t$ allowed for by the longest network connection r_c indicated with blue crosses. This is in contrast to what was found in another study, where r_c determines the velocity [183].

The comparison of the mean velocities for the different networks shows us that we cannot differentiate between the underlying network type by merely looking at the mean front velocities. Nevertheless, we can learn something from the space-time plots. A closer look onto the time evolution of the fronts reveals jumps in the front propagation on the power-law network (indicated as red dots in Fig. 6.15, Fig. 6.16 and Fig. 6.14), similar to those observed in the Faraday flow experiments due to the filaments (Fig. 4.8 a,b). Figure 6.20 and Fig. 6.21 show the extracted values of these red dots, the front progression $x(t)$ vs. t for the Gaussian and the power-law network. Jumps are completely absent in the Gaussian case. For the power-law networks jumps are most pronounced for intermediate values of μ. This can be explained as follows: For small μ the tails of the power-law distribution become ever more important making large displacements more probable. Therefore, in this case and at a fixed mean

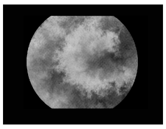

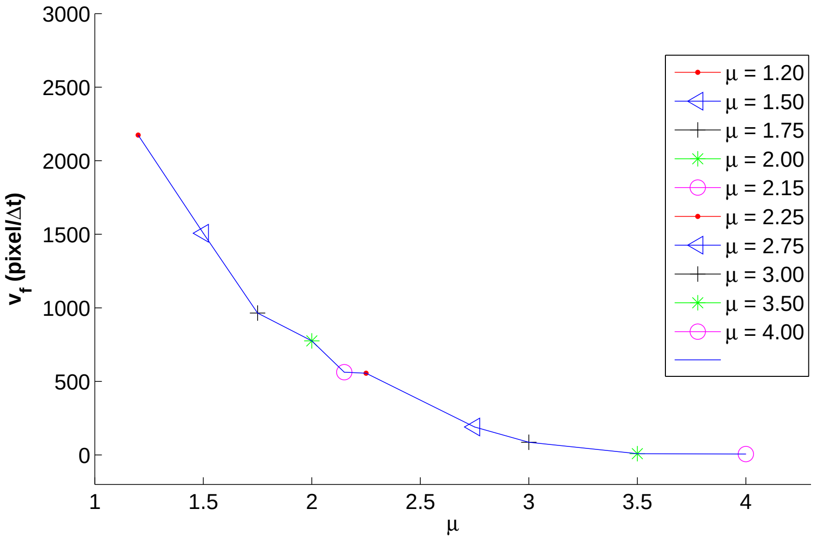

Fig. 6.18: The front velocity of the excitation wave in the power-law network in dependence on the exponent μ. As expected the velocity of the excitation wave increases for fatter tails coinciding with a smaller μ.

connection degree k, the spread of the excitation wave is limited by the cut-off value b, or equivalently the long connections in the network, as Fig. 6.14 shows. In contrast to this, for $\mu > 3$ the power law distributions rapidly decay to zero for large r (see also Sec. 1.2.3) and the cut-off value b does not play an important role anymore. For both cases of small and large μ there are thus no jumps, but rather a continuous propagation of the excitation front. Only for intermediate values of μ the intermittent propagation of the front causes a wavy pattern in the front's time evolution. For short time scales, the front velocity can thus be very large coinciding with a very long jump of excited media, while the mean velocity is finite and thus not different to that of a normal diffusion process. Further, a clear curvature of the front can be seen in the space-time plots in Fig. 6.16 for small times, indicating that there is accelerated movement which is also absent in the Gaussian case.

Even though, by mere eye inspection the two patterns developing on the two different networks can be easily distinguished it is much harder to do so using established analysis tools. The question is how we can derive from the front propagation what kind of transport process provokes it? Can we recover from the excitation pattern the distribution we assumed when constructing the network? This question is important for situations where one is interested in the fastest way the front can travel during a certain timestep, rather than in its overall mean velocity where solely the cut off value determines the limit. Or

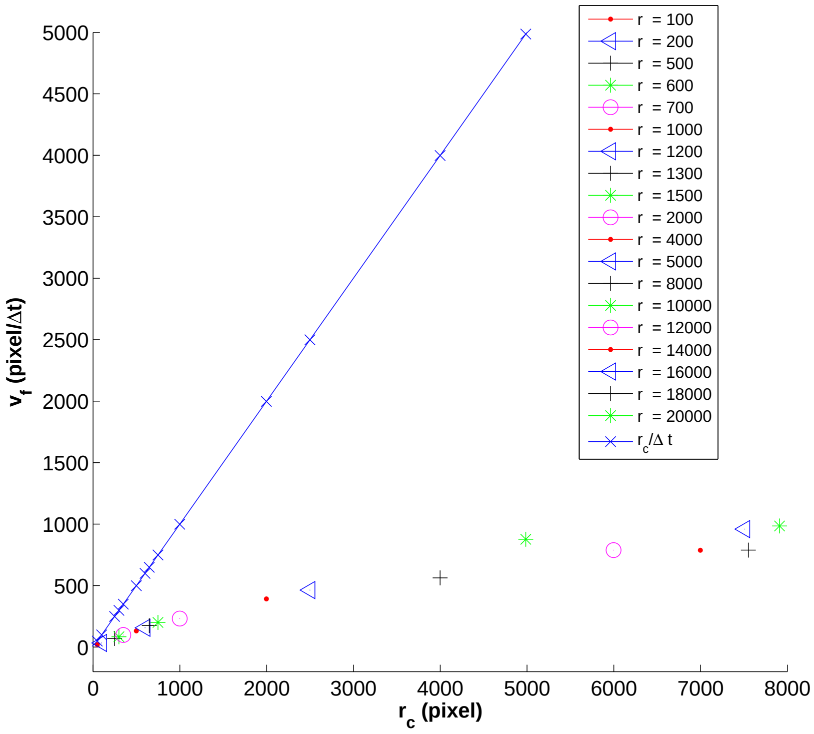

Fig. 6.19: The front velocity of the excitation wave in the power-law network in dependence on the cut-off value b. The velocity of the excitation wave increases for increasing b but as in the Gaussian case, Fig. 6.17, the velocity is much slower than the limit velocity given by $v_c = r_c/\Delta t$ indicated as blue crosses.

putting it otherwise, this question is important when one is interested in the intermittency of the process which can be observed in Fig. 6.22 and Fig. 6.23. The mean excitation front profiles in time perpendicular to the excitation front expansion look very different for both network connectivities used here, see Fig. 6.22. Even though the velocity of both cases depicted here is similar, the shape of the front is highly intermittent in the case of the power-law network and smooth in the Gaussian case. However, the mean excitation front profiles for the power-law network and the experimental case resemble more and more a Gaussian when the average is taken over many fronts. This behaviour has been reported for truncated Lévy flights [184] in dependence on the initial conditions and the power exponent μ. Intermittency in the front profiles can also be analysed as a deviation of the single fronts from a mean front profile. Figure 6.23 shows single front profiles and the resulting mean front profile for the experimental, the power-law network and the Gaussian network excitation fronts. The excitation fronts on the Gaussian network collapse and the mean

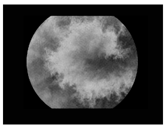

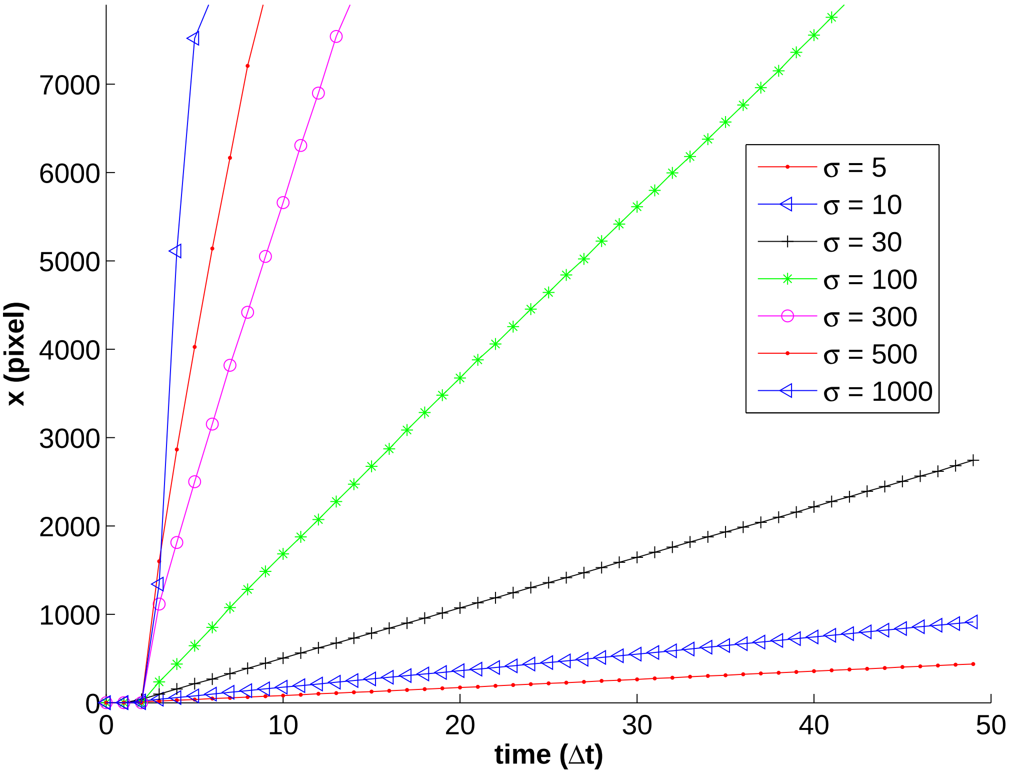

Fig. 6.20: The progression of the excitation front $x(t)$ in pixel is plotted in function of time for the Gaussian network for different σ. The curves are smooth and since there are no jumps the definition of the front velocity is straightforward. The curves show the same information as the red dots in Fig. 6.15 but are summarized here for a better comparison.

front represents the single fronts well. This is different in the other two cases, where the mean is less well defined and shows still wiggles even after large averages are taken. We calculate the probability $p(d)$ of a deviation of size d of a single front profile from the mean front profile. We see that deviations are up to almost a decade larger for the experimental excitation front and the power-law network case than for the Gaussian case. These results show that predictability of front propagation is seriously affected by the scale-free transport as modelled by the power-law network.

Returning now to the previous question: Can we recover knowledge about the underlying transport process (here in the form of the network structure) from the dynamics of the excitation front? Using the masking algorithm introduced previously in Chap. 5 to define the local spread of the front [20] we can regain some information that was used to create the network. Figure 6.24

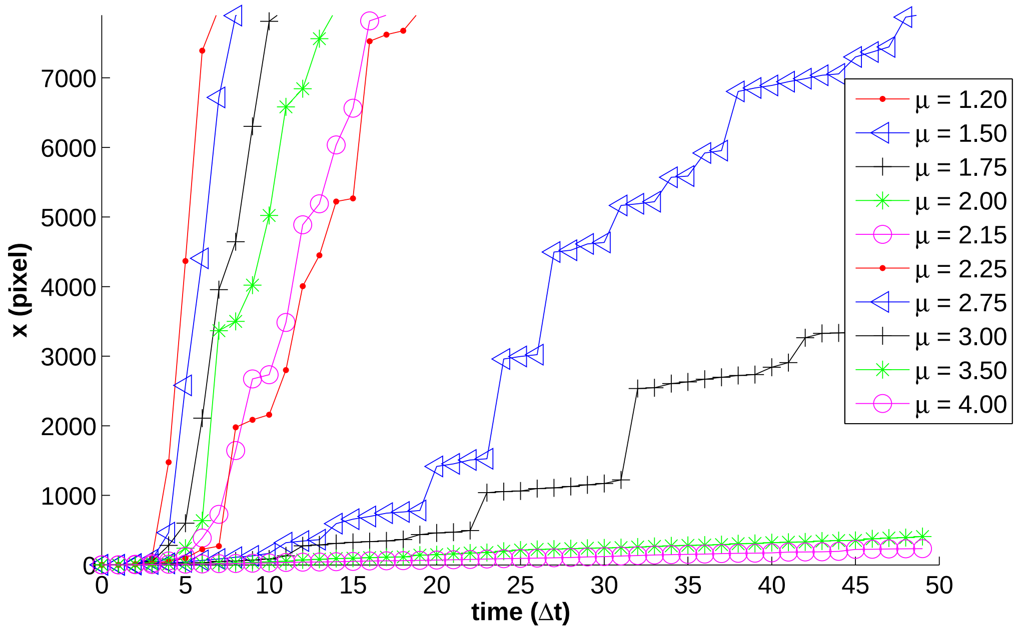

Fig. 6.21: The progression of the excitation front $x(t)$ in pixel is plotted in function of time for the power-law network for different μ. The curves show distinct jumps for values of exponent $\mu \leq 3$ which complicates the definition of a mean front velocity. The curves show the same information as the red dots in Fig. 6.14 but are summarized here for a better comparison.

shows the number of jump-counts ahead of the front of parts of the previous front in function of distance for a Gaussian and power-law network excitation wave in a semi-logarithmic plot respectively. We can immediately see that the resulting probability distributions are very different for the excitation fronts in the Gaussian and the power-law network even though the largest displacements are of similar size. The Gaussian network probability distribution exhibits an exponential tail which can be fitted by a straight line in the semi-logarithmic plot, while the power-law network probability distribution is well fitted by a power-law having the same exponent μ as was used to construct the network. This result was tested for different power-law network realizations using different exponents μ and different cut-off length b and proved rather robust. The masking algorithm might thus constitute a measure that allows to recover information about the underlying local transport processes.

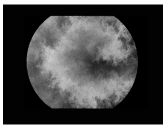

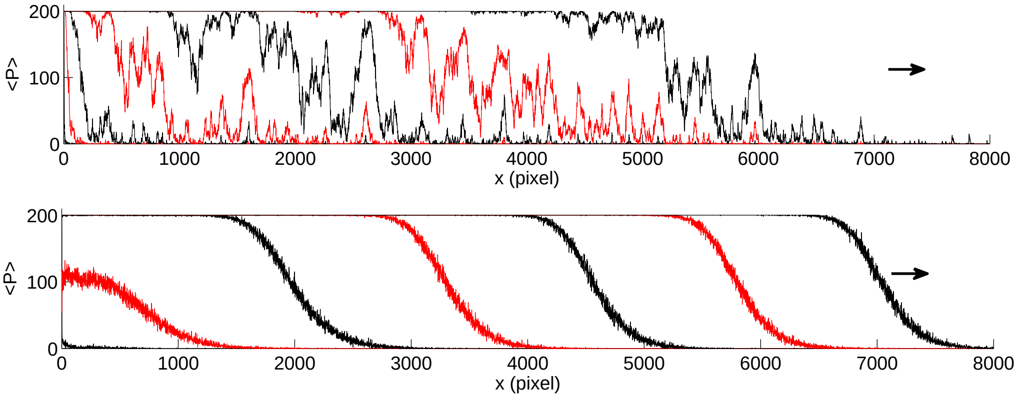

Fig. 6.22: A cut along the direction of excitation front expansion at successive times reveals the intermittency of the progression of the front in the power-law network (upper panel). In the Gaussian case the front is determined by a Gaussian as is expected analytically (lowerpanel) [184]. $< P >$ stands for the average over a strip of 200 pixel width perpendicular to the direction of excitation front expansion. For the power-law $\mu = 2.15$, $b = 3999$. For the Gaussian $\sigma = 300$.

6.5 Conclusion

We conclude that a mere diffusive parametrization, modelled by a Gaussian connected network can account for the mean velocity of front propagation in a geographically scale-free network, as long as there is a limited cut-off value b limiting the velocity. However, a Gaussian connected network cannot account for intermittency phenomena occurring in these geographically scale-free networks and in turbulent fluid flows. These phenomena include the existence of jumps, the acceleration of fronts, the deviation from a mean front profile and the local expansion of the excitation fronts. We find that these phenomena occurring also in our experiments on a chemical reaction in a turbulent fluid flow are better described by geographically scale-free networks. The occurrence of jumps as well as the velocity of the excitation front propagation depends thereby sensitively on the details of the power-law distribution employed to construct the network, i.e., the exponent μ and the cut-off value b. Further, we were able to construct a measure of the local front expansion that allows us to restore the power-law exponent μ of the network. This measure makes it possible to differentiate in between dynamics on Gaussian and power-law networks. Thus, as a main result we found a simple model that displays many of the characteristics of the spread of excitation in a turbulent flow and should be preferred over Gaussian connections when turbulent dynamics are modelled. The extreme simplicity of the model make it advantageous for fast pilot-studies

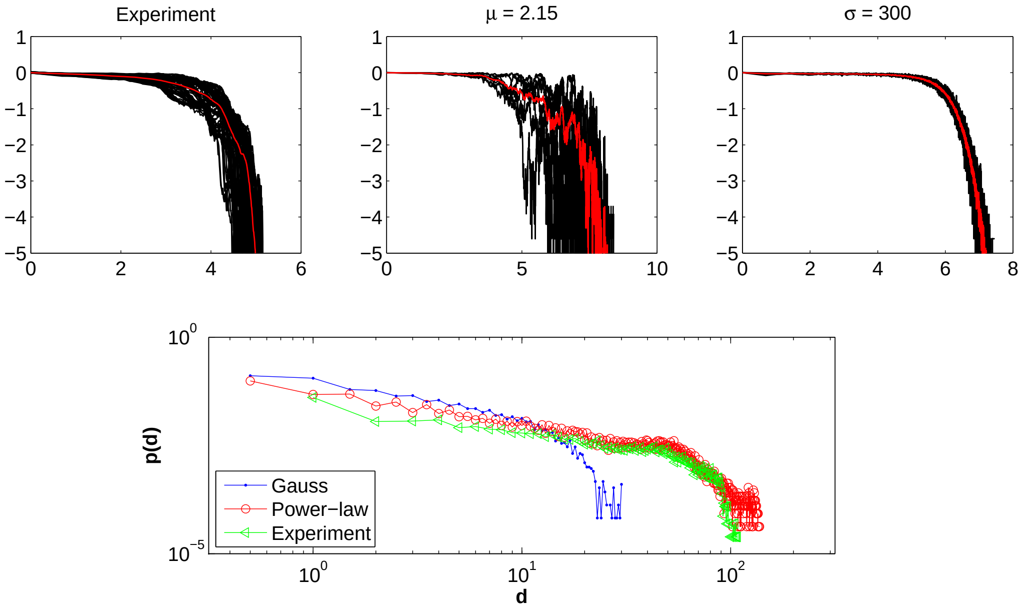

Fig. 6.23: The intermittency of the front expansion affects the deviation from the mean front profile. The single fronts of the experimental excitation wave, the power-law network excitation wave and the Gaussian network one are plotted in black. The corresponding mean front profiles are overlaid in red. The deviations d of the single fronts from the mean are visualized by the distribution function $p(d)$. Large deviations occur in the experimental wave front and in the excitation wave on the power-law network, while in the Gaussian network the largest deviations are about a decade smaller. The mean shape of the front in the power-law case seems to converge to a Gaussian for very large ensembles, the deviations d from the mean characterize the intermittency of this convergence.

concerning local scale-free dynamics in different systems. The network structure of the algorithm simulating the scale-free transport makes a parallelisation of the code easily feasible.

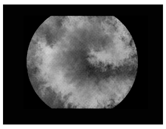

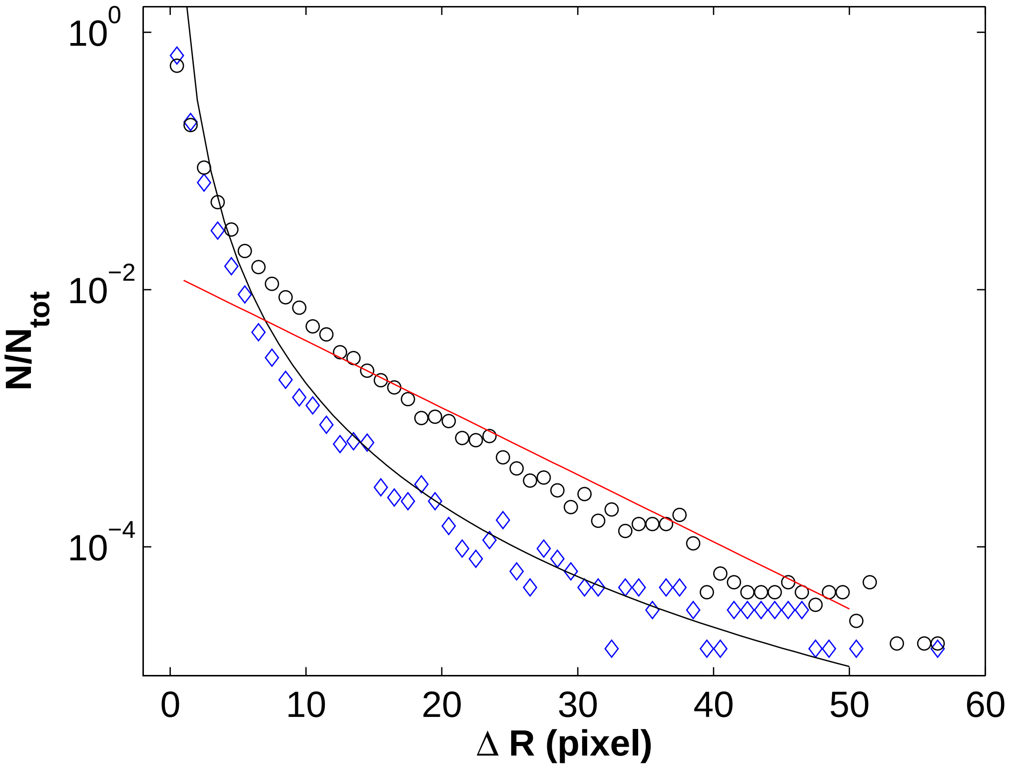

Fig. 6.24: By applying the masking algorithm introduced in the last chapter we can determine the local front dynamics and recover the power-law exponent that was created to construct the power-law network. The symbols show the counts of the occurrence of an excitation ΔR ahead of the front, diamonds stand for the power-law network and circles for the Gaussian network. The blue dahsed line indicates the power-law used to construct the power-law network and the red continuous line is an exponential fit to the tail of the Gaussian case. The plot is in semi-logarithmic scales.

7

Diffusion and Superdiffusion in a Model Flow

In this chapter we study the non-trivial dependence of the asymptotic diffusion on noise intensity for a Hamiltonian flow mimicking the Gulf Jet Stream. Three different diffusion regimes are observed depending on the noise intensity. For intermediate noise levels, the asymptotic diffusion decreases with noise intensity at a rate which is linearly dependent on the flow's meander amplitude. Increasing the noise, the fluid transport passes through a superdiffusive regime and finally becomes diffusive again at large noise intensities. The presence of inner circulation regimes in the flow is found to be determinant to explain the observed behaviour.

The contents of this chapter correspond in large parts to the published article [15]

7.1 Introduction

In the ocean, detailed knowledge of the dispersion of passive tracers is crucial in order to make predictions about the transport of physical, chemical and biological tracers. Important processes range from heat and mass transfer, transport in global bio-chemical cycles or the spread of pollutants [185], to the transport of plankton [186] and fish larvae [187]. Especially in coarse climate models, transport on smaller scales has to be parametrized and statistical transport measures like the eddy diffusivity are common [188]. As we have seen in the previous chapters, normal diffusion is a special case of diffusive transport and a simple model that does not always capture the behaviour of real processes correctly. Let us recall the equations introduced in Sec. 1.2.3, that state that diffusion can be defined in terms of the relative dispersion of diffusing particles which has a time dependence of the form

$$\langle R^2(t)\rangle = \langle |\mathbf{r}_i(t) - \mathbf{r}_j(t)|^2\rangle \sim t^\gamma, \tag{7.1}$$

. For normal diffusion $\gamma = 1$, while for $\gamma > 1$ the Lagrangian dispersion is considered as superdiffusion [71, 75, 189] . Power-law anomalous superdiffusion ($\gamma > 1$) can occur in developed turbulence [20, 21, 170, 190] as we have seen in Chap. 5 and in chaotic flows [153, 164]. The subdiffusive case ($\gamma < 1$) is found in motion through highly heterogeneous media where particles can be trapped in certain regions for long periods of time, such as transport in porous media, gel electrophoresis of polymers (e.g. DNA) and soluble proteins in the nucleus of living cells [191, 192].

It has been shown that for long times and under the assumption of an underlying stationary stochastic process, the presence of a weak fluctuation causes anomalous diffusion to asymptotically become normal at crossover times t_c. These crossover times are inversely proportional to the noise intensity ξ, i.e., $t_c \propto \xi^{-\beta}$ with some exponent β of the order of unity [193, 194]. In terms of the waiting time distribution, the transition to normal diffusion is reflected by an exponentially decreasing distribution $\psi(t) \sim \exp(-\xi t)/t^\mu$ [193, 194]. Consequently, as the noise vanishes $\xi \to 0$, the exponential term becomes one and the crossover time goes to infinity. In the limit $t \to \infty$ and for finite noise ξ, the diffusion process is normal and the asymptotic diffusion coefficient

$$D_A = \lim_{t\to\infty} \frac{\langle R^2(t)\rangle}{t} \tag{7.2}$$

can be determined. This coefficient has been shown to depend on noise intensity as

$$D_A \sim \frac{1}{\xi^\alpha} \tag{7.3}$$

for $\xi \ll 1$, while $\alpha = f(\beta)$ depends on the model used [16, 193–195]. However, taking the limit $\xi \to 0$, D_A gives an infinite result. Karney et al. [196] showed that exchanging the limits, i.e., taking $\xi \to 0$ before $t \to \infty$ in (7.2), the value of D_A depends on the initial location of the tracers. This dependence of D_A on initial conditions is especially pronounced in flows with circulation regimes where tracers may be trapped. In particular, the relative distance in between these sticky trapping regions and the position and size of initial tracer patches turn out to influence the asymptotic value of D_A [196].

Here, we numerically study this limit and show that Eq. (7.3) does not always hold. For that purpose, we determine the effect of additive noise on the transport in a Hamiltonian system leading to a non-trivial dependence of the asymptotic diffusion coefficient on the noise intensity ξ.

7.2 Flow Model and Numerical Details

The meandering jet flow was introduced as a simple kinematic model for the Gulf Stream and is frequently used to describe western boundary current extensions in the ocean [197–204]. This flow is usually represented in a reference frame $\zeta = x' - c_x t', \delta = y'$ moving with the phase velocity c_x of the meander, where x' and y' are Cartesian coordinates, positive eastward and northward respectively. Then, the corresponding nondimensional streamfunction can be written as

$$\psi(x, y) = -\tanh\left(\frac{y - B\cos\kappa x}{R^{1/2}}\right) + Cy, \tag{7.4}$$

where $(x, y) = (\zeta, \delta)/\lambda$ are the dimensionless coordinates. The velocity field $\mathbf{V}(x, y)$ in this moving frame is obtained from the streamfunction as $\mathbf{V}(x, y) = \mathbf{e_z} \times \nabla\psi$.

We consider an additional noise perturbation $\eta(t)$ that mimics environmental fluctuations, and we arrive at the following coupled differential equations for the particle velocity,

$$\begin{aligned} \dot{x} &= \frac{1}{R^{1/2}\cosh^2\theta} - C + \eta(t) \qquad (7.5) \\ \dot{y} &= -\frac{B\kappa\sin\kappa x\,(1 + B^2\kappa^2 - By\kappa^2\cos\kappa x)}{R^{3/2}\cosh^2\theta} + \eta'(t) \end{aligned}$$

with

$$\begin{aligned} R &= 1 + (B\kappa\sin\kappa x)^2 \\ \theta &= \frac{y - B\cos\kappa x}{R^{1/2}}. \end{aligned}$$

Here $\eta(t)$ is a Gaussian stochastic process with zero mean, a temporal correlation function $\langle\eta(t)\eta(t')\rangle = 2\xi\delta(t - t')$ and noise intensity ξ.

The original parameters of the model are: the total eastward transport $2\psi_0$, the width λ, the amplitude A and the wavenumber $k = 2\pi/L$ of a sinusoidal meander. These are converted to dimensionless quantities $B = \lambda^{-1}A$, $\kappa = k\lambda$, $C = \lambda\psi_0^{-1}c_x$, and the dimensionless time $t = \psi_0\lambda^{-2}t'$. The parameters of the model are chosen such that they properly represent geophysical features of the

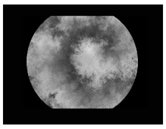

ψ_0	4000 km^2 d^{-1}		
λ	40 km		
c_x	20 km d^{-1}	C	0.2
A	80 km	B	2.0
L	266.67π km	κ	0.3

Table 7.1: List of parameters used in the Gulf Stream model.

Gulf Stream. Table 7.1 summarizes these values. Equations are then integrated using the *Heun* scheme [205] and a time step of $\Delta t = 10^{-3}$.

Figure 7.1 shows the jet flow in the co-moving frame for this set of parameters. This flow can be divided into three distinct regimes: a central meandering eastward jet (A), closed circulation above meander troughs and below crests (B), and exterior retrograde westward motion (C). Fluid particles are restricted to each of these regimes and no cross-stream mixing occurs. In the presence of an added temporal variability, the boundaries between regimes break up, allowing transport and exchange of fluid between regimes. For the jet amplitude $B > B_{crit}$, the geometry of the flow changes drastically and the central meandering jet moves westward. For the set of parameters indicated in Table 7.1, $B_{crit} \approx 3$ [202–204].

For the numerical experiments, initially a cluster of $N = 500$ particles separated from each other by a distance $\delta_0 = 10^{-3}$ was located at the stationary point inside the closed circulation core (B) $(x_0, y_0) = (0, B - \cosh^{-1} C^{-1/2})$. Then, the temporal evolution of the relative dispersion $\langle R^2(t) \rangle$ (7.1) of this cluster is calculated for times up to $t = 10^7$. It was found that the statistical properties calculated throughout this paper do not depend on the number of tracers, provided that the corresponding computation time is sufficiently long.

7.3 Results

The time evolution of the relative dispersion for three noise intensities is shown in Fig. 7.2 a. We estimate the power-law growth at large times for different noise intensities. Figure 7.2 b shows the values of the exponent γ in Eq. (7.1) as a function of the noise intensity, calculated for two periods of time. Our results show that the exponent $\gamma > 1$ for intermediate noise intensities, while for small and large values of noise, $\gamma = 1$. For large noise $1/\xi \to 0$ the exponent evolves as $\gamma \to 1$ because inner cores become blurred by noise and diffusion is dominant. For intermediate noise intensities some particles intermittently enter within the inner cores where they may remain for some time, while others travel long distances and this causes $\langle R^2(t) \rangle$ to increase superdiffusively [206]. The

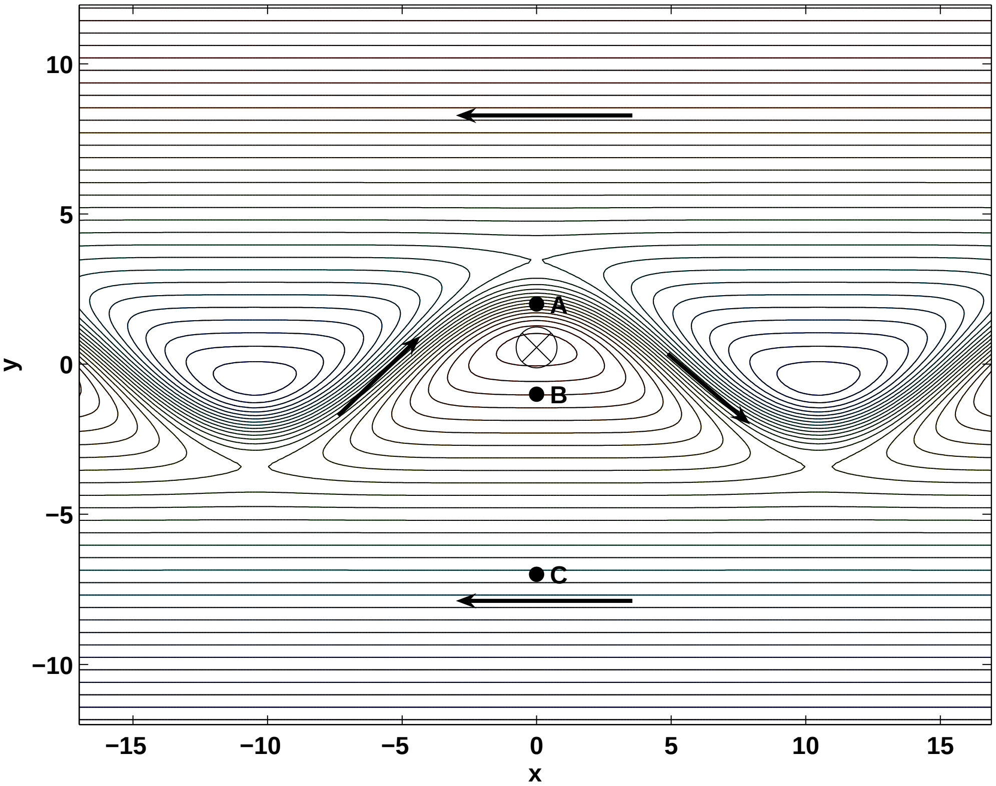

Fig. 7.1: Stream function of the jet flow (7.4). Arrows indicate the direction of motion and dots correspond to the different regimes in the flow for the jet amplitude $B < B_{crit}$. The high density of contour lines indicates the position of the central eastward jet. The cross indicates the position of the stationary point inside the inner circulation core. The domain shown in the figure is extended periodically in x-direction. Set of parameters as in Table 7.1.

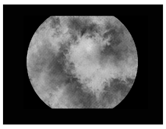

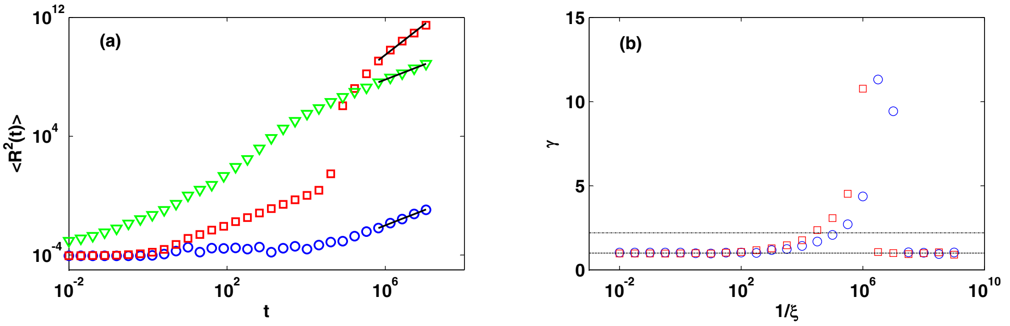

Fig. 7.2: (a) Relative dispersion $\langle R^2(t)\rangle$ for three values of noise intensity. Solid lines correspond to the best fitting to Eq. (7.1) to extract γ. Noise intensities: $\xi = 10^{-9}$ (circles), $\xi = 10^{-5}$ (squares), and $\xi = 10^{-2}$ (triangles). (b) Exponent γ as a function of noise intensity for two intervals of time, $t \in [7 \cdot 10^5, 1 \cdot 10^7]$ (circles) and $t \in [2 \cdot 10^5, 6 \cdot 10^5]$ (squares). Lines indicate normal (--, lower line) and ballistic (·-, upper line) dispersion. Rest of parameters as in Table 7.1.

very high values of γ up to 10 for intermediate noise intensities in Fig. 7.2 b can be understood looking at the two curves (red squares and green triangles) in Fig. 7.2 a. Both curves show a type of transitory behavior with a high slope. This transition is expected to appear for all noise values, i.e., even for an arbitrary long integration time of the system there is always a noise intensity, such that the transition occurs at the end of the simulation. Thus, the peak in Fig. 7.2 b shifts to lower noise intensities (right of the figure) as integration time increases, cf. the two curves in Fig. 7.2 b. For small noise, $1/\xi \to \infty$ the exponent evolves as $\gamma \to 1$ because particles have not yet left the inner circulation cores, i.e., the typical waiting time is longer than the simulation time.

Theoretically, it is expected that in the limit $t \to \infty$ the diffusion should become normal and $\gamma \to 1$ for any noise intensity. However, we find that for intermediate noise intensities this limit may be well beyond an experiment's lifetime and was not approached in this numeric study. When the asymptotic case of normal diffusion is not reached, D_A as defined in (7.2) is not a constant value and we estimate a lower bound for D_A at the maximum simulation time $t = 10^7$.

The asymptotic diffusion coefficient D_A measured as a function of the noise intensity is shown in Fig. 7.3. For very large diffusion (regime HN), the trivial relation $D_A \propto \xi$ is observed, as the random walk of the particles is dominated by the added noise. For intermediate noise intensities (regime IN), D_A scales with the noise intensity as in Eq. (7.3) [16, 193]. In between these two regimes,

$D_A \propto \xi$ (HN) and $D_A \propto \xi^{-\alpha}$ (IN), a local minimum at $\xi \sim 10^{-0.5}$ is observed. This minimum in diffusion value is especially striking as it neither depends on the model parameters nor on the initial particle positions. Finally, as noise intensity decreases, D_A reaches a maximum value D_A^{max} that depends on the jet amplitude B. In the limit of vanishing noise $1/\xi \to \infty$, $D_A \propto \xi$ for any value of B. For computing times greater than 10^7, we reproduce the same qualitative behavior although the maximum D_A value is displaced towards small noise intensity values (shifted to the right in Fig. 7.3).

Increasing the noise, the boundaries between the jet flow regimes described in Fig. 7.1 become permeable to particle crossings due to the random component $\eta(t)$ and $\eta'(t)$ in the equations of motion. The exchange process is similar to the one described in [207] where lobes of fluid are entrained and detrained from the edge of the jet. The onset for this particle exchange occurs at a finite non-zero value of the perturbation [202–204] and above it, anomalous transport develops. This onset displaces towards lower non-zero values of noise as time increases and $D_A^{max} \propto t$. This is an important point because it implies that Eq. (7.3) does not hold for small noise intensities since we find that $\lim_{t,\xi} D_A < D_A^{max}$, if $\xi \to 0$ before $t \to \infty$.

The effect of the jet amplitude B on the asymptotic diffusion coefficient D_A^{max} is analyzed in Figure 7.4. Note that D_A^{max} decreases as a power law with increasing jet amplitude B and the scaling factor α in Eq. (7.3) decreases linearly with B, as it is shown in Figs. 7.4 a, b, respectively. From panel (a) we also note that D_A^{max} grows with time t by the same factor for any value of B, and we find that $D_A^{max} \propto t/B^{\chi}$ ($\chi \approx 1$).

Finally, the influence of the initial tracer positions (x_0, y_0) on the diffusion was analyzed. As expected, for $\xi \to \infty$, $D_A \sim \xi$ independently of (x_0, y_0). However, as predicted by Karney et al [196], for $\xi \to 0$, D_A depends on the initial conditions and attains a constant value for (x_0, y_0) values far from the inner circulation core. In those regions, the laminar peripheral westward currents do not disperse the tracers and $\langle R^2(t)\rangle \approx const.$ For initial conditions inside the circulation core or at the jet stream, the results do not differ qualitatively from those described here.

7.4 Conclusion

To conclude, we have analyzed the non-trivial dependence of the asymptotic diffusion coefficient D_A on noise mimicking environmental fluctuations in a kinematic model of the Gulf Stream. Above a certain non-zero value of noise intensity the closed flow regimes become permeable to particle crossings which explains the presence of a maximum asymptotic diffusion coefficient. For in-

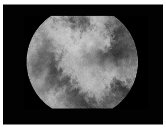

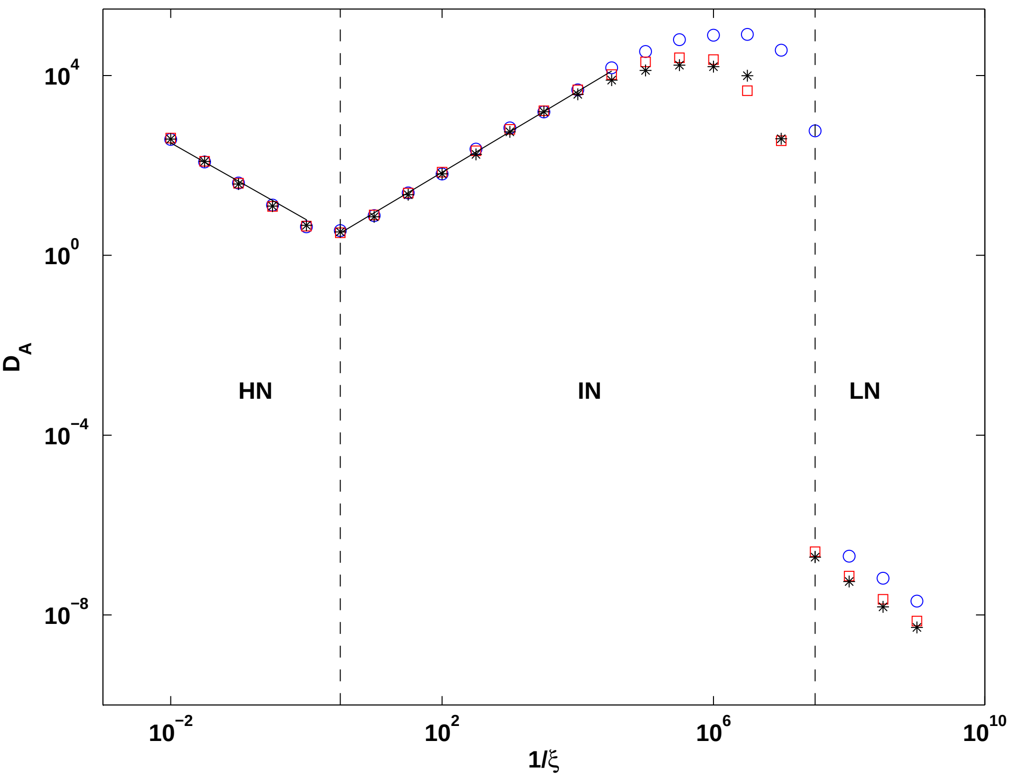

Fig. 7.3: Asymptotic diffusion coefficient D_A (7.2) at time $t = 10^7$ as a function of noise intensity for different values of the jet amplitude. From left to right, solid lines correspond to $D_A \sim \xi$ and $D_A \sim \xi^{-\alpha}$ with $\alpha = 0.90 \pm 0.03$. Dashed vertical lines separate regions for high (HN), intermediate (IN) and low (LN) noise. Set of parameters: $B = 1$ (circles), $B = 3$ (squares) and $B = 5$ (stars). Rest of parameters as in Table 7.1.

termediate noise intensities, $D_A \sim \xi^{-\alpha}$ and the transport becomes superdiffusive [16, 193, 206]. However, as an important result we find that this dependence does not hold for $\xi \to 0$. The scaling coefficient α was found to decrease with the jet amplitude. Finally, for large noise intensities $D_A \sim \xi$ as expected. The transport at large times, diffusive for small noise intensities, becomes superdiffusive at intermediate noise intensities and then normal at large noise. The presence of a trapping remnant regular region in the flow for low and intermediate noise intensities seems to be important to explain the non-trivial dependence of the asymptotic transport on the perturbation strength. For very small noise we did not find superdiffusive behavior within the computing times used in this Report ($\sim 10^4$ years). The results even remain unchanged when

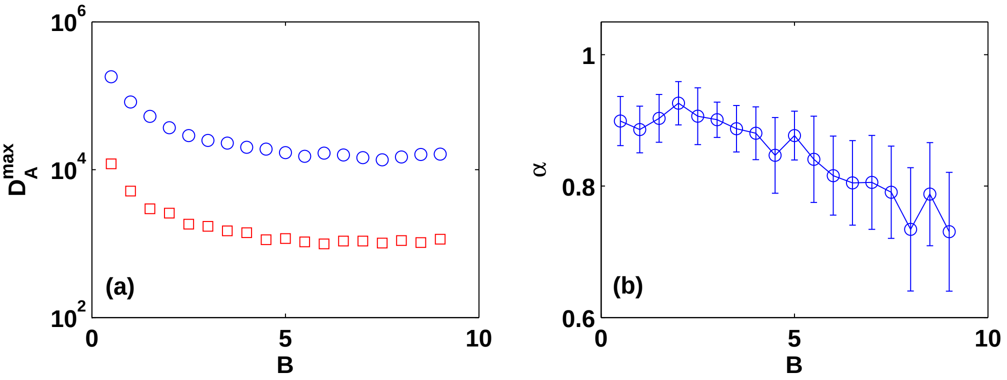

Fig. 7.4: Logarithmic plot of the maximum value of D_A at two instants of time ($t = 7 \cdot 10^5$ (squares) and $t = 1 \cdot 10^7$ (circles)) (a) and the scaling coefficient α, Eq. (7.3) (b) as a function of the jet amplitude B. Parameters as in Table 7.1.

$B > B_{crit}$ and the direction of the jet is reversed which indicates that they might be applicable to other flows consisting of jets and trapping regions.

We are confident that in real experiments with comparably short lifetimes, the three described diffusion regimes can be observed. The jet stream model cannot only be used to describe the Gulf Stream, but also others like the Kuroshio current [208] or the polar jet in the atmosphere. Our results may therefore help to interpret and predict the transport of tracers in a jet which is subject to environmental fluctuations.

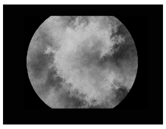

8

Conclusion and Outlook

This thesis aimed to increment the knowledge about pattern formation in reaction-diffusion-advection systems. This goal has been achieved in so far, as entirely new yet familiar patterns have been obtained and analysed. As an important by-product of this work we discovered the Faraday flow. This discovery is especially promising for low-cost reaction-diffusion-advection experiments such as shown in Chap. 4 and Chap. 5. The dynamics and patterns observed raise new questions and open up new fields of possible studies touching a variety of different themes such as superdiffusion, turbulent transport and wave-vortex interactions. The results obtained throughout this work strongly indicate that very often the details of the timescales of the active and passive processes are crucial for the emerging transport and patterns.

8.1 Main Findings

Here I summarise the main findings of this thesis point by point.

- We discovered that the Faraday experiment, consisting in the vertical vibration of a liquid with a free surface, produces an important horizontal fluid flow in a shallow liquid layer which we call the Faraday flow. The Faraday flow shows many characteristics that are typical for two-dimensional turbulence, in particular, an inverse energy cascade and the corresponding scalings of the structure functions and the Richardson dispersion of particle pairs suspended to the flow. In contrast to other realisations of quasi two-dimensional fluid flows, the Faraday flow has some advantages. One especially intricate advantage is the fact that the vortices that seem to drive the fluid flow are somehow correlated to the Faraday wave pattern which implies that their exact location and orientation changes with time. This characteristic causes the mean forcing over time to be very isotropic as was shown in the full energy spectra Fig. 3.10, especially for high forcing amplitudes. This is an effect that can not be obtained with Lorentz-force driven turbulence, the state-of-the-art experimental realization of quasi two-dimensional fluid flows. For a direct comparison refer to Tabeling [53]. It is thus possible to obtain a highly turbulent flow with a very isotropic aspect by implementing the Faraday flow.

- We observe the emergence of boosted patterns when an excitable chemical reaction, here the Belousov-Zhabotinsky reaction, is subjected to the Faraday flow. The mere existence of the boosted patterns is an important result in itself, as it indicates that the parametrization of a turbulent fluid flow with a turbulent or effective diffusion constant D_* can be justified for the timescales of the full front. A conclusion which to our knowledge has not been demonstrated experimentally for active media.

- We find that the front velocity of the boosted patterns follows, on average, the celebrated FKPP (Fisher-Kolmogorov-Petrovski-Piskunov) relation which states, that the front speed depends on the reaction timescale and the square-root of the turbulent diffusion coefficient.

- Even though the overall boosted patterns resemble those of the molecular diffusion induced autowaves, we also find deviations. The aspect of the boosted wavefronts is much more filamentary and the leading edge of the wavefront does not scale with the diffusion coefficient as expected from the molecular diffusion driven counterparts. Here, the details of the reaction timescales seem to play a crucial role.

- We find that locally the expansion of the boosted wavefronts deviates from a normally diffusive process and local propagation of the front can be described as scale-free on certain time and length scales. This is most likely related to a transient superdiffusive regime observed in the measurements of absolute diffusion.

- We managed to formulate a strongly simplified model of the excitable kinetics able to reflect some of the most fundamental aspects of the local front expansion. Its main advantage lies in its speed of calculus and simple parallelisation.

- We observe the non-trivial dependence of diffusion and superdiffusion on the noise-level for a jet-like fluid flow. This included the observation of the limitations of the validity of an asymptotic relation in between the diffusion constant and the noise level.

8.2 Interconnection of the Different Studies Presented

This thesis may differ from other ones concerning the variety of different subjects studied, involving aspects of fluid dynamics, dynamical systems theory, chemistry, biology (if applied to real world dynamics such as plankton blooms) and statistics. Instead of the usual focus on one specific scientific question, this work is rather a study on the question of what kind of questions one can ask about patterns forming in reaction-diffusion-advection systems. The scarceness of experimental work on reaction-diffusion-advection equations, especially for excitable or oscillatory dynamics [135, 136, 158] surely added to a great extent to this initial uncertainty in the aims of the study. This study is thus a first scan of the events and patterns possible. In particular, this was achieved by the experimental realisation of a reaction-diffusion-advection system.

It is thus an overall accomplishment of this thesis to provide for a fully functioning experimental set-up which can measure the chemical concentration of ferroin as an indicator of an activator wave and produce a well defined turbulent fluid flow. First tests have been made which show that the measurements of the velocity fields and the chemical concentrations can even be done simultaneously. This tool gives us the basis for the proper formulation of analysis techniques. Phenomenon, such as superdiffusion gain a whole new denotation when one asks for the timescales on which they occur and if they coincide with those timescales that govern the dynamics of the active media present. Certainly, the usual importance of the asymptotic behaviour of diffusion and transport fades in comparison to the existence of interaction of various dynamical processes. This work suggests some rather local measures of transport, such as the masking algorithm for the wavefronts that could overcome the deficiencies of the usual asmptotic measures in this regard.

During this work, the problem of the adequate analysis method in order to characterize the chemical wavefronts was encountered several times. In chapter 6 a highly simplified network based model for the local scale-free propagation of the reactive wavefront is proposed. While there are obviously many shortcomings of using a network approach to retain the transport observed in a turbulent fluid flow, the main characteristics such as the existence of large fluctuations around the mean front velocity and front profile, as well as the local scale-free dynamics are recovered. The masking algorithm applied for the characterization of the local wavefront expansion of the experimental wave is also able to detect the locally scale-free dynamics of the model wavefront. To our knowledge, a geographically local scale-free network has not been studied so far. Thus, the mere approach itself can be considered an improvement.

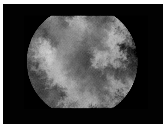

Scale free dynamics of particles are also observed in many fluid flows that are not yet turbulent but rather chaotic. This is due to the existence of coherent structures in phase-space where particles become trapped. Especially fluid flows with geographically close but dynamically highly distinct regions, such as jets and vortices, can show a high sensitivity on the sub-scale diffusion or noise level. The noise in these cases defines the usual time-scale during which a particle remains trapped in the coherent structures. In this thesis, we numerically studied a model flow for a typical jetlike structure as it appears for instance in the gulf-stream in the ocean. The results show how careful one generally needs to consider the exact value of the underlying noise (or small scale diffusivity), since the scaling of the relative dispersion of particle pairs shows a large sensitivity to the noise level.

8.3 Applicability and Outlook

Concerning the applicability of the results, we can suggest possible implications on real-world processes. Maybe in this regard, the first notion should be that turbulence is a self-similar phenomenon and thus the basic results of our study should scale-up with the system size. That signifies that also in other large aspect ratio quasi two-dimensional systems we should be able to observe the emergence of two-dimensional transport from a forcing in direction of the third dimension.

Under certain conditions the atmosphere and the ocean might be examples of such systems and the convective fluxes due to heat gradients could take the role of a forcing in the third dimension in place of the Faraday waves [47, 209]. As an idea for a continuing study, we thus suggest the revelation of the details of this energy redistribution process involving some kind of wave-vortex interaction. This work could be done analytically and numerically accompanied with experiments using an ultra-fast camera and particles submersed in the liquid subjected to the Faraday experiment.

The up-scaling of the results should further also be valid for the observations on active media. It is possible that the observed boosted patterns could also occur in plankton dynamics in the ocean, at least when the concept of iron-fertilization for CO_2 reduction in the atmosphere should really prevail the actual experimental tests, optimal conditions for a proper growth of the plankton bloom could give these experiments a different level of impact.

A

Supplementary Movie description and Image sequences

A.1 Supplementary Movie M1.

Figure A.1 shows the image sequence of the boosted spiral wave in Fig. 4.1 which corresponds to movie M1 on the supplementary DVD. Forcing parameters: $f = 70\,\mathrm{Hz}$, $a_0 = 1.8\,\mathrm{g}$. Chemical parameters: Initial sulfuric acid concentration $[H_2SO_4] = 1.2\,\mathrm{M}$. The spiral wave forms out of a broken target wave at the bottom of the image and stabilizes during its evolution, dominating the target wave at the bottom. Finally, after 11 revolutions (at $t \approx 143\,\mathrm{s}$) and a complex movement of the tip, the wave front of the spiral breaks in the upper left corner of the image due to another pattern which forms spontaneously. This broken wave front gives rise to a second clock-wise rotating spiral and other patterns at the top of the image. The temporal persistence of the spiral is thus limited. Typical rectangular Faraday waves due to the vertical forcing can be distinguished on the top of the fluid surface. Image processing of movie M1: The usage of a thicker diffuser caused light loss and the images were noisier. Therefore, in this movie images were slightly smoothed by a Gaussian filter (standard deviation $\sigma = 1.0$ pixel). Maximum and minimum values of the greyscale of the movie were adjusted to maximize the contrast.

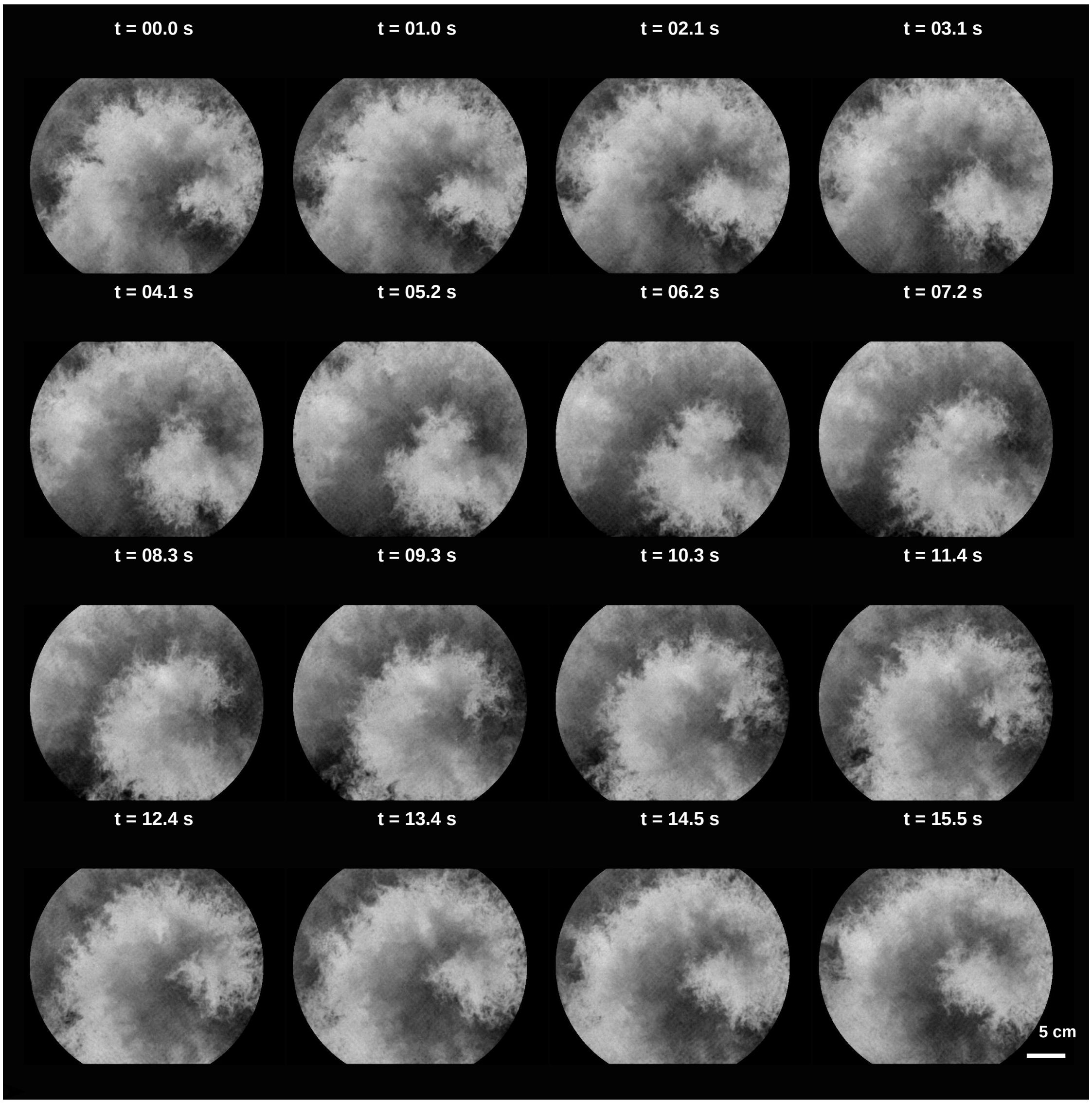

Fig. A.1: Exemplary image sequence of the boosted spiral wave in Fig. 4.1 and movie M1.

A.2 Supplementary Movie M2.

Figure A.2 shows the image sequence of the boosted target wave for low forcing, Fig. 4.1 and Fig. 4.8 a, corresponds to movie M2 on the supplementary DVD. Forcing parameters: $f = 50\,\mathrm{Hz}$, $a_0 = 1.2\,\mathrm{g}$. Chemical parameters: Initial sulfuric acid concentration $[H_2SO_4] = 0.6\,\mathrm{M}$. The center of the target wave can clearly be seen at the left side of the image. Persistent coherent structures and a higher Damköhler number (see discussion Fig. 4.8) lead to prominent filamentous structures at the leading front of the wave (cf. Supplementary Movie M8). Typical rectangular Faraday waves due to the vertical forcing can be distinguished on the top of the fluid surface. Image processing of movie M2: Maximum and minimum values of the greyscales of the movie were adjusted to maximize the contrast.

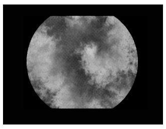

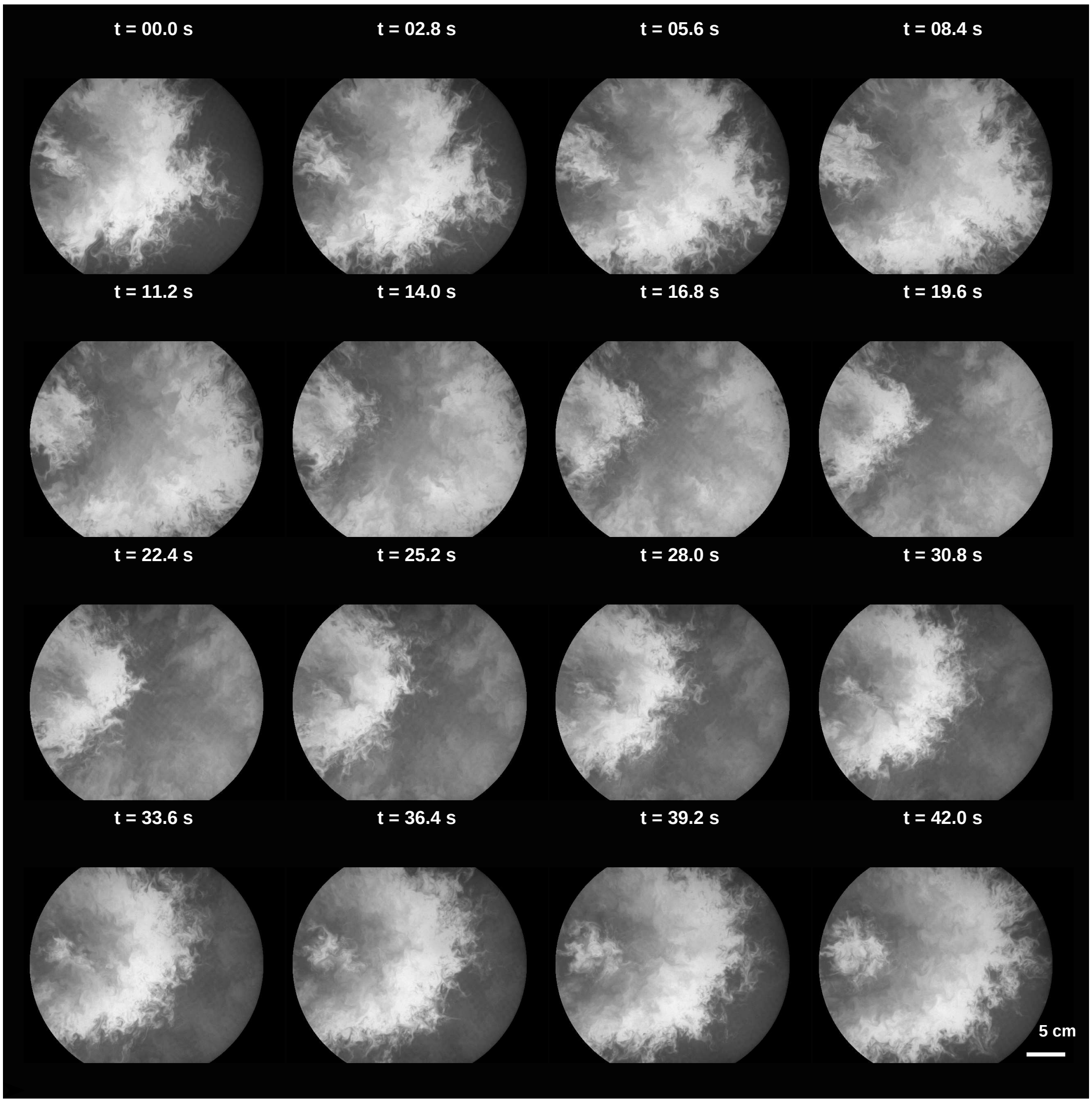

Fig. A.2: Exemplary image sequence of the boosted target wave in Fig. 4.1 and movie M2.

A.3 Supplementary Movie M3.

Figure A.3 shows the image sequence of the exemplary boosted spiral wave for measurements of the period of the tip and corresponds to movie M3 on the supplementary DVD. Forcing parameters: $f = 50\,$Hz, $a_0 = 1.9\,$g. Chemical parameters: Initial sulfuric acid concentration $[H_2SO_4] = 0.6\,$M. Note the complex movement of the spiral tip. The leading edge and the tail of the front are smoother at higher forcings due to a smaller Damkhler number and less coherent structures in the fluid flow (see discussion Fig. 3). The typical rectangular Faraday waves due to the vertical forcing can be distinguished on the top of the fluid surface. Image processing of movie M3: The usage of a thicker diffuser caused light loss and the images were noisier. Therefore, in this movie images were slightly smoothed by a Gaussian filter (standard deviation $\sigma = 1.0\,$pixel). Maximum and minimum values of the greyscales of the movie were adjusted to maximize the contrast.

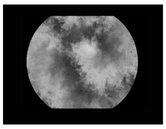

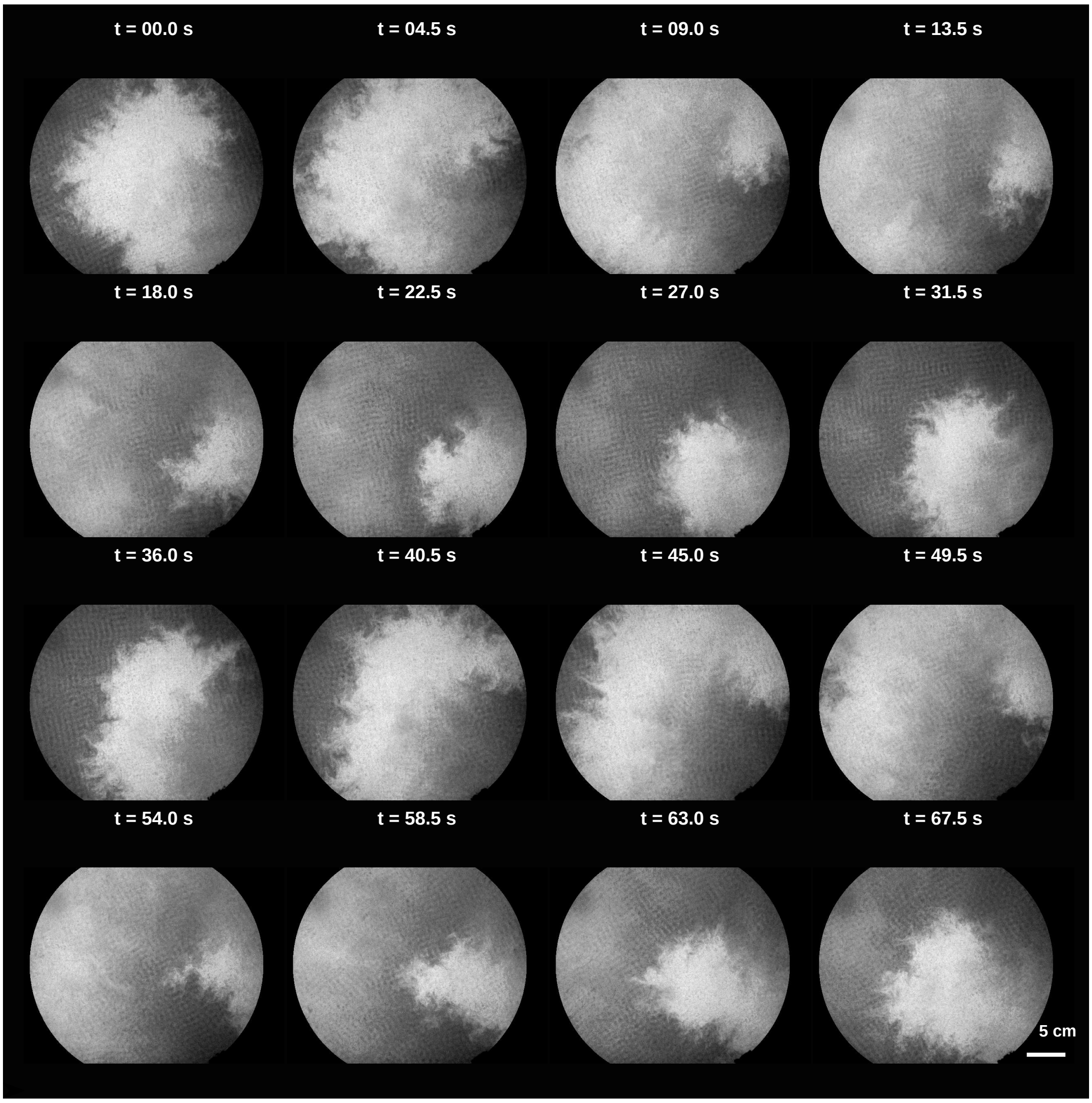

Fig. A.3: Exemplary image sequence of the boosted spiral wave, movie M3.

A.4 Supplementary Movie M4.

Figure A.4 shows the image sequence of a pinned boosted spiral wave for low forcing and corresponds to movie M4 on the supplementary DVD. Forcing parameters: $f = 50\,\text{Hz}$, $a_0 = 1.3\,\text{g}$. Chemical parameters: Initial sulfuric acid concentration $[H_2SO_4] = 0.6\,\text{M}$. The spiral wave is pinned to a round obstacle of $54\,\text{mm}$ diameter. Note the long time of persistence of this pattern: Only after a time of $t \approx 62\,\text{min}$, other patterns forming at the border interact with the spiral and cause its break-up. Finally, chaotic spatiotemporal patterns appear. The typical period for the completion of one round of the pinned spirals is in between $T_{pin} = 30$–$50\,\text{s}$ for all forcings and thus in the very same range as for the free spirals. For lower forcings the pinning was more difficult to attain and the tip detached easily indicating that the obstacle was still too small to suppress the meandering. The typical rectangular Faraday waves due to the vertical forcing can be distinguished on the top of the fluid surface. Image processing of movie M4: Maximum and minimum values of the greyscales of the movie were adjusted to maximize the contrast.

A.5 Supplementary Movie M5.

The movie M5 on the supplementary DVDSshows the same pinned boosted spiral wave as in M4 but in real-time to give an impression of the speed of the phenomenon. Forcing parameters: $f = 50\,\text{Hz}$, $a_0 = 1.3\,\text{g}$. Chemical parameters: Initial sulfuric acid concentration $[H_2SO_4] = 0.6\,\text{M}$. The movie shows a real-time revolution of the spiral in movie M4. The temporal evolution of filaments of high ferriin concentration, generated by jets in the turbulent flow, can be nicely distinguished. The typical rectangular Faraday waves due to the vertical forcing can be observed on the top of the fluid surface. Image processing of movie M5: Maximum and minimum values of the greyscales of the movie were adjusted to maximize the contrast.

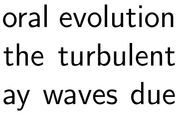

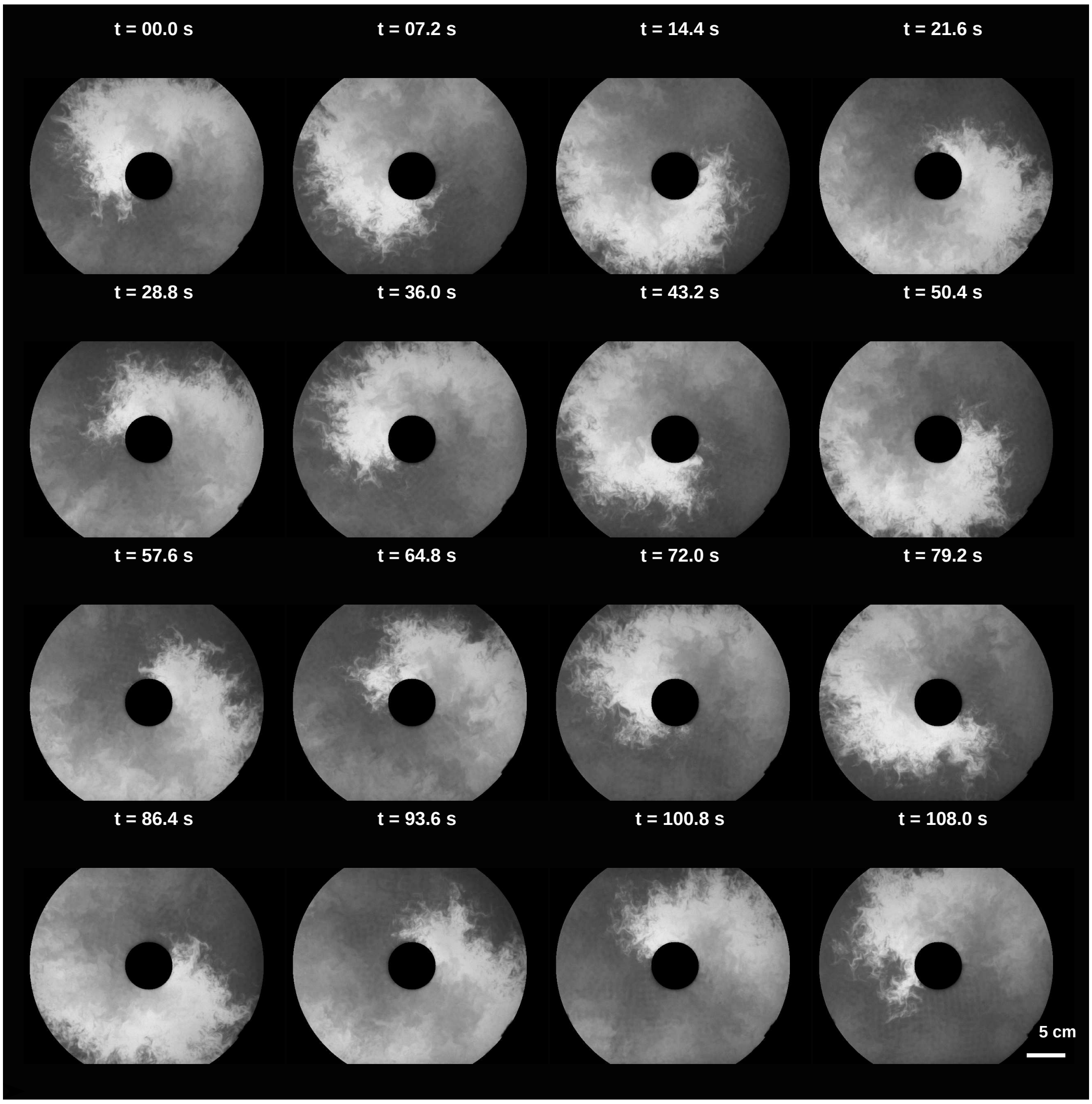

Fig. A.4: Exemplary image sequence of the pinned boosted spiral wave for low forcing, movie M4 and M5.

A.6 Supplementary Movie M6.

Figure A.5 shows the image sequence of a pinned boosted spiral wave for high forcing which corresponds to movie M6 on the supplementary DVD. Forcing parameters: $f = 50\,\mathrm{Hz}$, $a_0 = 2.2\,\mathrm{g}$. Chemical parameters: Initial sulfuric acid concentration $[H_2SO_4] = 0.6\,\mathrm{M}$. The spiral wave is pinned to a round obstacle of $54\,\mathrm{mm}$ diameter. Note the long time of persistence of this pattern: After a time $t \approx 27\,\mathrm{min}$ the spiral detaches from the obstacle and starts a complex movement which finally causes its break-up at the border. The typical rectangular Faraday waves due to the vertical forcing can be distinguished on the top of the fluid surface. Image processing of movie M6: Maximum and minimum values of the greyscales of the movie were adjusted to maximize the contrast.

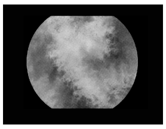

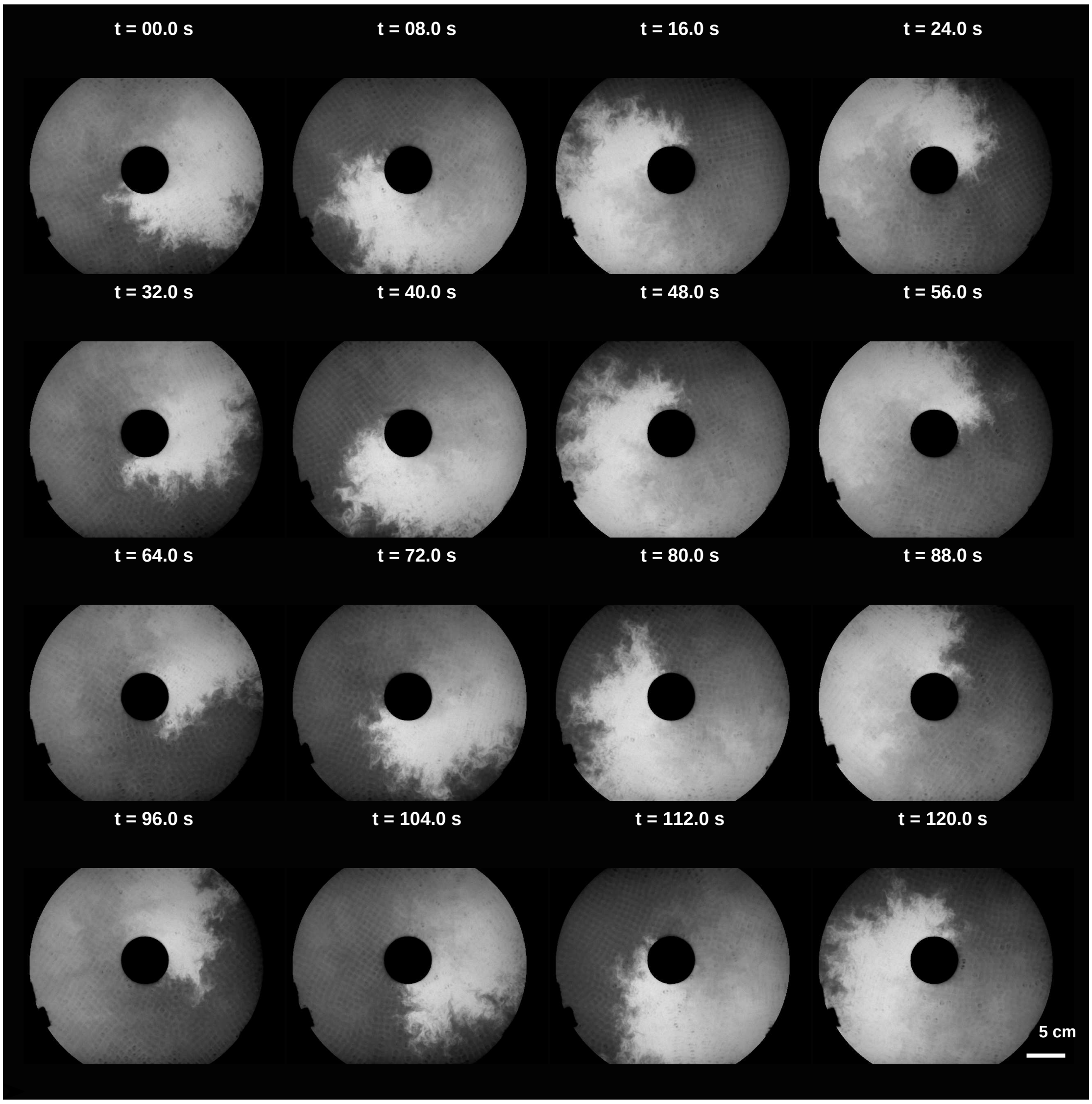

Fig. A.5: Exemplary image sequence of the pinned boosted spiral wave for high forcing , movie M6.

A.7 Supplementary Movie M7.

Figure A.6 shows the image sequence of the boosted double spiral wave. Forcing parameters: $f = 105\,$Hz, $a_0 = 0.9\,$g. Chemical parameters: Initial sulfuric acid concentration $[H_2SO_4] = 0.6\,$M. A counter-rotating double spiral wave developed from the break-up of a target. The typical rectangular Faraday waves due to the vertical forcing can be distinguished on the top of the fluid surface. Image processing of movie M7: Maximum and minimum values of the greyscales of the movie were adjusted to maximize the contrast. This movie was recorded without a green contrast foil.

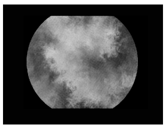

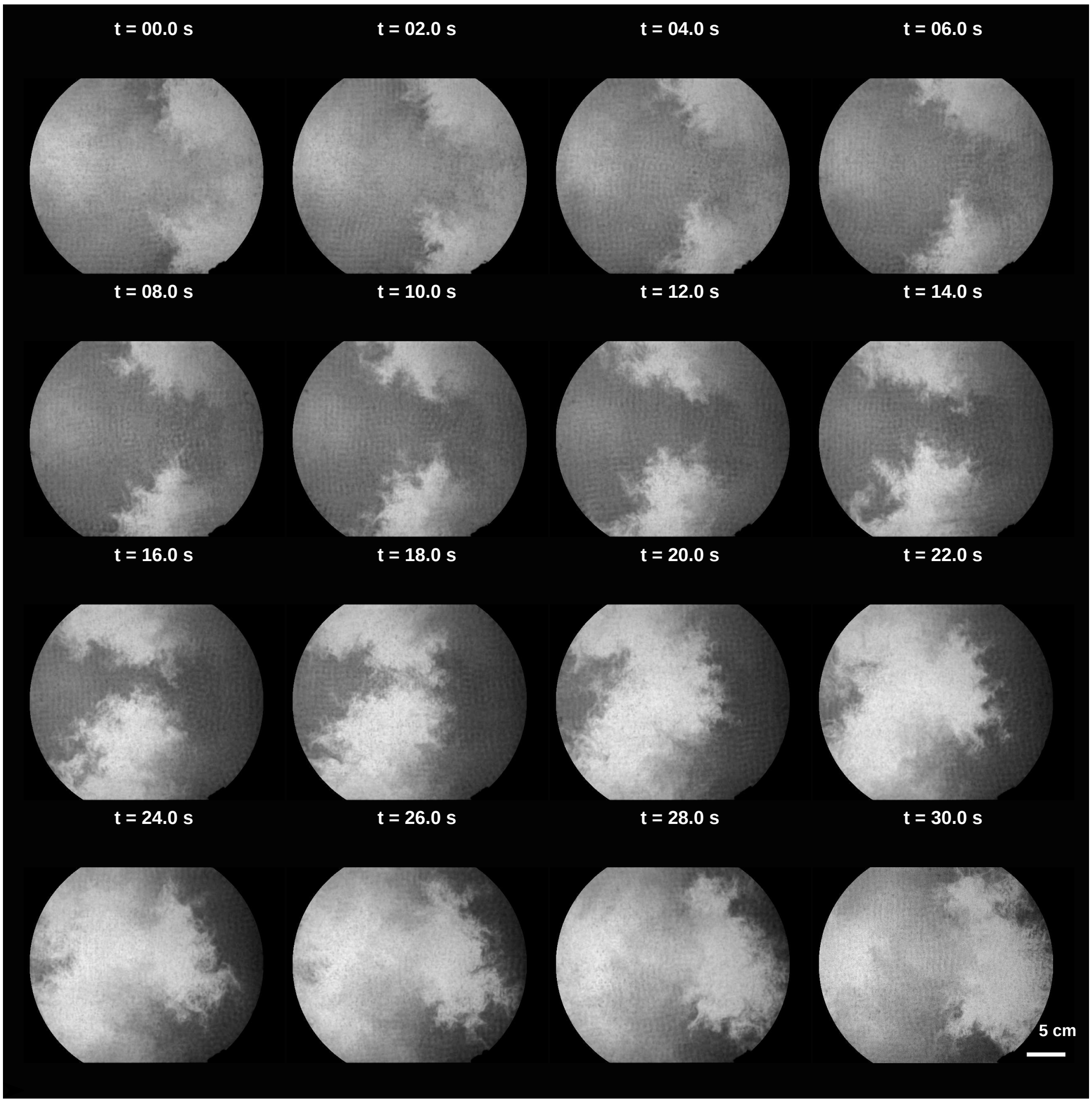

Fig. A.6: Exemplary image sequence of the boosted double spiral wave, movie M7.

A.8 Supplementary Movie M8.

Figure A.7 shows the image sequence of the boosted target wave for high forcing, Fig. 4.8 b. Forcing parameters: $f = 50\,\mathrm{Hz}$, $a_0 = 2.2\,\mathrm{g}$. Chemical parameters: Initial sulfuric acid concentration $[H_2SO_4] = 0.6\,\mathrm{M}$. A big target develops at the border of the container. Its curvature is small and the front is almost planar. Note the broad tail of the target wave related to the slower timescale of the backward reaction (see also discussion of Fig. 4.8 b). Also its leading front is less filamentous and smoother than the one of the target wave at low forcing (cf. movie M2). The typical rectangular Faraday waves due to the vertical forcing can be distinguished on the top of the fluid surface. Image processing of movie M8: Maximum and minimum values of the greyscales of the movie were adjusted to maximize the contrast.

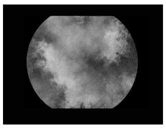

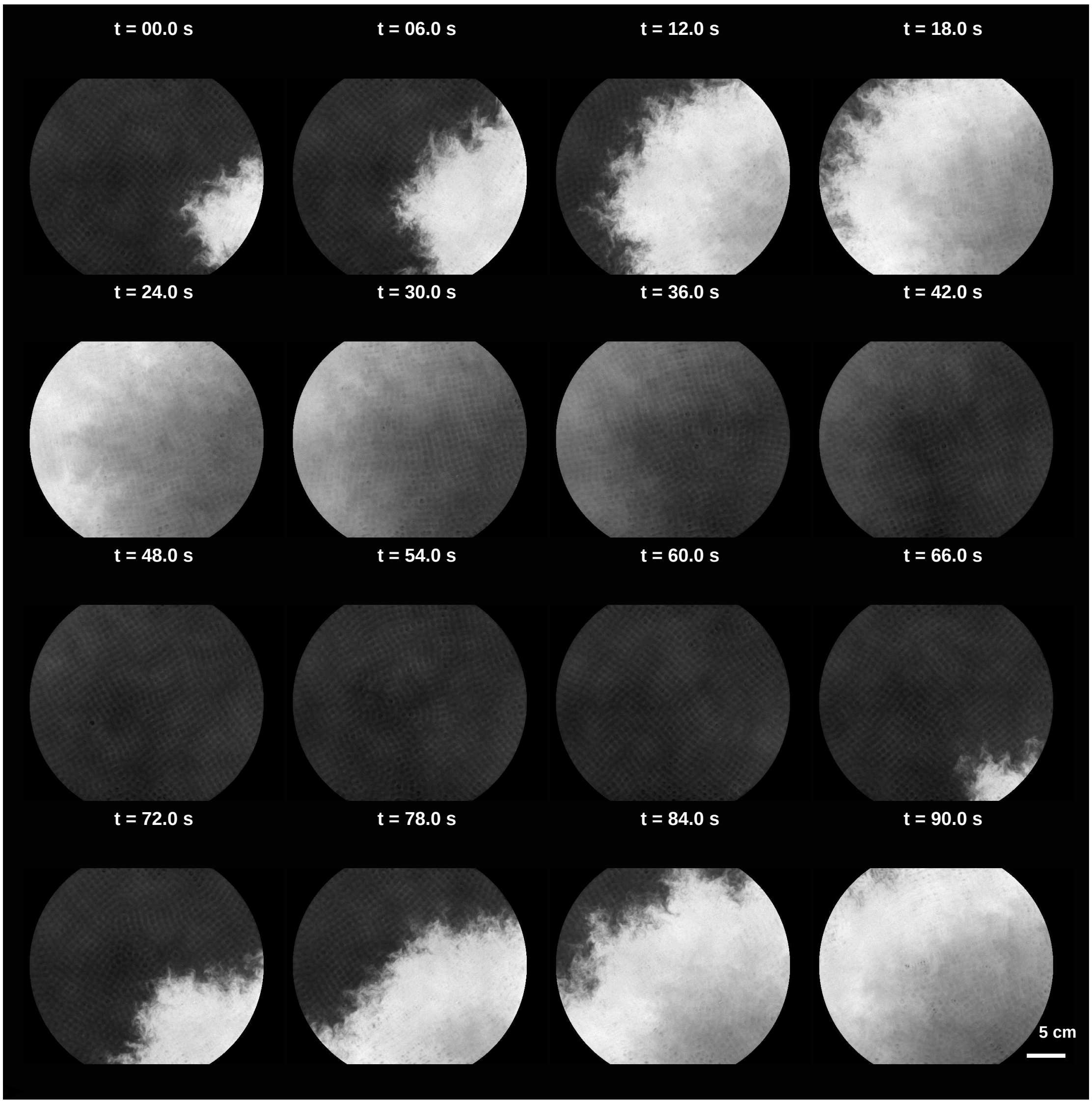

Fig. A.7: Exemplary image sequence of the boosted target wave, movie M8.

Bibliography

[1] Y. Kuramoto, *Chemical Oscillations, Waves and Turbulence*. Springer, Berlin Heidelberg, 1984.

[2] J. Murray, *Mathematical Biology*. Springer, Berlin Heidelberg, 1989.

[3] Z. Neufeld and E. Hernández-García, *Chemical and Biological Processes in Fluid Flows*. Imperial College Press, London, 2010.

[4] I. Prigogine, *Time, Structure and Fluctuations*. Nobel Lectures, Chemistry 1971-1980, World Scientific Publishing Co., Singapore, 1993, 1977.

[5] A. Golovin, B. Matkowsky, and V. Volpert, "Turing pattern formation in the brusselator model with superdiffusion," *SIAM Journal on Applied Mathematics*, vol. 69, no. 1, pp. 251–272, 2008.

[6] V. Gafiychuk and B. Datsko, "Pattern formation in a fractional reaction-diffusion," *Physica A*, vol. 365, p. 300306, 2006.

[7] V. Gafiychuk and B. Datsko, "Stability analysis and oscillatory structures in time-fractional reaction-diffusion systems," *Phys. Rev. E*, vol. 75, p. 055201, 2007.

[8] L. Hufnagel, D. Brockmann, and T. Geisel, "Forecast and control of epidemics in a globalized world," *Proceedings of the National Academy of Sciences of the United States of America*, vol. 101, no. 42, pp. 15124–15129, 2004.

[9] B. Porterie, N. Zekri, J. Clerc, and J. Loraud, "Modeling forest fire spread and spotting process with small world networks," *Combustion and Flame*, vol. 149, no. 1-2, pp. 63–78, 2007.

[10] F. Huhn, A. von Kameke, V. Pérez-Muñuzuri, M. J. Olascoaga, and F. J. Beron-Vera, "The impact of advective transport by the South Indian Ocean Countercurrent on the Madagascar plankton bloom," *Geophys. Res. Lett.*, vol. 39, p. L06602, 2012.

[11] R. Guimer, S. Mossa, A. Turtschi, and L. A. N. Amaral, "The worldwide air transportation network: Anomalous centrality, community structure, and cities' global roles," *Proceedings of the National Academy of Sciences*, vol. 102, no. 22, pp. 7794–7799, 2005.

[12] D. Brockmann, L. Hufnagel, and T. Geisel, "The scaling laws of human travel," *Nature*, vol. 439, pp. 462–465, 2006.

[13] G. Vallis, *Atmospheric and Oceanic Fluid Dynamics*. Cambridge England: Cambridge University Press, 2006.

[14] R. Benzi, S. Ciliberto, R. Tripiccione, C. Baudet, F. Massaioli, and S. Succi, "Extended self-similarity in turbulent flows," *Phys. Rev. E*, vol. 48, pp. R29–R32, Jul 1993.

[15] A. von Kameke, F. Huhn, and V. Pérez-Muñuzuri, "Asymptotic diffusion coefficients and anomalous diffusion in a meandering jet flow under environmental fluctuations," *Phys. Rev. E*, vol. 85, p. 017201, 2012.

[16] E. G. Altmann and H. Kantz, "Hypothesis of strong chaos and anomalous diffusion in coupled symplectic maps," *EPL*, vol. 78, no. 1, p. 10008, 2007.

[17] G. Fernández-García, D. I. Roncaglia, V. Pérez-Villar, A. P. Muñuzuri, and V. Pérez-Muñuzuri, "Chemical-wave dynamics in a vertically oscillating fluid layer," *Phys. Rev. E*, vol. 77, p. 026204, 2008.

[18] M. Faraday *Philos Trans. R. Soc. London*, vol. 121, pp. 319–340, 1831.

[19] J. Miles and D. Henderson *Annu. Rev. Fluid Mech.*, vol. 22, p. 143, 1990.

[20] A. von Kameke, F. Huhn, G. Fernández-García, A. P. Muñuzuri, and V. Pérez-Muñuzuri, "Double cascade turbulence and Richardson dispersion in a horizontal fluid flow induced by Faraday waves," *Phys. Rev. Lett.*, vol. 107, p. 074502, 2011.

[21] A. von Kameke, F. Huhn, G. Fernández-García, A. P. Muñuzuri, and V. Pérez-Muñuzuri, "Propagation of a chemical wave front in a quasi-two-dimensional superdiffusive flow," *Phys. Rev. E*, vol. 81, no. 6, p. 066211, 2010.

[22] R. Mantegna and H. Stanley, "Scaling behaviour in the dynamics of an economic index," *Nature*, vol. 376, pp. 46–49, 1995.

[23] M. Srokosz, G. Quartly, and J. Buck, "A possible plankton wave in the Indian Ocean," *Geophys. Res. Lett.*, vol. 31, p. L13301, 2004.

[24] R. Metzler and J. Klafter, "The restaurant at the end of the random walk: recent developments in the description of anomalous transport by fractional dynamics," *Journal of Physics A: Mathematical and General*, vol. 37, no. 31, p. R161, 2004.

[25] R. Kapral and K. Showalter, eds., *Chemical Waves and Patterns*. Kluwer Academic, Dordrecht, 1993.

[26] R. Field, E. Körös, and R. Noyes, "Oscillations in chemical systems. 2. Thorough analysis of temporal oscillations in the bromate-cerium-malonic acid system," *J. Am. Chem. Soc.*, vol. 94 (25), pp. 8649–8664, 1972.

[27] K. Kurin-Csörgei, A. Zhabotinsky, M. Orbán, and E. I.R., "Bromate-1,4-cyclohexanedione-ferroin gas-free oscillating reaction. 1. basic features and crossing wave patterns in a reaction-diffusion system without gel," *J. Phys. Chem.*, vol. 100, pp. 5393–5397, 1996.

[28] H. Haken, *Advanced Synergetics*. Springer-Verlag, Berlin, 1987.

[29] R. Field and R. Noyes, "Explanation of spatial band propagation in the Belousov reaction," *Nature*, vol. 237, p. 390, 1972.

[30] J. J. Tyson, "Analytic representation of oscillations, excitability, and traveling waves in a realistic model of the Belousov-Zhabotinskii reaction," *The Journal of Chemical Physics*, vol. 66(3), pp. 905–915, 1977.

[31] J. J. Tyson, "Oscillations, bistability, and echo waves in models of the Belousov-Zhabotinskii reaction," *Annals New York Academy of Sciences*, pp. 279–295, 1979.

[32] E. Mori, I. Schreiber, and J. Ross, "Profiles of chemical waves in the ferroin-catalyzed Belousov-Zhabotinskii reaction," *The Journal of Physical Chemistry*, vol. 95, no. 23, pp. 9359–9366, 1991.

[33] J. Guiu-Souto, J. Carballido-Landeira, and A. P. Muñuzuri, "Characterizing topological transitions in a turing-pattern-forming reaction-diffusion system," *Phys. Rev. E*, vol. 85, p. 056205, 2012.

[34] V. P.-M. nuzuri, C. Souto, M. Gómez-Gesteira, A. M. nuzuri, V. Davydov, and V. Pérez-Villar, "Use of v-shaped stable patterns to study high negative curvature-velocity dependence of an excitable medium," *Physica D: Nonlinear Phenomena*, vol. 94, no. 3, pp. 148 – 156, 1996.

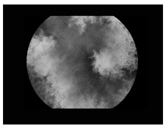

[35] A. Mikhailov, *Foundations of synergetics I: Distributed active systems.* Springer, 1990.

[36] A. Mikhailov and V. Zykov, "Spiral waves in weakly exitable media," *In: Kapral, R. & Showalter, K. Chemical waves and patterns Kluwer Academic Publishers, Dordrecht*, 1995.

[37] G. Guigas and M.Weiss, "Sampling the cell with anomalous diffusion - The discovery of slowness," *Biophysical Journal*, vol. 94, p. 9094, 2008.

[38] T. Tél, A. de Moura, C. Grebogi, and G. Krolyi, "Chemical and biological activity in open flows: A dynamical system approach," *Physics Reports*, vol. 413, no. 23, pp. 91 – 196, 2005.

[39] P. Manneville, *Instabilities, Chaos and Turbulence*. Imperial College Press, London, 2004.

[40] C. Foias, O. Manley, R. Rosa, and R. Temam, *Navier-Stokes-Equations and Turbulence*. Cambridge University Press, 2001.

[41] S. B. Pope, *Turbulent Flows*. Cambridge University Press, 2000.

[42] A. Crisanti, M. Falcioni, G. Paladin, and A. Vulpiani, "Lagrangian chaos: Transport, mixing and diffusion in fluids," *La Rivista del Nuovo Cimento*, vol. 14 (2), p. 1, 1991.

[43] P. K. Kundu and I. M. Cohen, *Fluid Mechanics*. Academic press, An imprint of Elsevier Science, 1990.

[44] L. Richardson, *Weather Prediction by Numerical Process. Cambridge*. University Press (Reprinted by Dover Publications, New York, 1965), 1922.

[45] J. LaCasce, "Statistics from Lagrangian observations," *Progress in Oceanography*, vol. 77, no. 1, pp. 1 – 29, 2008.

[46] L. A. Y. Mikhailov, Alexander S., *Foundations of Synergetics II*, vol. 52. Springer-Verlag (Berlin, Heidelberg), 1991.

[47] A. S. Monin and A. M. Yaglom, *Statistical Fluid Mechanics: Mechanics of Turbulence*. Dover Pubns, 2007 (1965).

[48] R. Ecke, "The turbulence problem: An experimentalist's perspective," *Los Alamos Science*, vol. 29, pp. 124–140, 2005.

[49] S. P. Singh and S. Mittal, "Energy spectra of flow past a circular cylinder," *International Journal of Computational Fluid Dynamics*, vol. 18, no. 8, pp. 671–679, 2004.

[50] P. Fischer, C.-H. Bruneau, and H. Kellay, "Multiresolution analysis for 2D turbulence. Part 2: A physical interpretation," *Discrete and Continuous Dynamical Systems - Series B*, vol. 7(4), pp. 717–734, 2007.

[51] M. Lesieur, *Turbulence in Fluids*. Kluwer Academic Publishers, 1990.

[52] E. Gkioulekas and K.-K. Tung, "Recent developments in understanding two-dimensional turbulence and the nastrom-gage spectrum," *Journal of Low Temperature Physics*, vol. 145, pp. 25–57, 2006.

[53] P. Tabeling, "Two-dimensional turbulence: a physicist approach," *Phys. Rep.*, vol. 362, pp. 1–62, 2002.

[54] M. M. Farazmand, *Controlling the Dual Cascade of Two-dimensional Turbulence*. Open Access Dissertations and Theses (Paper 4251), 2010.

[55] R. H. Kraichnan, "Inertial ranges in two-dimensional turbulence," *Physics of Fluids*, vol. 10, no. 7, pp. 1417–1423, 1967.

[56] G. Boffetta and R. Ecke, "Two-dimensional turbulence," *Annu. Rev. Fluid Mech.*, vol. 44, pp. 427–451, 2012.

[57] S. Danilov and D. Gurarie, "Quasi-two-dimensional turbulence," *Physics-Uspekhi*, vol. 43(9), pp. 863–900, 2000.

[58] M. A. Rutgers, "Forced 2d turbulence: Experimental evidence of simultaneous inverse energy and forward enstrophy cascades," *Phys. Rev. Lett.*, vol. 81, pp. 2244–2247, 1998.

[59] A. Cenedese, S. Espa, and M. Miozzi, "Experimental study of two-dimensional turbulence using feature tracking," *http://www.scientificcommons.org/42319187*, 2008.

[60] G. Boffetta and S. Musacchio, "Evidence for the double cascade scenario in two-dimensional turbulence," *Phys. Rev. E*, vol. 82, p. 016307, 2010.

[61] H. Xia, D. Byrne, G. Falkovich, and M. Shats, "Upscale energy transfer in thick turbulent fluid layers," *Nature Physics*, vol. 7, pp. 321–324, 2011.

[62] R. H. Kraichnan, "Eddy viscosity in two and three dimensions," *Journal of the Atmospheric Sciences*, vol. 33(8), p. 15211536, 1976.

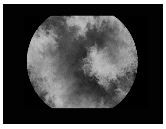

[63] G. Boffetta, A. Cenedese, S. Espa, and S. Musacchio, "Effects of friction on 2d turbulence: An experimental study of the direct cascade," *EPL*, vol. 71, no. 4, p. 590, 2005.

[64] L. Biferale, S. Musacchio, and F. Toschi, "Inverse energy cascade in three-dimensional isotropic turbulence," *Phys. Rev. Lett.*, vol. 108, p. 164501, 2012.

[65] W. McComb, *The physics of fluid turbulence*. Oxford University Press, Oxford, 1990.

[66] G. Eyink, "Local energy flux and the refined similarity hypothesis," *Journal of Statistical Physics*, vol. 78, pp. 335–351, 1995.

[67] D. Kelley and N. Ouellette, "Spatiotemporal persistence of spectral fluxes in two-dimensional weak turbulence," *Phys. Fluids*, vol. 23, p. 045103, 2011.

[68] U. Frisch, *Turbulence The Legacy of A. N. Kolmogorov*. Cambridge University Press, 1995.

[69] E. Lindborg, "Can the atmospheric kinetic energy spectrum be explained by twodimensional turbulence?," *Journal of Fluid Mechanics*, vol. 388, pp. 259–288, 1999.

[70] M. Shlesinger and J. Klafter, "Random walks in liquids," *J. Phys. Chem.*, vol. 93, pp. 7023–7026, 1989.

[71] D. del Castillo-Negrete, *Anomalous Transport*, ch. 6, pp. 163–211. Wiley, Weinheim, 2008.

[72] R. Adrian, "Twenty years of particle image velocimetry," *Exp. Fluids*, vol. 39, p. 159, 2005.

[73] K. D. Jensen, "Flow measurements," *J. of the Braz. Soc. of Mech. Sci. & Eng.*, vol. Vol. XXVI, No. 4, p. 401, 2004.

[74] A. Majda and P. Kramer, "Simplified models for turbulent diffusion: Theory, numerical modelling, and physical phenomena," *Phys. Rep.*, vol. 314, pp. 237–574, 1999.

[75] G. Boffetta, A. Celani, M. Cencini, G. Lacorata, and A. Vulpiani, "Nonasymptotic properties of transport and mixing," *Chaos: An Interdisciplinary Journal of Nonlinear Science*, vol. 10, no. 1, pp. 50–60, 2000.

[76] M. Isichenko, "Percolation, statistical topography, and transport in random media," *Rev. Mod. Phys.*, vol. 64(4), pp. 961–1043, 1992.

[77] E. W. Montroll and G. H. Weiss, "Random walks on lattices. II," *J. Math. Phys.*, vol. 6(2), pp. 167–181, 1965.

[78] G. Zaslavsky, "Chaos, fractional kinetics, and anomalous transport," *Physics Reports*, vol. 371, pp. 461–580, 2002.

[79] T. B. Benjamin and F. Ursell, "The stability of the plane free surface of a liquid in vertical periodic motion," *Proceedings of the Royal Society of London. Series A. Mathematical and Physical Sciences*, vol. 225, no. 1163, pp. 505–515, 1954.

[80] W. Zhang and J. Vials, "Numerical study of pattern formation in weakly damped parametric surface waves," *Physica D: Nonlinear Phenomena*, vol. 116, no. 12, pp. 225 – 243, 1998.

[81] H. W. Müller, "Periodic triangular patterns in the Faraday experiment," *Phys. Rev. Lett.*, vol. 71, pp. 3287–3290, Nov 1993.

[82] K. Kumar and L. Tuckerman, "Parametric instability of the interface between two fluids," *J. of Fluid Mech.*, vol. 279, pp. 49–68, 1994.

[83] N. Tufillaro, R. Ramshankar, and J. Gollub, "Oder-disorder transition in capillary ripples," *Phys. Rev. Lett.*, vol. 62, p. 4, 1989.

[84] A. Kudrolli and J. Gollub, "Patterns and spatiotemporal chaos in parametrically forced surface waves: a systematic survey at large aspect ratio," *Physica D*, vol. 97, pp. 133–154, 1996.

[85] P. Wright and J. Saylor, "Patterning of particulate films using Faraday waves," *Rev. Sci. Instrum.*, vol. 74(9), pp. 4063–4070, 2003.

[86] R. Ramshankar, D. Berlin, and J. P. Gollub, "Transport by capillary waves. Part I. Particle trajectories," *Physics of Fluids A: Fluid Dynamics*, vol. 2, no. 11, pp. 1955–1965, 1990.

[87] B. Haslam and P. Ronney, "Fractal properties of propagating fronts in a strongly stirred fluid," *Phys. Fluids*, vol. 7, pp. 1931–1937, 1995.

[88] E. Schröder, J. S. Andersen, M. T. Levinsen, P. Alstrom, , and W. I. Goldburg, "Relative particle motion in capillary waves," *Phys. Rev. Lett.*, vol. 76(25), pp. 4717–4720, 1996.

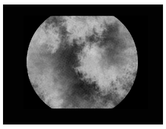

[89] A. Hansen, E. Schröder, P. Alstrom, J. S. Andersen, and M. T. Levinsen, "Fractal particle trajectories in capillary waves: Imprint of wavelength," *Phys. Rev. Lett.*, vol. 79(10), pp. 1845–1848, 1997.

[90] I. Szalai, K. Kurin-Csorgei, I. R. Epstein, and M. Orban, "Dynamics and mechanism of bromate oscillators with 1,4-cyclohexanedione," *The Journal of Physical Chemistry A*, vol. 107, no. 47, pp. 10074–10081, 2003.

[91] K. Kereszturi and I. Szalai, "Dynamics of bromate oscillators with 1,4-cyclohexanedione in a continuously fed stirred tank reactor," *Chemical Physics Letters*, vol. 428, no. 46, pp. 288 – 292, 2006.

[92] P. Foerster, S. Müller, and B. Hess, "Critical size and curvature of wave formation in an excitable chemical medium," *Proc. Natl. Acad. Sci. USA*, vol. 86, pp. 6831–6834, 1989.

[93] M. Westra and W. Brinks, D.J. Van de Water, "Patterns of Faraday waves," *J. Fluid Mech.*, vol. 469, pp. 1–32, 2003.

[94] Y. Y. Kalishyn, M. Rachwalska, V. O. Khavrus, and P. E. Strizhak, "The effect of oxygen on time-dependent bifurcations in the Belousov-Zhabotinsky oscillating chemical reaction in a batch," *Phys. Chem. Chem. Phys.*, vol. 7, pp. 1680–1686, 2005.

[95] N. T. Ouellette, P. J. J. O'Malley, and J. P. Gollub, "Transport of finite-sized particles in chaotic flow," *Phys. Rev. Lett.*, vol. 101, p. 174504, 2008.

[96] N. Mori and K.-A. Chang, "Introduction to mpiv," *http://www.oceanwave.jp/softwares/mpiv/index.php*, 2003.

[97] O. Cardoso, D. Marteau, and P. Tabeling, "Quantitative experimental study of the free decay of quasi-two-dimensional turbulence," *Phys. Rev. E*, vol. 49, pp. 454–461, 1994.

[98] D. F. Swinehart, "The Beer-Lambert law," *Journal of Chemical Education*, vol. 39, no. 7, p. 333, 1962.

[99] D. T. Newcombe, T. J. Cardwell, R. W. Cattrall, and S. D. Kolev, "An optical redox chemical sensor based on ferroin immobilised in a nafion membrane," *Analytica Chimica Acta*, vol. 401, no. 12, pp. 137 – 144, 1999.

[100] J. Saylor and A. Kinard, "Simulation of particle deposition beneath Faraday waves in thin liquid films," *Phys. Fluids*, vol. 17, pp. 047106–1, 2005.

[101] P. Engels, C. Atherton, and M. A. Hoefer, "Observation of Faraday waves in a Bose-Einstein condensate," *Phys. Rev. Lett.*, vol. 98, p. 095301, Feb 2007.

[102] Y. Couder, A. Boudaoud, S. Protire, and E. Fort, "Walking droplets, a form of wave-particle duality at macroscopic scale?," *Europhysics News*, vol. 41(1), pp. 14–18, 2010.

[103] O. Mesquita, S. Kane, and J. Gollub, "Transport by capillary waves: Fluctuating stokes drift," *Phys. Rev. A*, vol. 45(6), pp. 3700–3705, 1992.

[104] G. Fernández-García and V. Pérez-Muñuzuri, "Superdiffusive wave front propagation in a chemical active flow," *The European Physical Journal Special Topics*, vol. 165(1), pp. 169–174, 2008.

[105] M. Jullien, "Dispersion of passive tracers in the direct enstrophy cascade: Experimental observations," *Phys. Fluids*, vol. 15(8), pp. 2228–2237, 2003.

[106] M. M. Farazmand, N. K.-R. Kevlahan, and B. Protas, "Controlling the dual cascade of two-dimensional turbulence," *Journal of Fluid Mechanics*, vol. 668, pp. 202–222, 2011.

[107] G. Falkovich, A. Weinberg, P. Denissenko, and S. Lukaschuk, "Floater clustering in a standing wave," *Nature*, vol. 435, pp. 1045 –1046, 2005.

[108] S. L. P. Denissenko, G. Falkovich, "How waves affect the distribution of particles that float on a liquid surface," *Phys. Rev. Lett.*, vol. 97, p. 244501, 2006.

[109] Z. Xiao, M. Wan, S. Chen, and G. L. Eyink, "Physical mechanism of the inverse energy cascade of two-dimensional turbulence: a numerical investigation," *J. Fluid Mech.*, vol. 619, pp. 1–44, 2009.

[110] S. Chen, R. E. Ecke, G. L. Eyink, M. Rivera, M. Wan, and Z. Xiao, "Physical mechanism of the two-dimensional inverse energy cascade," *Phys. Rev. Lett.*, vol. 96, p. 084502, Feb 2006.

[111] G. Boffetta, M. Cencini, S. Espa, and G. Querzoli, "Chaotic advection and relative dispersion in an experimental convective flow," *Physics of Fluids*, vol. 12, no. 12, pp. 3160–3167, 2000.

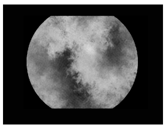

[112] O. G. Bakunin, *Reviews of Plasma Physics Volume*, vol. 24o, ch. 2 Correlations and Anomalous Transport Models, pp. 53–203. 2008.

[113] G. Boffetta and I. Sokolov, "Statistics of two-particle dispersion in two-dimensional turbulence," *Phys. Fluids*, vol. 14, pp. 3224–3232, 2002.

[114] S. Ott and J. Mann, "An experimental investigation of the relative diffusion of particle pairs in three-dimensional turbulent flow," *J. Fluid Mech.*, vol. 422, pp. 207–223, 2000.

[115] M. Rivera and R. Ecke, "Pair dispersion and doubling time statistics in two-dimensional turbulence," *Phys. Rev. Lett.*, vol. 95, p. 194503, 2005.

[116] M. Bourgoin, N. T. Ouellette, H. Xu, J. Berg, and E. Bodenschatz, "The role of pair dispersion in turbulent flow," *Science*, vol. 311, no. 5762, pp. 835–838, 2006.

[117] E. Martin and J. Vega, "The effect of surface contamination on the drift instability of standing Faraday waves," *Journal of Fluid Mechanics*, vol. 546, pp. 203–225, 2006.

[118] A. C. Poje, A. C. Haza, T. M. Özgökmen, M. G. Magaldi, and Z. D. Garraffo, "Resolution dependent relative dispersion statistics in a hierarchy of ocean models," *Ocean Modelling*, vol. 31, no. 12, pp. 36 – 50, 2010.

[119] J. Paret and P. Tabeling, "Experimental observation of the two-dimensional inverse energy cascade," *Phys. Rev. Lett.*, vol. 79, pp. 4162–4165, 1997.

[120] J. Paret, M. Jullien, and P. Tabeling, "Vorticity statistics in the two-dimensional enstrophy cascade," *Phys. Rev. Lett.*, vol. 83(17), pp. 3418–3421, 1999.

[121] C. N. Baroud, B. Plapp, Brendan, Z.-S. She, and H. L. Swinney, "Anomalous self-similarity in a turbulent rapidly rotating fluid," *Phys. Rev. Lett.*, vol. 88, p. 114501, Feb 2002.

[122] G. Lewis and H. Swinney, "Velocity structure functions, scaling, and transitions in high-Reynolds-number Couette-Taylor flow," *Phys. Rev. E*, vol. 59(5), pp. 5457–5467, 1999.

[123] J. Paret and P. Tabeling, "Intermittency in the two-dimensional inverse cascade of energy: Experimental observations," *Phys. Fluids*, vol. 10, p. 3126, 1998.

[124] H. Kellay and W. Goldburg, "Two-dimensional turbulence: a review of some recent experiments," *Rep. Prog. Phys.*, vol. 65, p. 845894, 2002.

[125] J. Vega, E. Knobloch, and C. Martel, "Nearly inviscid Faraday waves in annular containers of moderately large aspect ratio," *Physica D: Nonlinear Phenomena*, vol. 154, pp. 3–4, 2001.

[126] E. Martin, C. Martel, and J. Vega, "Drift instability of standing Faraday waves," *J. Fluid Mech.*, vol. 467, pp. 57–79, 2002.

[127] R. Kapral and K. Showalter, *Chemical waves and patterns*. Kluwer Academic Publishers, Dordrecht, 1995.

[128] Y. Yua, L. Santos, L. Mattiace, M. Costa, L. Ferreira, K. Benabou, A. Kime, J. Abrahams, M. Bennett, and R. Rozental, "Reentrant spiral waves of spreading depression cause macular degeneration in hypoglycemic chicken retina," *PNAS*, vol. 109(7), pp. 2585–2589, 2012.

[129] L. Stefan, F. H. Fenton, B. G. Kornreich, A. Squires, P. Bittihn, D. Hornung, M. Zabel, J. Flanders, A. Gladuli, L. Campoy, E. M. Cherry, G. Luther, G. Hasenfuss, V. I. Krinsky, A. Pumir, R. F. Gilmour, and E. Bodenschatz, "Low-energy control of electrical turbulence in the heart," *Nature*, vol. 475, pp. 235–241, 2011.

[130] V. Pérez-Muñuzuri, R. Aliev, B. Vasiev, V. Pérez-Villar, and V. Krinsky, "Super-spiral structures in an excitable medium," *Nature*, vol. 353, pp. 740–742, 1991.

[131] R. Grigoriev and H. Schuster, *Transport and mixing in laminar flows*. Wiley-VCH, Berlin, 2011.

[132] V. Smetacek, C. Klaas, V. Strass, P. Assmy, M. Montresor, B. Cisewski, N. Savoye, A. Webb, F. d'Ovidio, J. Arrieta, U. Bathmann, R. Bellerby, G. M. Berg, P. Croot, S. Gonzalez, J. Henjes, G. J. Herndl, L. J. Hoffmann, H. Leach, M. Losch, M. M. Mills, C. Neill, I. Peeken, R. Rottgers, O. Sachs, E. Sauter, M. M. Schmidt, J. Schwarz, A. Terbruggen, and D. Wolf-Gladrow, "Deep carbon export from a southern ocean iron-fertilized diatom bloom," *Nature*, vol. 487, pp. 313–319, 2012.

[133] S. Derevyanko, G. Falkovich, and S. Turitsyn, "Evolution of non-uniformly seeded warm clouds in idealized turbulent conditions," *New J. Phys.*, vol. 10, p. 075019, 2008.

[134] P. Ronney, B. Haslam, and N. Rhys, "Front propagation rates in randomly stirred media," *Phys. Rev. Lett.*, vol. 74, p. 3804, 1995.

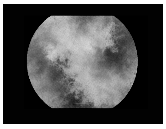

[135] J. R. Boehmer and T. H. Solomon, “Fronts and trigger wave patterns in an array of oscillating vortices,” *EPL*, vol. 83, no. 5, p. 58002, 2008.

[136] P. E. Arratia and J. P. Gollub, “Predicting the progress of diffusively limited chemical reactions in the presence of chaotic advection,” *Phys. Rev. Lett.*, vol. 96, p. 024501, 2006.

[137] J. Butcher, *Numerical Methods for Ordinary Differential Equations*. John Wiley & Sons, Ltd, Chichester, UK., 2005.

[138] V. Pérez-Muñuzuri and F. Huhn, “The role of mesoscale eddies time and length scales on phytoplankton production,” *Nonlin. Processes Geophys.*, vol. 17, pp. 177–186, 2010.

[139] F. Huhn, A. von Kameke, A. Muñuzuri, and V. Pérez-Muñuzuri *In preparation*, 2012.

[140] L. Kuhnert, H.-J. Krug, and L. Pohlmann, “Velocity of trigger waves and temperature dependence of autowave processes in the Belousov-Zhabotinsky reaction,” *J. Phys. Chem.*, vol. 89, pp. 2022–2026, 1985.

[141] H. N. Brandenburg, A. and N. Babkovskaia, “Turbulent front speed in the Fisher equation: Dependence on Damköhler number,” *Phys. Rev. E*, vol. 83, p. 016304, 2011.

[142] J. Dockery and J. Keener, J.P.and Tyson, “Dispersion of travelling waves in the Belousov-Zhabotinskii reaction,” *Physica D*, vol. 30, pp. 177–191, 1988.

[143] C. Koudella and Z. Neufeld, “Reaction front propagation in a turbulent flow.,” *Phys. Rev. E*, vol. 70, p. 026307, 2004.

[144] T. Wyatt, “The biology of Oikopleura dioica and Fritillaria borealis in the Southern Bight,” *Mar. Biol.*, vol. 22, pp. 137–158, 1973.

[145] D. Dubois, “Simulation of the spatial structuration of a patch of predator-prey plankton populations in the Southern Bight of the North Sea,” *Mem. Soc. Roy. Sci. Liege, 6th series*, vol. VII, pp. 75–82, 1975.

[146] R. Fisher, “The wave of advance of advatageous genes,” *Ann. Eugenic.*, vol. 7, pp. 355–369, 1937.

[147] A. Bracco, J. von Hardenberg, A. Provenzale, J. Weiss, and J. McWilliams, “Dispersion and mixing in quasigeostrophic turbulence,” *Phys. Rev. Lett.*, vol. 92(8), pp. 084501–1, 2004.

[148] R. Castilla, J. M. Redondo, P. J. Gámez-Montero, and A. Babiano, "Particle dispersion processes in two-dimensional turbulence: a comparison with 2-d kinematic simulation.," *Nonlin. Processes Geophys.*, vol. 14, p. 139151, 2007.

[149] A. Provenzale, A. Babiano, and B. Villone, "Single-particle trajectories in two-dimensional turbulence," *Chaos, Solitons & Fractals*, vol. 5(10), pp. 2055–2071, 1995.

[150] D. Elhmaidi, H. Nefzi, X. Carton, and T. Lili, "Particle dispersion in the western mediterranean basin," *The Open Oceanography Journal*, vol. 4, pp. 137–143, 2010.

[151] M. Shlesinger, *Anomalous Transport*. Wiley, Weinheim, 2008.

[152] R. Ramshankar and J. P. Gollub, "Transport by capillary waves. Part II: Scalar dispersion and structure of the concentration field," *Physics of Fluids A: Fluid Dynamics*, vol. 3, no. 5, pp. 1344–1350, 1991.

[153] T. H. Solomon, E. R. Weeks, and H. L. Swinney, "Observation of anomalous diffusion and Lévy flights in a two-dimensional rotating flow," *Phys. Rev. Lett.*, vol. 71, pp. 3975–3978, 1993.

[154] T. H. Solomon, E. R. Weeks, and H. L. Swinney, "Chaotic advection in a two-dimensional flow: Lévy flights and anomalous diffusion," *Physica D*, vol. 76, pp. 70–84, 1994.

[155] R. Gorenflo, F. Mainardib, D. Morettic, G. Pagninid, and P. Paradisie *Physica A*, vol. 305, pp. 106–112, 2002.

[156] R. Mantegna and H. Stanley, "Stochastic process with ultraslow convergence to a gaussian: The truncated lévy flight," *Phys. Rev. Lett.*, vol. 73, p. 22, 1994.

[157] A. Blumen, G. Zumofen, and J. Klafter, "Transport aspects in anomalous diffusion: Lévy walks," *Phys. Rev. A*, vol. 40, p. 7, 1989.

[158] T. Solomon, A. T. Lee, and M. Fogleman, "Resonant flights and transient superdiffusion in a time-periodic, two-dimensional flow," *Physica D: Nonlinear Phenomena*, vol. 157, no. 12, pp. 40 – 53, 2001.

[159] M. Fogleman, M. Fawcett, and P. T.H. Solomon *Phys. Rev. E*, vol. 63, p. 020101(R), 2001.

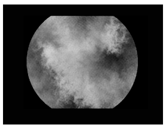

[160] D. Zanette, "Persistence in lévy-flight anomalous diffusion," *Phys. Rev. E*, vol. 55, pp. 6632–6635, 1997.

[161] R. Mancinelli, D. Vergni, and A. Vulpiani, "Superfast front propagation in reactive systems with non-Gaussian diffusion," *Europhys. Lett.*, vol. 60(4), pp. 532–538, 2002.

[162] G. Zumofen and J. Klafter, "Reaction dynamics controlled by enhanced diffusion," *Phys. Rev. E*, vol. 50(6), pp. 5119–5122, 1994.

[163] M. Paoletti and T. Solomon, "Front propagation and mode-locking in an advection-reaction-diffusion system," *Phys. Rev. E*, vol. 72, p. 046204, 2005.

[164] M. Paoletti, C. R. Nugent, and T. H. Solomon, "Synchronization of oscillating reactions in an extended fluid system," *Phys. Rev. Lett.*, vol. 96, p. 124101, 2006.

[165] R. Gorenflo and F. Mainardi, *Anomalous Transport*. Wiley, Weinheimfo, 2008.

[166] O. Steinbock, C. Hamik, and B. Steinbock, "Oxygen inhibition of oscillations in the belousov-zhabotinsky reaction," *J. Phys. Chem. A*, vol. 104, pp. 6411–6415, 2000.

[167] J. Bouchaud and A. Georges, "Comment on "stochastic pathway to anomalous diffusion"," *Phys. Rev. A*, vol. 41, p. 1156, 1990.

[168] X.-J. Wang, "Dynamical sporadicity and anomalous diffusion in the lévy motion," *Phys. Rev. A*, vol. 45(12), pp. 8407–8417, 1992.

[169] J. Klafter, A. Blumen, and M. Shlesinger, "Stochastic pathway to anomalous diffusion," *Phys. Rev. A*, vol. 35(7), pp. 3081–3085, 1987.

[170] M. Shlesinger, B. West, and J. Klafter, "Lévy dynamics of enhanced diffusion: Application to turbulence," *Phys. Rev. Lett.*, vol. 58(11), pp. 1100–1103, 1987.

[171] R. Mantegna, "Fast, accurate algorithm for numerical simulation of lévy stable stochastic processes," *Phys. Rev. E*, vol. 49(5), pp. 4677–4683, 1994.

[172] B. West and W. Deering, "Fractal physiology for physicists: Lvy statistics," *Physics Reports*, vol. 246(1-2), pp. 1–100, 1994.

[173] D. Brockmann and L. Hufnagel, "Front propagation in reaction-superdiffusion dynamics: Taming lévy flights with fluctuations," *Phys. Rev. Lett.*, vol. 98, p. 178301, 2007.

[174] D. del Castillo-Negrete, B. Carreras, and V. Lynch, "Front dynamics in reaction-diffusion systems with levy flights: A fractional diffusion approach," *Phys. Rev. Lett.*, vol. 91(1), pp. 018302–1, 2003.

[175] S. Edouard, B. Legras, F. Lefèvre, and R. Eymard, "The effect of small-scale inhomogeneities on ozone depletion in the Arctic," *Nature*, vol. 384, pp. 444–447, 1996.

[176] E. Hanert, "Front dynamics in a two-species competition model driven by Lévy flights," *Journal of Theoretical Biology*, vol. 300, no. 0, pp. 134–142, 2012.

[177] M. Markus and B. Hess, "Isotropic cellular automaton for modelling excitable media," *Nature*, vol. 347, pp. 56–58, 1990.

[178] R. Brune private communication.

[179] W. Janke, *Pseudo Random Numbers: Generation and Quality Checks published in Quantum Simulations of Complex Many-Body Systems: From Theory to Algorithms, Lecture Notes*, vol. 10, pp. 447–458. John von Neumann Institute for Computing, Jülich, NIC Series, 2002.

[180] R. Albert, H. Jeong, and A.-L. Barabasi, "Error and attack tolerance of complex networks," *Nature*, vol. 406, pp. 378–382, 2000.

[181] R. Wagner, "Mersennetwister.h mersenne twister random number generator – a c++ class mtrand based on code by makoto matsumoto, takuji nishimura, and shawn cokus richard j. wagner v1.1 28 september 2009 wagnerr@umich.edu."

[182] M. Matsumoto and T. Nishimura, "Mersenne twister: A 623-dimensionally equidistributed uniform pseudo-random number generator," *ACM Transactions on Modeling and Computer Simulation*, vol. 8(1), pp. 3–30, 1998.

[183] N. Vladimirov, R. D. Traub, and Y. Tu, "Wave speed in excitable random networks with spatially constrained connections," *PLoS ONE*, vol. 6, no. 6, p. e20536, 2011.

[184] D. del Castillo-Negrete, "Truncation effects in superdiffusive front propagation with Lévy flights," *Phys. Rev. E*, vol. 79, p. 031120, 2009.

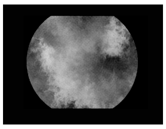

[185] I. Mezić, S. Loire, V. Fonoberov, and P. Hogan, "A new mixing diagnostic and Gulf oil spill movement," *Science*, vol. 330, no. 6003, pp. 486–489, 2010.

[186] A. Bracco, S. Clayton, and C. Pasquero, "Horizontal advection, diffusion, and plankton spectra at the sea surface," *J. Geophys. Res.*, vol. 114, p. C02001, 2009.

[187] R. K. Cowen, C. B. Paris, and A. Srinivasan, "Scaling of connectivity in marine populations," *Science*, vol. 311, no. 5760, pp. 522–527, 2006.

[188] E. Shuckburgh, H. Jones, J. Marshall, and C. Hill, "Understanding the regional variability of eddy diffusivity in the pacific sector of the southern ocean," *J. Phys. Oceanogr.*, vol. 39, p. 20112023, 2009.

[189] G. Lacorata, E. Aurell, B. Legras, and A. Vulpiani, "Evidence for a $k^{5/3}$ spectrum from the EOLE Lagrangian balloons in the low stratosphere," *J. Atmos. Sci.*, vol. 61, p. 29362942, 2004.

[190] M. F. Shlesinger, G. M. Zaslavsky, and J. Klafter, "Strange kinetics," *Nature*, vol. 363, pp. 31–37, 1993.

[191] T. Geisel and S. Thomae, "Anomalous diffusion in intermittent chaotic systems," *Phys. Rev. Lett.*, vol. 52, pp. 1936–1939, 1984.

[192] G. Drazer and D. H. Zanette, "Experimental evidence of power-law trapping-time distributions in porous media," *Phys. Rev. E*, vol. 60, pp. 5858–5864, 1999.

[193] R. Bettin, R. Manella, B. West, and P. Grigolini, "Influence of the environment on anomalous diffusion," *Phys.Rev. E*, vol. 51(1), pp. 212–219, 1995.

[194] E. Floriani, R. Mannella, and P. Grigolini, "Noise-induced transition from anomalous to ordinary diffusion: The crossover time as a function of noise intensity," *Phys.Rev. E*, vol. 52(6), pp. 5910–5917, 1995.

[195] G. Boffetta, D. del Castillo-Negrete, C. López, G. Pucacco, and A. Vulpiani, "Diffusive transport and self-consistent dynamics in coupled maps," *Phys. Rev. E*, vol. 67, p. 026224, 2003.

[196] C. F. Karney, A. B. Rechester, and R. B. White, "Effect of noise on the standard mapping," *Physica D: Nonlinear Phenomena*, vol. 4, no. 3, pp. 425 – 438, 1982.

[197] A. M. Bower, "A simple kinematic mechanism for mixing fluid parcels across a meandering jet," *J. Phys. Oceanogr.*, vol. 21, p. 173, 1991.

[198] R. M. Samelson, "Fluid exchange across a meandering jet," *J. Phys. Oceanogr.*, vol. 22, p. 431444, 1992.

[199] S. Dutkiewicz, A. Griffa, and D. Olson, "Particles diffusion in a meandering jet," *Journal of Geophysical Research*, vol. 98, pp. 16487 – 16500, 1993.

[200] J. Duan and S. Wiggins, "Nonlinear stability of one-layer geostrophic fronts," *Physica D*, vol. 98, pp. 335–342, 1996.

[201] G. Boffetta, G. Lacorata, G. Redaelli, and A. Vulpiani, "Detecting barriers to transport: a review of different techniques," *Physica D: Nonlinear Phenomena*, vol. 159, no. 12, pp. 58 – 70, 2001.

[202] S. V. Prants, M. V. Budyansky, M. Y. Uleysky, and G. M. Zaslavsky, "Chaotic mixing and transport in a meandering jet flow," *Chaos*, vol. 16(3), p. 033117, 2006.

[203] M. Y. Uleysky, M. V. Budyansky, and S. V. Prants, "Effect of dynamical traps on chaotic transport in a meandering jet flow," *Chaos: An Interdisciplinary Journal of Nonlinear Science*, vol. 17, no. 4, p. 043105, 2007.

[204] M. V. Budyansky, M. Y. Uleysky, and S. V. Prants, "Detection of barriers to cross-jet Lagrangian transport and its destruction in a meandering flow," *Phys. Rev. E*, vol. 79, p. 056215, 2009.

[205] P. E. Kloeden and E. Platen, *Numerical Solution of Stochastic Differential Equations*. Springer-Verlag (Berlin), 1992.

[206] R. Ishizaki, H. Shibata, and H. Mori, "Effects of external noise on anomalous diffusion in hamiltonian dynamical systems," *Prog. Theor. Phys.*, vol. 103(2), pp. 245–259, 2000.

[207] M. S. Lozier, L. J. Pratt, A. M. Rogerson, and P. D. Miller, "Exchange geometry revealed by float trajectories in the gulf stream," *Journal of Physical Oceanography*, vol. 27, pp. 2327–2341, 1997.

[208] C. Mendoza, A. M. Mancho, and M.-H. Rio, "The turnstile mechanism across the kuroshio current: analysis of dynamics in altimeter velocity fields," *Nonlinear Processes in Geophysics*, vol. 17, no. 2, pp. 103–111, 2010.

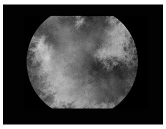

[209] P. L. Read, "Transition to geostrophic turbulence in the laboratory, and as a paradigm in atmospheres and oceans," *Surveys in Geophysics*, vol. 22, pp. 265–317, 2001.

Acknowledgements

First of all I want to thank my Professors Alberto Pérez Muñuzuri and Vicente Pérez Muñuzuri for all their help and faith in my work and Professor Vicente Pérez Villar for the opportunity to do research in his group. I know that most *bosses* would not have given me the liberty to realize my crazy ideas, as for instance doing PIV measurements despite having a wavy surface. It is just fun to be able to discuss physical matters and live in general with you. You always gave me the feeling that science is something good, that collaboration is better than competition and that communication is crucial. It is all but normal that you send your students to congresses around the world to experience the positive side of being a scientist. I truly want to thank you for all that. Now I exactly know the meaning of the word *Doktorvater*. Even though it seems I am a lucky girl and have more than one.

Secondly, I want to thank Guillermo who introduced me into the experiments and the numerics and this field of study. I thank him also especially for his initial patience concerning my Spanish. Thanks also to *my* students, Lisa, Guillermo and Antonio. You have all been special and a challenge for me, each in his own way. I am confident that all the articles will be written one day ;). I hope you find what you are looking for in or out of science and I hope I could fullfill your high expectations. Of course I also want to thank all the other students and Phd-students that coincided with me in the laboratory and collaborated with me on some work: Dani, Dario, Jacobo, Jorge, Jorge, Eva, Lucia, Alberto, Carlos, Alexandre. It has been a fabulous time with you all! Many of you I consider close friends now. I hope you forgive me my temporary absence from any social live due to this crucial work you are just holding in your hands right now. Thanks Dario for the hardware help.. also on Sundays. Jacobo I will always remember your first talk in English. It was enlightening! How many balls were in that box and how did you shake it? Guys, I will never forget the Paella at Furnas. It seems like half a live ago already. Alberto your the best andalusian cook for sure! Thanks to all of you for all the patience and help with the Spanish administration, especially to Alexandre and Jacobo. Talking about administration I have to mention the incredible Benito, who I adore for

his unlimited patience and friendliness no matter what law, rule or form is to be obeyed. Here I also have to thank the people from the Cactus, Minha and Maruxa, who we FPU belong to (administratively speaking). Thanks also to Prof. Gonzalo Míguez Macho for his advice and friendship. Thank you Victor Mosquera Tallón for keeping the Department running. Concerning my time in the U.S.A. I want to thank Prof. Brockmann for hosting me in his group. Also I thank Olivia, Daniel and Nir as well as Jule who coincided with me when I was there. Thank you Hannah! You were the best thing that happened to me in the States and that not only because of your cooking skills. Thanks NU crew for hosting me in your house, even if I was kind of the grandma. Many thanks also to my former group and long-time collaborators in Heidelberg: Prof. Andreas Draguhn, Martin Both and Suse Reichinnek. It will work out one day, right? Your amazing ability to keep on going even if it seems it will never work out is exemplary and you proof that its worth it, too. I also want to thank all my friends in the faculty and cafeteria who helped me concerning my humour during the long days when nothing works out. Thanks for many Doc-Meets and already two (!!) Nerd-Nites. Thanks Jorge Mira and Javier Mas for the support on these activities. Thanks also Antia, Dr. Shock and Emilio for setting up and running the DOC-MEET with Flo and me.

I wish to thank also all the scientists who I do not know for the many enlightening articles that you wrote. Its been great to personally get to know a few of you. Your work was a huge motivation. In this regard I want to thank Stefano Mussachio and Guido Boffetta for final comments on the interpretation of some of the results from the Faraday flow. I also want to thank quite some anonymous referees for constructive criticism which improved my work and even opened up new fields of science (I expressly exclude two anonymous referees from this list).

My dear parents, my dear family, I thank you for your support. I want to thank my closest collaborator and husband Florian Huhn, eventhough its difficult to motivate you its always worth it. You are a great scientist and of course I do not only say that because you are my husband.

Last but not least I want to thank the Spanish Government for the FPU-scholarship with the number AP-2009-0713. This work was supported by the Ministerio de Educacion y Ciencia and the Xunta de Galicia under Research Grants No. FIS$2010-21023$, No. FIS2007-64698, FIS2010-21023 and No. PGIDIT07PXIB-206077PR.

Thank God!

List of Publications

Articles in Peer-reviewed Journals

- **A. von Kameke**, F. Huhn, A. P. Muñuzuri, V. Pérez-Muñuzuri: The Faraday Flow and its two-dimensional characteristics. (in preparation).
- **A. von Kameke**, A. Yañez Santamaria, F. Huhn, A. P. Muñuzuri, V. Pérez-Muñuzuri, and D. Brockmann: Geograpically scale free propagation of excitable media on a network (in preparation).
- A. Yañez Santamaria, **A. von Kameke**, M. Both, A. Draguhn, S. Reichinnek, and A. P. Muñuzuri: A simple frequency switch in self-sustained oscillatory networks (in preparation).
- J. Guiu-Souto, L. Michaels, **A. von Kameke**, J. Carballido-Landeira, and A. P. Muñuzuri: Self-organization on Turing instability under centrifugal forces (submitted), 2012.
- **A. von Kameke**, F. Huhn, A. P. Muñuzuri, and V. Pérez-Muñuzuri: Large spiral and target waves: Turbulent diffusion boosts scales of pattern formation (under revision at PRL), 2012.
- F. Huhn, **A. von Kameke**, V. Pérez-Muñuzuri, M.J. Olascoaga, and F.J. Beron-Vera: The impact of advective transport by the South Indian Ocean Countercurrent on the Madagascar plankton bloom, *Geophys. Res. Lett.* 39, L06602, 2012.
- **A. von Kameke**, F. Huhn, and V. Pérez-Muñuzuri: Asymptotic diffusion coefficients and anomalous diffusion in a meandering jet-flow under environmental fluctuations, *Phys. Rev. E* 85, 017201, 2012.
- S.Reichinnek, **A. von Kameke**, A. M. Hagenston, E.Freitag, F. C. Roth, H.Bading, M. T. Hasan, A. Draguhn, M. Both: Reliable optical detection of coherent neuronal activity in fast oscillating networks in vitro, *NeuroImage*, Vol. 60, 1, 139152, 2012.

- F. Huhn, **A. von Kameke**, S. Allen-Perkins, P. Montero, A. Venancio, and V. Pérez-Muñuzuri: Horizontal Lagrangian transport in a tidal-driven estuary - transport barriers attached to prominent coastal boundaries, *Cont. Shelf Res.* 39-40, 1-13, 2012.

- **A. von Kameke**, F. Huhn, G. Fernández-García, A. P. Muñuzuri, and V. Pérez-Muñuzuri: Double Cascade Turbulence and Richardson Dispersion in a Horizontal Fluid Flow Induced by Faraday Waves, *Phys. Rev. Lett.* 107, 074502, 2011.

- **A. von Kameke**, F. Huhn, G. Fernández-García, A. P. Muñuzuri, and V. Pérez-Muñuzuri: Propagation of a chemical wave front in a quasi-two-dimensional superdiffusive flow, *Phys. Rev. E* 81, 066211, 2010.